



**ALEXANDRE ALVES DE CASTRO**

**Potential Inhibitors Targeting SARS-CoV-2 Proteins Probed  
by in silico Methods**

**LAVRAS-MG**

**2021**

**ALEXANDRE ALVES DE CASTRO**

**Potential Inhibitors Targeting SARS-CoV-2 Proteins Probed  
by in silico Methods**

Tese apresentada à Universidade Federal de Lavras,  
como parte das exigências do Programa de Pós-  
Graduação em Agroquímica, área de concentração  
em Química/Bioquímica, para a obtenção do título  
de Doutor.

Orientador

Dra. Elaine Fontes Ferreira da Cunha

Coorientador

Dr. Teodorico de Castro Ramalho

**LAVRAS-MG**

**2021**

**Ficha catalográfica elaborada pelo Sistema de Geração de Ficha Catalográfica da Biblioteca  
Universitária da UFLA, com dados informados pelo(a) próprio(a) autor(a).**

de Castro, Alexandre Alves.

Potential Inhibitors Targeting SARS-CoV-2 Proteins Probed by  
in silico Methods / Alexandre Alves de Castro. - 2021.

249 p. : il.

Orientador(a): Elaine Fontes Ferreira da Cunha.

Coorientador(a): Teodorico de Castro Ramalho.

Tese (doutorado) - Universidade Federal de Lavras, 2021.

Bibliografia.

1. Química Computacional. 2. Farmacologia. 3. COVID-19. I.  
da Cunha, Elaine Fontes Ferreira. II. Ramalho, Teodorico de  
Castro. III. Título.

**ALEXANDRE ALVES DE CASTRO**

**Potential Inhibitors Targeting SARS-CoV-2 Proteins Probed by in silico Methods**

Tese apresentada à Universidade Federal de Lavras, como parte das exigências do Programa de Pós-Graduação em Agroquímica, área de concentração em Química/Bioquímica, para a obtenção do título de Doutor.

APROVADA em 31 de maio de 2021.

Dr. Mauro Martins Teixeira	UFMG
Dra. Katia Júlia de Almeida	UFLA
Dr. Daniel Henriques Soares Leal	UNIFEI
Dr. Felipe de Almeida La Porta	UTFPR

Orientador

Dra. Elaine Fontes Ferreira da Cunha

Coorientador

Dr. Teodorico de Castro Ramalho

**LAVRAS-MG**

**2021**

*Dedico este trabalho aos meus queridos pais, AURI e MARIA.  
Com carinho, OFEREÇO.*

## **AGRADECIMENTOS**

Agradeço primeiramente a Deus, por sempre ter me guiado e por todas as oportunidades concebidas ao longo da minha vida.

Aos meus pais, Auri e Maria, agradeço, pelo apoio, amor, compreensão e a confiança, durante um longo caminho até chegar aqui, e aos meus irmãos pelo incentivo.

Aos meus orientadores, professores Elaine e Teodorico, pela presença, incentivo, confiança e pela oportunidade de realizar este trabalho e outros. Agradeço, pelos diálogos e pelas valiosas dicas recebidas durante minha vida acadêmica.

À Universidade Federal de Lavras e ao Departamento de Química, pela minha formação acadêmica.

A todos os amigos do Grupo de Química Computacional, pela amizade e convivência durante todo esse período.

A todos os meus colegas de turma 2009/02, pelos bons momentos que passamos juntos e pelo companheirismo.

Aos amigos conquistados ao longo desses anos, obrigado pelo dia a dia, por cada um contribuir à sua maneira para a minha formação.

Agradeço a todos que tiveram uma participação direta ou indireta nesta tese.

Agradeço ao CNPq e FAPEMIG pelo apoio no desenvolvimento deste trabalho.

O presente trabalho foi realizado com apoio da Coordenação de Aperfeiçoamento de Pessoal de Nível Superior – Brasil (CAPES) – Código de Financiamento 001.

**MUITO OBRIGADO!**

*To raise new questions, new possibilities, to regard  
old problems from a new angle, requires creative  
imagination and marks real advance in science.*

Albert Einstein

## RESUMO GERAL

No final de 2019, um novo coronavírus foi identificado como a causa de um conjunto de casos de pneumonia em Wuhan, uma cidade na província de Hubei, na China, sendo posteriormente denominada COVID-19, a qual significa doença de coronavírus 2019. O vírus que causa a COVID-19 é designado por coronavírus 2 da síndrome respiratória aguda grave (SARS-CoV-2). Importantes enzimas virais, tais como a principal protease ( $M^{pro}$ ) e a RNA polimerase (RdRp) são importantes alvos terapêuticos para o tratamento da COVID-19. Neste sentido, esta tese tem como objetivo o uso de abordagens computacionais, as quais podem efetivamente contribuir para a descoberta e desenvolvimento racional de novas terapias, principalmente através do reposicionamento de fármacos. Para a realização destes trabalhos, utilizamos diversas técnicas computacionais, empregando métodos da mecânica quântica e mecânica molecular, para avaliar os modos de interação dos compostos no sítio ativo dos alvos moleculares. Nossos compostos nitroderivados do óxido de quinolina mostraram-se bons inibidores da enzima viral  $M^{pro}$ , de acordo com nossos resultados teóricos, sendo promissores para posteriores estudos experimentais. Nossos resultados também sugerem que a combinação de medicamentos é efetiva devido ao aumento de suas propriedades funcionais, fornecendo uma maneira inovadora de conectar mudanças estruturais com a cinética de transferência eletrônica. Diversos fármacos reposicionados e derivados foram avaliados em relação às suas propriedades inibidoras, cujos resultados de afinidade sugerem que estes compostos são potenciais inibidores da  $M^{pro}$  e RdRp. Por fim, os modos de interação destes fármacos também foram investigados, bem como os modos de interação de seus fragmentos no estudo do metabolismo. Estes estudos mostraram que estes fármacos podem gerar fragmentos metabólitos de diferentes reatividades e toxicidade.

Palavras-chave: Farmacologia, Química Computacional, SARS-CoV-2, Reposicionamento de Fármacos, COVID-19.



## GENERAL ABSTRACT

In late 2019, a new coronavirus was identified as the cause of a set of pneumonia cases in Wuhan, a city in China's Hubei province, later denominated COVID-19, which means coronavirus disease 2019. The virus that causes COVID-19 is called severe acute respiratory syndrome coronavirus 2 (SARS-CoV-2). Important viral enzymes, such as the main protease ( $M^{pro}$ ) and RNA polymerase (RdRp) are important therapeutic targets for the treatment of COVID-19. In this sense, this thesis aims to use computational approaches, which can effectively contribute to the discovery and rational development of new therapies, mainly through the drug repositioning. To carry out these works, we used several computational techniques, employing methods of quantum mechanics and molecular mechanics, to evaluate the interaction modes of the compounds in the active site of the molecular targets. Our quinoline oxide nitroderivative compounds showed to be good inhibitors of the viral enzyme  $M^{pro}$ , according to our theoretical results, being promising for further experimental studies. Our results also suggest that the drug combination is effective due to their increased functional properties, providing an innovative way to connect structural changes with electron transfer kinetics. Several repositioned drugs and derivatives were evaluated for their inhibitory properties, whose affinity results suggest that these compounds are potential inhibitors of  $M^{pro}$  and RdRp. Finally, the interaction modes of these drugs were also investigated, as well as the interaction modes of their fragments in the study of metabolism. These studies showed that these drugs can generate metabolite fragments with different reactivity and toxicity.

Keywords: Pharmacology, Computational Chemistry, SARS-CoV-2, Drug Repositioning, COVID-19.

## LIST OF FIGURES

### CHAPTER 2

- Figura 1** - Representation of virus lodged in the lung (A), highlighting a normal (B) and affected (C) lungs. A scanning electron microscope image of SARS-CoV-2 is shown in (D). The scheme of entry of virus in the host cell is also presented (E), together with the structural representation of the crystallographic structures of M<sup>pro</sup> (F), RdRp (G) and RBD (pale green ribbon) bound ACE2 (surface) (H). Credits: NIAID-RML.....41
- Figura 2** - Chemical structures of (a) gilteritinib, (b) ipatasertib, (c) prinomastat, (d) marimastat, (e) chloroquine, (f) hydroxychloroquine, (g) favipiravir, (h) remdesivir, (i) azithromycin, (j) clarithromycin, (k) erythromycin, (l) ivermectin, (m) cyclosporine, (n) dacomitinib, (o) salinomycin, (p) PF-07321332 and (q) PF-07304814.....46

### CHAPTER 3

- Figure 1**- Crystallographic structure of the COVID-19 virus M<sup>pro</sup> enzyme with the co-crystallized ligand 6-(ethylamino)pyridine-3-carbonitrile (PDB code 5R82) (up), and re-docking result of the co-crystallized ligand through AutoDock Vina as implemented in the MolAr software (down).....76
- Figure 2** - Optimised structures of nitro derivatives of (a) Q and (b) QO and computed electrostatic potential maps with contour value of 0.004.....78
- Figura 3** - Intermolecular interactions performed by the inhibitors (A) N-4-Q, (B) N-4-QO, (C) CQ, (D) CQO, (E) HCQ and (F) HCQO in the M<sup>pro</sup> active site.....81
- Figure 4** - Overlap of the initial (red) and representative (blue) structures of the 20-ns simulation of MD.....83
- Figura 5** - Interactions performed during 20ns in the MD simulation with the (A) M<sup>pro</sup>/N-4-Q, (B) M<sup>pro</sup>/N-4-QO, (C) M<sup>pro</sup>/CQ, (D) M<sup>pro</sup>/CQO, (E) M<sup>pro</sup>/HCQ, (F) M<sup>pro</sup>/HCQO complexes.....87
- Figure S1** - Simulated (a and b) UV-vis and (c and d) IR spectra of nitro derivatives of Q and QO.....100

<b>Figure S2</b> - Frontier molecular orbital representation (with a contour value of 0.020) for the nitro derivatives of Q and QO.....	101
<b>Figure S3</b> - Chemical structures of the species employed in the MD simulations.....	102
<b>Figure S4</b> - RMSD, Total Energy, Hydrogen Bond, Interaction Energy and RMSF graphs of a 20 ns simulation of the N-4-Q.....	103
<b>Figure S5</b> - RMSD, Total Energy, Hydrogen Bond, Interaction Energy and RMSF graphs of a 20 ns simulation of the N-4-QO.....	104
<b>Figure S6</b> - RMSD, Total Energy, Hydrogen Bond, Interaction Energy and RMSF graphs of a 20 ns simulation of the CQ.....	105
<b>Figure S7</b> - RMSD, Total Energy, Hydrogen Bond, Interaction Energy and RMSF graphs of a 20 ns simulation of the CQO.....	106
<b>Figure S8</b> - RMSD, Total Energy, Hydrogen Bond and Interaction Energy graphs of a 20 ns simulation of the HCQ.....	107
<b>Figure S9</b> - RMSD, Total Energy, Hydrogen Bond, Interaction Energy and RMSF graphs of a 20 ns simulation of the HCQO.....	108
<b>Figure S10</b> - Chemical structures of the $\alpha$ -ketoamides used in the work.....	109
<b>Figure S11</b> - Intermolecular interactions performed by the $\alpha$ -ketoamide inhibitors 11n, 11r and 11s in the M <sup>Pto</sup> active site.....	110
<b>Figure S12</b> - General Temperature and Pressure graphs acquired from the equilibration process of the systems.....	111

## CHAPTER 4

<b>Figure 1</b> - Representation of optimized co-crystal structures in this study. (a) CQ/AZ; (b) CQ/CL; (c) CQ/ER; (d) HQ/AZ; (e) HQ/CL and (f) HQ/ER.....	115
<b>Figure 2</b> - Overlap obtained from re-docking calculations of the experimental co-crystallized active ligand N3 (PDB code: 6lu7) through MVD.....	117
<b>Figure 3</b> - Simulated IR spectra of the co-crystals formed between (left) Chloroquine and (right) Hydroxychloroquine with macrolide antibiotics at the PM6 theoretical level.....	119
<b>Figure 4</b> - Simulated UV-vis spectra and frontier molecular orbitals of the co-crystals using a contour value of 0.020. For each co-crystal, the HOMO orbitals are represented on the left and LUMO orbitals on the right in the same figure.....	120

<b>Figure 5</b> - Representation of the conformation of the most stabilizing HQ/AZ in the M <sup>pro</sup> active site.....	123
<b>Figure 6</b> - Intermolecular interactions of the co-crystals in the viral M <sup>pro</sup> active site. E: glutamate, G: glycine, H: histidine, C: cysteine, S: serine, Y: tyrosine, L: leucine, Q: glutamine, P: proline, R: arginine, N: asparagine, F: phenylalanine, T: threonine.....	125
<b>Figura S1</b> - Intermolecular interactions of single-crystals in the viral M <sup>pro</sup> active site and overlap obtained from re-docking calculations of the experimental co-crystallized active ligand N3 (PDB code: 6lu7) through MVD.....	147

## CHAPTER 5

<b>Figura 1</b> - Chemical structure and tautomeric form of favipiravir.....	150
<b>Figura 2</b> - Optimized structures and ESP maps (with surface isovalue of 0.0004) for the halogenated favipiravir tautomeric forms: (a) 1-F; (b) 1-Cl; (c) 1-Br; (d) 2-F; (e) 2-Cl and (f) 2-Br.....	154
<b>Figura 3</b> - Computed (a) IR and (b) Raman spectra of the derivatives.....	157
<b>Figura 4</b> - Computed (a and b) UV-Vis and emission, (c and d) ECD spectra and (e) MOs shapes (with a surface isovalue of 0.03) of both (a) 1 and (b) 2 derivative tautomer forms.....	159
<b>Figura 5</b> - EI-MS diagrams, trajectories and intermediaries of all studied derivatives. (a) 1-F, (b) 1-Cl, (c) 1-Br, (d) 2-F, (e) 2-Cl and (f) 2-Br structures.....	162
<b>Figura 6</b> - Re-docking overlaps and representation of the interactions performed by co-crystallized ligand for SARS-CoV-2 M <sup>pro</sup> and SARS-CoV-2 RdRp sites. Interactions: green= Hydrogen bond, pink = hydrophobic and orange = coulombians.....	165
<b>Figura 7</b> - Representation of the interactions performed by favipiravir and its derivatives in the SARS-CoV-2 RNA polymerase site.....	170
<b>Figura 8</b> - Representation of the interactions performed by favipiravir and its derivatives in the M <sup>pro</sup> active site.....	171

## CHAPTER 6

<b>Figura 1</b> - Schematic representation of computational strategy proposed in this study to the investigation of the metabolism effect in drug design. The strategy used to build these models have based on three different situations: (a) no previous metabolism and (b) prior effect of metabolism to the inhibitory process.....	183
<b>Figura 2</b> - EI-MS fragmentation spectra and trajectories of a) Favipiravir, b) Galidesivir, c) Nitazoxanide, d) Remdesivir and e) Ribavirin.....	186
<b>Figura 3</b> - Intermolecular interactions of the drugs investigated in the RdRp binding site.....	200
<b>Figura 4</b> - Intermolecular interactions of the drugs investigated in the M <sup>pro</sup> binding site.....	201
<b>S2</b> - Optimized structures, bond lengths of functional groups and esp maps (with surface isovalue of 0.0004) of a) favipiravir, b) galidesivir; c) nitazoxanide, d) remdesivir, and e) ribavirin.....	214
<b>S3</b> - Estimated a) uv-vis and b) ecd spectra of the drugs.....	215
<b>S5</b> - Theoretical (black) and experimental (pink) ei-ms spectra of a) chloroquine and b) hydroxychloroquine, and their respective trajectories, by means of gfn2-xtb. theoretical (black) and experimental (pink) ei-ms spectra of c) chloroquine and d) hydroxychloroquine resulted from the gfn1-xtb method.....	217
<b>S6</b> - Pharmacophoric maps showing the intermolecular interactions of the fragments of diverse drugs in the RdRp and M <sup>pro</sup> active site.....	220

## LIST OF ABBREVIATIONS

<b>3C<sup>pro</sup></b>	3C-like proteinase
<b>ACE2</b>	Angiotensin-converting enzyme 2
<b>ADMET</b>	Absorption-Distribution-Metabolism-Excretion-Toxicity
<b>ATZ</b>	Atazanavir
<b>AZ</b>	Azithromycin
<b>CADD</b>	Computer-aided drug design
<b>CL</b>	Clarithromycin
<b>CoV<sub>s</sub></b>	Coronavirus
<b>CQ</b>	Chloroquine
<b>CQO</b>	Chloroquine <i>N</i> -oxide
<b>CNT</b>	Carbon nanotubes
<b>DFT</b>	Density Functional Theory
<b>ECD</b>	Electronic Circular Dichroism
<b>EI-MS</b>	Electron Ionization Mass Spectrometry
<b>ER</b>	Erythromycin A
<b>ESIPT</b>	Excited States Intramolecular Proton Transfer
<b>FDA</b>	Food and Drug Administration
<b>FRET</b>	Förster Resonance Energy Transfer
<b>HCQ</b>	Hydroxychloroquine
<b>HCQO</b>	Hydroxychloroquine <i>N</i> -oxide
<b>HOMO</b>	Highest Occupied Molecular Orbital
<b>IC<sub>50</sub></b>	The half maximal inhibitory concentration
<b>LD<sub>50</sub></b>	Median lethal dose
<b>LUMO</b>	Lowest Unoccupied Molecular Orbital
<b>MERS</b>	Middle East Respiratory Syndrome
<b>MolAr</b>	Molecular Architecture
<b>MD</b>	Molecular Dynamics
<b>MM</b>	Molecular Mechanics
<b>MOs</b>	Molecular Orbitals
<b>M<sup>pro</sup></b>	Main protease

<b>NBO</b>	Natural Bond Orbitals
<b>PDB</b>	Protein data bank
<b>PES</b>	Potential energy surface
<b>PL<sup>pro</sup></b>	Papain-like protease
<b>QCEIMS</b>	Quantum Chemistry Electron Ionization Mass Spectrometry
<b>QM</b>	Quantum Mechanics
<b>Q</b>	Quinoline
<b>RBDs</b>	Receptor-binding domains
<b>RdRp</b>	RNA-dependent RNA polymerase
<b>RNAP</b>	RNA polymerase
<b>RMSD</b>	Root mean square deviation
<b>RMSF</b>	Root mean square fluctuation
<b>SARS</b>	Severe Acute Respiratory Syndrome
<b>TDDFT</b>	Time-dependent density functional theory
<b>VMD</b>	Visual Molecular Dynamics
<b>VS</b>	Virtual Screening
<b>WHO</b>	World Health Organization

## SUMMARY

<b>CHAPTER 1 - Introduction and Theoretical Background</b> .....	18
<b>1. Introduction</b> .....	18
<b>2. General objective</b> .....	19
<b>3. Theoretical Background</b> .....	19
3.1 COVID-19 .....	19
3.2 Computational Chemistry .....	21
3.3 Virtual Screening .....	24
3.4 Molecular Docking.....	25
3.5 Molecular Dynamics.....	26
3.6 Principles of Quantum .....	27
3.7 Density Functional Theory (DFT) .....	28
3.7.1 Basis set .....	31
3.7.2 Density Functional .....	32
3.8 Additional methods of analysis .....	32
<b>4. References</b> .....	33
<b>CHAPTER 2 - Insights into the Computational Drug Repositioning for Potential Pharmacotherapy of COVID-19</b> .....	39
<b>CHAPTER 3 - Nitro derivatives of quinoline and quinoline <i>N</i>-oxide as low-cost alternative for the treatment of SARS-CoV-2 infection: a computational evidence</b> .....	73
Supplementary Material .....	96
<b>CHAPTER 4 - New in silico insights into the application of the (hydroxy)chloroquine with macrolide antibiotics co-crystals against the SARS-CoV-2 virus</b> .....	112
Supplementary Material .....	130
<b>CHAPTER 5 - Theoretical insights into the effect of halogenated substituent on the electronic structure and spectroscopic properties of the favipiravir tautomeric forms and its implications on the treatment of COVID-19</b> .....	148
<b>CHAPTER 6 - Effect of drug metabolism in the treatment of SARS-CoV-2 from an entirely computational perspective</b> .....	179
Supplementary Material .....	206
<b>CONCLUSIONS</b> .....	236
<b>ATTACHMENT</b> .....	237



## **CHAPTER 1**

### *Introduction and Theoretical Background*

## 1. Introduction

The novel coronavirus disease 2019 (COVID-19) has posed significant threats to world health and the economy. The COVID-19 caused an outbreak of pulmonary disease in the capital of Hu-bei province in China, called Wuhan. The virus has spread rapidly around the world, resulting in millions of deaths since December 2019 (Wu et al., 2020; Zhou et al., 2020). Properly, the International Committee on the Taxonomy of Viruses denominated the virus as severe acute respiratory syndrome coronavirus 2 (SARS-CoV-2). This denomination comes from the fact of the RNA genome is about 82% identical to the SARS coronavirus (SARS-CoV) (Zhang et al., 2020). At the beginning of the outbreak, cases were connected to the Huanan seafood and animal market in Wuhan. From that moment, efficient human-to-human transmission has gained strength, and consequently, it is observed an exponential growth in the number of cases in all over the world (Zhang et al., 2020; Zhang and Liu, 2020). The World Health Organization (WHO) responded quickly to the COVID-19 threat by developing diagnostics and providing guidance on patient monitoring as well as up-to-date information. The WHO declared the outbreak a pandemic on March 11 (Arabi et al., 2020; Munster et al., 2020).

The coronavirus, initially isolated in 1937, became known in 2002 and 2003 for causing a severe acute respiratory syndrome in humans denominated SARS. In season, the epidemic was responsible for many cases of serious infections in the lower respiratory system, accompanied by fever and, often respiratory failure (Fung et al., 2020). However, it was rapidly controlled and only a few countries like China, Canada and the USA were affected by the virus (Schwartz and Graham, 2020). Eighteen years after the first SARS-CoV cases, this new virus denominated SARS-CoV-2 is responsible for the rapid spread of the disease at global levels. This new strain is less lethal than other family members, such as SARS-CoV and the virus that causes Middle East Respiratory Syndrome (MERS-CoV), which appeared in Saudi Arabia, 2012. However, although the strains are originated from a common ancestor, SARS-CoV-2 has greater potential of dissemination (Fauci et al., 2020; Gates, 2020).

In line with this worrying and chaotic scenario, it is crucial the development of novel and promising therapies to treat COVID-19. Today, systematic computational drug repositioning methods are efficient approaches to infer potential indications for drugs and can improve their efficiency. Computational analyses amplify the traditional approaches because they allow the researchers to generate, evaluate, and prioritize data for several drugs and

diseases simultaneously. These studies can optimize the experimental design, and even resulting in cost savings (Hurle et al., 2013).

## 2. General objective

This thesis is focused on theoretical approaches applied to processes of drug discovery and development for the treatment of COVID-19. Diverse compounds were investigated regarding their therapeutic potential to combat the disease, and novel computational approaches were developed in order to raise new insights about the remediation modes of COVID-19.

The specific objectives can be described as follows:

- 1) Review in the literature about the use of computational tools in the discovery of novel drugs for COVID-19 treatment, through the drug repositioning approach.
- 2) Computational study of nitro derivative compounds and their corresponding oxides as potent inhibitors targeting the M<sup>pro</sup> enzyme.
- 3) Predicting the formation of co-crystals by employing repositioned drugs and assessment of their interaction modes in the M<sup>pro</sup> active site, seeking to optimize the inhibition process.
- 4) Investigation of all tautomeric forms derived from favipiravir and their halogenated derivatives toward the viral M<sup>pro</sup> and RNA polymerase (RdRp).
- 5) Investigations into the metabolism of diverse drugs in order to better comprehend the action modes of these agents within the therapeutic targets (M<sup>pro</sup> and RdRp).

## 3. Theoretical Background

### 3.1 COVID-19

COVID-19 has become a threat at the global level. By early January 2020, the virus-related sequence was determined. According to the molecular structure revealed for SARS-CoV-2, it is shown a sequence identity of 88% in relation to two coronaviruses found in bats (bat-SLCoVZC45 and bat-SL-CoVZXC21). The bat is believed to be the original host of SARS-CoV-2, and this animal-to-human transmission is considered the origin of epidemics. Moreover, an intermediate host may still exist in the process of transmission from bats to human

beings. This evidence is supported by the fact that many patients reported to have visited the Huanan Seafood Wholesale Market in Wuhan (Lu, Stratton e Tang, 2020). In addition, the SARS-CoV-2 reveals 79% identity with SARS (Severe Acute Respiratory Syndrome) coronavirus and 50% identity with MERS (Middle Eastern Respiratory Syndrome) coronavirus (Park, Thwaites e Openshaw, 2020). It is important to notice that this is the third coronavirus that has emerged in the past 2 decades. In this worrying scenario, the novel coronavirus has caused multiple outbreaks at the global level and substantial morbidity and mortality (Munster et al., 2020; Perlman, 2020).

The overall situation is getting serious day by day in diverse countries. For the development of further techniques of prevention and control, it is crucial that we have a better comprehension of the pandemic nature. On January 30, 2020, the WHO brought to the public that the COVID-19 outbreak is the sixth public health emergency of global concern, following H1N1 (2009), polio (2014), Ebola (2014 - West Africa), Zika (2016) and Ebola (2019 - Democratic Republic of Congo) (Dey et al., 2020; Yoo, 2020). Note that, like MERS and SARS, there are no distinguishing clinical features of COVID-19 and symptoms overlap significantly with other severe acute respiratory infections (Arabi et al., 2017; Arabi, Murthy e Webb, 2020; Chen et al., 2020; Huang et al., 2020). Clinical characterization protocols are now being collected on patients worldwide to better define the illness, in terms of its natural history, mode of transmission, clinical profiles, management and specific risk factors, in order to prevent or overcome the damaging effects of the disease (Arabi, Murthy e Webb, 2020; Zhang, T. et al., 2020).

COVID-19 replicates in an efficient way in the upper respiratory tract, and infected patients generate a large quantity of virus contributing to the spread of infection (Chan et al., 2020). Non-pharmaceutical interventions are essential for the management of the COVID-19, along with licensed available vaccines or even coronavirus antivirals (Heymann e Shindo, 2020). Based on clinical observations, it is noticed that the proportion of individuals infected by COVID-19 who remain asymptomatic over the course of infection has not yet been definitely evaluated. Note that even these asymptomatic patients can potentially be a source of infection. The forms of transmission are usually through respiratory droplets and contacting. Unfortunately, people are generally susceptible to the virus (Deng e Peng, 2020). In symptomatic patients, the characteristic symptoms of the disease usually start after less than a week, consisting of fever, cough, nasal congestion, fatigue, along with other signs of upper

respiratory tract infections (Guan et al., 2020). This worrying scenario raises important issues on how to deal with this global threat, and the emergence of novel forms of therapies become essential.

In the process of drug discovery, two major therapeutic targets have been intensively investigated, the protease ( $M^{pro}$ ) and RNA polymerase (RdRp). The  $M^{pro}$  is a viral enzyme, which plays a central role in mediating viral replication and transcription, making it an attractive target for the development of novel drugs. The  $M^{pro}$  is a cysteine protease present in coronavirus and was previously studied as a molecular target for the design and discovery of antivirals for the treatment of SARS and MERS. As a consequence, it became one of the most studied molecular targets worldwide, in the search for pharmacological therapies for the COVID-19 treatment (Almeida et al., 2020). The RdRp is another quite important therapeutic target, consisting of a replicase enzyme, which catalyzes the synthesis of a new complementary RNA molecule, through using viral genomic RNA as a template, thus allowing to give rise to a new virus. Its main function is to ensure that the replication of the virus RNA genetic material occurs effectively (Almeida et al., 2020). These molecular targets were employed in our studies.

### **3.2 Computational Chemistry**

Initially, we could consider two of the major divisions of the computational chemistry methods. Molecular Mechanics (MM) and Quantum Mechanics (QM), wherein the former uses laws of classical mechanics and QM uses laws of quantum mechanics and physical constants. Computing chemists employ programs and methodologies applied to specific chemical problems. Computational techniques that deal from nanotechnology to the simulation of industrial processes can be used. One can thus solve the problems integrally, from the molecular level to the macroscopic level. In this sense, we have the conditions to find the appropriate solution for each situation that presents itself. These works are characterized by their efficient techniques and by always allowing improvements in the procedures, besides the reduction of costs (SIEGBAHN; BLOMBERG, 2000).

With the advance and sophistication of computational methods in recent years, a large amount of information has been increasingly rapidly processed and, with the aid of new tools and computational methodologies, better and more accurate results have been obtained in an attempt to simulate a variety of chemical parameters and correlates (CARVALHO et al., 2003).

One of the great advantages of computational methods is their low cost in comparison to those of experimental methods, since they avoid the experimental repetitions of analyzes and reactions, as well as the expense of reagents and materials. Furthermore, computational simulations can be made in order to improve and understand processes, reactions, intra- and intermolecular interactions of the molecular systems under investigation. The application of computational methods to solve chemical problems extends to areas where chemistry plays an important role, of direct or indirect form. In this context, more detailed knowledge about biological processes, such as the interaction between the SARS-CoV-2 viral enzymes and different drugs, should be evaluated and simulated by using computational chemistry methods, in an attempt to investigate the pharmacological potential of diverse therapeutic agents for applications in the COVID-19 treatment.

Molecular modeling softwares and networked databases are now fundamental tools for the discovery and planning of new compounds. The analyses using these kinds of tools allow a rapid assessment of the biological activity *versus* physical-chemical properties of a number of molecules of interest (CARVALHO et al., 2003).

Molecular modeling, according to IUPAC, is the investigation of molecular structures and properties, through the use of computational chemistry and graphic visualization techniques, aiming at providing a three-dimensional representation under a given data set (CARVALHO et al., 2003; SANT'ANNA, 2002). This is possible through the generation, manipulation and/or realistic representation of these structures (SILVA, 2006).

One of the most important advances in the planning and discovery of new drugs has been performed by using molecular modeling. It has established itself as an indispensable tool not only in the process of discovering novel drugs, but also in the optimization of an already existing prototype. The great development of this area was due, in large part, to the advance of computational resources in terms of hardware (calculation speed) and software (molecular modeling programs) (RODRIGUES, 2001).

The theoretical methods related to this approach allow to calculate properties of individual molecules (stable conformations, charges and atomic interactions), energies of molecules, in order to display, overlap, and compare geometric and electronic molecular models, as well as to access, manipulate and manage chemical and biological databases (SILVA, 2006). The modeling and its graphic representations are, therefore, tools used for the

construction, edition, visualization, analysis and storage of complex molecular systems (BARREIRO; RODRIGUES, 1997; COHEN et al., 1990).

These tools provide important information, allowing the obtaining of specific parameters of a molecule that can influence the interaction with the receptor (SILVA, 2006). As examples, we can cite the electrostatic potential map, the electron density contour, as well as the energy and coefficients of the HOMO (Highest Occupied Molecular Orbital) and LUMO (Lowest Unoccupied Molecular Orbital) frontiers. This tool also has the potential to theoretically plan new molecules that satisfy the electronic and structural properties for a perfect fit in the receptor site (RODRIGUES, 2001).

Most modeling programs are able to draw the molecular structure, performing geometric optimization calculations and conformational analysis studies. The output files of these calculations can be used as input files for other programs. In this way, the first step of molecular modeling is to design the structure of the molecule. Then, the molecule is optimized, aiming to find geometric parameters, such as lengths and binding angles, which are close to experimentally determined values (CARVALHO et al., 2003; RODRIGUES, 2001).

The MM-based methods are really important in molecular modeling. They promote the modification of the angles and lengths of the bonds of the original atoms and provide new conformations with the corresponding energy calculations (CARVALHO et al., 2003; PATRICK; FLANAGAN, 2001). Didactically, it can be said that in MM, molecules are described as a set of “connected atoms”, in which each atom is considered as a point mass that is connected by springs, which are the chemical bonds. The movement of each atom is determined by the forces acting on it by all the other atoms. These forces acting on each particle are calculated at each step using force fields (SANT’ANNA, 2009).

The choice of the energy minimization method will depend on certain factors related, for example, the size of the molecule, the availability of parameters, stored data and computational resources (CARVALHO et al., 2003). There are several options regarding the calculation method to be applied in a particular molecular modeling strategy. These methods can be classical or quantum. The application of one or the other is determined by the variables: time, precision of the results and complexity of the system being studied (COHEN et al., 1990). Among the molecular modeling methods, we can mention molecular docking and molecular dynamics (MD).

### 3.3 Virtual Screening

Virtual Screening (VS) is a large-scale computational analysis of large databases in order to identify new potentially active molecules. The databases used in the VS can contain thousands of commercially available compounds, with physico-chemical and biological properties similar to those exhibited by recognized drugs, commercially available or accessible by organic synthesis, hypothetical molecules (designed on a computer before synthesis) or even products of natural origin (Rodrigues et al., 2012; Montanari et al., 2011). In addition to the identification of new bioactive compounds, VS also aims to eliminate molecules with marked toxicity and that have unfavorable pharmacodynamic and pharmacokinetic properties, thus reducing the development cycle time and increasing the chances of success when selecting potentially active molecules. VS strategies can be classified into two approaches: screening based on ligands and screening based on the structure of the molecular target (Varnek, 2011).

For methods that are based on the structure of ligands, the VS uses organic molecules with known biological activity, acting as templates for screening in databases of new chemical entities with some level of similarity, which share the same biological activity. Thus, compounds are selected according to the most varied methods of molecular and pharmacophoric similarity, guided by relationships between structural properties and biological activity (Montanari, et al., 2011). Techniques based on the molecular target structure consider the three-dimensional (3D) structure of the therapeutic target, using as major strategy the docking calculations for selection of potential ligands, with structural factors that favor interactions with the binding site of the molecular target. The planning of bioactive substances based on the structure of the molecular target is one of the most robust strategies for identification of new ligands, able to contribute to the entire process, from the analysis of the 3D structure of the therapeutic target until the optimization of molecular interactions and pharmacokinetic properties of the candidate compounds for clinical trials (Rodrigues et al., 2012).

For the accomplishment of the virtual screening, the use of a library of chemical compounds is a crucial step that must supply compounds with the highest possible degree of molecular diversity. The quality of the database used is quite important as it is the source from where the promising compounds will be selected for future biological trials (Rodrigues et al., 2012).



### 3.4 Molecular Docking

The computational simulation of molecular docking is one of the most important investigation techniques of the molecular interactions between the protein and a ligand in cases in which the 3D structure of the protein has already been elucidated. This kind of simulation finds the most stable structure of the protein-ligand complex and calculates this relative stability. In order to find the lower energy structure, without any previous assumption, it is necessary to analyze all interaction modes, considering the conformational flexibility of the ligand to be introduced in the protein active site. Because these two problems are interconnected, they can be solved at the same time; however, the number of combinations involved is very large (MIZUTANI; NIWA; TANAKA, 1994).

An interesting way to search for the most stable structure of the complex (not necessarily the global minimum) was proposed by Kuntz et al. (KUNTZ et al., 1982). The initial fundamental idea of this method is to represent both the binding molecule and the macromolecular surface by a set of spheres and to look for (stochastic method) which is the best pairing of the spheres. The complementarity of the molecular form is very important in the docking method. Subsequently, a more efficient method for the molecular coupling of flexible ligands was developed by Leach and Kuntz. The method consists first of determining the position and orientation of the rigid fragments of the ligand and then investigating the conformations of the flexible region of the ligand in a systematic way. The intermolecular interaction energy is calculated by summing the energy contributions between all atoms of the two molecules, disregarding the interactions between the atoms of the same molecule (LEACH; ZNOJIL, 1992).

The interactions between ligand and receptor require complex studies. Ligands need to change their conformation as they fit into the protein active site. Binding-induced conformational changes in the receptor also occur in such a way that activation or inhibition of a given protein becomes possible (GONÇALVES, 2008). Docking methods use the energy involved in the process to identify the conformation of the ligand energetically more favorable when attached to the target.

Generally, lower energy values stand for better protein-ligand interactions, compared to higher energy values. Thus, molecular docking determines the most likely conformation of the

ligand in the enzyme, taking into account the interaction mode with the lowest energy (THOMSEN; CHRISTENSEN, 2006).

### 3.5 Molecular Dynamics

Molecular Dynamics (MD) simulations have been widely used to study the dynamics and structure of macromolecules, such as proteins, nucleic acids and lipid bilayers (DURRANT; MCCAMMON, 2011; MELLER, 2001). MD studies are generally carried out after molecular docking in selected conformations of each ligand, in order to provide a better understanding of the ligand-enzyme interactions as a function of time, and thus provide a possible explanation of the forces involved in the ligand-receptor complex or the role of the solvent in protein dynamics (ALONSO; BLIZNYUK; GREASY, 2006; GUIMARÃES; RAMALHO; FRANÇA, 2014; KARPLUS; MCCAMMON, 2002). Some of the most common programs used in MD studies are AMBER (WEINER; KOLLMAN, 1981), CHARMM (BROOKS et al., 1983), NAMD (KALÉ et al., 1999; PHILLIPS, 2005) e GROMACS (SCOTT et al., 1999).

In a general MD simulation, molecules that have a certain kinetic energy are able to overcome small potential energy barriers, which allows limited exploration of the potential energy surface (PES) in the search for other stable conformations. MD calculations solve Newton's equations of motion for each atom  $i$  of the molecular system, as represented in Equation 1:

$$\vec{F}_i = m_i \cdot \vec{a}_i \quad (1)$$

Where  $F_i$  is the force that causes acceleration in an atom of mass  $m_i$ . The classic analytical treatment only allows the solution of these equations for systems with up to two independent particles. Resolution for larger systems is made using additional numerical methods and approximations to reduce the complexity of general strength assessments. Given this, we can quote the Verlet Algorithm, which has the function of assisting in the integration of Newton's equations. If the position at time  $t$  is  $r(t)$ , the position after a short time interval  $\Delta t$  can be obtained by the following Taylor series, as follows (Equation 2):

$$r(t+\Delta t) = r(t) + \frac{dr}{dt} \Delta t + \frac{d^2r}{dt^2} \frac{\Delta t^2}{2} + \dots \quad (2)$$

The numerical solution then depends on the knowledge of the position  $r(t)$ , the speed  $dr/dt$  and the acceleration  $d^2R/dt^2$  for each atom. The time interval,  $\Delta t$ , of each step of the path is a very important parameter in an MD calculation. First,  $\Delta t$  must be small enough that the acceleration can be considered constant in that interval; however, very short intervals would make the calculation times of the complete reaction path prohibitive. In practice, the  $\Delta t$  used is 0.5 to 1 fs in order to adequately sample the oscillations of hydrogen bonds (DURRANT; MCCAMMON, 2011; MELLER, 2001).

### 3.6 Principles of Quantum

In 1926, the Austrian physicist Schrödinger, inspired by De Broglie's thesis and Hamilton-Jacobi's theory (a version of classical mechanics), developed the wave equation of wave mechanics. This equation was applied to the Bohr atom model and it was shown that the values of the energies thus quantized were in agreement with the experimental results and were exactly the same as those obtained by a more abstract method developed a year earlier by Heisenberg. This equation, now called the Schrödinger equation, is the basis of the energies calculations of atoms and molecules (ALCÁCER, 2007).

The Schrödinger equation, time-independent, can be generalized to the three dimensions of space:

$$\left[ -\frac{\hbar^2}{2m} \left( \frac{\partial^2}{\partial x^2} + \frac{\partial^2}{\partial y^2} + \frac{\partial^2}{\partial z^2} \right) + V(x, y, z) \right] \Psi(x, y, z) = E \Psi(x, y, z) \quad (3)$$

Given that it is the Laplacian, generally represented by  $\nabla^2$  or  $\Delta$ , we can write the Schrödinger equation in the following form:

$$\left[ -\frac{\hbar^2}{2m} \nabla^2 + V(x, y, z) \right] \Psi(x, y, z) = E \Psi(x, y, z) \quad (4)$$

In fact, the whole bracket is a mathematical operator, called Hamiltonian, which is usually represented by  $H$ . We can therefore write the Schrödinger equation briefly, as in Equation 5,

wherein  $r$  stands for the set of three space coordinates,  $r = (x, y, z)$ . In most chemistry problems, we intend to calculate the possible energy values of the system,  $E$  (ALCÁCER, 2007).

$$\hat{H}\psi(r) = E\psi(r) \quad (5)$$

This equation describes the wave functions (the states) of the particles when their energy is well defined, i.e., it describes steady states. With it, we can obtain most of the results of non-relativistic quantum mechanics, such as the energy spectrum of the hydrogen atom. The Schrödinger equation is especially important in quantum chemistry calculations, covering several computational methods. In this sense, we can cite the Density Functional Theory (DFT), which is a widely employed technique.

### 3.7 Density Functional Theory (DFT)

Due to the large number of atoms in proteins and the fact that reactions involve the breaking and formation of chemical bonds, enzymatic catalysis is a great challenge for computational chemistry (BORMAN, 2004). High-level quantum-mechanical methods are limited to applications in systems with relatively small numbers of atoms. The combination of both quantum-mechanical and molecular mechanics (QM/MM) methods exceeds the domain of QM calculations to macromolecules. In the QM region, atoms are represented by nuclei and electrons, and the potential surface is constructed within the Born-Oppenheimer approximation (BORMAN, 2004).

One method to obtain the QM results is the Density Functional Theory (DFT). The method was formulated by Hohenberg, Kohn and Sham (KOHN; HOLTHAUSEN, 2001). According to Ziegler (1991, p. 651): "The basic notion in DFT that the energy of a particular electronic system can be expressed in terms of its density is almost as old as quantum mechanics itself [...]". Hohenberg and Kohn also showed that energy, wave function and other molecular properties are uniquely determined by this electronic probability density  $\rho [x, y, z]$  (according to Hohenberg-Kohn's theorem), i.e., electron density and Hamiltonian have a functional relationship that allows the computation of all molecular properties in the ground state without

a wave function. But these theorems do not mention how to find the ground state energy from  $\rho$  or from  $\psi$ . This problem was circumvented by Kohn and Sham in the 1960s, when they proposed that the purely electronic energy of a molecule with many electrons in the ground state would be (Equation 6):

$$E_0 = -\frac{1}{2} \sum_{i=1}^n \langle \Psi_i(1) | \nabla_1^2 | \Psi_i(1) \rangle - \sum_{\alpha} \int \frac{Z_{\alpha} \rho(1)}{r_{1\alpha}} dv_1 + \frac{1}{2} \iint \frac{\rho(1)\rho(2)}{r_{12}} dv_1 dv_2 + E_{xc}[\rho] \quad (6)$$

Wherein  $\Psi_i(\mathbf{1})$ ,  $i = 1, 2, \dots, n$  are the Kohn-Sham orbitals, and  $E_{xc}[\rho]$  is the energy of exchange and correlation. Kohn and Sham also showed that exact " $\rho$ " for the ground state could be determined by the  $\Psi_i$  orbitals (Equation 7):

$$\rho = \sum_{i=1}^n |\Psi_i|^2 \quad (7)$$

The third Hohenberg-Kohn theorem says that  $E_0[\rho] \leq E_0[\rho']$ , where  $\rho$  is the exact density and  $\rho'$  is the approximate density by expansion (Equation 10) for finite "n". This theorem is equivalent to the Hartree-Fock variational theorem. The Kohn-Sham orbitals can be determined by the following expression (Equation 8):

$$\hat{F}_{KS}(\mathbf{1}) \Psi_i(\mathbf{1}) = \varepsilon_{i,KS} \Psi_i(\mathbf{1}) \quad (8)$$

Wherein  $\hat{F}_{KS}$  is the Kohn-Sham operator shown by Equation 9:

$$\hat{F}_{KS} \equiv -\frac{1}{2} \nabla_1^2 - \sum_{\alpha} \frac{Z_{\alpha}}{r_{1\alpha}} + \sum_{j=1}^n \hat{J}_j(\mathbf{1}) + V_{xc}(\mathbf{1}) \quad (9)$$

Wherein the  $V_{xc}$  potential is the main difference between the Hartree-Fock and DFT methods (MORGON, 1995).

In this way, the energy in relation to the density can be minimized through the boundary conditions (Equation 10):

$$\frac{\partial E_0}{\partial \bar{\rho}} = 0 \quad (10)$$

Being the integral  $\rho' dr=N$ , wherein N is the number of electrons in the system.

The main problem of the method is the lack of a systematic process to determine  $E_{xc}[\rho]$ , so several kinds of functionals have already been proposed. This functional is actually divided into two parts: exchange and correlation.

One of the most used exchange functionals is the B3, proposed by Becke, in 1993 (BECKE, 1993), being employed in this work (Equation 11):

$$E_x = (1 - \alpha_0)E_x^{LSDA} + \alpha_0 E_x^{HF} + \alpha_x \Delta E_x^{B88} \quad (11)$$

For correlation, the functional proposed by Lee, Yang and Parr (LEE; CHUNG, 2009) was used. Thenceforth, important concepts in the theoretical description of chemical reactions, such as chemical potential and, concept of hardness and softness, are incorporated into DFT, since  $\rho(\mathbf{r})$  and the number of electrons N can be related more easily than diverse wave functions of many electrons.

The total energy of the system in the DFT method uses the resolution of the time-independent Schrödinger equation (Equation 12), which allows determining the ground state structure of a system with many electrons and nuclei:

$$\hat{H}\phi = E\phi \quad (12)$$

The exact resolution of the Schrödinger equation, Equation 12, presents a very high level of complexity. Thus, approximations are necessary to enable its use for real systems. One of the most important approximations is the so-called Born-Oppenheimer approximation. Basically, it disregards the movement of nuclei in the molecule, since the nuclear mass is several times greater than the mass of the electrons. Thus, the Schrödinger equation is solved

only for the electrons, which are described by a purely electronic wave function in the presence of a potential produced by the nuclei that assume fixed positions in space (ALCÁCER, 2007). The DFT method is able to solve systems efficiently; however, it is quite dependent on the choices of the functional and basis set.

### 3.7.1 Basis set

The basis set is a set of functions used to create the molecular orbitals. Essentially, there are two types of basis set used in electronic structure calculations: Slater-type atomic orbitals (STOs) and Gaussian-type atomic orbitals (GTOs). The Slater functions were the first basis set created; they have important characteristics, once they are associated to representations of hydrogen orbitals. This type of function has the form described in Equation 13.

$$X_{\zeta,n,l,m}(r, \theta, \varphi) = NY_{l,m}(\theta, \varphi)r^{n-1}e^{\zeta r} \quad (13)$$

Wherein N is a normalization,  $Y_{l,m}$  constants are the usual spherical harmonic functions and  $\zeta = \frac{Z-W}{n}$  is a constant. The term Z-W stands for the effective nuclear charge, wherein W is a shielding constant. Although the exponential part of the STOs represents well the dependence on the distance between nucleus and electron for the hydrogen atom, it does not have any radial node. These are introduced by making linear combinations of STOs (JENSEN, 1999). The Gaussian-type basis sets (GTOs) were created as an alternative to the use of STOs. In this case, the integrals are more easily solved. The GTOs can be written in terms of polar coordinates, as shown in Equation 14.

$$X_{\zeta,n,l,m}(r, \theta, \varphi) = NY_{l,m}(\theta, \varphi)r^{2(n-1)-l}e^{\zeta r^2} \quad (14)$$

Due to the computational efficiency achieved through the use of GTOs, they are normally preferred and widely used as basic functions in electronic structure calculations

(JENSEN, 1999). Thus, it was observed that the basis set of STOs followed an exponential behavior  $x = r$ , while the GTOs functions followed an exponential behavior  $x = r^2$ .

### 3.7.2 Density Functional

Different classes of approximations for the XC functional followed during the development of the DFT method. The simplest approximation was proposed by Hohenberg and Kohn in 1964, and it is called local density approximation (LDA). The exchange and correlation energy of the LDA functional can be represented according to Equation 15.

$$E_{xc}[n] = \int dr^3 n(r) \xi_{xc}(n(r)) \quad (15)$$

Wherein  $E_{XC}$  is the energy of exchange and correlation per particle in an electronic density  $n(r)$ . Another type of exchange and correlation functional is the so-called Generalized Gradient Approximation (GGA). The GGA functional is an improvement applied to the LDA and LSDA functionals. It consisted in the implementation of the density gradient, which can be represented in the electronic correlation energy according to Equation 16.

$$E_{XC}[n^\alpha, n^\beta] = \int d^3r \xi_x^{GGA}(n^\alpha(r), n^\beta(r), \nabla n^\alpha(r), \nabla n^\beta(r)) \quad (16)$$

A functional widely used in GGA is the PBE, which was developed by Perdew, Burke and Ernzerhof. The results obtained with the PBE approach show that, for the binding energies of molecules, there is a significant improvement, as well as those of atomization, when compared to the results using the LDA (ORGANUM, 2016).

### 3.8 Additional methods of analysis



In addition, the Natural Bond Orbitals (NBO) technique provides results which lead us to a better comprehension of molecular orbitals localized in the chemical bonds. This concept of natural orbitals is used to distribute electrons from atomic to molecular orbitals, in order to describe atomic charges and molecular bonds from the electron density involved among atoms. The NBO method is based on an analysis for optimally transforming a certain wave function into localized form, corresponding to the one-center ("lone pairs") and two-center ("bonds") elements of the chemist's Lewis structure model (SILVA et al., 2017).

#### 4.0 REFERENCES

ALCÁCER, L. **Introdução à química quântica computacional**. Lisboa: IST Press, 2007. 325 p.

ALMEIDA, JULIANA O. DE, VICTORIA REGINA T. DE OLIVEIRA, JOÃO LUCAS DOS S. AVELAR, BRUNA SIMÕES MOITA, L. M. L. COVID-19: Fisiopatologia e Alvos para Intervenção Terapêutica. **Revista Virtual de Química**, v. 12, n. 6, p. 1464–1497, Sept. 2020.

ALONSO, H.; BLIZNYUK, A. A.; GREASY, J. E. Combining docking and molecular dynamic simulations in drug design. **Medicinal Research Reviews**, New York, v. 26, n. 5, p. 531-568, Sept. 2006.

ARABI, Y. M. *et al.* Critically Ill Patients With the Middle East Respiratory Syndrome: A Multicenter Retrospective Cohort Study. **Critical care medicine**, v. 45, n. 10, p. 1683–1695, Oct. 2017.

ARABI, Y. M.; MURTHY, S.; WEBB, S. COVID-19: a novel coronavirus and a novel challenge for critical care. **Intensive care medicine**, v. 46, p. 833-836, Mar. 2020.

BARREIRO, E. J.; RODRIGUES, C. R. Modelagem molecular: uma ferramenta para o planejamento racional de fármacos em química medicinal. **Química Nova**, São Paulo, v. 20, n. 3, p. 300-310, Jun. 1997.

BECKE, A. D. Density-functional thermochemistry. III. The role of exact exchange. **Journal of Chemical Physics**, New York, v. 98, p. 5648-5652, 1993.

BORMAN, S. A. Much ado about enzyme mechanism. **Chemical and Engineering News**, Washington, v. 82, n. 8, p. 35-39, Aug. 2004.

BROOKS, B. R. et al. CHARMM: a program for macromolecular energy, minimization, and dynamics calculations. **Journal of Computational Chemistry**, New York, v. 4, n. 2, p. 187-217, Jun. 1983.

CARVALHO, I. et al. Introdução a modelagem molecular de fármacos no curso experimental de química farmacêutica. **Química Nova**, São Paulo, v. 26, n. 3, p. 428-438, May/Jun. 2003.

CHAN, J. F.-W. *et al.* A familial cluster of pneumonia associated with the 2019 novel coronavirus indicating person-to-person transmission: a study of a family cluster. **The Lancet**, v. 395, n. 10223, p. 514–523, Feb. 2020.

CHEN, N. *et al.* Epidemiological and clinical characteristics of 99 cases of 2019 novel coronavirus pneumonia in Wuhan, China: a descriptive study. **The Lancet**, v. 395, n. 10223, p. 507–513, Feb. 2020.

COHEN, N. C. et al. Molecular modeling software and methods for medicinal chemistry. **Journal of Medicinal Chemistry**, Washington, v. 33, n. 3, p. 883–894, Mar. 1990.

DENG, S.-Q.; PENG, H.-J. Characteristics of and Public Health Responses to the Coronavirus Disease 2019 Outbreak in China. **Journal of clinical medicine**, v. 9, n. 2, p. 575, Feb. 2020.

DEY, S. K. *et al.* Analyzing the epidemiological outbreak of COVID-19: A visual exploratory data analysis approach. **Journal of medical virology**, v. 92, p. 632-638, Mar. 2020.

DURRANT, J. D.; MCCAMMON, J. A. Molecular dynamics simulations and drug discovery. **BMC Biology**, London, v. 9, p. 1-9, Oct. 2011.

FAUCI, A. S.; LANE, H. C.; REDFIELD, R. R. Covid-19 — Navigating the Uncharted. **New England Journal of Medicine**, v. 382, n. 13, p. 1268–1269, Feb. 2020.

FUNG, S.-Y. *et al.* A tug-of-war between severe acute respiratory syndrome coronavirus 2 and host antiviral defence: lessons from other pathogenic viruses. **Emerging Microbes & Infections**, v. 9, n. 1, p. 558–570, Jan. 2020.

GATES, B. Responding to Covid-19 — A Once-in-a-Century Pandemic? **New England Journal of Medicine**, v. 382, n. 18, p. 1677–1679, Feb. 2020.

GONÇALVES, R. B. **Desenvolvimento e validação de novos métodos de distribuição da**

**população inicial em algoritmos genéticos para o problema de docking proteína-ligante.**

2008. Doutorado (Mestrado em Computação) -Laboratório Nacional de Computação Científica, Petrópolis, 2008.

GUAN, W. *et al.* Clinical characteristics of 2019 novel coronavirus infection in China. **medRxiv**, p. 2020.02.06.20020974, Jan. 2020.

GUIMARÃES, A. P.; RAMALHO, T. C.; FRANÇA, T. C. C. Preventing the return of smallpox: molecular modeling studies on thymidylate kinase from variola virus. **Journal of Biomolecular Structure and Dynamics**, Guilderland, v. 32, n. 10, p. 1601-1612, 2014.

HEYMANN, D. L.; SHINDO, N. COVID-19: what is next for public health? **The Lancet**, v. 395, n. 10224, p. 542–545, Feb. 2020.

HUANG, C. *et al.* Clinical features of patients infected with 2019 novel coronavirus in Wuhan, China. **The Lancet**, v. 395, n. 10223, p. 497–506, Feb. 2020.

HURLE, M. R. *et al.* Computational drug repositioning: from data to therapeutics. **Clinical pharmacology and therapeutics**, v. 93, n. 4, p. 335–341, Apr. 2013.

JENSEN, F. Introduction to Computational Chemistry. **Wiley**, 1999, 660 p.

KALÉ, L. *et al.* NAMD2: greater scalability for parallel molecular dynamics. **Journal of Computational Physics**, Orlando, v. 151, n. 1, p. 283-312, May 1999.

KARPLUS, M.; MCCAMMON, J. A. Molecular dynamics simulations of biomolecules. **Nature Structural Biology**, New York, v. 9, n. 9, p. 646-652, Sept. 2002.

KOHN, W.; HOLTHAUSEN, M. C. **A chemist's guide to density functional theory**. 2. ed. New York: John Wiley, 2001. 293 p.

KUNTZ, I. D. *et al.* A geometric approach to macromolecule-ligand interactions. **Journal of Molecular Biology**, London, v. 161, n. 2, p. 269-288, Oct. 1982.

LEACH, P. G. L.; ZNOJIL, M. On the elementary Schrodinger bound-states and their multiplets. **Journal of Mathematical Physics**, New York, v. 33, n. 8, p. 2785-2794, Apr. 1992.

LEE, S. G.; CHUNG, Y. C. Molecular dynamics investigation of interfacial mixing behavior in transition metals (Fe, Co, Ni)-Al multilayer system. **Journal of Applied Physics**, New York, v. 105, n. 3, p. 4902, Feb. 2009.

LU, H.; STRATTON, C. W.; TANG, Y.-W. Outbreak of pneumonia of unknown etiology in

Wuhan, China: The mystery and the miracle. **Journal of Medical Virology**, v. 92, n. 4, p. 401–402, Apr. 2020.

MELLER, J. Molecular dynamics. **eLS**, Torún, p. 1-8, 2001.

MIZUTANI, M.; NIWA, T.; TANAKA, S. On the Law of entropy increasing of a one-dimensional infinite system. **Journal of Mathematics of Kyoto University**, Kyoto, v. 34, n. 4, p. 699-708, 1994.

MONTANARI, C. A. Química medicinal: métodos e fundamentos em planejamento de fármacos. **Edusp**, São Paulo, 2011.

MORGON, N. H. Paralelização em química. **Química Nova**, São Paulo, v. 18, n. 5, p. 481-489, Feb. 1995.

MUNSTER, V. J. *et al.* A Novel Coronavirus Emerging in China — Key Questions for Impact Assessment. **New England Journal of Medicine**, v. 382, n. 8, p. 692–694, Jan. 2020.

ORGANUM, P.; LDA, T. Teoria do funcional da densidade Uma Possível Solução para o Problema de Muitos Elétrons da Mecânica Quântica. **Physicae Organum** v. 2, n. 1, p. 1-14, Mar. 2016.

PARK, M.; THWAITES, R. S.; OPENSHAW, P. J. M. COVID-19: Lessons from SARS and MERS. **European Journal of Immunology**, v. 50, n. 3, p. 308–311, Mar. 2020.

PATRICK, D. L.; FLANAGAN, J. Contact mechanics and bond rupture in chemical force microscopy: a study using atomistic molecular dynamics simulation. **Abstracts of Papers of the American Chemical Society**, Amsterdam, v. 221, p. 341-341, 2001.

PERLMAN, S. Another Decade, Another Coronavirus. **The New England journal of medicine**, v. 382, p. 760-762, Feb. 2020.

PHILLIPS, J. C. *et al.* Scalable molecular dynamics with NAMD. **Journal of Computational Chemistry**, New York, v. 26, n. 16, p. 1781-1802, Dec. 2005.

RODRIGUES, C. R. Processos modernos no desenvolvimento de fármacos: modelagem molecular. **Cadernos Temáticos de Química Nova na Escola**, São Paulo, n. 3, p. 1-7, May. 2001.

RODRIGUES, R. *et al.* Estratégias de Triagem Virtual no Planejamento de Fármacos Virtual Screening Strategies in Drug Design. **Revista Virtual de Química**, v. 4, p. 739, Dec. 2012.

SANT'ANNA, C. M. R. Glossary of terms in theoretical organic chemistry. **Química Nova**, São Paulo, v. 25, n. 3, p. 505-512, May. 2002.

SANT'ANNA, C. M. R. Molecular modeling methods in the study and design of bioactive compounds: An introduction. **Revista Virtual de Química**, Seropédica, v. 1, n. 1, Feb. 2009.

SCHWARTZ, D. A.; GRAHAM, A. L. Potential Maternal and Infant Outcomes from (Wuhan) Coronavirus 2019-nCoV Infecting Pregnant Women: Lessons from SARS, MERS, and Other Human Coronavirus Infections. **Viruses**, v. 12, n. 2, Feb. 2020.

SCOTT, W. R. P. et al. The GROMOS biomolecular simulation program package. **The Journal of Physical Chemistry A**, Washington, v. 103, n. 19, p. 3596-3607, Apr. 1999.

SIEGBAHN, P. E. M.; BLOMBERG, M. R. A. Transition metal systems in biochemistry studied by high accuracy quantum chemical methods. **Chemical Reviews**, Easton, v. 100, n. 2, p. 421-437, Feb. 2000.

SILVA, T. C.; DE ALMEIDA, K. J.; PIRES, M. S.; DE CASTRO, A. A.; GONÇALVES, M. A.; DA CUNHA, E. F. F.; RAMALHO, T. C. Theoretical structural and electronic analyses with emphasis on the reactivity of iron oxide prototypes in methane C-H bond activation. **Reaction Kinetics, Mechanisms and Catalysis**, v. 120, p. 195-208, Feb. 2017.

SILVA, T. H. A. **Modelagem molecular com o auxílio do computador**. Belo Horizonte: Editora da UFMG, 2006. 46 p.

THOMSEN, R.; CHRISTENSEN, M. H. MolDock: a new technique for high accuracy molecular docking. **Journal of Medicinal Chemistry**, Easton, v. 49, n. 11, p. 3315-3332, Jun. 2006.

VARNEK, A. Fragment descriptors in structure-property modeling and virtual screening. **Methods in molecular biology (Clifton, N.J.)**, v. 672, p. 213-243, 2011.

WEINER, P. K.; KOLLMAN, P. A. AMBER: Assisted Model Building with Energy Refinement. A general program for modeling molecules and their interactions. **Journal of Computational Chemistry**, New York, v. 2, n. 3, p. 287-303, Sep. 1981.

WU, F. *et al.* A new coronavirus associated with human respiratory disease in China. **Nature**, v. 579, n. 7798, p. 265-269, Mar. 2020.

YOO, J. H. The Fight against the 2019-nCoV Outbreak: an Arduous March Has Just Begun. **Journal of Korean medical science**, Korea (South), v. 35, n. 4, p. e56, Feb. 2020.

ZHANG, L. *et al.* Crystal structure of SARS-CoV-2 main protease provides a basis for design

of improved  $\alpha$ -ketoamide inhibitors. **Science**, v. 368, n. 6489, p. 409-412, Apr. 2020.

ZHANG, L.; LIU, Y. Potential interventions for novel coronavirus in China: A systematic review. **Journal of medical virology**, v. 92, n. 5, p. 479–490, May. 2020.

ZHANG, T. *et al.* Clinical trials for the treatment of Coronavirus disease 2019 (COVID-19): A rapid response to urgent need. **Science China. Life sciences**, v. 63, n. 5, p. 774-776, Feb. 2020.

ZHOU, P. *et al.* A pneumonia outbreak associated with a new coronavirus of probable bat origin. **Nature**, v. 579, n. 7798, p. 270–273, Mar. 2020.

ZIEGLER, T. Approximate density functional theory as a practical tool in molecular energetics and dynamics. **Chemical Reviews**, Washington, v. 91, n. 5, p. 651-667, Jul. 1991.

## CHAPTER 2

### *Review article*

Insights into the Computational Drug Repositioning for Potential Pharmacotherapy of  
COVID-19

*Submitted to Journal of Chemical Information and Modeling*

## Abstract

Society currently faces many challenges caused by the coronavirus outbreak, known as SARS-CoV-2, and in addition, its variant strains tend to be still more aggressive. Therefore, there is an enormous need to accelerate the development of novel remediation techniques against SARS-CoV-2. In an attempt to help in the front line, computational drug repositioning has intensively been explored as a consolidated strategy in diverse preclinical research in order to find an effective treatment protocol against SARS-CoV-2 infection. Hence, our review highlights the state-of-the-art and potential strategies based on *in silico* models for drug repositioning against the SARS-CoV-2 and their key variants.

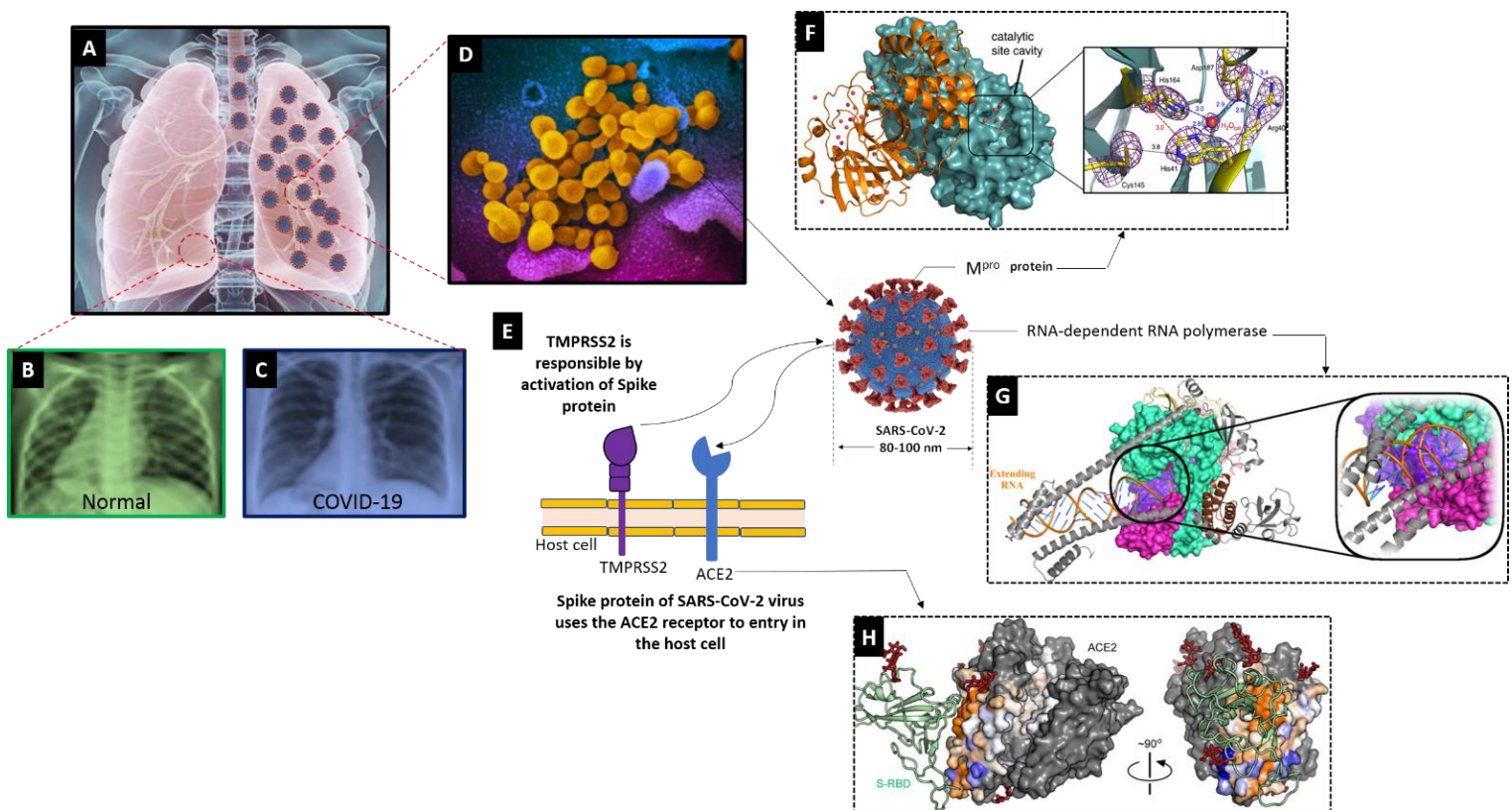
**Keywords:** COVID-19, Pandemic, Computational Chemistry, Drug Repositioning

## 1. Introduction to SARS-CoV-2

In the spotlight is the coronavirus (CoVs), which belongs to a wide class of viruses that has been identified in many host species, including humans, birds, and other mammals.<sup>1-4</sup> We are currently facing a new coronavirus and its key variant strains (SARS-CoV-2) are popularly referred to as COVID-19.<sup>5-7</sup> The sequenced genomes of the SARS-CoV-2 virus suggest about 96.2% homology with Bat-CoV-RaTG13 and 79.5% homology with SARS-CoV.<sup>8,9</sup> Thus, much efforts has been expended in elucidating the crystallographic SARS-CoV-2 structure and understanding its mechanism of action.<sup>5,10-18</sup> It is well-known that SARS-CoV-2 is an enveloped virus (approximately spherical) with its diameter in the range of 80-120 nm, positive-sense, single-stranded RNA (+ssRNA) that is associated with a nucleoprotein, which is surrounded by a capsid of matrix protein.<sup>19-24</sup> Systematic analysis rises that the SARS-CoV-2 virus has 29,903 nucleotides in its genome and encodes about 9860 amino acids in 14 open reading frames (ORFs) and 27 proteins.<sup>25-27</sup> The 5' region, which covers more than two-thirds of the viral genome encodes polyproteins pp1a and pp1ab and can be cleaved into 16 putative non-structural proteins (nsps) that are likely involved in the SARS-CoV-2 transcription/replication.<sup>28-30</sup> While the 3' region consists of genes that encode structural proteins, such as the spike surface glycoprotein, peripheral membrane and transmembrane, the small envelope protein, membrane, and nucleocapsid.<sup>25-27</sup> More specifically, the spike surface glycoprotein has two domains, known as S1 and S2, which bind to host receptors via different receptor-binding domains (RBDs).<sup>1,31-35</sup> Thus, the SARS virus's main protease (M<sup>pro</sup> or 3CLpro) plays a pivotal role in the viral processing of polyproteins and hence has broadly been



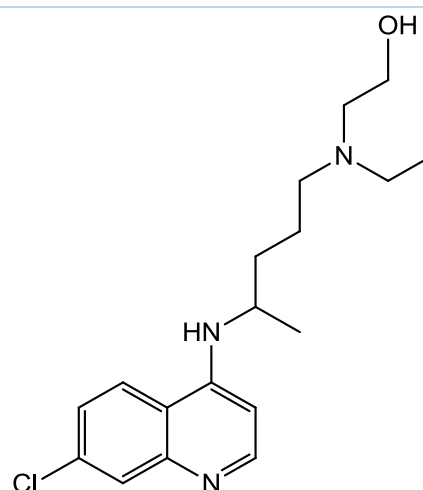
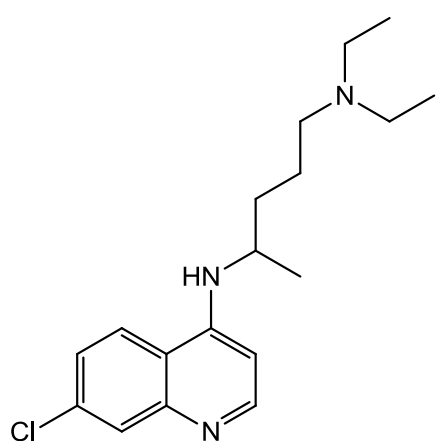
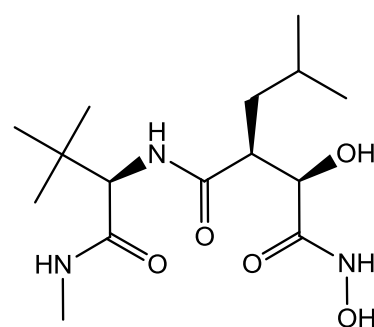
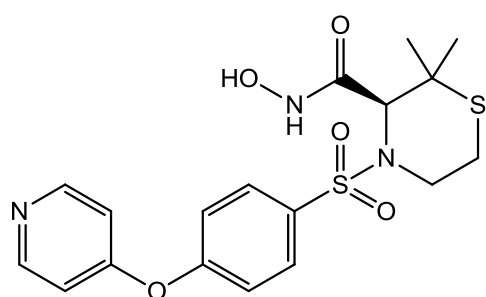
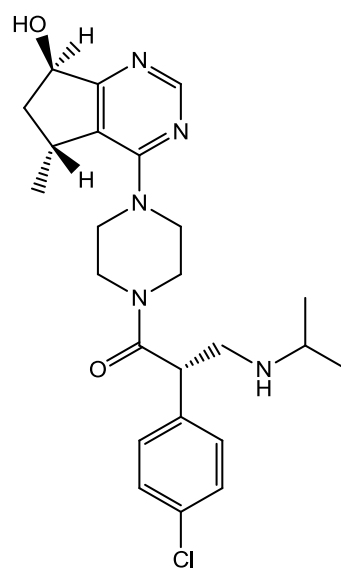
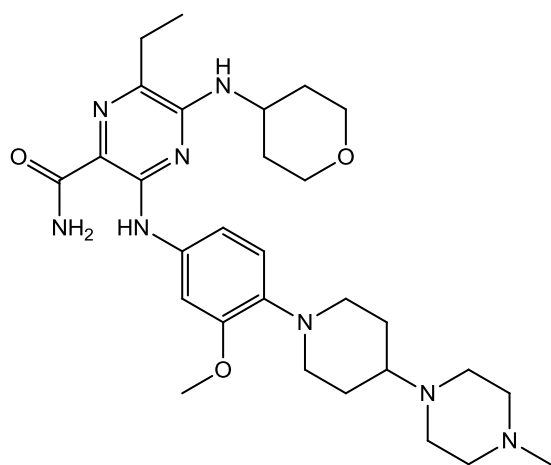
investigated as a molecular target.<sup>15–17</sup> Previous studies have identified that the occurrence of the SARS-CoV-2 infection is due to the binding of the spike protein to the ACE2 receptors (angiotensin-converting enzyme 2) of human host cells (**Figure 1**), i.e., via the S1 and S2 subunits, which are the key entry points of SARS-CoV-2.<sup>4,31,33,35–37</sup> After the SARS-CoV-2 enters a human host cell, in particular, the complex process of viral replication is initiated with the participation of the RNA-dependent RNA polymerase (RdRp), helicase, as well as, other accessory proteins.<sup>30,35,38</sup> Therefore, based on previous studies, the following were identified as promising candidate drug targets for treatment:  $M^{pro}$ , the papain-like protease ( $PL^{pro}$ ), and the RdRp of SARS-CoV-2, as well as, the ACE2 receptor.<sup>5,6,11–16,39</sup>

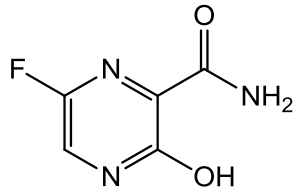


**Figure 1.** Representation of virus lodged in the lung (A), highlighting a normal (B) and affected (C) lungs. A scanning electron microscope image of SARS-CoV-2 is shown in (D). The scheme of entry of virus in the host cell is also presented (E), together with the structural representation of the crystallographic structures of  $M^{pro}$  (F), RdRp (G) and RBD (pale green ribbon) bound ACE2 (surface) (H). Credits: NIAID-RML,<sup>40–43</sup>

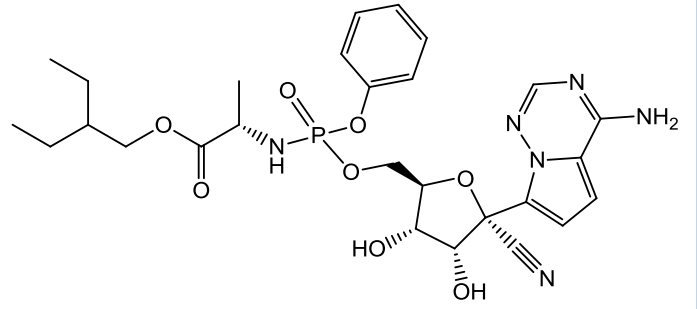
Furthermore, in the first five months after discovery, the genetic diversity of the SARS-CoV-2 virus has been evaluated and it was revealed that several regions of the genome had already accumulated diversity.<sup>44-46</sup> As a result, recurrent mutations have been identified in the genome of the SARS-CoV-2.<sup>47-53</sup> About 80% of these produced non-synonymous changes at the protein level, which implying possible ongoing adaptations of the SARS-CoV-2 virus to the human host cell.<sup>44</sup> Correlation analyzes have already shown that strains with mutations in ORF1ab 4715L and protein S 614G have significant positive correlations with fatality rates, which can affect the severity of COVID-19.<sup>47</sup>

Extensive efforts are being made to elucidate the variations present in the genomes, however, at present, data on the SARS-CoV-2 genome are still limited, and further advances will allow greater understanding of the dissemination, prevention, and control of the disease.<sup>5,10,11,44,46,47,50,52,53</sup> Stukalov et al.<sup>54</sup> have performed a multi-omics study of both SARS-CoV-2 and SARS-CoV. As a result, the authors in that study found that gilteritinib ( $C_{29}H_{44}N_8O_3$ ; a designated FLT3/AXL inhibitor), ipatasertib ( $C_{24}H_{32}ClN_5O_2$ ; AKT inhibitor), prinomastat ( $C_{18}H_{21}N_3O_5S_2$ ), and marimastat ( $C_{15}H_{29}N_3O_5$ ; matrix metalloprotease inhibitors) exhibited the highest antiviral activity (**Figure 2**). That study highlighted many targets from profiling the interactome of both viruses (e.g. transcriptome, proteome, ubiquitinome and phosphoproteome) from a lung-derived origin, thus providing a rational guide for the development of directed therapies.<sup>54</sup>

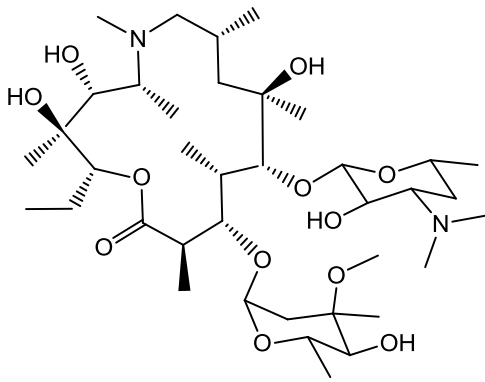




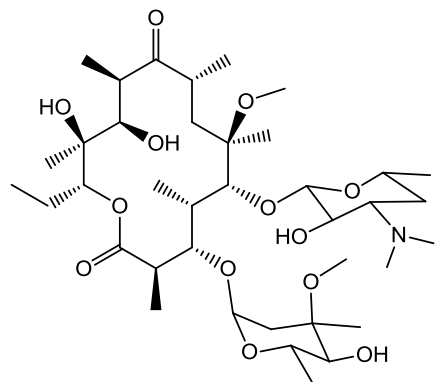
(g)



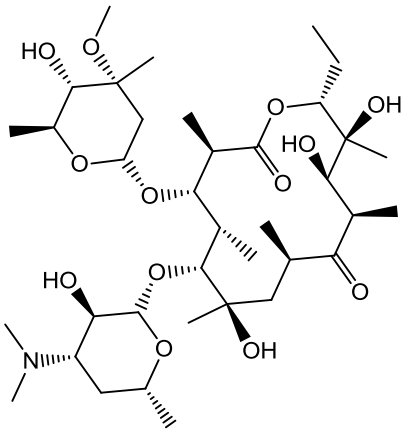
(h)



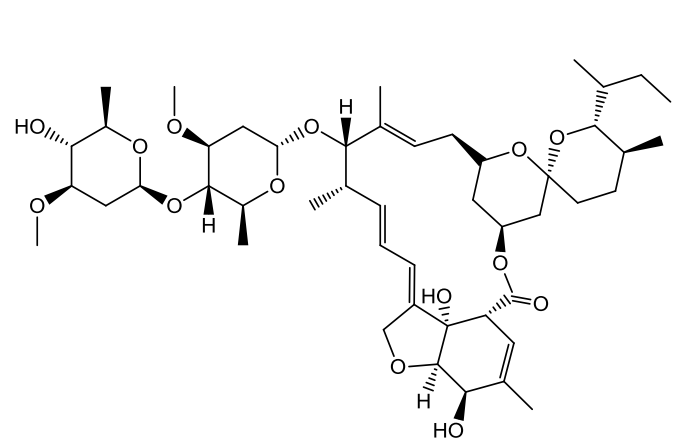
(i)



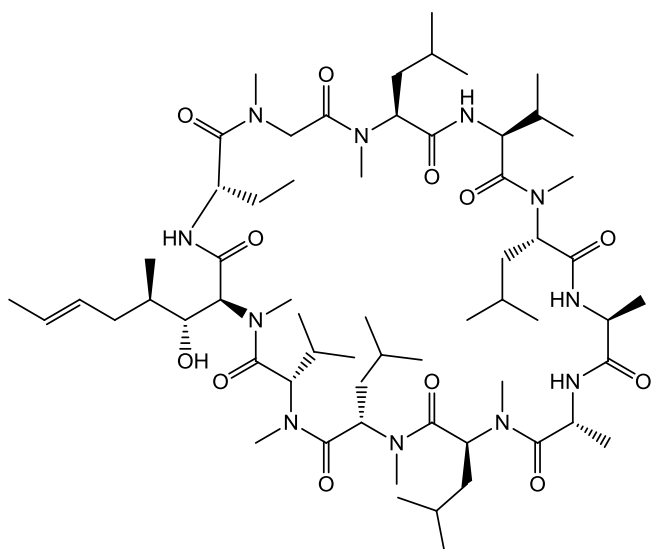
(j)



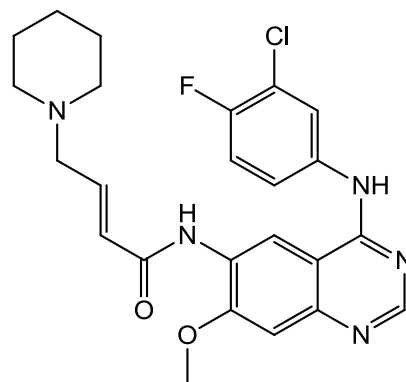
(k)



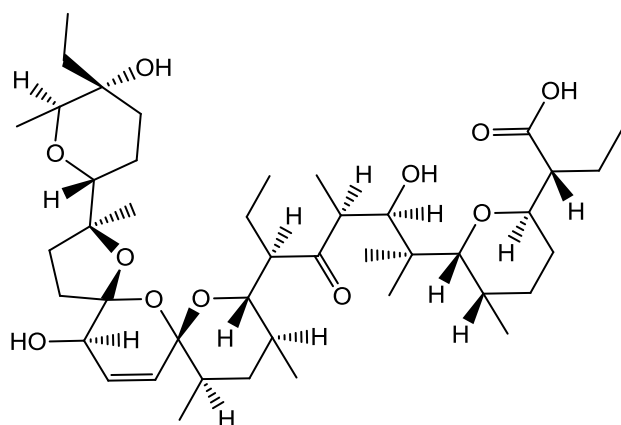
(l)



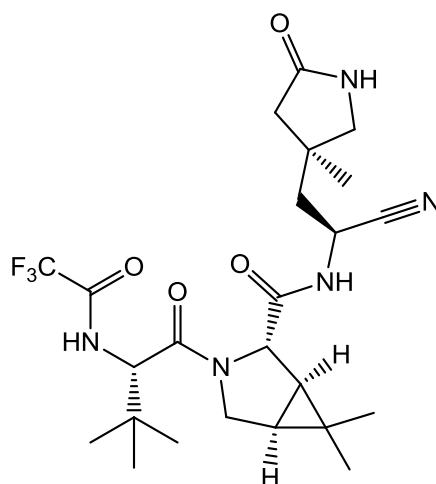
(m)



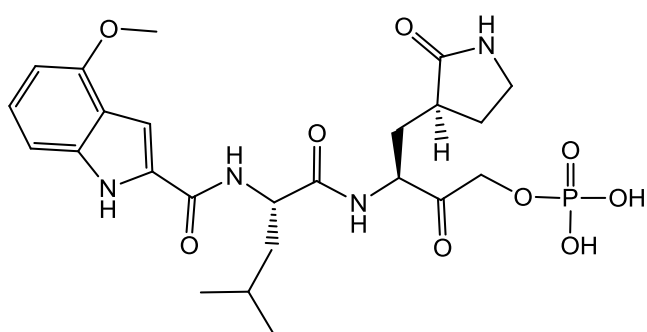
(n)



(o)



(p)



(q)

**Figure 2:** Chemical structures of (a) gilteritinib, (b) ipatasertib, (c) prinomastat, (d) marimastat, (e) chloroquine, (f) hydroxychloroquine, (g) favipiravir, (h) remdesivir, (i) azithromycin, (j) clarithromycin, (k) erythromycin, (l) ivermectin, (m) cyclosporine, (n) dacomitinib, (o) salinomycin, (p) PF-07321332 and (q) PF-07304814.

Diverse scientists are striving to search for novel therapies to treat COVID-19.<sup>12,18,55–57</sup> In this line, it is well-known that drug repositioning has a crucial role in drug discovery in preclinical research.<sup>56,58,59</sup> Approaches involving computational screening of various drugs can boost the emergence of new therapeutic options for the treat of COVID-19. Among the hundreds of compounds analyzed from the modern computational strategies, the most promising can then be rationally selected for in vitro and in vivo tests, accelerating hence the development of new drugs.<sup>60–67</sup>

In this review, we have focused on the recent advances in drug discovery and development for COVID-19 treatment through computational prediction tools. We started by introducing the computational strategies relevant to case studies. Next, we briefly describe a summary of computational approaches in drug discovery and development.

## 2. Brief Summary of Computational Strategies

Computational chemistry consists of a range of tools capable of boosting and optimizing the process of drug development and discovery.<sup>68–72</sup> For instance, understanding the mechanisms by which enzymatic catalysis occurs at the atomic level is prospectively beneficial for designing new inhibitors by allowing the prediction of drug-target sites.<sup>73</sup> Thus, computational methods and techniques can, in principle, be employed to unveil the interaction modes and reactivity of various repositioned drugs for COVID-19 treatment, providing a significant reduction of research time and costs.<sup>74</sup>

Researches in a wide range of applied sciences seek to develop not only useful biomolecules and advanced materials, but also to understand, design, and control their functional properties.<sup>75–77</sup> These efforts may lead to new interpretations for carrying out experiments. In this context, it is well-known that computational strategies have been widely applied to such specific chemical problems (e.g., proteins, DNA, and cell membranes), and have led to efficient approaches for analysing the enzymatic activity.<sup>73,78,79</sup>

Accurate models for the computing chemical properties of drug candidates and proteins are essential for drug discovery and design.<sup>80</sup> Thus, the notable use of computer-aided drug design (CADD) based quantum mechanical (QM) methods is fueled by present-day growth computing power; however it is mainly due to the fact that QM methods can provide higher accuracy in terms of computations and results.<sup>63,81–83</sup> And yet, the interest in the use of QM methods in CADD has boosted the development of further methodologies; for instance, the correlation of this approach with docking, scoring, improvement of known lead compounds, and even the unraveling of reaction mechanisms.<sup>84</sup>

QM methods<sup>80,84</sup> are widely used to quantify energies and optimise structures, and also to calculate electronic properties. Such strategies are helpful for interpreting the reactivities of biomolecules, which are usually guided by the transfer of energy and structural transformations.<sup>84</sup> Note that the currently available computing power cannot yet perform direct *ab initio* QM calculations of biomacromolecules. However, an important emerging approach employs the hybrid QM/MM method as strategy.<sup>78</sup> These methods provide accurate results for many properties of interest, including but not limited to, partial charges, bond strength, torsion angles and so on. These fundamental properties are important for the parameterisation of force-fields and other descriptors that can be used to build quantitative structure activity relationship (QSAR) models or quantitative structure-property relationship (QSPR) models.<sup>84</sup> Also, the MM methods are valuable tools for studying big systems, such as biological ones. Particularly, it is well-known that the MM consists of considering nuclear movements and treating electrons in a non-explicit way, unlike quantum methods that are characterized by studying the electronic structure for a fixed nuclear position.<sup>85</sup> Hence, the MM model describes molecules as a set of atoms connected to each other by elastic or harmonic forces, where each atom is considered as a point mass that is connected by springs, which correspond to chemical bonds. The movement of each atom is defined by the forces acting on it by all the other atoms.<sup>75</sup> These forces acting on each particle are described by the potential energy functions of the structural contributions, such as the bond length ( $r$ ), bond angle ( $\theta$ ), dihedral angle ( $\phi$ ) and unbound interactions ( $\sigma/q$ ), as described in equation 1.<sup>86</sup>

$$v(r^N) = \sum_{bonds} \frac{k_i}{2} (r_i - r_{i,0})^2 + \sum_{angles} \frac{k_i}{2} (\theta_i - \theta_{i,0})^2 + \sum_{torsions} V_n [1 + \cos \phi] + \sum_{i=1}^N \sum_{j=1}^N \left( 4\epsilon_{ij} \left[ \left( \frac{\sigma_{ij}}{r_{ij}} \right)^{12} - \left( \frac{\sigma_{ij}}{r_{ij}} \right)^6 \right] + \frac{q_i q_j}{4\pi\epsilon_0 r_{ij}} \right) \quad (1)$$

The equation 1 represents a common force-field. However, force fields can include other terms, such as those that specify the coupling of oscillations between angles or lengths of connection. In general, the choice of the force-field is a very important step and depends on the properties that will be studied in the system because it directly influences the reliability of the results.<sup>75,87</sup> In biomolecular systems, the most used force fields are: CHARMM,<sup>88</sup> GROMOS,<sup>89</sup> AMBER,<sup>90</sup> OPLS,<sup>91</sup> among others. All these well-consolidated strategies might unveil complex processes of interest at the biological level,<sup>78</sup> more specifically, has widely been used in drug repositioning for potential pharmacotherapy of COVID-19.

The molecular docking simulation provides information about the interaction between small molecules and biomacromolecules based on the principle that the spatial shape and intermolecular energy of the two species coincide.<sup>75,92</sup> During a molecular docking simulation, it is necessary to associate two components: a search algorithm and a scoring function.<sup>78,93–95</sup> Thus, the search algorithm analyses the diverse degrees of freedom of the side chains of the biomacromolecules, such as proteins, and the molecular structure of the ligands, giving rise to a conformation and orientation of the ligand at the active site of the molecular target.<sup>92,95</sup> Some search algorithms cited in the literature are: Monte Carlo,<sup>96</sup> Lamarckian Genetic Algorithm,<sup>97,98</sup> Differential Evolution Algorithm,<sup>94,99,100</sup> Fast Shape Matching<sup>101</sup> and Simulated Annealing,<sup>102</sup> while the scoring functions estimate the free energy of the intermolecular bond from the approach that the lowest energy score represents the best orientation after the docking simulation.<sup>78</sup> Currently, there are several docking softwares, such as GOLD®,<sup>103</sup> AUTODOCK [4,5],<sup>97,104</sup> FLEXX,<sup>105</sup> MOLEGRO VIRTUAL DOCKER (MVD) ®.<sup>94</sup>

Simulation based on classical molecular dynamics (MD) is often used to investigate the structure, dynamics and thermodynamics of biomacromolecules and their complexes, thereby providing microscopic information about the forces involved in the interaction of these systems as a function of time.<sup>75,78,87,106-108</sup> Generally, MD calculations are based on the numerical solution of Newton's equation of motion,<sup>75,87,109</sup> where each atom  $i$  of the molecular system is represented by equations 2 and 3:

$$\vec{F}_i(t) = m_i \vec{a}_i \quad (2)$$

$$\vec{F}_i(t) = \frac{\partial V_{(ri)}}{\partial r_i} \quad (3)$$



where  $F_i$  represents the force acting on each atom of the system and  $a_i$  is the acceleration of each atom  $i$  of mass  $m_i$ . The traditional analytical treatment only calculates the resolution of these equations for systems with a maximum of two independent particles in more complex systems. It is necessary to use numerical methods and additional approximations, such as the Taylor series (equation 4), as follows:

$$r(t + \Delta t) = r(t) + \frac{dt}{dt} \Delta t + \frac{d^2_r}{dt^2} \frac{\Delta t^2}{2} + \dots \quad (4)$$

The solution to the equation depends on the position  $r(t)$ , the speed  $dr/dt$  and the acceleration  $d^2r/dt^2$  for each particle. The time interval ( $\Delta t$ ) must be very small so that the acceleration can be considered as constant in this interval.<sup>95,103</sup> Some of the most common programs used in MD studies are AMBER,<sup>90</sup> CHARMM,<sup>88</sup> NAMD,<sup>110,111</sup> and GROMACS.<sup>89</sup>

Virtual Screening (VS) is a large-scale computational analysis of large databases for identify new potentially active molecules.<sup>112-119</sup> The databases used in the VS process may contain thousands of commercially available compounds, with physico-chemical and biological properties similar to those displayed by recognized drugs, commercially available or accessible by organic synthesis, hypothetical molecules (designed on a computer before synthesis) or even products of natural origin.<sup>120,121</sup> In addition to identifying new bioactive compounds, VS also aims to eliminate molecules with marked toxicity and have unfavorable pharmacodynamic and pharmacokinetic properties, consequently reducing the development cycle time and increasing the chances of success when selecting potentially active molecules.<sup>115-119,121</sup>

### 3. Prospect of drug repositioning as a strategy to treatment of SARS-CoV-2 infection

Computational drug repositioning is related to discovering new uses for existing drugs outside the scope of the original therapeutic indication and have a great potential for discovering new therapies for the treatment of COVID-19.<sup>71,122-125</sup> The present academic landscape should enable promising research programs for drug repositioning, by employing different techniques from computational chemistry, along with *in vitro* and *in vivo* experimental investigations.<sup>71,124,125</sup> High-throughput screening tools efficiently provide gains in speed and quickly screen large numbers of potential drug candidates for repositioning. In principle, this approach can be successfully applied in the search for novel therapies for the treatment of diverse diseases.<sup>126-136</sup>

Fischer et al. have performed computationally screened a compound library of over 606 million compounds for binding to the recently solved crystal structure of the M<sup>Pro</sup> of SARS-CoV-2.<sup>21</sup> As a result of that effort, the authors presented a list of 12 purchasable compounds with good affinity for viral proteases. We also evaluated approved antiviral drugs and other protease inhibitors for drug repurposing, where apixaban (C<sub>25</sub>H<sub>25</sub>N<sub>5</sub>O<sub>4</sub>) and nelfinavir (C<sub>32</sub>H<sub>45</sub>N<sub>3</sub>O<sub>4</sub>S) were highlighted as promising. The authors concluded that further experimental validation and subsequent optimisation of their proposed early lead compounds might offer a valuable strategy to conquer SARS-CoV-2.<sup>21</sup>

Petit et al. came up with an interesting work, by which they investigated the aquatic world to provide a source of possibilities to treat COVID-19.<sup>133</sup> Herein, the functionalities of diverse molecules (such as phycocyanobilin, phycoerythrobilin, phycourobilin, and folic acid) expressed by the genus *Arthrospira* are computationally evaluated. The work concludes by suggesting that further studies of these four molecules should be performed to evaluate their ability to compete with the SARS-CoV-2/ACE2 complex, through both *in vitro* and *in vivo* experiments.<sup>133</sup>

Because RdRp is an essential protein involved in replicating the virus, it can be used as a potential drug target.<sup>134–138</sup> In this sense, Saha et al. investigated the efficacy of plant-based products against RdRp, and analysed their potential to inhibit COVID-19.<sup>139</sup> In this work, the efficacy of about 248 plant compounds against the catalytic subunit of RdRp was investigated through molecular docking simulations. The molecules with the highest affinity toward RdRp were tellimagrandin I (C<sub>34</sub>H<sub>26</sub>O<sub>22</sub>), saikosaponin B2 (C<sub>42</sub>H<sub>68</sub>O<sub>13</sub>), hesperidin (C<sub>28</sub>H<sub>34</sub>O<sub>15</sub>) and epigallocatechin gallate (C<sub>22</sub>H<sub>18</sub>O<sub>11</sub>), which are stabilized in the binding site during the molecular dynamics process. The authors demonstrate that saikosaponinB2 exhibits the strongest binding affinity and may serve as a potential molecule for developing an effective therapy against COVID-19.<sup>139</sup>

In a study by Assis et al., computational design was carried out to study isomers based on the nitro-derivatives of quinoline and quinoline *N*-oxide as potential active molecules, providing low-cost alternatives for the treatment of COVID-19.<sup>18</sup>

#### **4. Déjà vu: new uses for old drugs from *in silico* methods**

##### **4.1 Chloroquine/hydroxychloroquine**

Chloroquine ( $C_{18}H_{26}ClN_3$ ; abbreviated as CQ, **Figure 2e**) and its derivative hydroxychloroquine ( $C_{18}H_{26}ClN_3O$ ; abbreviated as HCQ, **Figure 2f**) are organic compounds in which present the pharmacophoric group quinoline found usually in the bark of the *Cinchona officinalis* plant.<sup>140</sup> These compounds are old drug used to treat malaria,<sup>141</sup> amebiasis,<sup>142</sup> rheumatoid,<sup>143</sup> arthritis and lupus erythematosus syndrome.<sup>141,144</sup> CQ and HCQ act in the inhibition of proteolytic processes and interfere with the intracellular pH of the endosomes and in the glycosylation of the host receptors, preventing the insertion of the virus into the cells.<sup>145</sup> In addition, both compounds can block autophagy, lysosome activities and the production of pro-inflammatory cytokines in host cells.<sup>146,147</sup> Therefore, CQ and HCQ have anti-inflammatory/immunoregulatory properties, being considered good antiviral agents. According to some current studies, these antiviral agents could present the possibility of attenuating the inflammatory response of SARS-CoVs, since the replication of the COVID-19 virus causes damage to pulmonary endothelial and epithelial cells, resulting in an inflammatory increase of cytokines in the plasma.<sup>147</sup>

Hussein and Elkhair proposed the coordination of some chloroquine/hydroxychloroquine zinc compounds in order to potentiate the inhibitory activity of these compounds within the active site of the  $M^{pro}$  enzyme (PDB ID 6LU7). As a result, they observed that the CQ/HCQ complexes coordinated with Zn interacted better at the enzyme active site than without coordination, since they presented lower intermolecular interaction energies and several interactions of the hydrogen bond type at the active site.<sup>148</sup>

However, in the work from Ghazy et al., the authors state that CQ/HCQ treating did not decrease the mortality of COVID-19 patients. Otherwise, it has been observed the emergence of diverse side effects, such as diarrhea, rash, headache, elevated transaminases, fatigue, and also anemia.<sup>149</sup>

## 4.2 Azithromycin

Azithromycin ( $C_{38}H_{72}N_2O_{12}$ ; AZM, **Figure 2i**) belongs to the azalide group and is a macrolide antimicrobial agent. It is used to treat a variety of bacterial infections (i.e., gram-positive and gram-negative), as well as having anti-inflammatory properties and improving lung function in individuals with various lung diseases, such as cystic fibrosis and asthma. In addition, this drug inhibits mRNA translation by binding to the bacterial 50s ribosomal subunit, resulting in the blockage of bacterial protein synthesis. Recently, it was reused for management in patients with COVID-19, and in most cases, the therapy performed is the combination of azithromycin with chloroquine or hydroxychloroquine.<sup>150–152</sup>

Arouche et al. analysed the reuse of the drugs (such as AZM, ivermectin, lopinavir, ritonavir, oseltamivir, and heparin), from the use of molecular docking techniques to treat COVID-19.<sup>153</sup> For this purpose, the authors selected two molecular targets: the structure of the M<sup>pro</sup> SARS-CoV-2 and the structural base of the protease 3CL SARS-CoV-2. This study suggested that the development of a single antiviral agent targeting the M<sup>pro</sup>, 3CL protease, or therapeutic combinations, in principle, may provide a most effective line of defence against coronavirus-associated diseases.<sup>153</sup> On the other hand, Ghazy et al.<sup>149</sup> showed that AZM alone or in combination with CQ/HCQ increased the duration of hospital stay and hence did not show any beneficial effect for the SARS-CoV-2 treatment. Thus, the employment of further theoretical methods of analysis is important in order to raise new insights about the modes of action of the drug candidate as a whole. In the work, from Arouche et al.,<sup>153</sup> docking calculations were carried out. However, their results are not conclusive and further theoretical analyses make necessary.

### 4.3 Ivermectin

Discovered in 1975, Ivermectin (C<sub>48</sub>H<sub>74</sub>O<sub>14</sub>; **Figure 21**) is widely used to treat, prevent and control parasites that are common in humans worldwide. Currently, research shows that ivermectin can inhibit the viral replication of SARS CoV-2 *in vitro*.<sup>141,154</sup> Caly et al. reported that ivermectin showed broad spectrum antiviral activity *in vitro*, that is, ivermectin is an inhibitor of the causative virus (SARS-CoV-2).<sup>155</sup>

Choudhury et al.<sup>156</sup> explored an *in silico* approach to analyze the effectiveness of ivermectin binding against: SARS-CoV-2 M<sup>pro</sup> and RdRp, human ACE2 and TMPRSS2 receptor. The results showed the potential of ivermectin to target the main pathogenic proteins of SARS-CoV-2, which can be a possible option, as well as illuminating the possibility of using this drug in clinical trials with COVID-19.<sup>156</sup> On the other hand, the data is insufficient to recommend the wide use of ivermectin in preventing or treating SARS-CoV-2 infection.<sup>157</sup>

Hence, a deep understanding of their pharmacokinetic properties is important to help assess the modes of action of a drug candidate. Computational drug repositioning approaches are good strategies for this purpose and a full toolbox of theoretical methods pertinent to the study should be employed.<sup>70</sup>

## 5. *In silico* methods targeting drugs with potential application toward COVID-19

## 5.1 Favipiravir

Favipiravir or T-705 ( $C_5H_4FN_3O_2$ ; **Figure 2g**) was developed in 2014 by Fujifilm group Company Toyama Chemical in Japan to treat a new strain of influenza. Currently, this drug has a broad-spectrum action against different RNA viruses, such as Ebola, influenza, norovirus, chikungunya and enterovirus.<sup>141,158–160</sup> It is known to selectively inhibit RdRp by acting as a purine analogue. Favipiravir is then converted inside the cell into its active phosphorylated form and, thus, can be incorporated into the stretching of the viral RNA strand. This process interrupts the insertion of other nucleotides in the strand, thus hampering viral replication in the host cell. Therefore, in SARS-CoV-2, Favipiravir induces a mutagenic effect responsible for inhibiting the virus replication.<sup>141,158–160</sup>

Rad et al.<sup>161</sup> theoretically investigated the adsorption properties of the drug favipiravir in different metallopherenes, as drug carriers for COVID-19 treatment.<sup>161</sup> Doping was performed with five transition metals, such as Ti, Cr, Cr, Fe, Ni and Zn, and in-depth examination was performed to select the most suitable metallofullerenes. It was observed that fullerenes doped with chromium (−148.2 kJ/mol), iron (−149.6 kJ/mol), and nickel (−146.6 kJ/mol) provided the best results for adsorbing favipiravir.<sup>161</sup>

## 5.2 Clarithromycin / Erythromycin

Clarithromycin ( $C_{38}H_{69}NO_{13}$ ; **Figure 2j**) and Erythromycin ( $C_{37}H_{67}NO_{13}$ ; **Figure 2k**) are semi-synthetic macrolide antibiotic with a structure similar to AZM. This compound has antimicrobial activity and has immunomodulatory effect. They inhibit protein synthesis by reversible binding of the 50S ribosomal subunits of the 70S ribosome in susceptible bacteria, which results in inhibition of RNA-dependent protein synthesis.<sup>162–164</sup>

Prashantha et al (2021) analyzed several drugs, based on *in silico* methods, such as antimalarials (CQ and HCQ), antibiotics (Eritromicin), anti-inflammatories (Thalidomide) and HIV protease inhibitors (Ritonavir) to find possible treatment strategies for COVID-19. The results showed that these drugs have a good affinity for the protein spike compared to antimalarial drugs, such as CQ, HCQ and Artemisinin. Their outcomes suggest that anti-inflammatory drugs, antibiotic inhibitors and HIV protease, are potential candidates for drugs aiming at protein spike. Through *in vitro* and *in vivo* analyzes, it can confirm the promising therapeutic capacity against COVID-19.<sup>165</sup>

## 6. *In silico* methods and a successful case for COVID-19

## 6.1 Remdesivir

Remdesivir ( $C_{27}H_{35}N_6O_8P$ ) is the first antiviral drug approved to treat hospitalized patients with COVID-19.<sup>166</sup> Remdesivir (**Figure 2h**) is an adenosine analogue that was initially developed for the treatment of infections by the Ebola and Marburg viruses. It is a monophosphate that undergoes tissue metabolism to the active form of nucleotide triphosphate C-adenosine. Its active form affects the function of RNA polymerase, resulting in a decrease in the production of viral RNA.<sup>158,159</sup> Remdesivir showed a broad spectrum of antiviral activity against Flaviviridae (Ebola) as well as Paramyxoviridae (Nipah) and exhibited encouraging results against both SARS-CoV and MERS-CoV infections.<sup>141,160,167</sup> Currently, many clinical trials have tested the effectiveness of this drug in COVID-19. Williamson et al.<sup>168</sup> investigated the *in vitro* efficacy of remdesivir treatment using the rhesus monkey model with SARS-CoV-2 infection. Therapeutic treatment of rhesus monkeys with remdesivir resulted in lower viral levels than in untreated monkeys.<sup>168</sup>

Novir and Aram studied the interaction between simple carbon nanotubes (CNTs) functionalized by carboxylic groups and CNTs doped with S-, Al- and Si and remdesivir.<sup>169</sup> From this, the authors showed that CNT doped with Si is the best system for drug delivery owing to its interesting properties.<sup>169</sup>

Besides Remdesivir, Dittmar et al.<sup>170</sup> found other drugs through screening a repurposing library of about 3,000 drugs through conducting experiments. The authors found some drugs with antiviral activity in lung epithelial cells. Three of these drugs (cyclosporine, dacomitinib, and salinomycin, **Figure 2m-o**) are USA Food and Drug Administration (FDA) approved. This work states that additional trials are required to determine the *in vivo* efficacy of these antivirals in COVID-19 patients, in order to inform future treatment strategies. Dacomitinib is a Pfizer's lung cancer drug, while the antibiotics cyclosporine and salinomycin are employed to prevent rejection in patients receiving organ transplants.<sup>170</sup> In addition, the accomplishment of computational studies by employing the diverse tools and methods exposed previously can provide a range of novel data about the interaction and modes of action of these drugs in the COVID-19 treatment.<sup>170-173</sup>

## 7. Conclusions

We discussed that computational drug repositioning is the fastest strategy to help in choosing the best candidates for its use in preclinical studies, which in turn contributes to the emergence of new therapeutic options against SARS-CoV-2 infection. Such strategies can

provide data not available from experiments to boosting the design of novel molecules.<sup>18,78,82,171</sup> Whereas this article is focused on drug repositioning; it is worth mentioning that the computational contribution is also critical for developing new drugs. In this context, we could cite the recently developed oral inhibitor from Pfizer, denominated PF-07321332 (**Figure 2p**). Previously, another inhibitor was developed by the same company, the so-called PF-07304814 (**Figure 2q**).<sup>172</sup> Both compounds are inhibitors of the viral M<sup>pro</sup>. In short, we conclude that computational chemistry can indeed facilitate and optimize the rational design of novel selective inhibitors targeting SARS-CoV-2.

## 8. Acknowledgments

The authors gratefully acknowledge the support from the Brazilian agencies CNPq, CAPES and FAPEMIG.

## 9. Notes

The authors declare no competing financial interest.

**Figure 1** was prepared according to diverse references from literature. Credits: NIAID-RML,<sup>40-43</sup>. All chemical structures in **Figure 2** were prepared through ChemDraw Ultra 12.0, available at <https://chemdraw-pro.software.informer.com/12.0/>.

## 10. References

- (1) Laha, S.; Chakraborty, J.; Das, S.; Manna, S. K.; Biswas, S.; Chatterjee, R. Characterizations of SARS-CoV-2 Mutational Profile, Spike Protein Stability and Viral Transmission. *Infect. Genet. Evol.* **2020**, *85*, 104445.
- (2) Elbe, S.; Buckland-merrett, G. Data , Disease and Diplomacy : GISAID ’ s Innovative Contribution to Global Health. *Glob. Chall.* **2017**, *1* (1), 33–46.
- (3) Weiss, S. R.; Leibowitz, J. L. Coronavirus Pathogenesis. *Adv. Virus Res.* **2011**, *81*, 85-164.
- (4) Zhu, N.; Zhang, D.; Wang, W.; Li, X.; Yang, B.; Song, J.; Zhao, X.; Huang, B.; Shi,

- W.; Lu, R.; et al. A Novel Coronavirus from Patients with Pneumonia in China, 2019. *N. Engl. J. Med.* **2020**, *382* (8), 727–733.
- (5) Zhou, P.; Yang, X. Lou; Wang, X. G.; Hu, B.; Zhang, L.; Zhang, W.; Si, H. R.; Zhu, Y.; Li, B.; Huang, C. L.; et al. A Pneumonia Outbreak Associated with a New Coronavirus of Probable Bat Origin. *Nature* **2020**, *579* (7798), 270–273.
- (6) Wu, F.; Zhao, S.; Yu, B.; Chen, Y.-M.; Wang, W.; Song, Z.-G.; Hu, Y.; Tao, Z.-W.; Tian, J.-H.; Pei, Y.-Y.; et al. A New Coronavirus Associated with Human Respiratory Disease in China. *Nature* **2020**, *579* (7798), 265–269.
- (7) Hilgenfeld, R. From SARS to MERS: Crystallographic Studies on Coronaviral Proteases Enable Antiviral Drug Design. *FEBS J.* **2014**, *281* (18), 4085–4096.
- (8) Tang, X.; Wu, C.; Li, X.; Song, Y.; Yao, X.; Wu, X.; Duan, Y.; Zhang, H.; Wang, Y.; Qian, Z.; et al. On the Origin and Continuing Evolution of SARS-CoV-2. *Natl. Sci. Rev.* **2020**, *7* (6), 1012–1023.
- (9) Lu, R.; Zhao, X.; Li, J.; Niu, P.; Yang, B.; Wu, H.; Wang, W.; Song, H.; Huang, B.; Zhu, N.; et al. Genomic Characterisation and Epidemiology of 2019 Novel Coronavirus: Implications for Virus Origins and Receptor Binding. *Lancet* **2020**, *395* (10224), 565–574.
- (10) Xiao, K.; Zhai, J.; Feng, Y.; Zhou, N.; Zhang, X.; Zou, J. J.; Li, N.; Guo, Y.; Li, X.; Shen, X.; et al. Isolation of SARS-CoV-2-Related Coronavirus from Malayan Pangolins. *Nature* **2020**, *583* (7815), 286–289.
- (11) Altay, O.; Mohammadi, E.; Lam, S.; Turkez, H.; Boren, J.; Nielsen, J.; Uhlen, M.; Mardinoglu, A. Current Status of COVID-19 Therapies and Drug Repositioning Applications. *iScience* **2020**, *23* (7), 101303.
- (12) Arabi, Y. M.; Murthy, S.; Webb, S. COVID-19: A Novel Coronavirus and a Novel Challenge for Critical Care. *Intensive Care Med.* **2020**, *46*, 833–836.
- (13) Zhang, T.; He, Y.; Xu, W.; Ma, A.; Yang, Y.; Xu, K.-F. Clinical Trials for the Treatment of Coronavirus Disease 2019 (COVID-19): A Rapid Response to Urgent Need. *Sci. China. Life Sci.* **2020**, *63*, 774–776.
- (14) Drosten, C.; Gunther, S.; Preiser, W.; van der Werf, S.; Brodt, H.-R.; Becker, S.; Rabenau, H.; Panning, M.; Kolesnikova, L.; Fouchier, R. A. M.; et al. Identification of



- a Novel Coronavirus in Patients with Severe Acute Respiratory Syndrome. *N. Engl. J. Med.* **2003**, *348* (20), 1967–1976.
- (15) Anand, K.; Ziebuhr, J.; Wadhvani, P.; Mesters, J. R.; Hilgenfeld, R. ( 3CL pro ) Structure: Basis for Design of Anti-SARS Drugs. *Science* **2003**, *300* (5626), 1763–1767.
- (16) Kumar, V.; Tan, K.-P.; Wang, Y.-M.; Lin, S.-W.; Liang, P.-H. Identification, Synthesis and Evaluation of SARS-CoV and MERS-CoV 3C-like Protease Inhibitors. *Bioorg. Med. Chem.* **2016**, *24* (13), 3035–3042.
- (17) Tan, J.; Verschuere, K. H. G.; Anand, K.; Shen, J.; Yang, M.; Xu, Y.; Rao, Z.; Bigalke, J.; Heisen, B.; Mesters, J. R.; et al. PH-Dependent Conformational Flexibility of the SARS-CoV Main Proteinase (Mpro) Dimer: Molecular Dynamics Simulations and Multiple X-Ray Structure Analyses. *J. Mol. Biol.* **2005**, *354* (1), 25–40.
- (18) Assis, L. C.; de Castro, A. A.; de Jesus, J. P. A.; Nepovimova, E.; Kuca, K.; Ramalho, T. C.; La Porta, F. A. Computational Evidence for Nitro Derivatives of Quinoline and Quinoline N-Oxide as Low-Cost Alternative for the Treatment of SARS-CoV-2 Infection. *Sci. Rep.* **2021**, *11* (1), 6397.
- (19) Chan, J. F. W.; Kok, K. H.; Zhu, Z.; Chu, H.; To, K. K. W.; Yuan, S.; Yuen, K. Y. Genomic Characterization of the 2019 Novel Human-Pathogenic Coronavirus Isolated from a Patient with Atypical Pneumonia after Visiting Wuhan. *Emerg. Microbes Infect.* **2020**, *9* (1), 221–236.
- (20) Wu, A.; Peng, Y.; Huang, B.; Ding, X.; Wang, X.; Niu, P.; Meng, J.; Zhu, Z.; Zhang, Z.; Wang, J.; et al. Genome Composition and Divergence of the Novel Coronavirus (2019-NCoV) Originating in China. *Cell Host Microbe* **2020**, *27* (3), 325–328.
- (21) Fischer, A.; Sellner, M.; Neranjan, S.; Smieško, M.; Lill, M. A. Potential Inhibitors for Novel Coronavirus Protease Identified by Virtual Screening of 606 Million Compounds. *Int. J. Mol. Sci.* **2020**, *21* (10), 3626.
- (22) Shang, J.; Wan, Y.; Luo, C.; Ye, G.; Geng, Q.; Auerbach, A.; Li, F. Cell Entry Mechanisms of SARS-CoV-2. *Proc. Natl. Acad. Sci.* **2020**, *117* (21), 11727 LP – 11734.
- (23) Mazzini, S.; Musso, L.; Dallavalle, S.; Artali, R. Putative SARS-CoV-2 Mpro

- Inhibitors from an In-House Library of Natural and Nature-Inspired Products: A Virtual Screening and Molecular Docking Study. *Molecules* **2020**, *25* (16), 3745.
- (24) Guy, J. S.; Breslin, J. J.; Breuhaus, B.; Vivrette, S.; Smith, L. G. Characterization of a Coronavirus Isolated from a Diarrheic Foal. *J. Clin. Microbiol.* **2000**, *38* (12), 4523 LP – 4526.
- (25) Li, F.; Li, W.; Farzan, M.; Harrison, S. C. Structural Biology: Structure of SARS Coronavirus Spike Receptor-Binding Domain Complexed with Receptor. *Science* **2005**, *309* (5742), 1864–1868.
- (26) Oostra, M.; de Haan, C. A. M.; Rottier, P. J. M. The 29-Nucleotide Deletion Present in Human but Not in Animal Severe Acute Respiratory Syndrome Coronaviruses Disrupts the Functional Expression of Open Reading Frame 8. *J. Virol.* **2007**, *81* (24), 13876–13888.
- (27) Khailany, R. A.; Safdar, M.; Ozaslan, M. Genomic Characterization of a Novel SARS-CoV-2. *Gene Reports* **2020**, *19*, 1–6.
- (28) Choudhry, N.; Zhao, X.; Xu, D.; Zanin, M.; Chen, W.; Yang, Z.; Chen, J. Chinese Therapeutic Strategy for Fighting COVID-19 and Potential Small-Molecule Inhibitors against Severe Acute Respiratory Syndrome Coronavirus 2 (SARS-CoV-2). *J. Med. Chem.* **2020**, *63* (22), 13205–13227.
- (29) Zumla, A.; Chan, J. F. W.; Azhar, E. I.; Hui, D. S. C.; Yuen, K.-Y. Coronaviruses — Drug Discovery and Therapeutic Options. *Nat. Rev. Drug Discov.* **2016**, *15* (5), 327–347.
- (30) V'kovski, P.; Kratzel, A.; Steiner, S.; Stalder, H.; Thiel, V. Coronavirus Biology and Replication: Implications for SARS-CoV-2. *Nat. Rev. Microbiol.* **2021**, *19* (3), 155–170.
- (31) Li, F. Structure, Function, and Evolution of Coronavirus Spike Proteins. *Annu. Rev. Virol.* **2016**, *3*, 237–261.
- (32) Tortorici, M. A.; Veessler, D. Structural Insights into Coronavirus Entry. *Adv. Virus Res.* **2019**, *105*, 93–116.
- (33) Hoffmann, M.; Kleine-Weber, H.; Schroeder, S.; Krüger, N.; Herrler, T.; Erichsen, S.; Schiergens, T. S.; Herrler, G.; Wu, N.-H.; Nitsche, A.; et al. SARS-CoV-2 Cell Entry

- Depends on ACE2 and TMPRSS2 and Is Blocked by a Clinically Proven Protease Inhibitor. *Cell* **2020**, *181* (2), 271-280.e8.
- (34) Anand, K.; Ziebuhr, J.; Wadhvani, P.; Mesters, J. R.; Hilgenfeld, R. Coronavirus Main Proteinase (3CLpro) Structure: Basis for Design of Anti-SARS Drugs. *Science* **2003**, *300* (5626), 1763–1767.
- (35) Letko, M.; Marzi, A.; Munster, V. Functional Assessment of Cell Entry and Receptor Usage for SARS-CoV-2 and Other Lineage B Betacoronaviruses. *Nat. Microbiol.* **2020**, *5* (4), 562–569.
- (36) Li, W.; Moore, M. J.; Vasilieva, N.; Sui, J.; Wong, S. K.; Berne, M. A.; Somasundaran, M.; Sullivan, J. L.; Luzuriaga, K.; Greenough, T. C.; et al. Angiotensin-Converting Enzyme 2. *Nat. Publ. Gr.* **2003**, *426*, 450–454.
- (37) Eastman, R. T.; Roth, J. S.; Brimacombe, K. R.; Simeonov, A.; Shen, M.; Patnaik, S.; Hall, M. D. Remdesivir: A Review of Its Discovery and Development Leading to Emergency Use Authorization for Treatment of COVID-19. *ACS Cent. Sci.* **2020**, *6* (5), 672–683.
- (38) Liang, P.-H. Characterization and Inhibition of SARS-Coronavirus Main Protease. *Curr. Top. Med. Chem.* 2006, *6* (4), 361–376.
- (39) Tan, J.; Verschueren, K. H. G.; Anand, K.; Shen, J.; Yang, M.; Xu, Y.; Rao, Z.; Bigalke, J.; Heisen, B.; Mesters, J. R.; et al. PH-Dependent Conformational Flexibility of the SARS-CoV Main Proteinase (M(pro)) Dimer: Molecular Dynamics Simulations and Multiple X-Ray Structure Analyses. *J. Mol. Biol.* **2005**, *354* (1), 25–40.
- (40) Kneller, D. W.; Phillips, G.; O'Neill, H. M.; Jedrzejczak, R.; Stols, L.; Langan, P.; Joachimiak, A.; Coates, L.; Kovalevsky, A. Structural Plasticity of SARS-CoV-2 3CL Mpro Active Site Cavity Revealed by Room Temperature X-Ray Crystallography. *Nat. Commun.* **2020**, *11* (1), 3202.
- (41) Mittal, A.; Manjunath, K.; Ranjan, R. K.; Kaushik, S.; Kumar, S.; Verma, V. COVID-19 Pandemic: Insights into Structure, Function, and HACE2 Receptor Recognition by SARS-CoV-2. *PLoS Pathog.* **2020**, *16* (8), e1008762–e1008762.
- (42) Procko, E. The Sequence of Human ACE2 Is Suboptimal for Binding the S Spike Protein of SARS Coronavirus 2. *bioRxiv* **2020**, 2020.03.16.994236.

- (43) Loey, M.; Smarandache, F.; M. Khalifa, N. E. Within the Lack of Chest COVID-19 X-Ray Dataset: A Novel Detection Model Based on GAN and Deep Transfer Learning. *Symmetry* **2020**, *12* (4), 651.
- (44) van Dorp, L.; Acman, M.; Richard, D.; Shaw, L. P.; Ford, C. E.; Ormond, L.; Owen, C. J.; Pang, J.; Tan, C. C. S.; Boshier, F. A. T.; et al. Emergence of Genomic Diversity and Recurrent Mutations in SARS-CoV-2. *Infect. Genet. Evol.* **2020**, *83* (May), 104351.
- (45) Azkur, A. K.; Akdis, M.; Azkur, D.; Sokolowska, M.; van de Veen, W.; Brüggem, M.-C.; O'Mahony, L.; Gao, Y.; Nadeau, K.; Akdis, C. A. Immune Response to SARS-CoV-2 and Mechanisms of Immunopathological Changes in COVID-19. *Allergy* **2020**, *75* (7), 1564–1581.
- (46) Forster, P.; Forster, L.; Renfrew, C.; Forster, M. Phylogenetic Network Analysis of SARS-CoV-2 Genomes. *Proc. Natl. Acad. Sci. U. S. A.* **2020**, *117* (17), 9241–9243.
- (47) Toyoshima, Y.; Nemoto, K.; Matsumoto, S.; Nakamura, Y.; Kiyotani, K. SARS-CoV-2 Genomic Variations Associated with Mortality Rate of COVID-19. *J. Hum. Genet.* **2020**, *65*, 1075–1082.
- (48) Hu, B.; Guo, H.; Zhou, P.; Shi, Z.-L. Characteristics of SARS-CoV-2 and COVID-19. *Nat. Rev. Microbiol.* **2021**, *19* (3), 141–154.
- (49) Zhou, H.; Chen, X.; Hu, T.; Li, J.; Song, H.; Liu, Y.; Wang, P.; Liu, D.; Yang, J.; Holmes, E. C.; et al. A Novel Bat Coronavirus Closely Related to SARS-CoV-2 Contains Natural Insertions at the S1/S2 Cleavage Site of the Spike Protein. *Curr. Biol.* **2020**, *30* (11), 2196–2203.e3.
- (50) Dearlove, B.; Lewitus, E.; Bai, H.; Li, Y.; Reeves, D. B.; Joyce, M. G.; Scott, P. T.; Amare, M. F.; Vasan, S.; Michael, N. L.; et al. A SARS-CoV-2 Vaccine Candidate Would Likely Match All Currently Circulating Variants. *Proc. Natl. Acad. Sci. U. S. A.* **2020**, *117* (38), 23652–23662.
- (51) Lam, T. T. Y.; Jia, N.; Zhang, Y. W.; Shum, M. H. H.; Jiang, J. F.; Zhu, H. C.; Tong, Y. G.; Shi, Y. X.; Ni, X. B.; Liao, Y. S.; et al. Identifying SARS-CoV-2-Related Coronaviruses in Malayan Pangolins. *Nature* **2020**, *583* (7815), 282–285.
- (52) Lv, L.; Li, G.; Chen, J.; Liang, X.; L, Y. Comparative Genomic Analysis Revealed

- Specific Mutation Pattern between Human Coronavirus SARS-CoV-2 and Bat-SARSR-CoV RaTG13. *bioRxiv* **2020**, *21* (1), 1–9.
- (53) Worobey, M.; Pekar, J.; Larsen, B. B.; Nelson, M. I.; Hill, V.; Joy, J. B.; Rambaut, A.; Suchard, M. A.; Wertheim, J. O.; Lemey, P. The Emergence of SARS-CoV-2 in Europe and North America. *Science* **2020**, *370* (6516), 564-570.
- (54) Stukalov, A.; Girault, V.; Grass, V.; Karayel, O.; Bergant, V.; Urban, C.; Haas, D. A.; Huang, Y.; Oubraham, L.; Wang, A.; et al. Multilevel Proteomics Reveals Host Perturbations by SARS-CoV-2 and SARS-CoV. *Nature* **2021**.
- (55) Zhang, L.; Lin, D.; Sun, X.; Curth, U.; Drosten, C.; Sauerhering, L.; Becker, S.; Rox, K.; Hilgenfeld, R. Crystal Structure of SARS-CoV-2 Main Protease Provides a Basis for Design of Improved  $\alpha$ -Ketoamide Inhibitors. *Science* **2020**, *368* (6489), 409-412.
- (56) Dong, L.; Hu, S.; Gao, J. Discovering Drugs to Treat Coronavirus Disease 2019 (COVID-19). *Drug Discov. Ther.* **2020**, *14* (1), 58–60.
- (57) Oliveira, M. D. L. de; Oliveira, K. M. T. de. Comparative Computational Study of SARS-CoV-2 Receptors Antagonists from Already Approved Drugs. *ChemRxiv* **2020**.
- (58) Savarino, A.; Di Trani, L.; Donatelli, I.; Cauda, R.; Cassone, A. New Insights into the Antiviral Effects of Chloroquine. *Lancet Infect. Dis.* **2006**, *6* (2), 67–69.
- (59) Wang, M.; Cao, R.; Zhang, L.; Yang, X.; Liu, J.; Xu, M.; Shi, Z.; Hu, Z.; Zhong, W.; Xiao, G. Remdesivir and Chloroquine Effectively Inhibit the Recently Emerged Novel Coronavirus (2019-NCoV) in Vitro. *Cell Res.* **2020**, *30* (3), 269–271.
- (60) Sousa, S. F.; Fernandes, P. A.; Ramos, M. J. Protein–Ligand Docking: Current Status and Future Challenges. *Proteins Struct. Funct. Bioinforma.* **2006**, *65* (1), 15–26.
- (61) Lin, X.; Li, X.; Lin, X. A Review on Applications of Computational Methods in Drug Screening and Design. *Molecules* **2020**, *25* (6), 1375.
- (62) Mohamed, K.; Yazdanpanah, N.; Saghadzadeh, A.; Rezaei, N. Computational Drug Discovery and Repurposing for the Treatment of COVID-19: A Systematic Review. *Bioorg. Chem.* **2021**, *106*, 104490.
- (63) Ou-Yang, S.; Lu, J.; Kong, X.; Liang, Z.; Luo, C.; Jiang, H. Computational Drug Discovery. *Acta Pharmacol. Sin.* **2012**, *33* (9), 1131–1140.

- (64) Roy, A.; Nair, S.; Sen, N.; Soni, N.; Madhusudhan, M. S. In Silico Methods for Design of Biological Therapeutics. *Methods* **2017**, *131*, 33–65.
- (65) Ramsay, R. R.; Popovic-Nikolic, M. R.; Nikolic, K.; Uliassi, E.; Bolognesi, M. L. A Perspective on Multi-Target Drug Discovery and Design for Complex Diseases. *Clin. Transl. Med.* **2018**, *7* (1), e3.
- (66) Martí, S.; Roca, M.; Andrés, J.; Moliner, V.; Silla, E.; Tuñón, I.; Bertrán, J. Theoretical Insights in Enzyme Catalysis. *Chem. Soc. Rev.* **2004**, *33* (2), 98–107.
- (67) Jorgensen, W. L. Computer-Aided Discovery of Anti-HIV Agents. *Bioorg. Med. Chem.* **2016**, *24* (20), 4768–4778.
- (68) Guido, R. V. C.; Andricopulo, A. D.; Oliva, G. Planejamento de Fármacos, Biotecnologia e Química Medicinal: Aplicações Em Doenças Infecciosas. *Estudos Avançados* **2010**, *24* (70), 81–98.
- (69) de Oliveira, O. V.; Rocha, G. B.; Paluch, A. S.; Costa, L. T. Repurposing Approved Drugs as Inhibitors of SARS-CoV-2 S-Protein from Molecular Modeling and Virtual Screening. *J. Biomol. Struct. Dyn.* **2020**, 1–10.
- (70) Galindez, G.; Matschinske, J.; Rose, T. D.; Sadegh, S.; Salgado-Albarrán, M.; Späth, J.; Baumbach, J.; Pauling, J. K. Lessons from the COVID-19 Pandemic for Advancing Computational Drug Repurposing Strategies. *Nat. Comput. Sci.* **2021**, *1* (1), 33–41.
- (71) Jarada, T. N.; Rokne, J. G.; Alhaji, R. A Review of Computational Drug Repositioning: Strategies, Approaches, Opportunities, Challenges, and Directions. *J. Cheminform.* **2020**, *12* (1), 46.
- (72) Almeida, J. S. F. D.; Botelho, F. D.; de Souza, F. R.; dos Santos, M. C.; Goncalves, A. da S.; et al. Searching for Potential Drugs against SARS-CoV-2 through Virtual Screening on Several Molecular Targets. *J. Biomol. Struct. Dyn.* **2021**, 1–14.
- (73) Lonsdale, R.; Ranaghan, K. E.; Mulholland, A. J. Computational Enzymology. *Chem. Commun.* **2010**, *46*, 2354–2372.
- (74) Nemukhin, A. V.; Grigorenko, B. L.; Lushchekina, S. V.; Varfolomeev, S. D. Quantum Chemical Modelling in the Research of Molecular Mechanisms of Enzymatic Catalysis. *Russ. Chem. Rev.* **2012**, *81* (11), 1011–1025.

- (75) La Porta, F. A.; Taft, C. A. *Emerging Research in Science and Engineering Based on Advanced Experimental and Computational Strategies*; Springer, Cham, **2020**.
- (76) Longo, E.; La Porta, F. A. *Recent Advances in Complex Functional Materials: From Design to Application*; **2017**.
- (77) *Functional Properties of Advanced Engineering Materials and Biomolecules*, 1st ed.; La Porta, F. de A., Taft, C. A., Eds.; Springer International Publishing, **2021**.
- (78) Ramalho, T. C.; de Castro, A. A.; Silva, D. R.; Silva, M. C.; Franca, T. C. C.; Bennion, B. J.; Kuca, K. Computational Enzymology and Organophosphorus Degrading Enzymes: Promising Approaches Toward Remediation Technologies of Warfare Agents and Pesticides. *Curr. Med. Chem.* **2016**, *23* (10), 1041–1061.
- (79) Senn, H. M.; Thiel, W. QM/MM Methods for Biomolecular Systems. *Angew. Chem. Int. Ed. Engl.* **2009**, *48* (7), 1198–1229.
- (80) Jorgensen, W. L. The Many Roles of Computation in Drug Discovery. *Science* **2004**, *303* (5665), 1813–818.
- (81) Cavalli, A.; Carloni, P.; Recanatini, M. Target-Related Applications of First Principles Quantum Chemical Methods in Drug Design. *Chem. Rev.* **2006**, *106* (9), 3497–3519.
- (82) Raha, K.; Peters, M. B.; Wang, B.; Yu, N.; Wollacott, A. M.; Westerhoff, L. M.; Merz, K. M. The Role of Quantum Mechanics in Structure-Based Drug Design. *Drug Discov. Today* **2007**, *12* (17), 725–731.
- (83) Santos, L. H.; Ferreira, R. S.; Caffarena, E. R. Computational Drug Design Strategies Applied to the Modelling of Human Immunodeficiency Virus-1 Reverse Transcriptase Inhibitors. *Memórias do Instituto Oswaldo Cruz* **2015**, *110* (7), 847–864.
- (84) Zhou, T.; Huang, D.; Caflisch, A. Quantum Mechanical Methods for Drug Design. *Curr. Top. Med. Chem.* **2010**, *10* (1), 33–45.
- (85) Cohen, N. C. Preface; COHEN, N. C. B. T.-G. on M. M. in D. D., Ed.; Academic Press: San Diego, 1996; pp xiii–xiv.
- (86) Sant’Anna, C. M. R. Molecular Modeling Methods in the Study and Design of Bioactive Compounds: An Introduction. *Rev. Virtual Química* **2009**, *1* (1), 49–57.
- (87) Namba, A. M.; Da Silva, V. B.; Da Silva, C. H. T. P. Dinâmica Molecular: Teoria e

- Aplicações Em Planejamento de Fármacos. *Eclét. Quím.* **2008**, 33 (4), 13–24.
- (88) Brooks, B. R.; Bruccoleri, R. E.; Olafson, B. D.; States, D. J.; Swaminathan, S.; Karplus, M. CHARMM: A Program for Macromolecular Energy, Minimization, and Dynamics Calculations. *J. Comput. Chem.* **1983**, 4 (2), 187–217.
- (89) Scott, W. R. P.; Hünenberger, P. H.; Tironi, I. G.; Mark, A. E.; Billeter, S. R.; Fennen, J.; Torda, A. E.; Huber, T.; Krüger, P.; van Gunsteren, W. F. The GROMOS Biomolecular Simulation Program Package. *J. Phys. Chem. A* **1999**, 103 (19), 3596–3607.
- (90) Weiner, P. K.; Kollman, P. A. AMBER: Assisted Model Building with Energy Refinement. A General Program for Modeling Molecules and Their Interactions. *J. Comput. Chem.* **1981**, 2 (3), 287–303.
- (91) Jorgensen, W. L.; Maxwell, D. S.; Tirado-Rives, J. Development and Testing of the OPLS All-Atom Force Field on Conformational Energetics and Properties of Organic Liquids. *J. Am. Chem. Soc.* **1996**, 118 (45), 11225–11236.
- (92) Tu, M.; Zheng, X.; Liu, P.; Wang, S.; Yan, Z.; Sun, Q.; Liu, X. Typical Organic Pollutant-Protein Interactions Studies through Spectroscopy, Molecular Docking and Crystallography: A Review. *Sci. Total Environ.* **2021**, 763, 142959.
- (93) de Castro, A. A.; Assis, L. C.; Silva, D. R.; Corrêa, S.; Assis, T. M.; Gajo, G. C.; Soares, F. V.; Ramalho, T. C. Computational Enzymology for Degradation of Chemical Warfare Agents: Promising Technologies for Remediation Processes. *AIMS Microbiol.* **2017**, 3 (1), 108–135.
- (94) Thomsen, R.; Christensen, M. H. MolDock: A New Technique for High Accuracy Molecular Docking. *J. Med. Chem.* **2006**, 49, 3315–3321.
- (95) Azevedo, L. S.; Moraes, F. P.; Xavier, M. M.; Pantoja, E. O.; Villavicencio, B.; Finck, J. A.; Proenca, A. M.; Azevedo, K. B. R. and W. F. de. Recent Progress of Molecular Docking Simulations Applied to Development of Drugs. *Current Bioinformatics.* **2012**, 7 (4), 352–365.
- (96) Liu, M.; Wang, S. MCDOCK: A Monte Carlo Simulation Approach to the Molecular Docking Problem. *J. Comput. Aided. Mol. Des.* **1999**, 13 (5), 435–451.
- (97) Goodsell, D. S.; Morris, G. M.; Olson, A. J. Automated Docking of Flexible Ligands:



- Applications of AutoDock. *J. Mol. Recognit.* **1996**, 9 (1), 1–5.
- (98) Rosenfeld, R. J.; Goodsell, D. S.; Musah, R. A.; Morris, G. M.; Goodin, D. B.; Olson, A. J. Automated Docking of Ligands to an Artificial Active Site: Augmenting Crystallographic Analysis with Computer Modeling. *J. Comput. Aided. Mol. Des.* **2003**, 17 (8), 525–536.
- (99) da Cunha, E. F. F.; Ramalho, T. C.; Reynolds, R. C. Binding Mode Analysis of 2, 4-Diamino-5-Methyl-5-Deaza-6-Substituted Pteridines with Mycobacterium Tuberculosis and Human Dihydrofolate Reductases. *J. Biomol. Struct. Dyn.* **2008**, 25 (4), 377–385.
- (100) Assis, L. C.; Santos-Garcia, L.; Cunha, T. C. R. and E. F. F. da. Interactions of Pyrimidine Derivatives with Dihydrofolate Reductase and Thymidylate Synthase: Directions Toward Combating Toxoplasmosis. *Curr. Bioact. Compd.* **2013**, 9 (2), 153–166.
- (101) Kuntz, I. D.; Blaney, J. M.; Oatley, S. J.; Langridge, R.; Ferrin, T. E. A Geometric Approach to Macromolecule-Ligand Interactions. *J. Mol. Biol.* **1982**, 161 (2), 269–288.
- (102) Kirkpatrick, S.; Gelatt, C. D.; Vecchi, M. P. Optimization by Simulated Annealing. *Science* (80-. ). **1983**, 220 (4598), 671–680.
- (103) Jones, G.; Willett, P.; Glen, R. C.; Leach, A. R.; Taylor, R. Development and Validation of a Genetic Algorithm for Flexible Docking<sup>1</sup> Edited by F. E. Cohen. *J. Mol. Biol.* **1997**, 267 (3), 727–748.
- (104) Goodsell, D. S.; Olson, A. J. Automated Docking of Substrates to Proteins by Simulated Annealing. *Proteins* **1990**, 8 (3), 195–202.
- (105) Rarey, M.; Kramer, B.; Lengauer, T.; Klebe, G. A Fast Flexible Docking Method Using an Incremental Construction Algorithm. *J. Mol. Biol.* **1996**, 261 (3), 470–489.
- (106) Azevedo, W. F. de. Molecular Dynamics Simulations of Protein Targets Identified in Mycobacterium Tuberculosis. *Curr. Med. Chem.* **2011**, 18 (9), 1353–1366.
- (107) Haile, J. M. *Molecular Dynamics Simulation: Elementary Methods*, 1st ed.; John Wiley & Sons, Inc.: New York, NY, USA, 1992.
- (108) Rapaport, D. C. *The Art of Molecular Dynamics Simulation*, 2nd ed.; Cambridge

University Press: Cambridge, **2004**.

- (109) Dubey, K. D.; Ojha, R. K. T. and R. P. Recent Advances in Protein–Ligand Interactions: Molecular Dynamics Simulations and Binding Free Energy. *Curr. Comput. Aided Drug Des.* **2013**, *9* (4), 518–531.
- (110) Kalé, L.; Skeel, R.; Bhandarkar, M.; Brunner, R.; Gursoy, A.; Krawetz, N.; Phillips, J.; Shinozaki, A.; Varadarajan, K.; Schulten, K. NAMD2: Greater Scalability for Parallel Molecular Dynamics. *J. Comput. Phys.* **1999**, *151* (1), 283–312.
- (111) Phillips, J. C.; Braun, R.; Wang, W.; Gumbart, J.; Tajkhorshid, E.; Villa, E.; Chipot, C.; Skeel, R. D.; Kalé, L.; Schulten, K. Scalable Molecular Dynamics with NAMD. *J. Comput. Chem.* **2005**, *26* (16), 1781–1802.
- (112) Lionta, E.; Spyrou, G.; Cournia, D. K. V. and Z. Structure-Based Virtual Screening for Drug Discovery: Principles, Applications and Recent Advances. *Curr. Top. Med. Chem.* **2014**, *14* (16), 1923–1938.
- (113) Giovanni, A. L. and C. Di. Virtual Screening Strategies in Drug Discovery: A Critical Review. *Curr. Med. Chem.* **2013**, *20* (23), 2839–2860.
- (114) Reddy, A. S.; Pati, S. P.; Kumar, P. P.; Sastry, H. N. P. and G. N. Virtual Screening in Drug Discovery - A Computational Perspective. *Curr. Protein Pept. Sci.* **2007**, *8* (4), 329–351.
- (115) Vázquez, J.; López, M.; Gibert, E.; Herrero, E.; Luque, F. J. Merging Ligand-Based and Structure-Based Methods in Drug Discovery: An Overview of Combined Virtual Screening Approaches. *Molecules* **2020**, *25* (20), 4723.
- (116) Drwal, M. N.; Griffith, R. Combination of Ligand- and Structure-Based Methods in Virtual Screening. *Drug Discov. Today Technol.* **2013**, *10* (3), e395–e401.
- (117) Gimeno, A.; Ojeda-Montes, M. J.; Tomás-Hernández, S.; Cereto-Massagué, A.; Beltrán-Debón, R.; Mulero, M.; Pujadas, G.; Garcia-Vallvé, S. The Light and Dark Sides of Virtual Screening: What Is There to Know? *Int. J. Mol. Sci.* **2019**, *20* (6), 1375.
- (118) Scior, T.; Bender, A.; Tresadern, G.; Medina-Franco, J. L.; Martínez-Mayorga, K.; Langer, T.; Cuanalo-Contreras, K.; Agrafiotis, D. K. Recognizing Pitfalls in Virtual Screening: A Critical Review. *J. Chem. Inf. Model.* **2012**, *52* (4), 867–881.

- (119) Kumar, A.; Zhang, K. Y. J. Hierarchical Virtual Screening Approaches in Small Molecule Drug Discovery. *Methods* **2015**, *71*, 26–37.
- (120) Maia, E. H. B.; Assis, L. C.; de Oliveira, T. A.; da Silva, A. M.; Taranto, A. G. Structure-Based Virtual Screening: From Classical to Artificial Intelligence. *Front. Chem.* **2020**, *8* (343), 1-18.
- (121) Varnek, A. Fragment Descriptors in Structure-Property Modeling and Virtual Screening. *Methods Mol. Biol.* **2011**, *672*, 213–243.
- (122) Ashburn, T. T.; Thor, K. B. Drug Repositioning: Identifying and Developing New Uses for Existing Drugs. *Nat. Rev. Drug Discov.* **2004**, *3* (8), 673–683.
- (123) Bouche, G.; Gedye, C.; Meheus, L.; Pantziarka, P. Drug Repurposing in Oncology. *Lancet Oncol.* **2020**, *21* (12), e542.
- (124) Yella, J. K.; Yaddanapudi, S.; Wang, Y.; Jegga, A. G. Changing Trends in Computational Drug Repositioning. *Pharmaceuticals* **2018**, *11* (2), 57.
- (125) Pushpakom, S.; Iorio, F.; Eyers, P. A.; Escott, K. J.; Hopper, S.; Wells, A.; Doig, A.; Guilliams, T.; Latimer, J.; McNamee, C.; et al. Drug Repurposing: Progress, Challenges and Recommendations. *Nat. Rev. Drug Discov.* **2019**, *18* (1), 41–58.
- (126) de Castro, A. A.; da Cunha, E. F. F.; Pereira, A. F.; Soares, F. V.; Leal, D. H. S.; Kuca, K.; Ramalho, T. C. Insights into the Drug Repositioning Applied to the Alzheimer's Disease Treatment and Future Perspectives. *Curr. Alzheimer Res.* **2018**, *15* (12), 1161–1178.
- (127) Anand, K.; Palm, G. J.; Mesters, J. R.; Siddell, S. G.; Ziebuhr, J.; Hilgenfeld, R. Structure of Coronavirus Main Proteinase Reveals Combination of a Chymotrypsin Fold with an Extra  $\alpha$ -Helical Domain. *EMBO J.* **2002**, *21* (13), 3213–3224.
- (128) Gao, Y.; Yan, L.; Huang, Y.; Liu, F.; Zhao, Y.; Cao, L.; Wang, T.; Sun, Q.; Ming, Z.; Zhang, L.; et al. Structure of the RNA-Dependent RNA Polymerase from COVID-19 Virus. *Science.* **2020**, *368* (6492), 779–782.
- (129) Hillen, H. S.; Kokic, G.; Farnung, L.; Dienemann, C.; Tegunov, D.; Cramer, P. Structure of Replicating SARS-CoV-2 Polymerase. *Nature* **2020**, *584* (7819), 154–156.
- (130) Zamyatkin, D. F.; Parra, F.; Machín, A.; Grochulski, P.; Ng, K. K.-S. Binding of 2'-

- Amino-2'-Deoxycytidine-5'-Triphosphate to Norovirus Polymerase Induces Rearrangement of the Active Site. *J. Mol. Biol.* **2009**, *390* (1), 10–16.
- (131) Lan, J.; Ge, J.; Yu, J.; Shan, S.; Zhou, H.; Fan, S.; Zhang, Q.; Shi, X.; Wang, Q.; Zhang, L.; et al. Structure of the SARS-CoV-2 Spike Receptor-Binding Domain Bound to the ACE2 Receptor. *Nature* **2020**, *581* (7807), 215–220.
- (132) Shahab, S.; Sheikhi, M.; Alnajjar, R.; Saud, S. Al; Khancheuski, M.; Strogova, A. DFT Investigation of Atazanavir as Potential Inhibitor for 2019-NCoV Coronavirus M Protease. *J. Mol. Struct.* **2021**, *1228*, 129461.
- (133) Petit, L.; Vernès, L.; Cadoret, J.-P. Docking and in Silico Toxicity Assessment of Arthrospira Compounds as Potential Antiviral Agents against SARS-CoV-2. *J. Appl. Phycol.* **2021**.
- (134) da Silva, F. M. A.; da Silva, K. P. A.; de Oliveira, L. P. M.; Costa, E. V; Koolen, H. H. F.; Pinheiro, M. L. B.; de Souza, A. Q. L.; de Souza, A. D. L. Flavonoid Glycosides and Their Putative Human Metabolites as Potential Inhibitors of the SARS-CoV-2 Main Protease (Mpro) and RNA-Dependent RNA Polymerase (RdRp). *Memórias do Instituto Oswaldo Cruz* **2020**, *115*, e200207.
- (135) Lung, J.; Lin, Y.-S.; Yang, Y.-H.; Chou, Y.-L.; Shu, L.-H.; Cheng, Y.-C.; Liu, H. Te; Wu, C.-Y. The Potential Chemical Structure of Anti-SARS-CoV-2 RNA-Dependent RNA Polymerase. *J. Med. Virol.* **2020**, *92* (6), 693–697.
- (136) Aftab, S. O.; Ghouri, M. Z.; Masood, M. U.; Haider, Z.; Khan, Z.; Ahmad, A.; Munawar, N. Analysis of SARS-CoV-2 RNA-Dependent RNA Polymerase as a Potential Therapeutic Drug Target Using a Computational Approach. *J. Transl. Med.* **2020**, *18* (1), 275.
- (137) Pokhrel, R.; Chapagain, P.; Siltberg-Liberles, J. Potential RNA-Dependent RNA Polymerase Inhibitors as Prospective Therapeutics against SARS-CoV-2. *J. Med. Microbiol.* **2020**, *69* (6), 864–873.
- (138) Assis, L. C.; Castro, A. A. de; Jesus, J. P. A. de; Ramalho, T. de C.; Porta, F. de A. La. Theoretical Insights into the Effect of Halogenated Substituent on the Electronic Structure and Spectroscopic Properties of the Favipiravir Tautomeric Forms and Its Implications on the Treatment of COVID-19. *ChemRxiv* **2020**.

- (139) Saha, S.; Nandi, R.; Vishwakarma, P.; Prakash, A.; Kumar, D. Discovering Potential RNA Dependent RNA Polymerase Inhibitors as Prospective Drugs Against COVID-19: An in Silico Approach. *Front. Pharmacol.* **2021**, *12*, 634047.
- (140) Goel, P.; Gerriets, V. Chloroquine.; Treasure Island (FL), 2021.
- (141) Naik, R. R.; Shakya, A. K. Therapeutic Strategies in the Management of COVID-19. *Front. Mol. Biosci.* **2021**, *7*, 636738.
- (142) Knight, R. The Chemotherapy of Amoebiasis. *J. Antimicrob. Chemother.* **1980**, *6* (5), 577–593.
- (143) Freedman, A.; Steinberg, V. L. Chloroquine in Rheumatoid Arthritis. *Ann. Rheum. Dis.* **1960**, *19* (3), 243–250.
- (144) Li, L.; Zhang, W.; Hu, Y.; Tong, X.; Zheng, S.; Yang, J.; Kong, Y.; Ren, L.; Wei, Q.; Mei, H.; et al. Effect of Convalescent Plasma Therapy on Time to Clinical Improvement in Patients With Severe and Life-Threatening COVID-19: A Randomized Clinical Trial. *JAMA* **2020**, *324* (5), 460–470.
- (145) Singh, A. K.; Singh, A.; Shaikh, A.; Singh, R.; Misra, A. Chloroquine and Hydroxychloroquine in the Treatment of COVID-19 with or without Diabetes: A Systematic Search and a Narrative Review with a Special Reference to India and Other Developing Countries. *Diabetes Metab. Syndr.* **2020**, *14* (3), 241–246.
- (146) Sanders, J. M.; Monogue, M. L.; Jodlowski, T. Z.; Cutrell, J. B. Pharmacologic Treatments for Coronavirus Disease 2019 (COVID-19): A Review. *JAMA* **2020**, *323* (18), 1824–1836.
- (147) Damilare, R.; Afolabi, B.; Adeyemi, O. COVID 19: Resveratrol as a Potential Supplement to Mitigate the Cardiotoxicity Associated with Chloroquine and Hydroxychloroquine Treatment. *Biointerface Res. Appl. Chem.* **2021**, *11*, 11172–11186.
- (148) Hussein, R. K.; Elkhair, H. M. Molecular Docking Identification for the Efficacy of Some Zinc Complexes with Chloroquine and Hydroxychloroquine against Main Protease of COVID-19. *J. Mol. Struct.* **2021**, *1231*, 129979.
- (149) Ghazy, R. M.; Almaghraby, A.; Shaaban, R.; Kamal, A.; Beshir, H.; Moursi, A.; Ramadan, A.; Taha, S. H. N. A Systematic Review and Meta-Analysis on Chloroquine

- and Hydroxychloroquine as Monotherapy or Combined with Azithromycin in COVID-19 Treatment. *Sci. Rep.* **2020**, *10* (1), 22139.
- (150) Venditto, V. J.; Haydar, D.; Abdel-Latif, A.; Gensel, J. C.; Anstead, M. I.; Pitts, M. G.; Creameans, J.; Kopper, T. J.; Peng, C.; Feola, D. J. Immunomodulatory Effects of Azithromycin Revisited: Potential Applications to COVID-19. *Front. Immunol.* **2021**, *12*, 574425.
- (151) Tarighi, P.; Eftekhari, S.; Chizari, M.; Sabernavaei, M.; Jafari, D.; Mirzabeigi, P. A Review of Potential Suggested Drugs for Coronavirus Disease (COVID-19) Treatment. *Eur. J. Pharmacol.* **2021**, *895*, 173890.
- (152) Ali, A. S.; ASattar, M. A.; Karim, S.; Kutbi, D.; Aljohani, H.; Bakhshwin, D.; Alsieni, M.; Alkreathy, H. M. Pharmacological Basis for the Potential Role of Azithromycin and Doxycycline in Management of COVID-19. *Arab. J. Chem.* **2021**, *14* (3), 102983.
- (153) Arouche, T. da S.; Martins, A. Y.; Ramalho, T. de C.; Júnior, R. N. C.; Costa, F. L. P.; Filho, T. S. de A.; Neto, A. M. J. C. Molecular Docking of Azithromycin, Ritonavir, Lopinavir, Oseltamivir, Ivermectin and Heparin Interacting with Coronavirus Disease 2019 Main and Severe Acute Respiratory Syndrome Coronavirus-2 3C-Like Proteases. *J. Nanosci. Nanotechnol.* **2021**, *21* (4), 2075–2089.
- (154) Ortega-Peña, M.; González-Cuevas, R. Familiar Dermatologic Drugs as Therapies for COVID-19. *Actas Dermo-Sifiliográficas English Ed.* **2021**, *112* (2), 118–126.
- (155) Caly, L.; Druce, J. D.; Catton, M. G.; Jans, D. A.; Wagstaff, K. M. The FDA-Approved Drug Ivermectin Inhibits the Replication of SARS-CoV-2 in Vitro. *Antiviral Res.* **2020**, *178*, 104787.
- (156) Choudhury, A.; Das, N. C.; Patra, R.; Bhattacharya, M.; Ghosh, P.; Patra, B. C.; Mukherjee, S. Exploring the Binding Efficacy of Ivermectin against the Key Proteins of SARS-CoV-2 Pathogenesis: An in Silico Approach. *Future Virol.* **2021**, *16* (4), 277–291.
- (157) Castañeda-Sabogal, A.; Chambergo-Michilot, D.; Toro-Huamanchumo, C. J.; Silva-Rengifo, C.; Gonzales-Zamora, J.; Barboza, J. J. Outcomes of Ivermectin in the Treatment of COVID-19: A Systematic Review and Meta-Analysis. *medRxiv* **2021**, 2021.01.26.21250420.

- (158) Vivekanandhan, K.; Shanmugam, P.; Barabadi, H.; Arumugam, V.; Daniel Raj Daniel Paul Raj, D.; Sivasubramanian, M.; Ramasamy, S.; Anand, K.; Boomi, P.; Chandrasekaran, B.; et al. Emerging Therapeutic Approaches to Combat COVID-19: Present Status and Future Perspectives. *Front. Mol. Biosci.* **2021**, *8*, 604447.
- (159) Raj, C. T. D.; Kandaswamy, D. K.; Danduga, R. C. S. R.; Rajasabapathy, R.; James, R. A. COVID-19: Molecular Pathophysiology, Genetic Evolution and Prospective Therapeutics—a Review. *Arch. Microbiol.* **2021**, 1-15.
- (160) Li, D.; Hu, J.; Li, D.; Yang, W.; Yin, S.-F.; Qiu, R. Reviews on Biological Activity, Clinical Trial and Synthesis Progress of Small Molecules for the Treatment of COVID-19. *Top. Curr. Chem.* **2021**, *379* (1), 4.
- (161) Rad, A. S.; Ardjmand, M.; Esfahani, M. R.; Khodashenas, B. DFT Calculations towards the Geometry Optimization, Electronic Structure, Infrared Spectroscopy and UV–Vis Analyses of Favipiravir Adsorption on the First-Row Transition Metals Doped Fullerenes; a New Strategy for COVID-19 Therapy. *Spectrochim. Acta Part A Mol. Biomol. Spectrosc.* **2021**, *247*, 119082.
- (162) Albasha, A. M.; Elnosh, M. M.; Osman, E. H.; Zeinalabdin, D. M.; Fadl, A. A. M.; Ali, M. A.; Altayb, H. N. Helicobacter Pylori 23S rRNA Gene A2142G, A2143G, T2182C, and C2195T Mutations Associated with Clarithromycin Resistance Detected in Sudanese Patients. *BMC Microbiol.* **2021**, *21* (1), 38.
- (163) Alvarez-Elcoro, S.; Enzler, M. J. The Macrolides: Erythromycin, Clarithromycin, and Azithromycin. *Mayo Clin. Proc.* **1999**, *74* (6), 613–634.
- (164) Takemori, N.; Ooi, H.-K.; Imai, G.; Hoshino, K.; Saio, M. Possible Mechanisms of Action of Clarithromycin and Its Clinical Application as a Repurposing Drug for Treating Multiple Myeloma. *Ecancermedicalscience* **2020**, *14*, 1088.
- (165) Prashantha, C. N.; Gouthami, K.; Lavanya, L.; Bhavanam, S.; Jakhar, A.; Shakthiraju, R. G.; Suraj, V.; Sahana, K. V.; Sujana, H. S.; Guruprasad, N. M.; et al. Molecular Screening of Antimalarial, Antiviral, Anti-Inflammatory and HIV Protease Inhibitors against Spike Glycoprotein of Coronavirus. *J. Mol. Graph. Model.* **2021**, *102*, 107769.
- (166) Aschenbrenner, D. S. Remdesivir Approved to Treat COVID-19 Amid Controversy. *Am. J. Nurs.* **2021**, *121* (1), 22–24.

- (167) Rezagholizadeh, A.; Khiali, S.; Sarbakhsh, P.; Entezari-Maleki, T. Remdesivir for Treatment of COVID-19; an Updated Systematic Review and Meta-Analysis. *Eur. J. Pharmacol.* **2021**, *897*, 173926.
- (168) Williamson, B. N.; Feldmann, F.; Schwarz, B.; Meade-White, K.; Porter, D. P.; Schulz, J.; van Doremalen, N.; Leighton, I.; Yinda, C. K.; Pérez-Pérez, L.; et al. Clinical Benefit of Remdesivir in Rhesus Macaques Infected with SARS-CoV-2. *Nature* **2020**, *585* (7824), 273–276.
- (169) Bagheri Novir, S.; Aram, M. R. Quantum Mechanical Studies of the Adsorption of Remdesivir, as an Effective Drug for Treatment of COVID-19, on the Surface of Pristine, COOH-Functionalized and S-, Si- and Al- Doped Carbon Nanotubes. *Physica. E. Low. Dimens. Syst. Nanostruct.* **2021**, *129*, 114668.
- (170) Dittmar, M.; Lee, J. S.; Whig, K.; Segrist, E.; Li, M.; Kamalia, B.; Castellana, L.; Ayyanathan, K.; Cardenas-Diaz, F. L.; Morrisey, E. E.; et al. Drug Repurposing Screens Reveal Cell-Type-Specific Entry Pathways and FDA-Approved Drugs Active against SARS-Cov-2. *Cell Rep.* **2021**, *35* (1).
- (171) Lodola, A.; De Vivo, M. The Increasing Role of QM/MM in Drug Discovery. *Adv. Protein Chem. Struct. Biol.* **2012**, *87*, 337–362.
- (172) Boras, B.; Jones, R. M.; Anson, B. J.; Arenson, D.; Aschenbrenner, L.; Bakowski, M. A.; Beutler, N.; Binder, J.; Chen, E.; Eng, H.; et al. Discovery of a Novel Inhibitor of Coronavirus 3CL Protease as a Clinical Candidate for the Potential Treatment of COVID-19. *bioRxiv* September **2020**.
- (173) Wang, J. Fast Identification of Possible Drug Treatment of Coronavirus Disease-19 (COVID-19) through Computational Drug Repurposing Study. *J. Chem. Inf. Model.* **2020**, *60* (6), 3277–3286.



## CHAPTER 3

### *Research article*

Computational evidence for nitro derivatives of quinoline and quinoline *N*-oxide as low-cost alternative for the treatment of SARS-CoV-2 infection

*Published in Scientific Reports*

## ABSTRACT

A new and more aggressive strain of coronavirus, known as SARS-CoV-2, which is highly contagious, has rapidly spread across the planet within a short period of time. Due to its high transmission rate and the significant time–space between infection and manifestation of symptoms, the WHO recently declared this a pandemic. Because of the exponentially growing number of new cases of both infections and deaths, development of new therapeutic options to help fight this pandemic is urgently needed. The target molecules of this study were the nitro derivatives of quinoline and quinoline *N*-oxide. Computational design at the DFT level, docking studies, and molecular dynamics methods as a well-reasoned strategy will aid in elucidating the fundamental physicochemical properties and molecular functions of a diversity of compounds, directly accelerating the process of discovering new drugs. In this study, we discovered isomers based on the nitro derivatives of quinoline and quinoline *N*-oxide, which are biologically active compounds and may be low-cost alternatives for the treatment of infections induced by SARS-CoV-2.

## INTRODUCTION

We are currently facing a new coronavirus disease designated as COVID-19. It started in China and has spread rapidly around the world, resulting in serious threats to international health and the economy.<sup>1,2</sup> The International Committee on the Taxonomy of Viruses denominated the virus as severe acute respiratory syndrome coronavirus 2 (SARS-CoV-2). This denomination is derived from the fact that the RNA genome is approximately 82% identical to the SARS coronavirus (SARS-CoV).<sup>3</sup> In addition, the SARS-CoV-2 reveals a 79% similarity with SARS (Severe Acute Respiratory Syndrome) coronavirus and a 50% similarity with MERS (Middle Eastern Respiratory Syndrome) coronavirus.<sup>4</sup>

The crystallographic structure of SARS-CoV-2 exhibits approximately 88% sequence identity with the other two coronaviruses found in bats (bat-SLCoVZC45 and bat-SLCoVZXC21).<sup>5</sup> For this reason, it is believed that the original host of the SARS-CoV-2 outbreak was bat-like.<sup>6</sup> Since discovery, an exponential growth in the number of cases of infections and deaths has been observed worldwide.<sup>3,7,8</sup> The World Health Organization (WHO) responded quickly to the COVID-19 threat by developing diagnostics and providing general guidance on

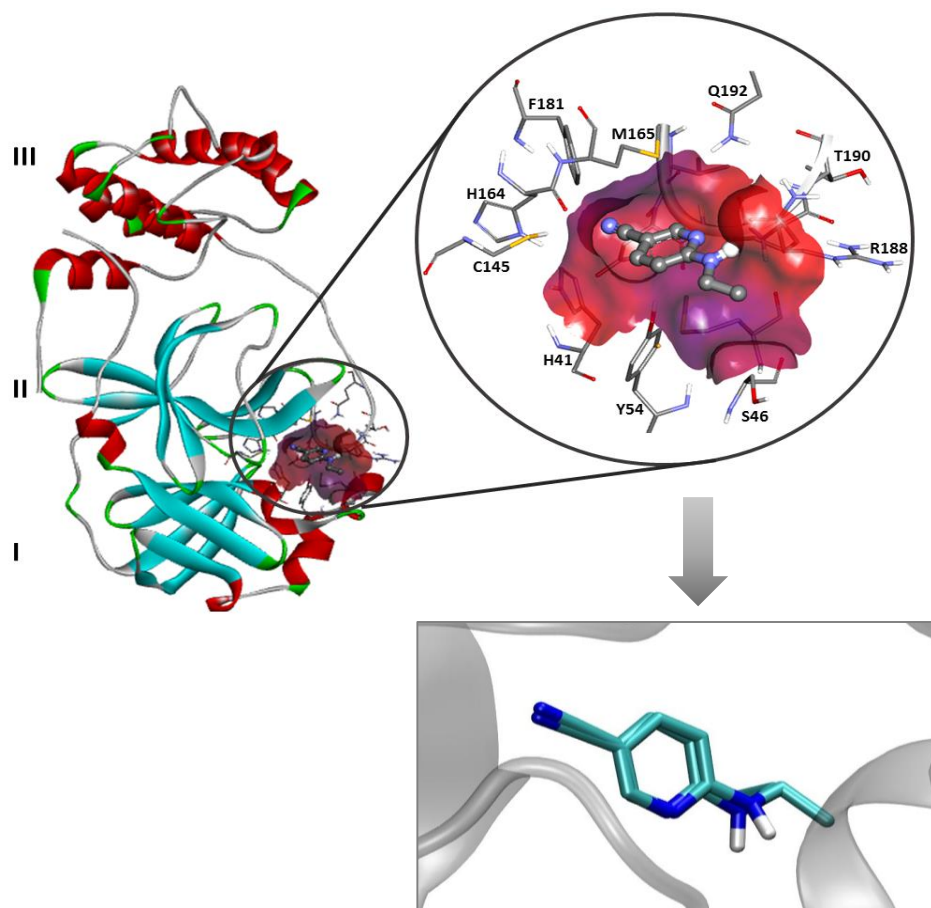
patient monitoring, as well as up-to-date information; it also declared the outbreak a pandemic on March 11, 2020.<sup>8,9</sup>

The overall situation is progressing daily worldwide.<sup>10</sup> In order to further the development of prevention and control techniques, we must have a better comprehension of the nature of the pandemic.<sup>11,12</sup> It is important to know that SARS-CoV-2 replicates in the upper respiratory tract, and infected patients produce a multitude of virus particles which further contributes to the spread of infection.<sup>13</sup> Similar to MERS and SARS, there are no distinguishing clinical features of COVID-19, and symptoms overlap significantly with other severe acute respiratory infections.<sup>9,14–16</sup>

Clinical characterization protocols are now being collected on patients worldwide to better define the illness, in terms of its natural history, mode of transmission, clinical profiles, management, and specific risk factors, to prevent or overcome the damaging effects of the disease.<sup>9,17</sup> What is known so far is that a significant proportion of individuals infected by COVID-19 remain asymptomatic and are thus an unbeknownst potential source of infection.<sup>18,19</sup> In symptomatic patients, the characteristic symptoms of the disease usually start less than a week after infection, and consist of fever, cough, nasal congestion, and fatigue, along with other signs of an upper respiratory tract infection.<sup>19</sup>

In early 2003, SARS-CoV was revealed as the causative agent of the emergence of SARS.<sup>20,21</sup> The SARS virus's main proteinase ( $M^{\text{pro}}$ ), also known as SARS-CoV 3C-like protease (3CL $^{\text{pro}}$ ), is a key enzyme responsible for the processing of viral polyproteins.<sup>21–23</sup> Together with the papain-like proteases, the  $M^{\text{pro}}$  is essential for the processing of polyproteins translated from the viral RNA.<sup>3,24</sup> In a structural analysis, the  $M^{\text{pro}}$  enzyme consists of three domains (Figure 1). Domains I (residues 8–101) and II (residues 102–184) are well-known  $\beta$ -barrels, which together resemble the structure of chymotrypsin. Contrarily, domain III (residues 201–306) primarily consists of  $\alpha$ -helices. Domains II and III, respectively, are connected by a long loop (residues 185–200). Also, located in a cleft between domains I and II, the  $M^{\text{pro}}$  active site presents a catalytic dyad formed by the conserved Cys145 and His41 amino acid residues. Equally important is the presence of a water molecule, which is a hydrogen atom bonded to His41; it can give rise to the third component of a catalytic triad.<sup>23</sup> It was indicated that domain III of  $M^{\text{pro}}$  is necessary for maintaining the proteolytic activity, which takes place by holding domain II and the long loop (residues 185–200) in a catalytically favorable orientation<sup>25</sup> and/or orienting the N-terminal residues that play an important role for the catalytic activity of the enzyme.<sup>26</sup> To date, no human proteases with a similar cleavage specificity are known,

suggesting that the inhibitors are unlikely to be toxic.<sup>3</sup> Based on this information, the present work has the main purpose of computationally designing new and more effective drugs to inhibition of the SARS-CoV-2 M<sup>pro</sup>.<sup>27–29</sup>



**Figure 1.** Crystallographic structure of the COVID-19 virus M<sup>pro</sup> enzyme with the co-crystallized ligand 6-(ethylamino)pyridine-3-carbonitrile (PDB code 5R82) (up),<sup>30</sup> and redocking result of the co-crystallized ligand through AutoDock Vina<sup>31</sup> as implemented in the MolAr software (down).<sup>32</sup> Image generated in the Discovery Studio Software 4.5 <https://discover.3ds.com/discovery-studio-visualizer-download>.

Researchers worldwide are undertaking the search for a vaccine while others search for a treatment regimen targeting SARS-CoV-2. Preliminary results demonstrated the application of both chloroquine (CQ) and hydroxychloroquine (HCQ) to be promising treatments for SARS-CoV-2.<sup>33–35</sup> CQ, for instance, exhibits inhibition of the SARS-CoV-2 infection at micromolar concentrations. Both compounds are classified as 4-aminoquinoline antimalarial

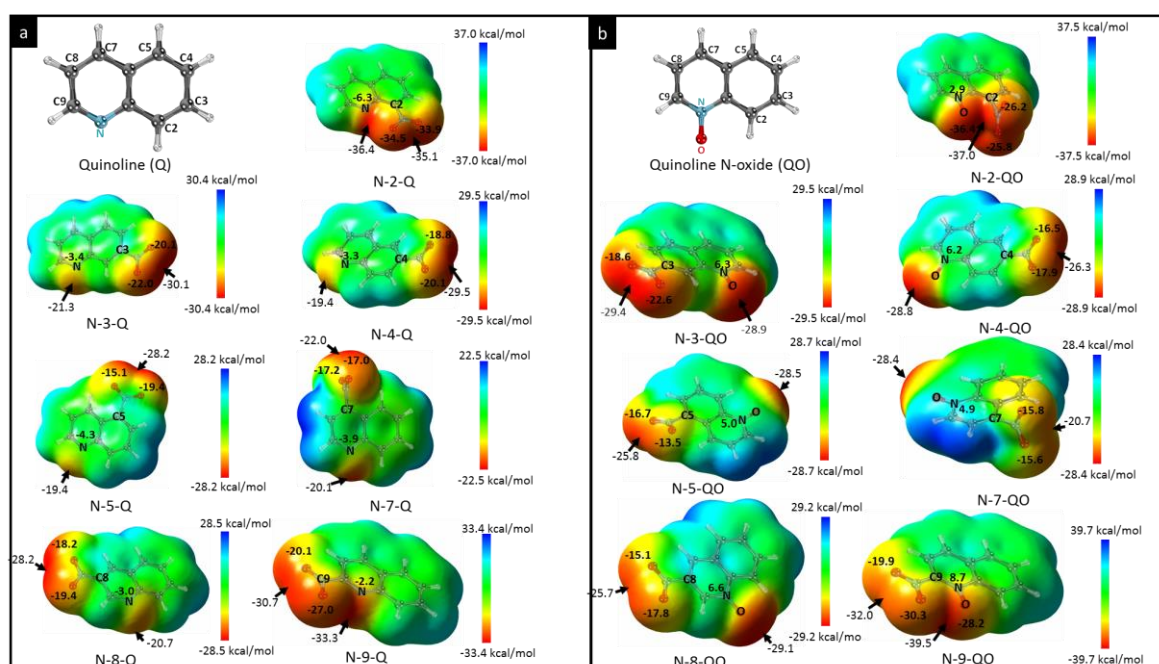
drugs.<sup>36</sup> However, further studies are needed to ensure the administration of these medicines is safe. Given the exposure so far, this work aims to provide significant contributions to accelerate the discovery of novel and efficient remediation methods against the damaging effects of COVID-19.

Computational screening is now the prime focus for solving the crisis of SARS-CoV-2 infections. This is likely because such strategies reveal rational pathways for the development of fast and efficient drugs. In this regard, the combination of quantum mechanics and molecular mechanics calculations are robust tools for investigating a vast range of drug candidates, as well as identifying potential molecular targets for the sites of action of these therapeutic agents.<sup>37</sup> In this work, the nitro derivatives of quinoline (Q) and quinoline *N*-oxide (QO) were computationally investigated. The choice of these derivatives was predominantly based on the nitration reaction they undergo, which is characterized by the replacement of a hydrogen atom with a nitro group, and also because it is one of the most industrially used reactions, not requiring the use of sophisticated equipment to be performed. This nitration reaction is therefore extremely attractive since synthesis requires low-cost materials and simple reaction paths, and any country can implement the large-scale manufacturing process for such products.<sup>38-42</sup> In this context, this research explores new therapeutic alternatives to combat the SARS-CoV-2 outbreak by utilizing computational simulations at the Density Functional Theory (DFT) level, molecular docking, and molecular dynamics methods as a well-reasoned strategy that provides insights on the physicochemical properties as well as the interaction and reactivity of these molecules as potential drug candidates.

## RESULTS AND DISCUSSION

As a first step, we have performed DFT and TDDFT calculations for the nitro derivatives of compounds Q and QO to better understand their electronic structure, spectroscopic properties, and chemical reactivity. Figure 2 shows the electrostatic surface potential for the optimised structure of all the nitro derivatives of Q and QO, which have screened in this *in silico* study. Hence, we can also see that the charge distribution mainly depends on the various orientations of the nitro groups - regions with negative potential (red) that act as an excellent electron acceptor - that were added to the Q and QO compounds, respectively, with the specific objective of conferring the most favorable interaction between the drug and the target. Note also that the nitro group increases the polarity of these compounds,

which is an attractive characteristic for pharmacological applications.<sup>43</sup> Additionally, nitro derivatives of QO compounds, in this case, have a more polarized structure. These slight structural changes are responsible for modulating the biological activity of these compounds, which may provide new clues for an in-depth interpretation of their microscopic behavior. These theoretical findings are consistent with the molecular docking simulations performed in this study.



**Figure 2.** Optimised structures of nitro derivatives of (a) Q and (b) QO and computed electrostatic potential maps with contour value of 0.004. Image generated in the GaussView 6.0 <https://gaussian.com/gaussview6/>.

All compounds were also identified in terms of computed IR-active modes and UV-vis absorbance spectroscopy, as we show in Figure S1. These results can easily be used to distinguish the isomers obtained. In parallel, a comparison of the difference between the total electronic energy ( $\Delta E$ ) for the computed Q and QO isomers, presented in Table S1, suggests that both N-4-Q and N-4-QO compounds in terms of energy are more stable. Additionally, the HOMO-LUMO gaps reveal a minor difference of 4.07 to 4.31 eV for nitro derivatives of Q and of 3.11 to 3.69 eV for nitro derivatives of QO, respectively (see Table S1). In this case, a lower HOMO-LUMO gap value for QO derivatives, in principle, suggests greater reactivity for these

isomers compared to Q derivatives. Figure S2 shows the shape of molecular orbitals (MOs) for all ligands studied. A detailed analysis of composition and localization of the MO reveals that the HOMO energies are, in principle, insufficient to describe the chemical behavior of these ligands. From the frontier effective-for-reaction molecular orbital (FERMO) concept, the reactions that are driven by HOMO, and those that are not, can be better explained for such compounds.<sup>44-47</sup> These findings are consistent with previous studies.<sup>46,47</sup>

To elucidate the modes through which our drug candidates interact SARS-CoV-2, the crystal structure of the M<sup>pro</sup> of the virus in complex with 6-(ethylamino)pyridine-3-carbonitrile was downloaded for study.<sup>30</sup> Once the enzyme had been prepared, the molecular docking protocol was initiated. In the first part of this investigation, re-docking calculations were performed using the MolAr software,<sup>32</sup> with implementation of the AutoDock Vina program.<sup>31</sup> To determine the ideal docking parameters, these re-docking calculations were performed according to the orientation and conformation adopted by the experimental co-crystallised active ligand present in the binding pocket. It is important to notice that the M<sup>pro</sup> enzyme used in this work was found in its native form.

The small RMSD variation (0.94) obtained from the re-docking calculations, suggested that the program was able to correctly and efficiently simulate the experimental results for the respective ligands. This preliminary outcome indicated that the conformational deviation of the molecular docking technique was suitable for our purposes and that the method was highly sensitive and specific. The re-docking overlap is presented in Figure 1. To simulate the modes through which our drug candidates interact with the SARS-CoV-2 M<sup>pro</sup> enzyme, we employed the best parameters provided by the data from the re-docking study carried out with the co-crystallised active ligand. All the computed interaction energy results are displayed in Table S2 and S3 in supplementary material.

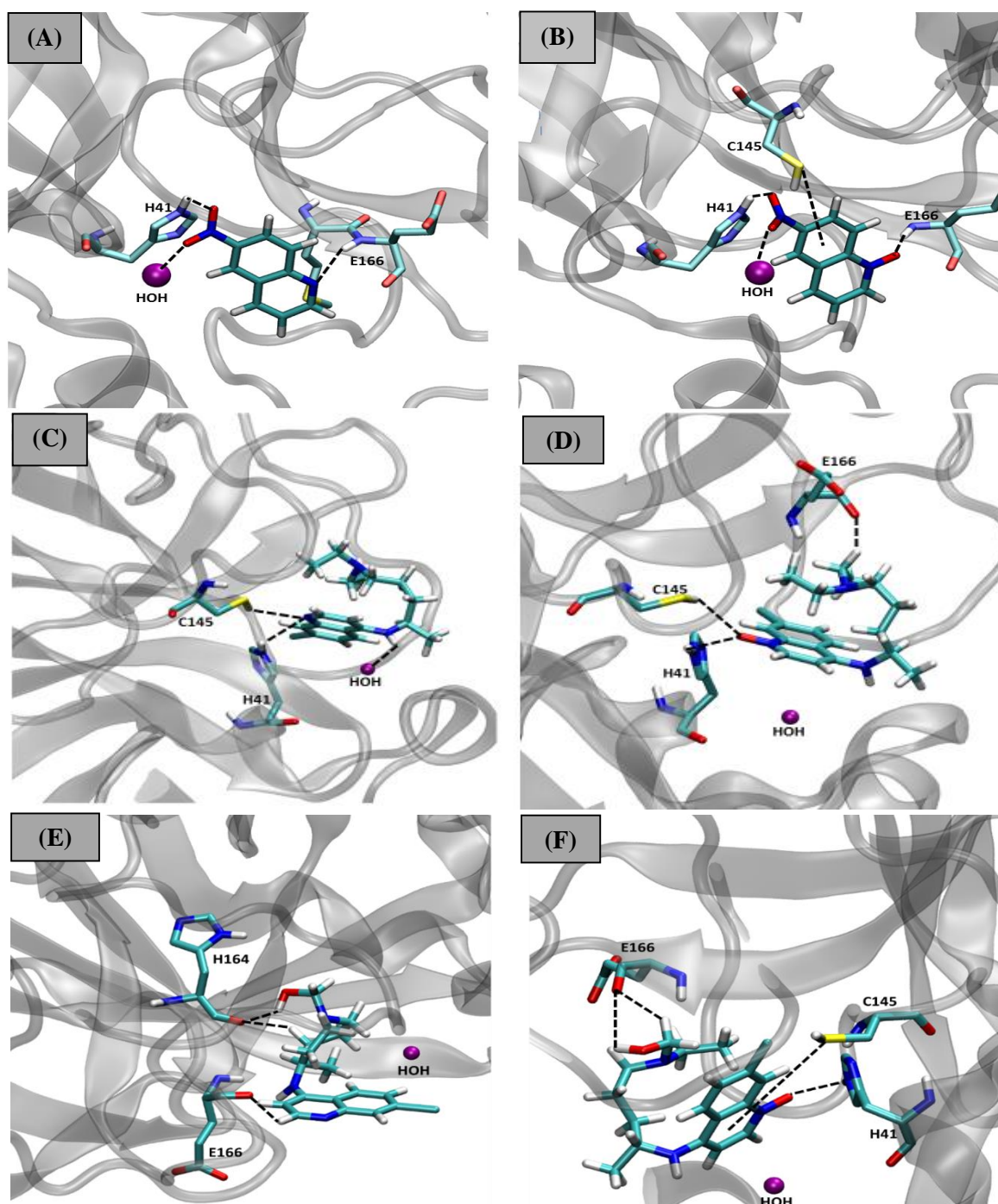
As shown in Table S2, all the drug candidates studied (i.e., nitro derivatives of Q and QO) interacted well with M<sup>pro</sup> active site, with interaction energy values in the range of -4.3 to -5.0 kcal mol<sup>-1</sup>. Some of the nitro-QO compounds, such as the inhibitors N-4-QO, N-9-QO, N-8-QO, together with QO, had slightly more stabilising interaction energy values than those of their corresponding nitro-quinolines (Table S2). In general, it is noteworthy that the compounds studied had a greater affinity for M<sup>pro</sup> than the co-crystallised ligand did (the latter showing an interaction energy value of -3.9 kcal mol<sup>-1</sup>). In order to assess the potential of such findings, using the same protocol, docking procedures were performed with the commercial drugs CQ and HCQ, and their interaction energy values were found to be -2.8 and -2.3 kcal mol<sup>-1</sup>,

respectively. A remarkable trend could be observed from these outcomes. Note that all of our drug candidates presented lower interaction energy values than CQ and HCQ, with a significant energy difference, of up to 2 kcal mol<sup>-1</sup>. Additionally, our study showed that the many of the nitro-QO compounds led to a more stabilising interaction energy in the M<sup>pro</sup> active site. Based on these findings, we also investigated the chloroquine and hydroxychloroquine *N*-oxides forms (denoted as CQO and HCQO), which displayed a significant improvement in interaction energy values of -3.0 and -3.1 kcal mol<sup>-1</sup>, respectively. Interestingly, the interaction energy of HCQO was almost 1 kcal mol<sup>-1</sup> more stabilizing than that of HCQ. This trend was deeply analyzed using molecular dynamics (MD) techniques. The influence of the *N*-oxide group was also investigated at different sites and through different combinations for the CQO and HCQO compounds (Table S3). According to that table, with all combinations investigated, we can observe that no improvement in interaction energy was detected for CQO. On the other hand, for HCQO, the presence of the *N*-oxide group at some sites led to slightly more favorable interaction energies. See table S3 for more details. Herein, our main goal was to determine whether the inhibitors studied could target the M<sup>pro</sup> enzyme. The molecular docking pose of each drug candidate indicated that they could indeed fit accurately within the substrate-binding pocket.

In the case of SARS-CoV-2 virus M<sup>pro</sup> enzyme, the protomer is composed of three domains, as commented previously (see Figure 1). The enzyme has a Cys145–His41 catalytic dyad, and the substrate-binding pocket is known to be located in a cleft between domains I and II.<sup>48</sup> Hence, the structural features determined from these data are important for guiding our assessment of the interaction modes of the inhibitors in the M<sup>pro</sup> active site. As shown in Figure 3, the N-4-QO performed hydrogen bonds with all the residues and the water molecule of the catalytic triad. In fact, these specific interactions constitute one of the parameters analysed in this docking study. This same trend is not observed for inhibitor N-4-Q, suggesting that the *N*-oxide version of this ligand adopts a more favourable conformation which allows for its



interaction with the catalytic triad, resulting in a slightly more stabilizing interaction energy. Similarly, the interactions performed by the other ligands can also be observed in Figure 3.

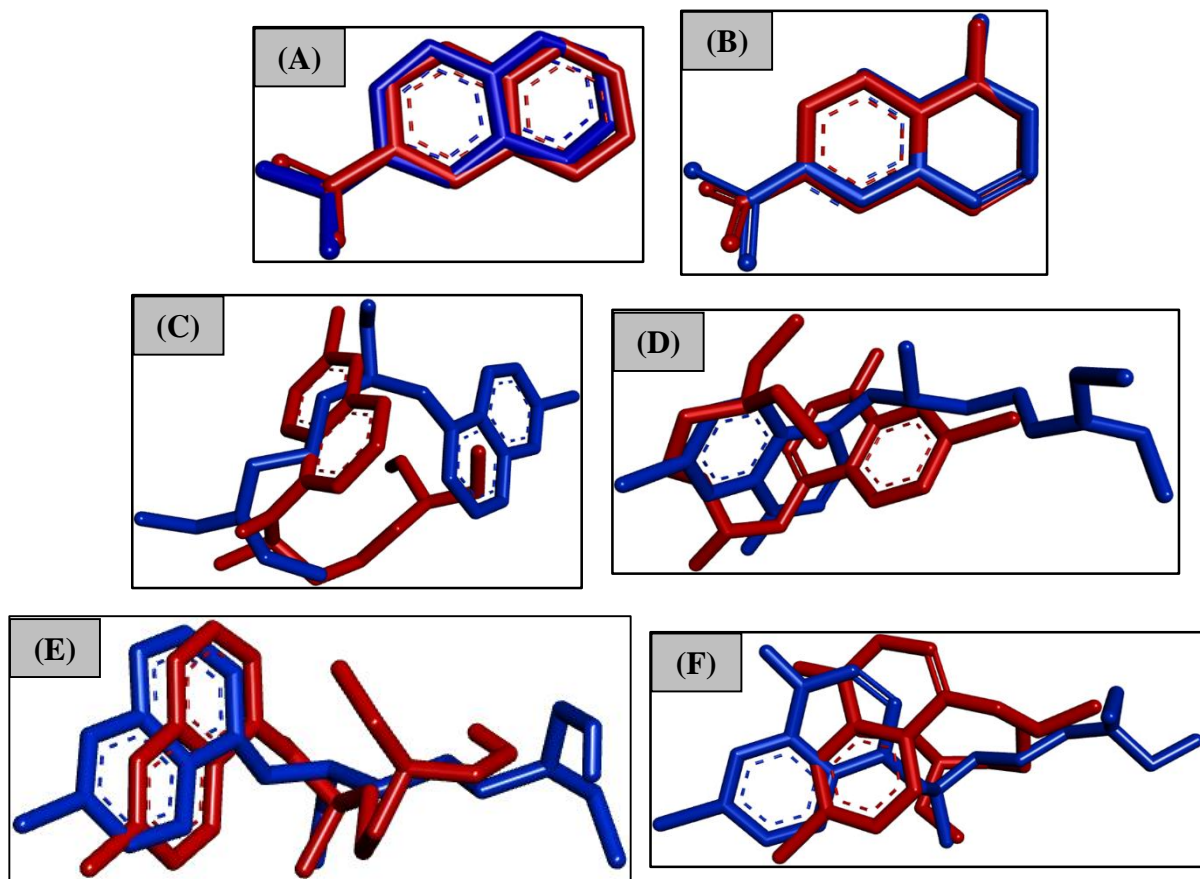


**Figure 3.** Intermolecular interactions performed by the inhibitors (A) N-4-Q, (B) N-4-QO, (C) CQ, (D) CQO, (E) HCQ and (F) HCQO in the M<sup>pro</sup> active site. Image generated in the Visual Molecular Dynamics 1.9.3 <https://www.ks.uiuc.edu/Research/vmd/>.

From the molecular docking calculations, it was possible to deduce that our drug candidates had a more stabilizing interaction energy effect than CQ and HCQ in the M<sup>pro</sup> binding pocket. To better assess the interaction modes of our inhibitors, N-4-Q and N-4-QO were chosen as representatives of the set for MD simulations. Likewise, the same calculations were performed for CQ and HCQ and their *N*-oxides CQO and HCQO (see Figure S3).

Additionally, in this study, the dynamic behavior of complexes M<sup>pro</sup>/N-4-Q, M<sup>pro</sup>/N-4-QO, M<sup>pro</sup>/CQ, M<sup>pro</sup>/CQO, M<sup>pro</sup>/HCQ, M<sup>pro</sup>/HCQO inside the SARS-CoV-2 M<sup>pro</sup> enzyme was investigated. The extracted frame, which was considered the representative conformational structure for all inhibitors throughout the MD simulation, corresponds to the average of the RMSD value. By analyzing the results of the RMSD plots, it was observed that most of the deviations from the N-4-Q and N-4-QO structures were very small, not exceeding 0.5 Å, i.e., these ligands are well-accommodated in the SARS-CoV-2 M<sup>pro</sup> active site according to Figures S4 and S5.

To get more insights into the intrinsic reactivity of each one of these ligands, in this study, we have performed the analysis of the strain effect along the MD simulation. Since these factors have a pivotal role and affect the reactivity of these ligands.<sup>49,50</sup> In the present study, the strain effect along the MD simulation can be clearly visualized by the overlap of the initial (red) and representative (blue) structures obtained after 20 ns of simulation, as shown in Figure 4. Based on that figure, we note that our compounds N-4-Q and N-4-QO showed a slight bending at the quinoline ring (strain), which makes this compound in principle more reactive, resulting in a small oscillation according to the RMSD graphs (Figures S4 and S5). Importantly, this trend is essential because it indicates a low variation of strain (deformation of the ligand along simulation), reaching a stabilizing conformation more quickly. On the other hand, due to larger molecular mass and bulk of the CQ, HCQ and their corresponding oxides, there was a very higher variation of strain (Figures 4 (c – f)). We believe that this slight strain can induce a high intrinsic reactivity for these ligands.



**Figure 4.** Overlap of the initial (red) and representative (blue) structures of the 20-ns simulation of MD. Image generated in the Discovery Studio Software 4.5 <https://discover.3ds.com/discovery-studio-visualizer-download>.

As shown in Figure 5 (a), the N-4-Q compound performed hydrogen bond interaction with Cys44 (2.78 Å) and hydrophobic interactions with Thr45, Ser46, Met49, Gln189, His41, Val42, Met165, Glu166, His164, Cys145, His163, Ser144, Gly143, respectively. These interactions are essential in inhibiting the enzymatic activity of  $M^{P10}$  and are in accordance with some other studies,<sup>51-53</sup> as well as the docking results of this work. By analyzing the graph of hydrogen interactions (see Figure S4), we found that the compound N-4-Q performed up to three hydrogen bond type interactions. However, there was only one effective interaction that occurred during the entire 20 ns of MD simulation, which is according to the pharmacophoric map (see Figure 5 (a)). In turn, the N-4-QO compound was stabilized by four hydrogen bonds with His41 (2.93 Å), His163 (2.72 Å), Gly143 (3.01 Å), Ser144 (3.04 Å), and hydrophobic interactions with Met49, Ser46, Gln189, Glu166, Met165, His164, Pro39, Leu27, Cys145, Gly146, and Ser147, respectively, as shown in Figure 5 (b). According to Zhang and coworkers,<sup>53</sup> in the catalytic site, the residues Glu166, His41, and Gys145, respectively, are key species of the target protease. Thus, the interaction of these amino acids with inhibitors is

essential for blocking the enzymatic activity of  $M^{pro}$ . Additionally, it is observed that the N-4-QO can make up to three bonds during the trajectory; however, occurs only one hydrogen bond in most of the entire simulation (Figure S5).

In the case of the dynamic behavior of both CQ and CQO compounds, we have observed that CQ remained unstable over the 20 ns of simulation, as shown in Figures S6. On the other hand, CQO remained stable during the same period of simulation. The CQ compound presented large oscillations in the  $M^{pro}$  active site, by rotating the N-diethyl-pentane-1,4-diamine portion. This ligand has many rotatable bonds, and because of the exposure to the solvent, this increases the ligand flexibility, making it more unstable in the active site. For the simulation with CQO, this ligand was better accommodated in the  $M^{pro}$  site over the 20 ns of simulation, and this fact leads us to believe that this oxo form significantly contributes to the compound stabilization. Although the RMSD deviation was high when compared to N-4-Q and N-4-QO compounds, they are coherent since the chemical structures of CQ and CQO are bulkier and had a larger molecular mass, as well as several rotatable bonds. Consequently, there is a change in the conformation (Figure 4 (c) and (d)), further increasing the flexibility of the inhibitors, and therefore is expected a more significant oscillation in the RMSD (see Figures S6 and S7). Through the pharmacophoric map, as shown in Figure 5 (c), hydrophobic interactions can be observed with the residues Asn119, Ile43, Thr45, Cys44, Ser46, Met49 and Gly143. We can also notice a halogen bond with the Asn142 amino acid residue (3.22 Å). On the other hand, in the case of CQO, this inhibitor performed hydrogen bonds with Gln189 (2.78 Å) and Met49 (2.30 Å), together with several hydrophobic interactions, specifically with the residues Glu166, Cys145, Cys44, Val42, Thr45, Met165, His41, Ser46, Met49, Asn51, Pro52, Tyr54, Asp187 and Arg188 (see Figure 5 (d)). These results are in accordance with the Hydrogen bond graph, since up to two hydrogen bonds are observed during the 20 ns of simulation (Figure S7).

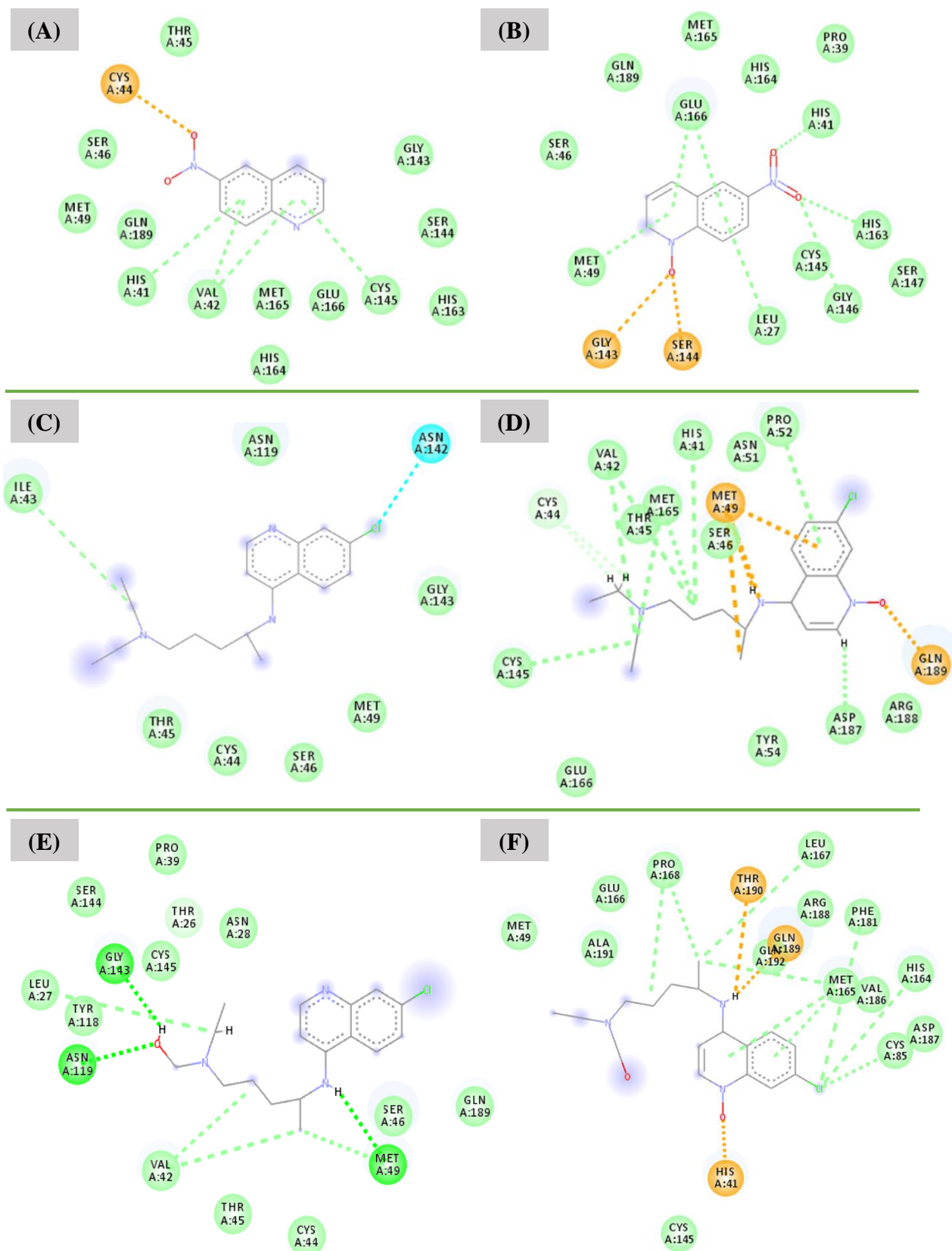
Likewise, the HCQ compound remained stable in the  $M^{pro}$  active site after 7.0 ns of simulation, mainly due to many conformational changes (Figure S8), such as in relation to the amino-pentyl(ethyl)aminoethanol group that underwent rotation, resulting in a more energetically favourable conformation compared to its initial chemical structure, i.e., thus decreasing the RMSD value (Figure S8 and Figure 5 (e)). However, the final configuration of HCQ had less strain than CQ. Therefore, we can speculate that the minimum strain, which is associated with a low RMSD value, is directly related to the toxicity of these compounds.

As shown in Figure 5 (e), the HCQ exhibit one hydrogen bond with Gly143 (2.10 Å), Asn119 (2.46 Å) and Met49 (2.30 Å), and several hydrophobic interactions with the residues Tyr118, Leu27, Ser144, Cys145, Pro39, Thr26, Asn28, Val42, Thr45, Cys44, Ser46 and Gln189, respectively. Through the Hydrogen bond graph, it was observed that for this compound after equilibration in the active site, up to three hydrogen bonds could be accomplished (Figure S8). While the HCQO compound showed the RMSD value of around 2.5 Å, due to the structural distortions in the N-diethyl-pentane portion during the 20 ns of simulation (Figure S9). The oscillation of the ligand in the site resulted in a less energetically favorable conformation compared to its initial chemical structure (Figure 4 (f)). Also, this compound performed three hydrogen bond interactions with Thr190 (2.98 Å), Gln189 (1.89 Å) and His41 (1.70 Å) and hydrophobic interactions with Cys145, Met49, Ala191, Glu166, Pro168, Leu167, Arg188, Gln192, Phe181, Met165, Val186, His164, Cys85 and Asp187, respectively, as we show in Figure 5 (f). Considering the hydrogen graph (Figure S9), the HCQO can make up to five hydrogen bonds.

In order to confirm the structural stabilization in the simulation environment, the RMSF was calculated from the average position of each amino acid residue of M<sup>PRO</sup> (Figures S4-S9). Higher RMSF values indicate that the residues have undergone major changes, corresponding to regions of loops. On the other hand, for the residues of the active site region and the alpha-helices/beta sheets regions, there is a lower RMSF value, thereby revealing the increased stability of these areas. The regions of loop are freely exposed to the solvent to a larger degree, and according to the graphs, we can observe that the sidechain has the largest variation of RMSF, indicating greater degree of freedom, that is, larger flexibility. In addition, the backbone presented a low variation of RMSF, this is expected because these residues are found in central regions of the protein, for example, inside the active cavity. Finally, it was possible to notice, from the RMSF values of the protein structure, the inexistence of large oscillations, maintaining itself conserved during the whole process of simulation.

From the MD simulation, we have estimated the interaction energies for all cases studied: N-4-Q (-96.54 kJ mol<sup>-1</sup>), N-4-QO (-107.35 kJ mol<sup>-1</sup>), CQ (-100.65 kJ mol<sup>-1</sup>), CQO (-82.27 kJ mol<sup>-1</sup>), HCQ (-116.60 kJ mol<sup>-1</sup>), HCQO (-148.20 kJ mol<sup>-1</sup>). An important outcome observed in this study is that the majority of the *N*-oxide compounds had an energetically more favorable affinity at the M<sup>PRO</sup> active site than their Q counterparts. These findings are consistent with the molecular docking calculations. The existence of intermolecular interactions strongly

guides these trends. Note that the N-4-QO performed more hydrogen bonds than N-4-Q, as shown in Figure 5. This fact helps explain the more stabilizing interaction energy found for N-4-QO. From the pharmacophoric maps shown in Figure 5, the accomplishment of hydrogen bonds, along with the hydrophobic interactions, are key to understand the biological activity of these inhibitors.



**Figure 5.** Interactions performed during 20ns in the MD simulation with the (A)  $M^{\text{pro}}/N-4-Q$ , (B)  $M^{\text{pro}}/N-4-QO$ , (C)  $M^{\text{pro}}/CQ$ , (D)  $M^{\text{pro}}/CQO$ , (E)  $M^{\text{pro}}/HCQ$ , (F)  $M^{\text{pro}}/HCQO$  complexes. Image generated in the Discovery Studio Software 4.5 <https://discover.3ds.com/discovery-studio-visualizer-download>.

Yet, the success of a novel drug candidate is commonly attributed to diverse factors, including their bioactivity, rich pharmacokinetic (PK) and pharmacodynamics (PD) profiles, as well as toxicity. It would be therefore of huge interest to investigate these properties in the preliminary stages to in silico design of safer and more efficient drugs. Hence, the ADMET evaluations involve sequential and iterative assessments of the efficacy, PK, PD, metabolic and toxicological properties in the model of potential drug candidates.<sup>54</sup> From the ADMET results, the theoretical parameters of toxicity ( $LD_{50}$ ) were obtained for each compound: N-4-Q (2.53 mol/kg), N-4-QO (2.56 mol/kg), CQ (2.95 mol/kg), CQO (2.68 mol/kg), HCQ (2.66 mol/kg), HCQO (2.69 mol/kg). We can observe that the parameter toxicity slightly varied from N-4-Q to N-4-QO, suggesting that the toxicity of these compounds is essentially equal. Similarly, this trend also is observed for HCQ and its corresponding *N*-oxide (HCQO). On the other hand, we have noticed a more significant variation for CQ and CQO compounds, indicating that CQO theoretically presents a higher level of toxicity. In addition, these molecular calculations also showed that HCQ is more toxic than CQ. Yet, this trend does not corroborate with previous experimental results.<sup>55</sup> It is essential to highlight that the molecular results obtained do not take into account the effects of the counterion and, for this reason, suggest a different trend to the experimental findings previously reported.<sup>55</sup> In particular, this divergence most-likely is related to the fact that the commercially used HCQ is a salt-based on hydroxychloroquine sulfate, while the CQ used is a salt-based on chloroquine diphosphate. It additionally is well-known that the counterion has a substantial effect not only on its biological activity but also on the toxicity of such compounds as well.<sup>56-59</sup> Therefore, our molecular results indicate that the presence of phosphate groups contributes to increasing the toxicity of CQ in the treatment of the SARS-CoV-2 infection. Consequently, we can conclude that for the same type of salt used, it is expected CQ to be less toxic than HCQ, according to the molecular trend observed in this study.

In the last part of this investigation, we carried out new molecular docking calculations with three selected  $\alpha$ -ketoamide derivatives (known inhibitors of coronavirus protease enzymes).<sup>60</sup> Consequently, this strategy might provide a more detailed data comparing their interaction modes in the  $M^{Pro}$  active site for these drugs designed. As such, the chemical structures of the  $\alpha$ -ketoamide inhibitors and biological activities are shown in Figure S10 of supplementary material. Based on the newly obtained results, the compounds 11n, 11r and 11s exhibited interaction energies of approximately  $-6.4 \text{ kcal mol}^{-1}$ ,  $-6.9 \text{ kcal mol}^{-1}$  and  $-7.0 \text{ kcal mol}^{-1}$ , respectively. From these results, note that these compounds showed slightly more stabilized interaction energies in comparison with those of our drug candidates. As such, the



intermolecular interactions with residues from the active site can be observed with more details in Figure S11. In parallel, from the ADMET analysis can be observed that  $\alpha$ -ketoamide compounds showed LD<sub>50</sub> values of 2.56 mol/kg (for 11n), 2.33 mol/kg (for 11r) and 2.43 mol/kg (for 11s). These results suggest that  $\alpha$ -ketoamide in comparison to our compounds is likely more toxic. In face with these theoretical outcomes, we can notice that our drug candidates demonstrate potential to be used as therapeutic agents for the COVID-19 treatment.

## CONCLUSION

We conclude that this *in silico* study to contribute toward the rational design of new and more efficient drugs for the treatment of SARS-CoV-2 infection. Hence, the most important lesson from this structure-based study was that the QO derivatives are better inhibitors than their Q counterparts. In light of these results, we can suggest that *in vitro* and *in vivo* experiments be urgently carried out to investigate the nitro derivatives of QO further, since there is as yet no efficient treatment for this disease. Finally, we emphasise that these compounds can be easily produced on a large scale (at a low-cost), making them a promising treatment option against SARS-CoV-2 infection.

## METHODS

**Datasets:** Herein, the crystal structure dataset for SARS-CoV-2 virus M<sup>pro</sup> enzyme was obtained from the Protein Data Bank (PDB; accession ID: 5R82, resolution 1.31Å).<sup>30</sup> Then, full optimizations and frequencies of nitro derivatives of Q and QO were achieved at B3LYP level of theory with 6-31+g(d,p) basis set in the Gaussian 09 package.<sup>61</sup> For a better description of the electronic parameters, it was also performed single-point energy Time-Dependent DFT (TD-DFT) calculations at B3LYP/6-31+g(d,p) level.

**Molecular Docking:** The molecular docking was conducted with the tool AutoDock Vina (version 1.1.2),<sup>31</sup> as implemented in the MolAr (Molecular Architecture) software.<sup>32</sup> For the crystallographic M<sup>pro</sup> structure preparation, the loop regions were rebuilt using the Modeller.<sup>62</sup> The ions and water molecules were removed from the original PDB, with the exception of water

molecules that were in the M<sup>pro</sup> active site. The addition of polar hydrogen atoms was performed according to the protonation state of the receptor at pH 7.4, by using the Chimera software.<sup>63</sup> For the docking protocol, the M<sup>pro</sup> enzyme and the structures of Q and QO derivatives were used as receptor and ligands, respectively. The grid box was centered on the co-crystallized ligand (6-[ethylamino]pyridine-3-carbonitrile) of SARS-CoV-2 virus M<sup>pro</sup> enzyme (5R82), and the coordinates were  $x = 12.053$ ,  $y = -0.871$  and  $z = 24.157$ , with 1 Å spacing. Docked poses were then selected on the basis of scoring functions and protein–ligand interactions. Binding interaction figures were generated using Discovery Studio 2017 R2.<sup>64</sup> AutoDock Vina employs the Iterated Local Search global optimizer.<sup>31</sup>

**Molecular Dynamics simulations:** In a further theoretical insight, the key docking complexes were evaluated by molecular dynamics (MD) simulation using the GROMOS54A7 all-atom force field<sup>65</sup> and performed using GROMACS 5.1 software.<sup>65,66</sup> The M<sup>pro</sup> complexes were inserted into a 12 Å water box with the SPC solvation model, and sodium and chlorine ions were added for charges neutralization under periodic boundary conditions. The calculation of electrostatic interactions was then performed by using the Particle Mesh Ewald method with a cut-off of 12 Å and time step of 1 fs. Initially, complexes were minimized over 5000 cycles using the steepest descent algorithm. After the minimization, a 500 ps equilibration was done in the NVT ensemble slowly increasing the temperature from 50 to 300 K, using Berendsen thermostat. In order to equilibrate the pressure of the system, a NPT equilibration was performed employing Parrinello-Rahman barostat<sup>67</sup> to maintain the system pressure of 1 bar. After the equilibration of the systems, they were submitted to a MD production step with 20 ns of simulation and a 1 fs integration time. Atom trajectories were analyzed using Visual Molecular Dynamic (VMD, version 1.9.3).<sup>68</sup> Due to the experimental inexistence of acute toxicity data for these compounds, in principle, we also provide a theoretical estimation for the LD<sub>50</sub> values from the using of a rat model-based admetSAR predictor, which is freely available online at <http://lmmd.ecust.edu.cn:8000/>.

## ACKNOWLEDGMENTS

The authors gratefully acknowledge the support from the Brazilian agencies CNPq, CAPES and FAPEMIG. We also especially grateful to the computational facilities at UFLA. It was supported by the Excellence project UHK.

## AUTHOR CONTRIBUTIONS

FAL designed the study. LCA and AAC contributed equally to this work, as well as, performed docking and dynamic molecular studies. JPAJ performed quantum chemical calculations. TCR, EN, KK and FAL conceived the project, supervised students and contributed to the review of the whole manuscript. All authors discussed the results and contributed to the final manuscript.

## COMPETING INTERESTS

All authors declare no competing interests.

## REFERENCES

1. Zhou, P. *et al.* A pneumonia outbreak associated with a new coronavirus of probable bat origin. *Nature* **579**, 270–273 (2020).
2. Wu, F. *et al.* A new coronavirus associated with human respiratory disease in China. *Nature* **579**, 265–269 (2020).
3. Zhang, L. *et al.* Crystal structure of SARS-CoV-2 main protease provides a basis for design of improved  $\alpha$ -ketoamide inhibitors. *Science* (80-. ). **3405**, eabb3405 (2020).
4. Park, M., Thwaites, R. S. & Openshaw, P. J. M. COVID-19: Lessons from SARS and MERS. *Eur. J. Immunol.* **50**, 308–311 (2020).
5. Lu, R. *et al.* Genomic characterisation and epidemiology of 2019 novel coronavirus: implications for virus origins and receptor binding. *Lancet* **395**, 565–574 (2020).
6. Lu, H., Stratton, C. W. & Tang, Y.-W. Outbreak of pneumonia of unknown etiology in Wuhan, China: The mystery and the miracle. *J. Med. Virol.* **92**, 401–402 (2020).
7. Zhang, L. & Liu, Y. Potential interventions for novel coronavirus in China: A systematic review. *J. Med. Virol.* **92**, 479–490 (2020).
8. Munster, V. J., Koopmans, M., van Doremalen, N., van Riel, D. & de Wit, E. A Novel Coronavirus Emerging in China — Key Questions for Impact Assessment. *N. Engl. J. Med.* **382**, 692–694 (2020).
9. Arabi, Y. M., Murthy, S. & Webb, S. COVID-19: a novel coronavirus and a novel challenge for critical care. *Intensive Care Med.* (2020) doi:10.1007/s00134-020-05955-1.
10. Heymann, D. L. & Shindo, N. COVID-19: what is next for public health? *Lancet* **395**, 542–545 (2020).
11. Yoo, J. H. The Fight against the 2019-nCoV Outbreak: an Arduous March Has Just Begun. *Journal of Korean medical science* vol. 35 e56 (2020).
12. Dey, S. K., Rahman, M. M., Siddiqi, U. R. & Howlader, A. Analyzing the epidemiological outbreak of COVID-19: A visual exploratory data analysis approach. *J. Med. Virol.* (2020) doi:10.1002/jmv.25743.
13. Chan, J. F.-W. *et al.* A familial cluster of pneumonia associated with the 2019 novel coronavirus indicating person-to-person transmission: a study of a family cluster. *Lancet* **395**,

- 514–523 (2020).
14. Huang, C. *et al.* Clinical features of patients infected with 2019 novel coronavirus in Wuhan, China. *Lancet* **395**, 497–506 (2020).
  15. Chen, N. *et al.* Epidemiological and clinical characteristics of 99 cases of 2019 novel coronavirus pneumonia in Wuhan, China: a descriptive study. *Lancet* **395**, 507–513 (2020).
  16. Arabi, Y. M. *et al.* Critically Ill Patients With the Middle East Respiratory Syndrome: A Multicenter Retrospective Cohort Study. *Crit. Care Med.* **45**, 1683–1695 (2017).
  17. Zhang, T. *et al.* Clinical trials for the treatment of Coronavirus disease 2019 (COVID-19): A rapid response to urgent need. *Sci. China. Life Sci.* (2020) doi:10.1007/s11427-020-1660-2.
  18. Deng, S.-Q. & Peng, H.-J. Characteristics of and Public Health Responses to the Coronavirus Disease 2019 Outbreak in China. *J. Clin. Med.* **9**, (2020).
  19. Wang, D. *et al.* Clinical Characteristics of 138 Hospitalized Patients with 2019 Novel Coronavirus-Infected Pneumonia in Wuhan, China. *JAMA - J. Am. Med. Assoc.* **323**, 1061–1069 (2020).
  20. Drosten, C. *et al.* Identification of a novel coronavirus in patients with severe acute respiratory syndrome. *N. Engl. J. Med.* **348**, 1967–1976 (2003).
  21. Anand, K., Ziebuhr, J., Wadhwani, P., Mesters, J. R. & Hilgenfeld, R. ( 3CL pro ) Structure : Basis for Design of Anti-SARS Drugs. *Science (80-. ).* **300**, 1763–1767 (2003).
  22. Kumar, V., Tan, K.-P., Wang, Y.-M., Lin, S.-W. & Liang, P.-H. Identification, synthesis and evaluation of SARS-CoV and MERS-CoV 3C-like protease inhibitors. *Bioorg. Med. Chem.* **24**, 3035–3042 (2016).
  23. Tan, J. *et al.* pH-dependent Conformational Flexibility of the SARS-CoV Main Proteinase (Mpro) Dimer: Molecular Dynamics Simulations and Multiple X-ray Structure Analyses. *J. Mol. Biol.* **354**, 25–40 (2005).
  24. Hilgenfeld, R. From SARS to MERS: crystallographic studies on coronaviral proteases enable antiviral drug design. *FEBS J.* **281**, 4085–4096 (2014).
  25. Anand, K. *et al.* Structure of coronavirus main proteinase reveals combination of a chymotrypsin fold with an extra  $\alpha$ -helical domain. *EMBO J.* **21**, 3213–3224 (2002).
  26. Yang, H. *et al.* The crystal structures of severe acute respiratory syndrome virus main protease and its complex with an inhibitor. *Proc. Natl. Acad. Sci. U. S. A.* **100**, 13190–13195 (2003).
  27. Jin, Z. *et al.* Structure of Mpro from SARS-CoV-2 and discovery of its inhibitors. *Nature* **582**, 289–293 (2020).
  28. Kneller, D. W. *et al.* Structural plasticity of SARS-CoV-2 3CL Mpro active site cavity revealed by room temperature X-ray crystallography. *Nat. Commun.* **11**, 3202 (2020).
  29. Mengist, H. M., Fan, X. & Jin, T. Designing of improved drugs for COVID-19: Crystal structure of SARS-CoV-2 main protease Mpro. *Signal Transduct. Target. Ther.* **5**, 67 (2020).
  30. Berman, H. M. *et al.* The Protein Data Bank. *Nucleic Acids Res.* **28**, 235–242 (2000).
  31. Trott, O. & Olson, A. J. AutoDock Vina: improving the speed and accuracy of docking with a new scoring function, efficient optimization, and multithreading. *J. Comput. Chem.* **31**, 455–

- 461 (2010).
32. Maia, E. H. B., Medaglia, L. R., da Silva, A. M. & Taranto, A. G. Molecular Architect: A User-Friendly Workflow for Virtual Screening. *ACS omega* **5**, 6628–6640 (2020).
  33. Savarino, A., Di Trani, L., Donatelli, I., Cauda, R. & Cassone, A. New insights into the antiviral effects of chloroquine. *The Lancet. Infectious diseases* vol. 6 67–69 (2006).
  34. Wang, M. *et al.* Remdesivir and chloroquine effectively inhibit the recently emerged novel coronavirus (2019-nCoV) in vitro. *Cell Res.* **30**, 269–271 (2020).
  35. Dong, L., Hu, S. & Gao, J. Discovering drugs to treat coronavirus disease 2019 (COVID-19). *Drug Discov. Ther.* **14**, 58–60 (2020).
  36. Cortopassi, W. A. *et al.* Docking studies on the binding of quinoline derivatives and hematin to plasmodium falciparum lactate dehydrogenase. *J. Biomol. Struct. Dyn.* **29**, 207–218 (2011).
  37. La Porta, F. de A. & Taft, C. A. *Emerging Research in Science and Engineering Based on Advanced Experimental and Computational Strategies.* (Springer, Cham, 2020). doi:10.1007/978-3-030-31403-3.
  38. Surrey, A. R. & Cutler, R. A. The Synthesis of Some 3-Nitro- and 3-Amino-4-dialkylaminoalkylaminoquinoline Derivatives. *J. Am. Chem. Soc.* **73**, 2413–2416 (1951).
  39. Narwal, S., Kumar, S. & Verma, P. K. Synthesis and therapeutic potential of quinoline derivatives. *Res. Chem. Intermed.* **43**, 2765–2798 (2017).
  40. Liu, Y., Wang, C., Lv, N., Liu, Z. & Zhang, Y. Synthesis of Quinoline N-Oxides by Cobalt-Catalyzed Annulation of Arylnitrones and Alkynes. *Adv. Synth. Catal.* **359**, 1351–1358 (2017).
  41. Okuma, K., Seto, J., Nagahora, N. & Shioji, K. Chemoselective synthesis of quinoline N-oxides from 3-(2-nitrophenyl)-3-hydroxypropanones. *J. Heterocycl. Chem.* **47**, 1372–1378 (2010).
  42. Doddaga, S. & Peddakonda, R. Chloroquine-N-oxide, a major oxidative degradation product of chloroquine: Identification, synthesis and characterization. *J. Pharm. Biomed. Anal.* **81–82**, 118–125 (2013).
  43. Sliwoski, G., Kothiwale, S., Meiler, J. & Lowe, E. W. Computational Methods in Drug Discovery. *Pharmacol. Rev.* **66**, 334 LP – 395 (2014).
  44. da Silva, R. R., Ramalho, T. C., Santos, J. M. & Figueroa-Villar, J. D. On the Limits of Highest-Occupied Molecular Orbital Driven Reactions: The Frontier Effective-for-Reaction Molecular Orbital Concept. *J. Phys. Chem. A* **110**, 1031–1040 (2006).
  45. La Porta, F. A., Ramalho, T. C., Santiago, R. T., Rocha, M. V. J. & da Cunha, E. F. F. Orbital Signatures as a Descriptor of Regioselectivity and Chemical Reactivity: The Role of the Frontier Orbitals on 1,3-Dipolar Cycloadditions. *J. Phys. Chem. A* **115**, 824–833 (2011).
  46. La Porta, F. A., Santiago, R. T., Ramalho, T. C., Freitas, M. P. & Da Cunha, E. F. F. The role of the Frontier orbitals in acid–base chemistry of organic amines probed by ab initio and chemometric techniques. *Int. J. Quantum Chem.* **110**, 2015–2023 (2010).
  47. Silva, R. R. da, Santos, J. M., Ramalho, T. C. & Figueroa-Villar, J. D. Concerning the FERMO concept and Pearson’s Hard and Soft acid-base principle. *J. Braz. Chem. Soc.* **17**, 223–226 (2006).

48. Jin, Z. *et al.* Structure of M<sup>&sup</sup>&pro</sup> from COVID-19 virus and discovery of its inhibitors. *bioRxiv* 2020.02.26.964882 (2020) doi:10.1101/2020.02.26.964882.
49. Bickelhaupt, F. M. & Houk, K. N. Analyzing Reaction Rates with the Distortion/Interaction-Activation Strain Model. *Angew. Chemie Int. Ed.* **56**, 10070–10086 (2017).
50. Takezawa, H., Shitozawa, K. & Fujita, M. Enhanced reactivity of twisted amides inside a molecular cage. *Nat. Chem.* (2020) doi:10.1038/s41557-020-0455-y.
51. Zhou, L. *et al.* Isatin compounds as noncovalent SARS coronavirus 3C-like protease inhibitors. *J. Med. Chem.* **49**, 3440–3443 (2006).
52. Yang, S. *et al.* Synthesis, crystal structure, structure-activity relationships, and antiviral activity of a potent SARS coronavirus 3CL protease inhibitor. *J. Med. Chem.* **49**, 4971–4980 (2006).
53. Zhang, L. *et al.* Crystal structure of SARS-CoV-2 main protease provides a basis for design of improved  $\alpha$ -ketoamide inhibitors. *Science* (80-. ). eabb3405 (2020) doi:10.1126/science.abb3405.
54. Cardoso Gajo, G., Rodrigues Silva, D., Barigye, S. J. & da Cunha, E. F. F. Multi-objective Optimization of Benzamide Derivatives as Rho Kinase Inhibitors. *Mol. Inform.* **37**, (2018).
55. Liu, J. *et al.* Hydroxychloroquine, a less toxic derivative of chloroquine, is effective in inhibiting SARS-CoV-2 infection in vitro. *Cell Discov.* **6**, 16 (2020).
56. Paulekuhn, G. S., Dressman, J. B. & Saal, C. Trends in Active Pharmaceutical Ingredient Salt Selection based on Analysis of the Orange Book Database. *J. Med. Chem.* **50**, 6665–6672 (2007).
57. Follmann, H. D. M. *et al.* Extent of shielding by counterions determines the bactericidal activity of N,N,N-trimethyl chitosan salts. *Carbohydr. Polym.* **137**, 418–425 (2016).
58. Moulin, B. & Ponchon, T. A comparative review of use of sulphate and phosphate salts for colonoscopy preparations and their potential for nephrotoxicity. *Endosc. Int. open* **6**, E1206–E1213 (2018).
59. Gupta, D., Bhatia, D., Dave, V., Sutariya, V. & Varghese Gupta, S. Salts of Therapeutic Agents: Chemical, Physicochemical, and Biological Considerations. *Molecules* **23**, 1719 (2018).
60. Zhang, L. *et al.*  $\alpha$ -Ketoamides as Broad-Spectrum Inhibitors of Coronavirus and Enterovirus Replication: Structure-Based Design, Synthesis, and Activity Assessment. *J. Med. Chem.* **63**, 4562–4578 (2020).
61. M. J. Frisch, G. W. Trucks, H. B. Schlegel, G. E. Scuseria, M. A. Robb, J. R. Cheeseman, G. Scalmani, V. Barone, G. A. Petersson, H. Nakatsuji, X. Li, M. Caricato, A. Marenich, J. Bloino, B. G. Janesko, R. Gomperts, B. Mennucci, H. P. Hratchian, J. V. Ort, W. C. Gaussian, Inc., Wallingford CT. (2009).
62. Webb, B. & Sali, A. Comparative Protein Structure Modeling Using MODELLER. *Curr. Protoc. Bioinforma.* **54**, 5.6.1-5.6.37 (2016).
63. Novoselov, K. P. *et al.* CHIMERA: A software tool for reaction rate calculations and kinetics and thermodynamics analysis. *J. Comput. Chem.* **23**, 1375–1389 (2002).
64. Accelrys Software. Discovery Studio Modeling Environment. (2012).

65. Scott, W. R. P. *et al.* The GROMOS Biomolecular Simulation Program Package. *J. Phys. Chem. A* **103**, 3596–3607 (1999).
66. Deepa, G., Sivakumar, K. C. & Sajeevan, T. P. Molecular simulation and in vitro evaluation of chitosan nanoparticles as drug delivery systems for the controlled release of anticancer drug cytarabine against solid tumours. *3 Biotech* **8**, 493 (2018).
67. Parrinello, M. & Rahman, A. Polymorphic transitions in single crystals: A new molecular dynamics method. *J. Appl. Phys.* **52**, 7182–7190 (1981).
68. Humphrey, W.; Dalke, A.; Schulten, K. VMD: Visual Molecular Dynamics. *J. Mol. Graph.* **14**, (1996).

## **SUPPLEMENTARY MATERIAL**

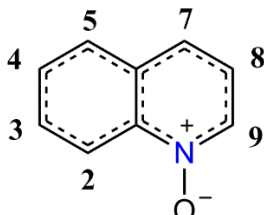
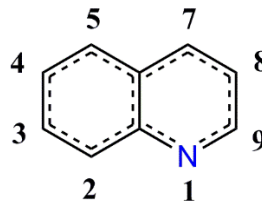
*Computational evidence for nitro derivatives of quinoline and quinoline N-oxide as low-cost alternative for the treatment of SARS-CoV-2 infection*



**Table S1.** Analysis of electronic properties of nitro derivatives of Q and QO.

System	$\Delta E$ (kcal/mol)	Bandgap $E_g$ (eV)	Hardness $\eta$ (eV)	Softness $S$ (eV)	Electronegativity $\chi$ (eV)	Electrophilicity $\omega$ (eV)
N-2-Q	9,65	4.15	2.08	0.48	-5.07	51.36
N-3-Q	0,52	4.24	2.12	0.47	-5.22	54.47
N-4-Q	0,00	4.23	2.11	0.47	-5.23	54.73
N-5-Q	3,64	4.20	2.10	0.48	-5.24	54.98
N-7-Q	7,76	4.31	2.15	0.46	-4.99	49.73
N-8-Q	1,32	4.07	2.04	0.49	-5.25	55.05
N-9-Q	1,51	4.19	2.09	0.48	-5.15	52.96
System	$\Delta E$ (kcal/mol)	Bandgap $E_g$ (eV)	Hardness $\eta$ (eV)	Softness $S$ (eV)	Electronegativity $\chi$ (eV)	Electrophilicity $\omega$ (eV)
N-2-QO	11.75	3.69	1.84	0.54	-4.53	41.04
N-3-QO	0.15	3.24	1.62	0.62	-4.93	48.59
N-4-QO	0.00	3.18	1.59	0.63	-4.92	48.46
N-5-QO	3.63	3.11	1.56	0.64	-4.93	48.66
N-7-QO	7.56	3.56	1.78	0.56	-4.72	44.65
N-8-QO	2.14	3.19	1.60	0.63	-5.00	50.00
N-9-QO	12.08	3.49	1.75	0.57	-5.02	50.48

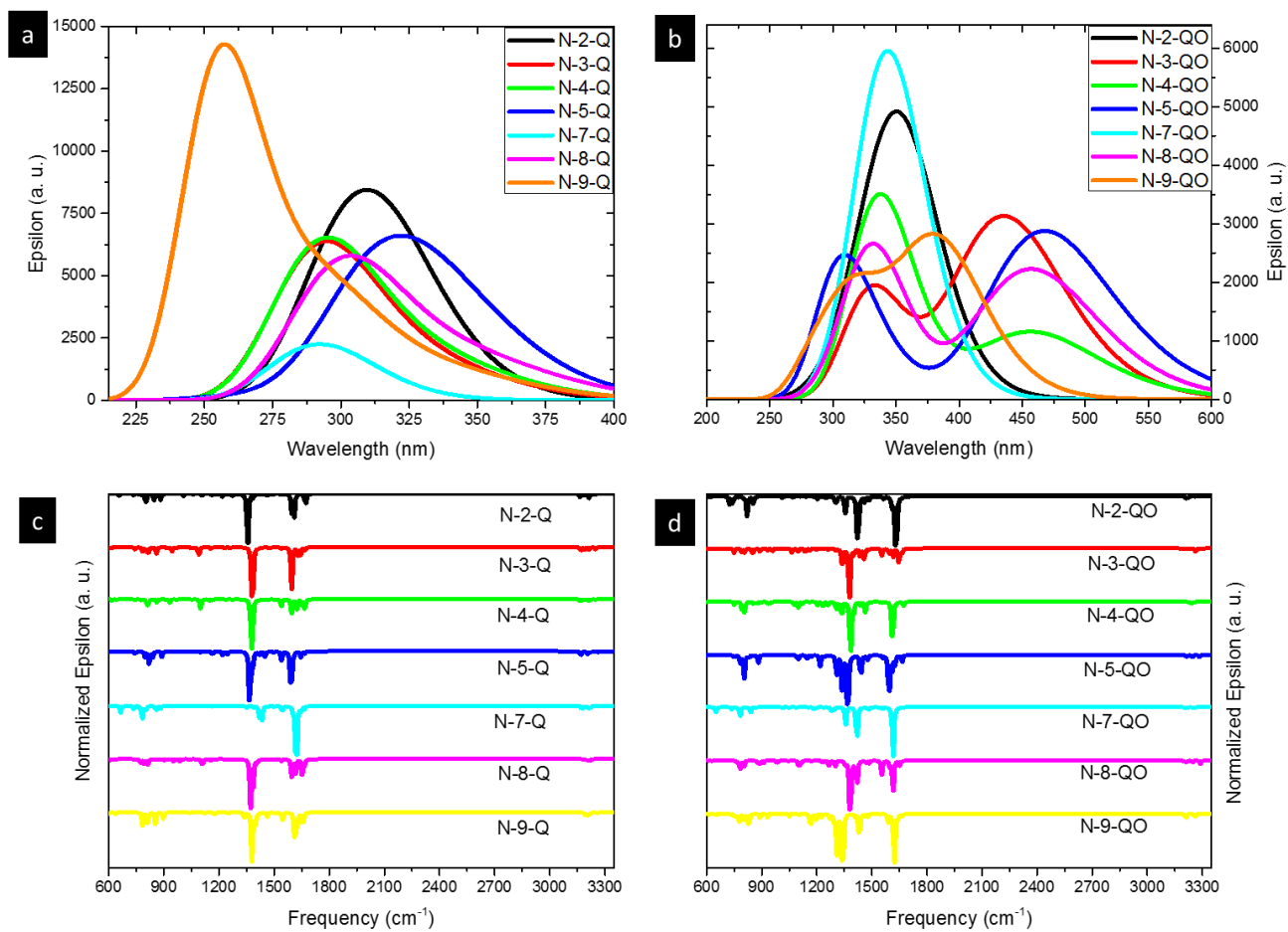
**Table S2.** Interaction energy (in kcal mol<sup>-1</sup>) of nitro derivatives computed through AutoDock Vina program.

			
Nitro group position	Interaction Energy (kcal mol <sup>-1</sup> )	Nitro group position	Interaction Energy (kcal mol <sup>-1</sup> )
N-4-QO	-5.0	N-4-Q	-4.6
N-9-QO	-5.0	N-9-Q	-4.6
N-7-QO	-4.9	N-7-Q	-5.0
N-2-QO	-4.8	N-2-Q	-4.8
N-5-QO	-4.8	N-5-Q	-4.8
N-8-QO	-4.8	N-8-Q	-4.6
N-3-QO	-4.5	N-3-Q	-4.5
QO	-4.5	N-1-Q	-4.3
CQO	-3.0	CQ	-2.8
HCQO	-3.1	HCQ	-2.3

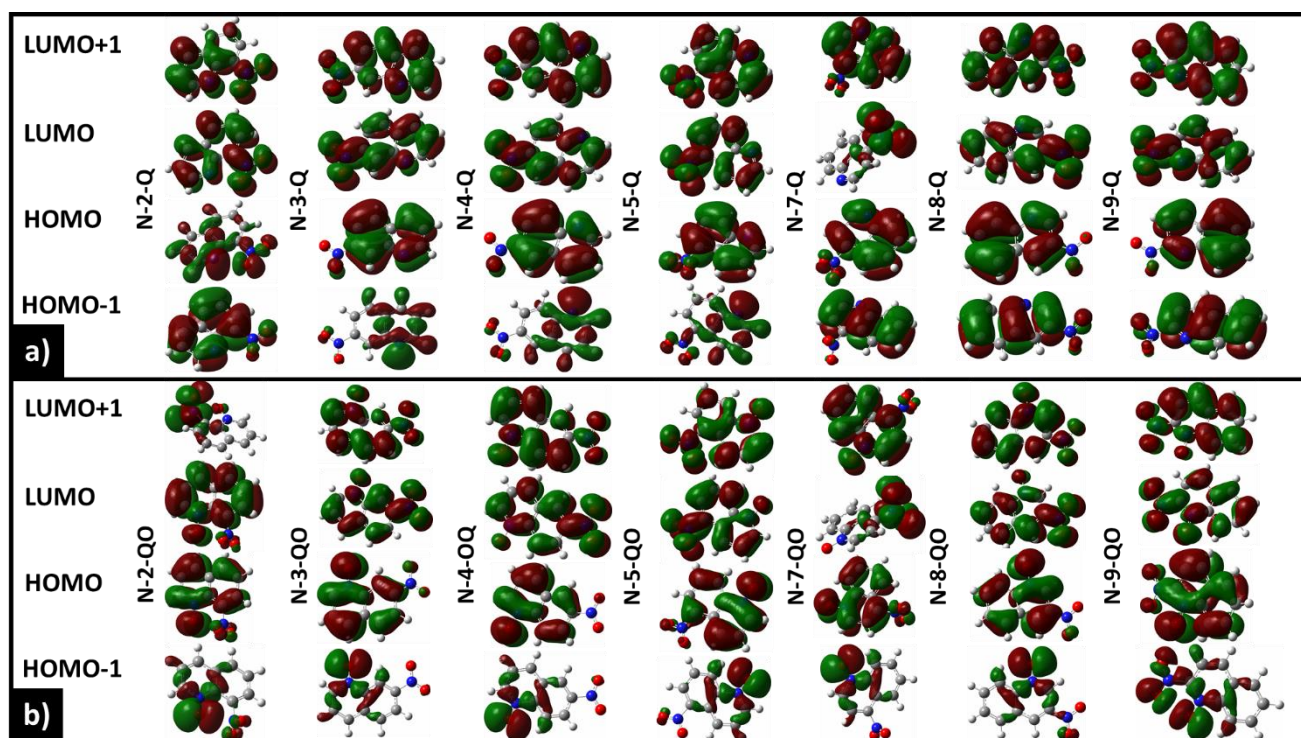
\*Q = quinoline, QO = quinoline *N*-oxide, CQO = chloroquine *N*-oxide, CQ = chloroquine, HCQO = hydroxychloroquine *N*-oxide, HCQ = hydroxychloroquine, N = nitro group.

**Table S3.** Interaction energy (in kcal mol<sup>-1</sup>) of chloroquine and hydroxychloroquine derivatives computed through AutoDock Vina program.

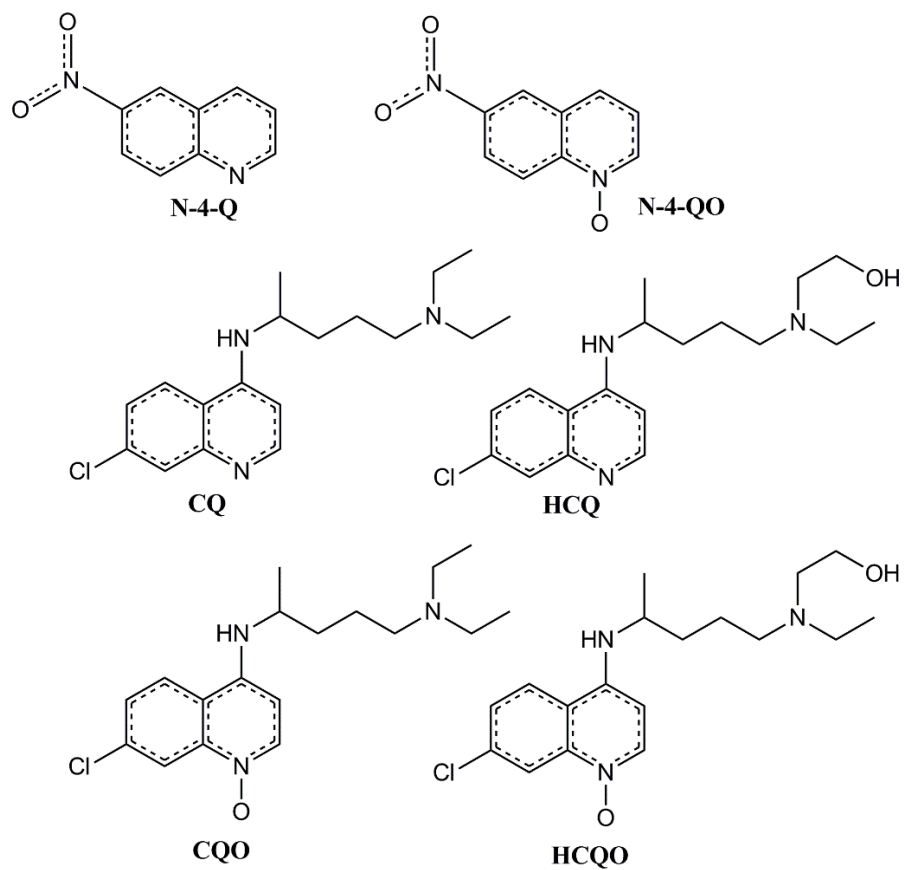
Oxide group position	Interaction Energy (kcal mol <sup>-1</sup> )	Oxide group position	Interaction Energy (kcal mol <sup>-1</sup> )
Sites 1,2	-2.9	Sites 1,2	-3.2
Sites 1,3	-2.4	Sites 1,3	-2.9
Sites 1,2,3	-2.6	Sites 1,2,3	-2.8
Sites 2	-3.0	Sites 2	-3.4
Sites 2,3	-3.0	Sites 2,3	-3.3
Sites 3	-2.9	Sites 3	-3.3



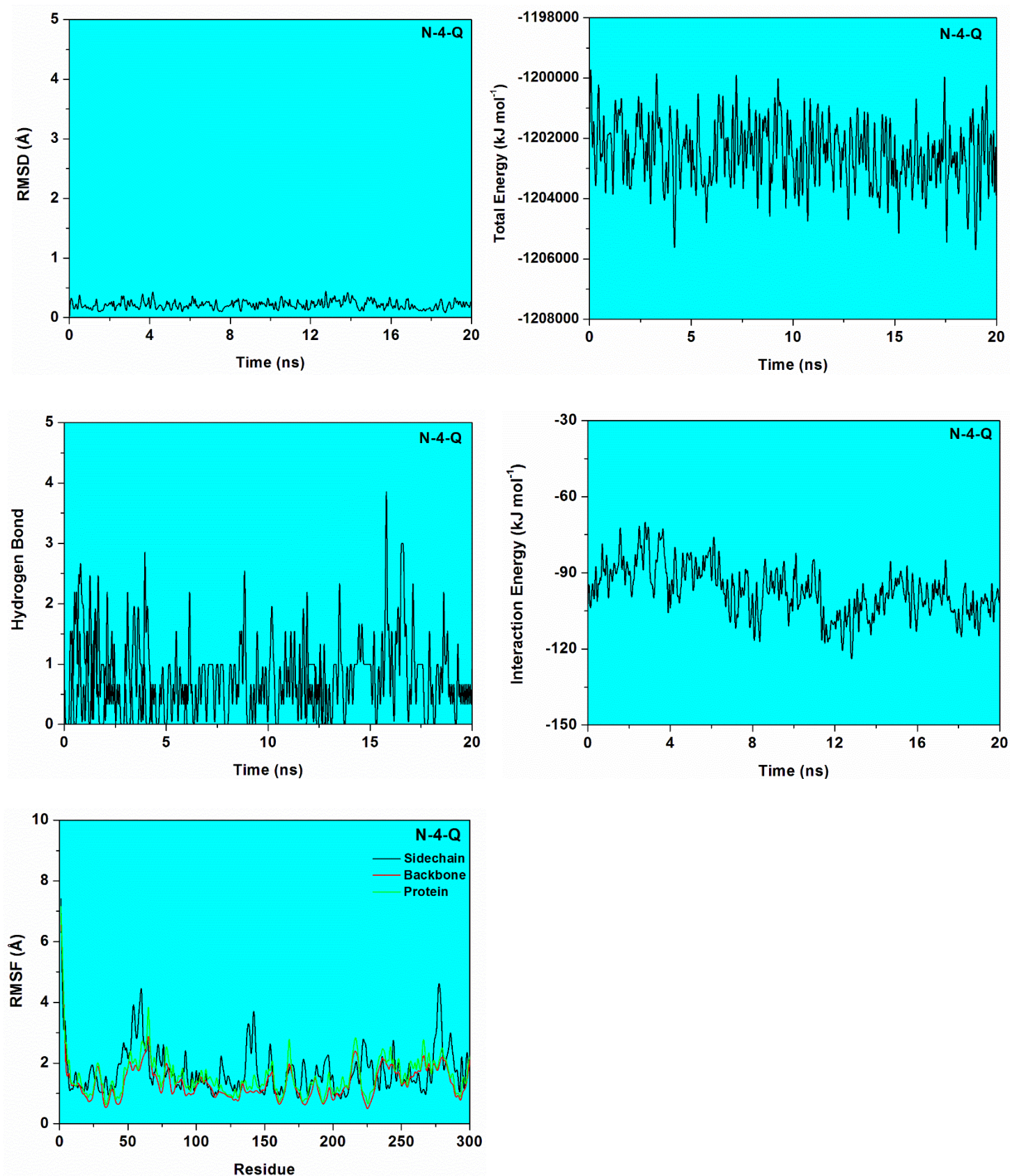
**Figure S1.** Simulated (a and b) UV-vis and (c and d) IR spectra of nitro derivatives of Q and QO.



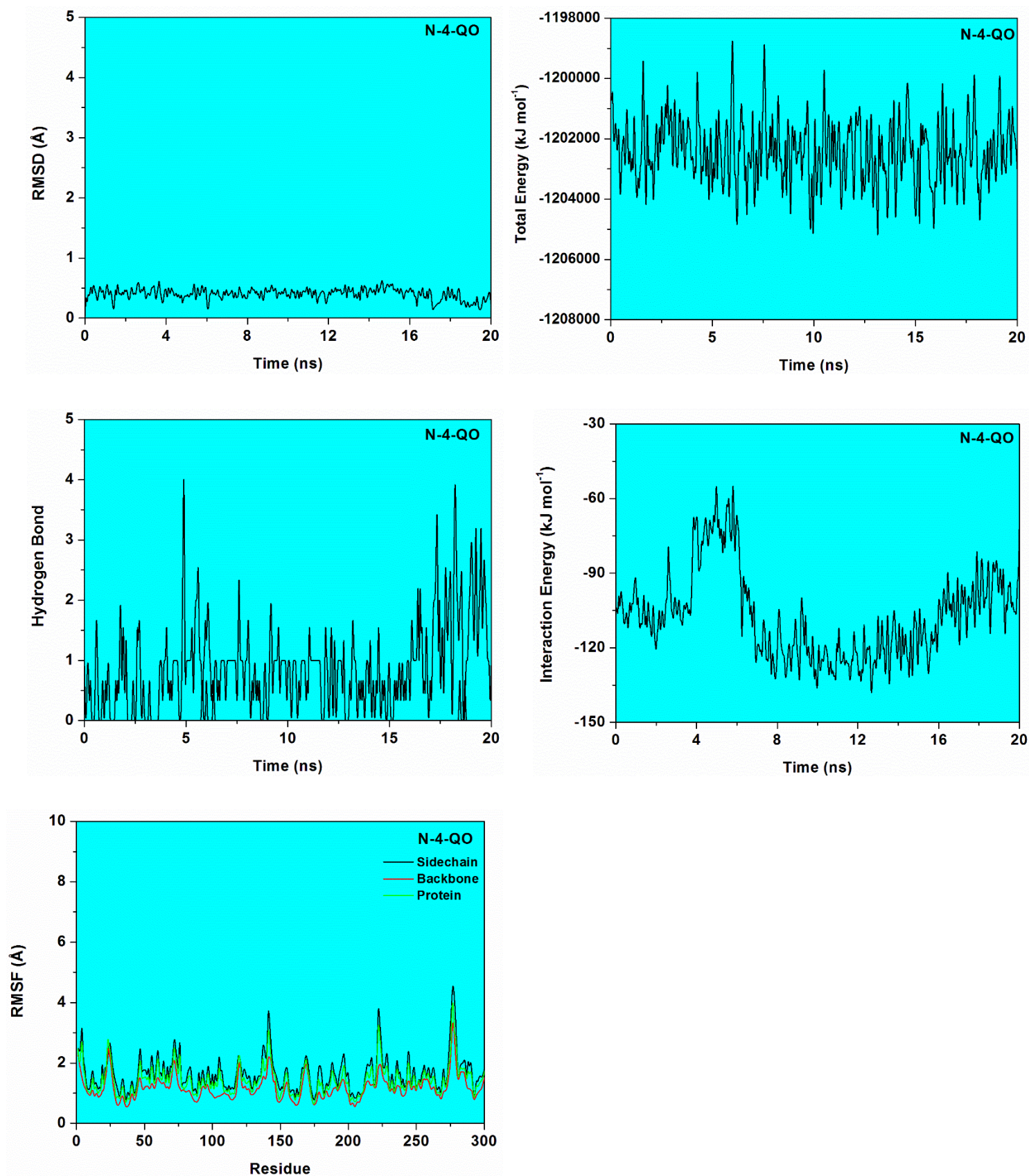
**Figure S2.** Frontier molecular orbital representation (with a contour value of 0.020) for the nitro derivatives of Q and QO.



**Figure S3.** Chemical structures of the species employed in the MD simulations.

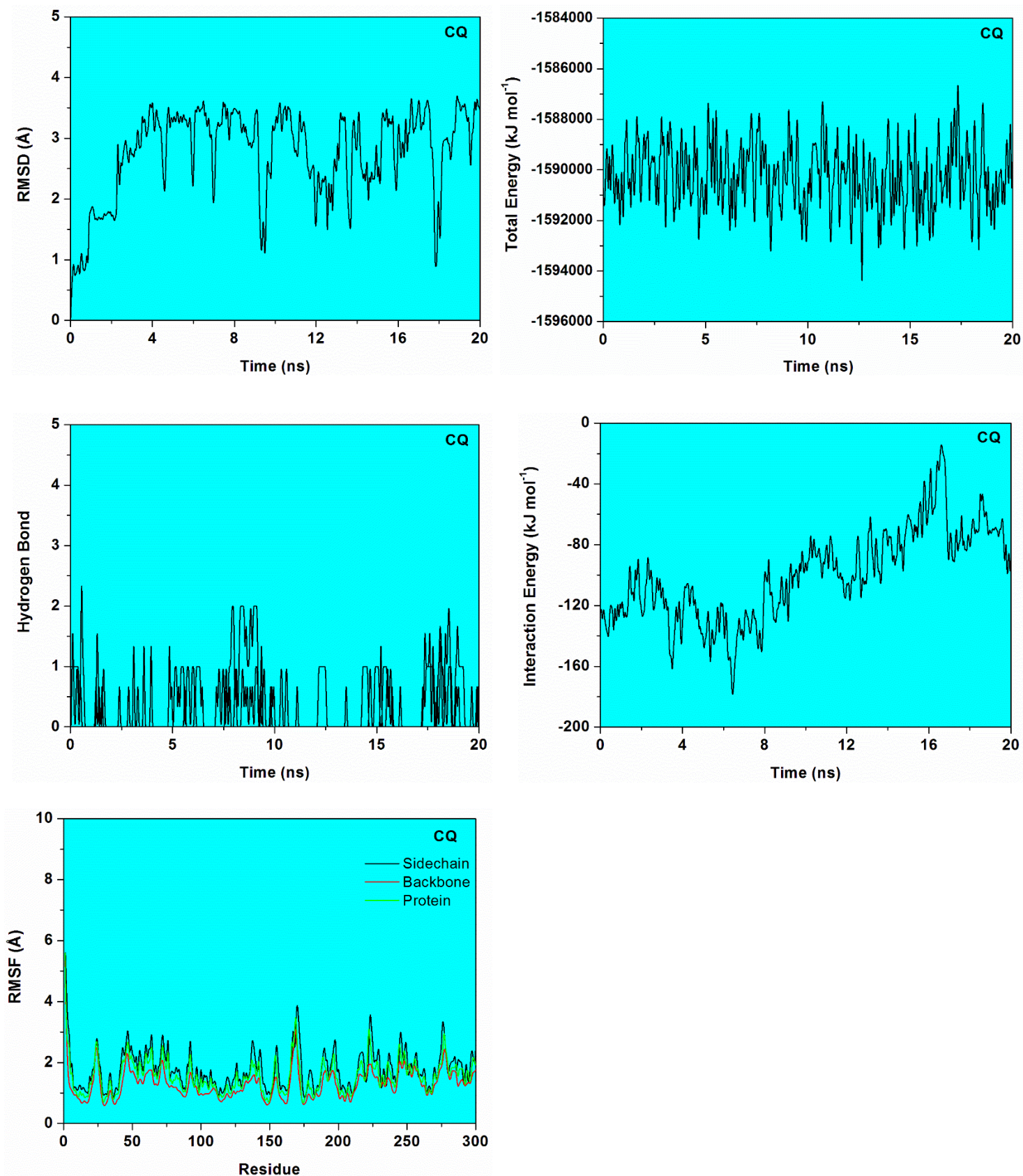


**Figure S4.** RMSD, Total Energy, Hydrogen Bond, Interaction Energy and RMSF graphs of a 20 ns simulation of the N-4-Q.

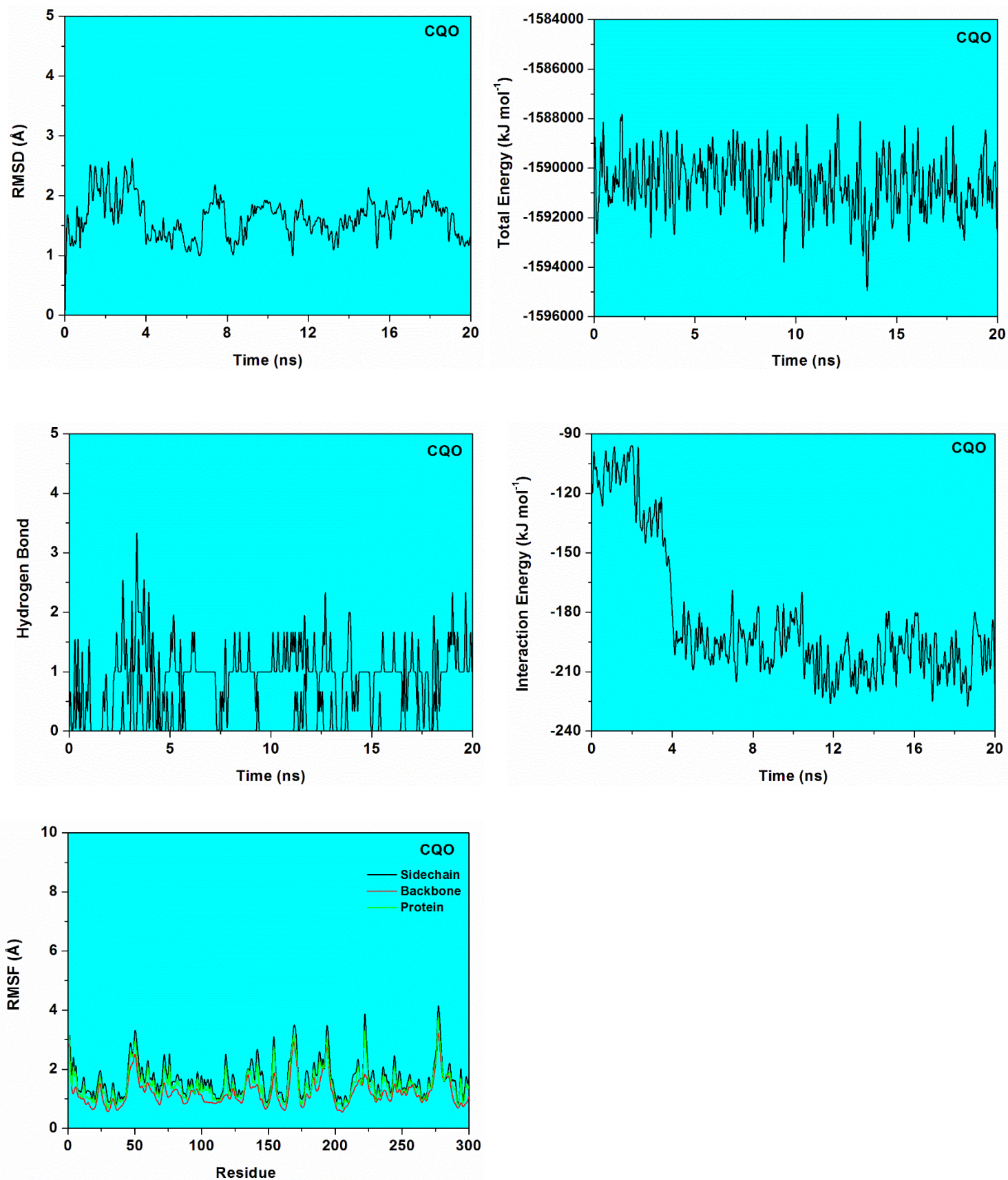


**Figure S5.** RMSD, Total Energy, Hydrogen Bond, Interaction Energy and RMSF graphs of a 20 ns simulation of the N-4-QO.

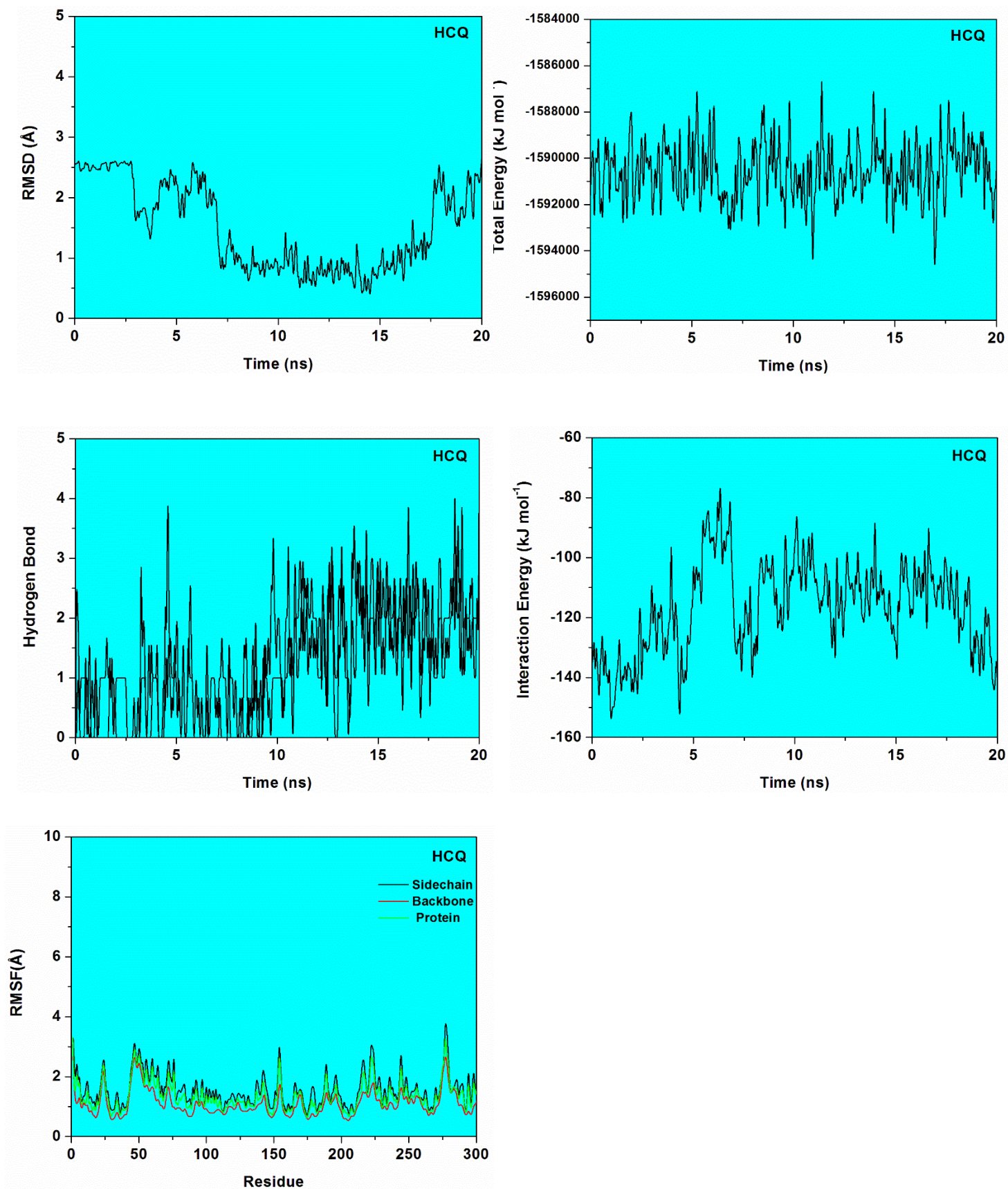




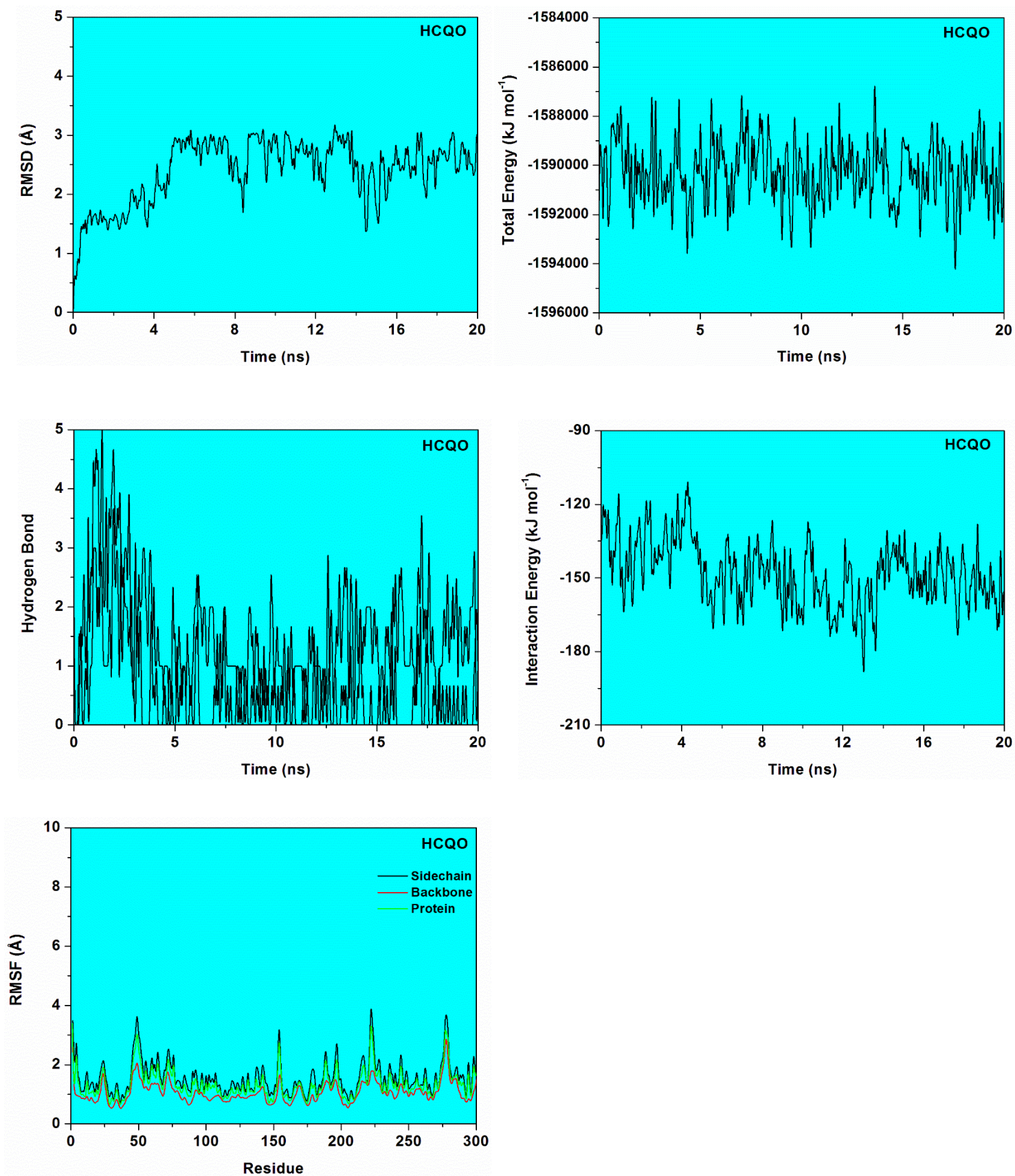
**Figure S6.** RMSD, Total Energy, Hydrogen Bond, Interaction Energy and RMSF graphs of a 20 ns simulation of the CQ.



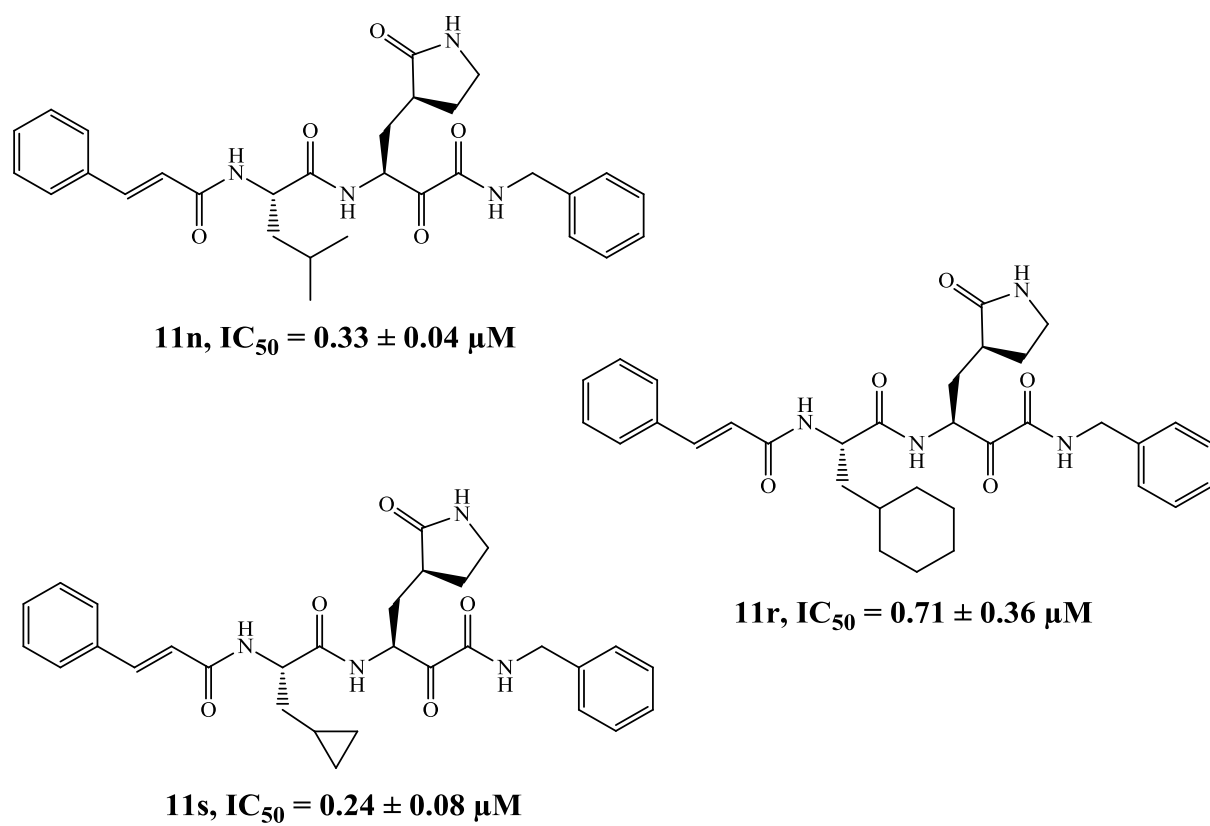
**Figure S7.** RMSD, Total Energy, Hydrogen Bond, Interaction Energy and RMSF graphs of a 20 ns simulation of the CQO.



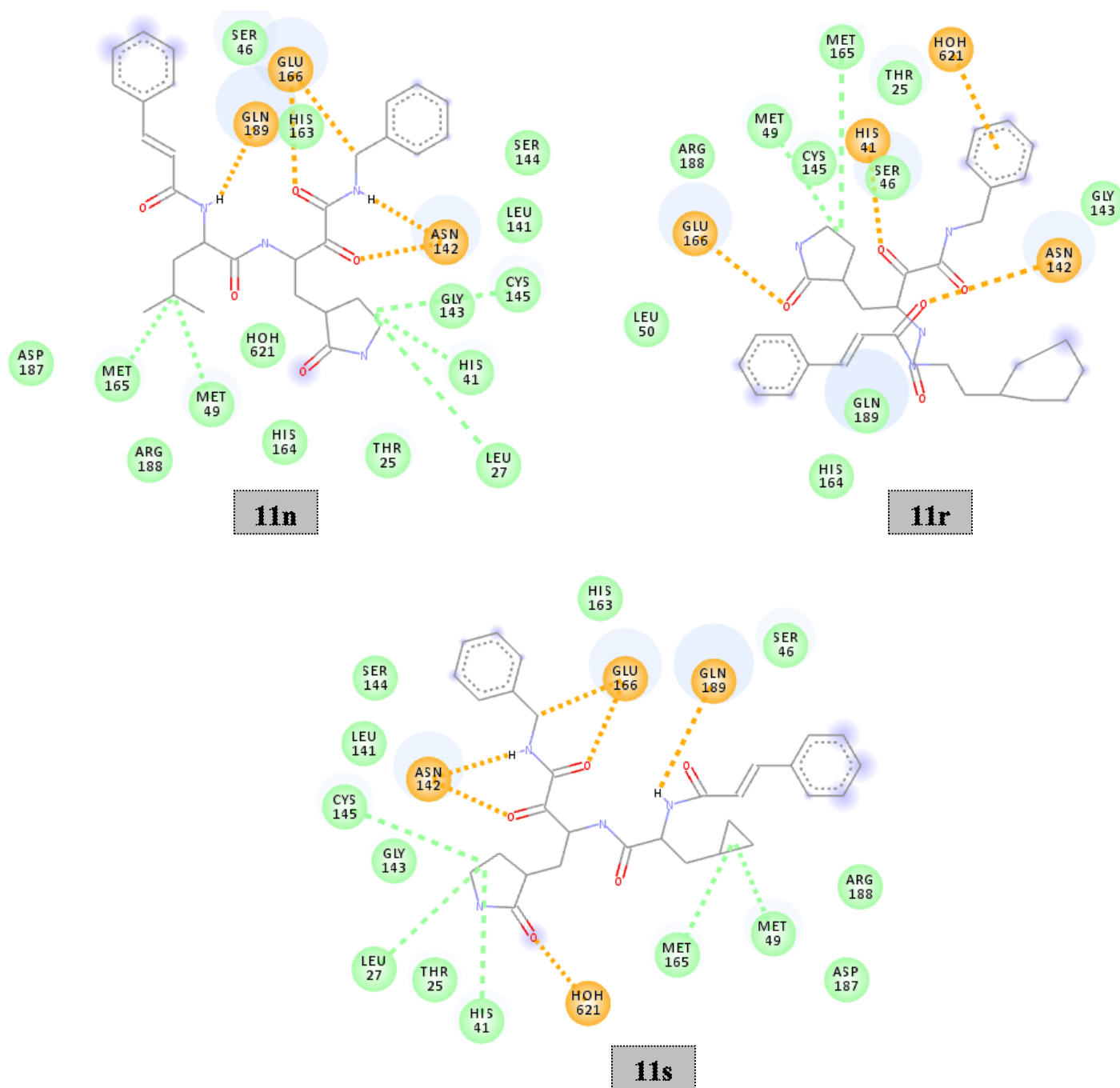
**Figure S8.** RMSD, Total Energy, Hydrogen Bond and Interaction Energy graphs of a 20 ns simulation of the HCQ.



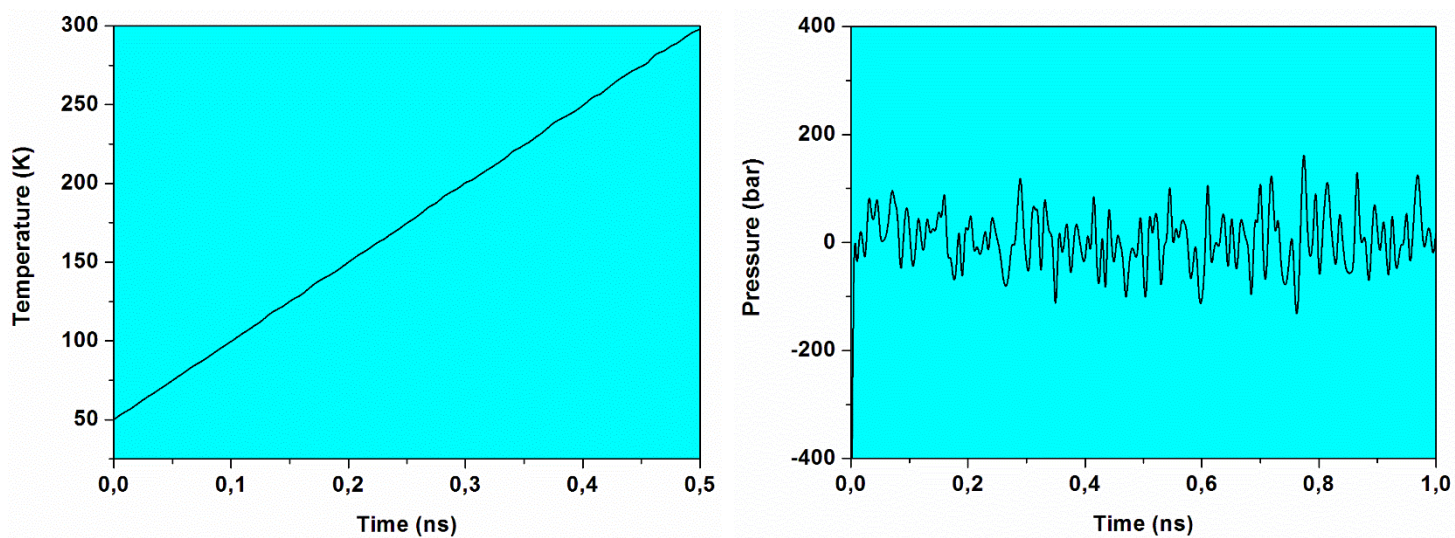
**Figure S9.** RMSD, Total Energy, Hydrogen Bond, Interaction Energy and RMSF graphs of a 20 ns simulation of the HCQO.



**Figure S10.** Chemical structures of the  $\alpha$ -ketoamides used in the work.



**Figure S11.** Intermolecular interactions performed by the  $\alpha$ -ketoamide inhibitors 11n, 11r and 11s in the  $M^{\text{pro}}$  active site.



**Figure S12.** General Temperature and Pressure graphs acquired from the equilibration process of the systems.

## CHAPTER 4

### *Research article*

New in silico insights into the application of the (hydroxy)chloroquine with macrolide antibiotics co-crystals against the SARS-CoV-2 virus

*Submitted to Molecular Diversity*



## ABSTRACT

In this *in silico* study, the different pharmaceutical co-crystals based on the (hydroxy)chloroquine with the macrolide antibiotics (azithromycin, clarithromycin, or erythromycin A) was analyzed for the first time. These findings present a new molecular perspective and, therefore, suggest that the combination of (hydroxy)chloroquine/azithromycin, in the stoichiometric ratio of 1:1, as model co-crystals systems have less toxicity as well as is the most effective for inhibiting the new coronavirus SARS-CoV-2.

**Keywords:** (hydroxy)chloroquine; macrolide antibiotics; co-crystals; SARS-CoV-2; Molecular Modelling

## 1. INTRODUCTION

Recently, enormous efforts have widely been focused on facing a new coronavirus, SARS-CoV-2, disease designated as COVID-19.<sup>[1]</sup> The World Health Organization (WHO), declared COVID-19 outbreak as a new pandemic, on March 11, 2020.<sup>[2]</sup> In order to contribute to the front line of the fight against this disease, researchers worldwide are moving the investigation of an effective treatment regimen (based mainly on known drugs) against infection caused by the SARS-CoV-2 virus.<sup>[1-5]</sup> Most recently, the combination of drugs as, for example, the (hydroxy)chloroquine with azithromycin (AZ) has been used as a strategy and also clinically tested to treat the SARS-CoV-2 outbreak.<sup>[6-11]</sup> As yet, the possible benefits of this therapeutic option are still being debated.<sup>[8-11]</sup> It is additionally expected, however, that computational screening can aid in accelerating the discovery as well as the development of new and more effective drugs against SARS-CoV-2.<sup>[1]</sup> To the best of our knowledge, no study reports the benefits of using pharmaceutical co-crystals to treat patients with infection caused by the SARS-CoV-2 virus. However, a simple consultation of the literature suggests that pharmaceutical co-crystals research has become a prevalent theme in the last years.<sup>[12-18]</sup>

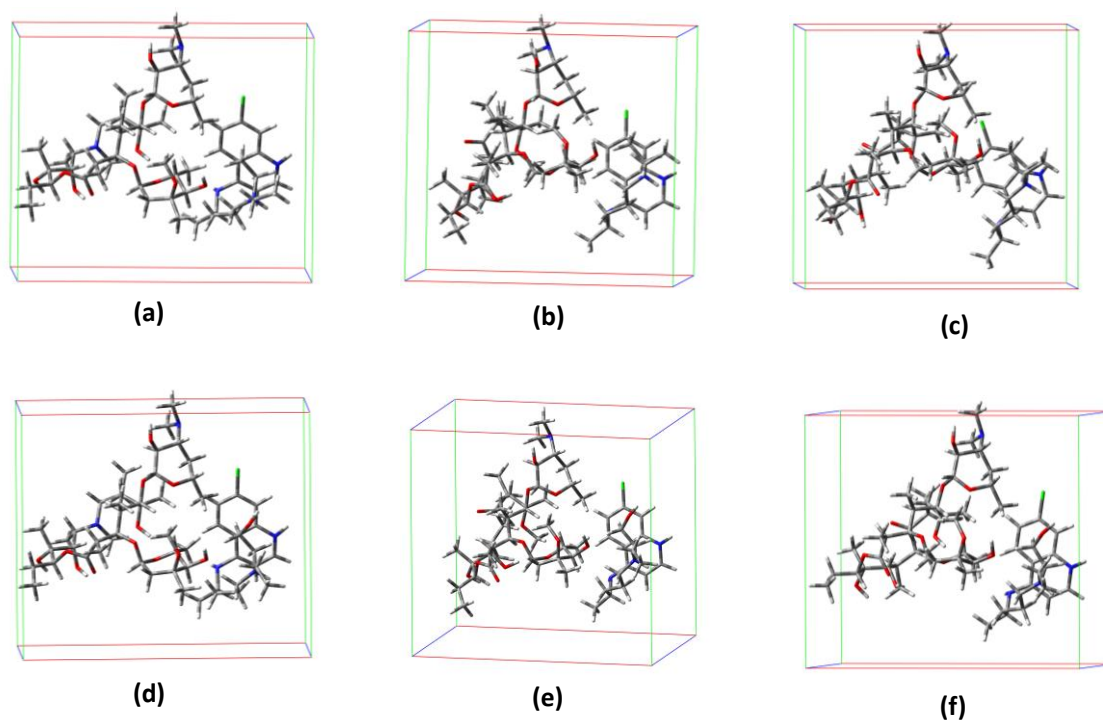
Particularly, pharmaceutical co-crystals are usually defined as multicomponent crystals that incorporates two or more drugs.<sup>[13,14,18]</sup> These co-crystals exhibit different and improved physical-chemical properties, and thus, they are widely considered good candidates for diverse therapeutic applications.<sup>[14]</sup> Also, a large variety of synthetic strategies has been successfully developed to obtain controlled pharmaceutical co-crystals with different structures. Notable examples include solid-state grinding, solution- and melt-crystallization, solvent evaporation,

and so on.<sup>[12,14–17]</sup> Therefore, in this perspective, we believe that a computational model of co-crystals systems is essential to gain further insight into their biological activity, aiding directly in the emergence of new experimental research to confront COVID-19.

In this paper, we have selected the (hydroxy)chloroquine with the macrolide antibiotics (such as AZ, clarithromycin (CL), or erythromycin A (ER)), in the stoichiometric ratio of 1:1, as a co-crystal model system to a computational screening study. First of all, these compounds were selected because of some preliminary clinical studies.<sup>[6–11]</sup> Second, the AZ and CL are well-known semi-synthetic derivatives of ER, the first and most-known macrolide antibiotic to be isolated in 1952.<sup>[19–21]</sup> These macrolide antibiotics are mainly used to treat patients with certain infections of the respiratory tract.<sup>[20]</sup> Also, it is well-known that the combination of AZ with antimalarial drugs (e.g., (hydroxy)chloroquine), shows some crucial benefits for the treatment of malaria.<sup>[22]</sup> A third relevant aspect of this study is that both (hydroxy)chloroquine and macrolide antibiotics usually crystallize in a monoclinic structure according to the CSD (Cambridge Structural Database),<sup>[23]</sup> which is fundamental for the construction of these co-crystals model systems. Therefore, in this perspective, we have developed the first theoretical model of co-crystals applied in the treatment of SARS-CoV-2. We believe that this strategy can bring additional benefits to the use of this therapy as well as contributing to a better understanding of a molecular point of view.

## 2. COMPUTATIONAL DETAILS

Six co-crystal model systems were prepared in this study, as shown in Figure 1, and are based on the combination of (hydroxy)chloroquine (denoted as HQ and CQ, respectively) with the AZ, CL or ER antibiotics, in the stoichiometric ratio of 1:1. As a strategy, the unit cell of these compounds was here replicated to the investigated set of single- and co-crystals, that is, their structural parameters have maintained close as possible. All these model systems were then optimized (as the starting point for docking studies) and their structural and vibrational properties were fully evaluated at the PM6 theoretical level, from using the Gaussian 09 package.<sup>[24]</sup> In order to better describe the electronic/optical properties for these model systems have also been employed the Kohn–Sham time-dependent density functional theory (TDDFT) using the B3LYP functional with the 6-31+G(d,p) basis set. In addition to the partial charges of the atoms was also elucidated by the natural bond orbital (NBO) calculations.



**Figure 1.** Representation of optimized co-crystal structures in this study. (a) CQ/AZ; (b) CQ/CL; (c) CQ/ER; (d) HQ/AZ; (e) HQ/CL and (f) HQ/ER.

In the docking studies, the affinity of the single and co-crystals in the  $M^{\text{pro}}$  active site was investigated. The compounds were then docked inside the crystallographic structure of viral protein  $M^{\text{pro}}$  (PDB code 6LU7; resolution = 2.16 Å),<sup>[25]</sup> using the Molegro Virtual Docker program (MVD®),<sup>[26]</sup> taking into account the same procedures employed previously.<sup>[27–29]</sup> According to our calculation protocol, it was considered a radius of about 20 Å, where the residues of the catalytic triad were kept as flexible. Due to the nature of the docking methods, the calculations were carried out, generating approximately 50 poses (hence such as conformation and orientation) for each ligand studied.

In the MVD program, the MolDock score algorithm method used as a scoring function is based on the piecewise linear potential, which fundamentally is a simplified potential whose parameters are in turn fitted to protein-ligand structures, binding data scoring functions and further extended in Generic Evolutionary Method for molecular docking, including a new hydrogen bonding term as well as new charge schemes.<sup>[26]</sup> Along this line, the docking scoring function values,  $E_{\text{score}}$ , are usually defined by Eq. 1:

$$E_{score} = E_{inter} + E_{intra} \quad (1)$$

Wherein:

$$E_{inter} = \sum_{i \in \text{ligand}} \sum_{j \in \text{protein}} \left[ E_{PLP}(r_{ij}) + 332.0 \frac{q_i q_j}{4r_{ij}^2} \right] \quad (2)$$

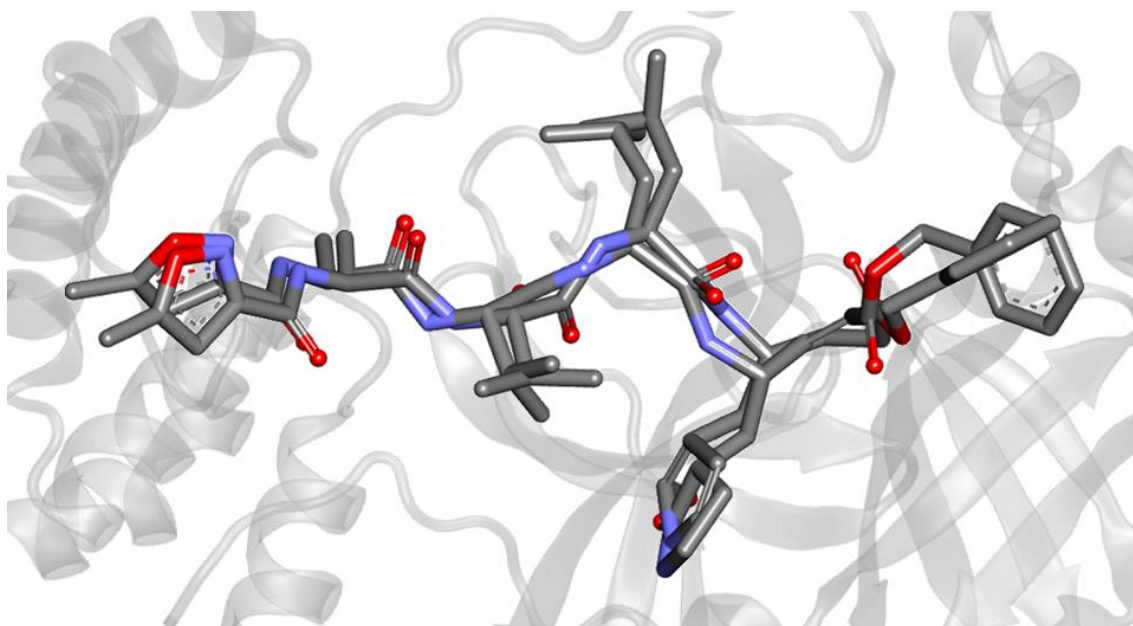
Note that the  $E_{PLP}$  represents “piecewise linear potential”, which consists of two different parameter sets, as described forward: one for the approximation of the steric term (i.e., Van der Waals) among atoms, as well as the other potential for the hydrogen bonding. As can be seen, the second term is, of course, related to the electrostatic interactions among overloaded atoms. Typically, it is a Coulomb potential with a dielectric constant dependent on the distance (which can be approximately described as  $D(r) = 4r$ ). Hence, for this, the numerical value of 332.0 is then responsible for the electrostatic energy unit to be given in kilocalories per molecule, as well.<sup>[26]</sup>

$E_{intra}$  is defined as the internal energy of each ligand. That is:

$$E_{intra} = \sum_{i \in \text{ligand}} \sum_{j \in \text{ligand}} E_{PLP}(r_{ij}) + \sum_{\text{flexiblebonds}} A[1 - \cos(m \cdot \theta - \theta_0)] + E_{clash} \quad (3)$$

Note that the first part of the equation (double summation) is among all pairs of atoms in the ligand, taking off those connected by two bonds. Thus, in this equation, the second term denotes the torsional energy, where  $\theta$  is the bond's torsional angle. Hence, if several torsions could be determined, then, each torsional energy is considered as an average among them. Being that the last term of this equation,  $E_{clash}$ , attributes (not taking into account infeasible ligand conformations) a penalty incurred of about 1.000 in those exhibiting the distance between two heavy atoms (e.g., with more than two bonds apart) is smaller than  $2.0 \text{ \AA}$ .<sup>[26]</sup> Thus, in the MVD program, the docking search algorithm is based on the whole the interactive optimization techniques (inspired by Darwinian evolution theory), which implies a new hybrid search algorithm conveniently so-called guided differential evolution. As such, this hybrid combines a differential evolution optimization technique with a cavity prediction algorithm during the search process. As a result, this approach leading that way a simple, fast, and accurate description of potential binding modes (poses).<sup>[26,30,31]</sup>

In order to validate the docking algorithms, we performed re-docking calculations. This procedure was based on the orientation and conformation adopted by the experimental co-crystallized active ligand present in the binding pocket. The RMSD variation (1.24 Å) suggested that the program was able to correctly and efficiently simulate the experimental results for the respective ligands. The re-docking overlap is presented in Figure 2. The parameters used in the re-docking protocol were maintained for the docking calculations of our co-crystals.



**Figure 2.** overlap obtained from re-docking calculations of the experimental co-crystallized active ligand N3 (PDB code: 6lu7) through MVD.

Additionally, taking into account the experimental inexistence of acute toxicity data for the compounds employed in this study, and in order to estimate the theoretical values of the lethal dose (denoted as LD<sub>50</sub>), a rat model-based admetSAR predictor was used. Hence, this admetSAR approach is freely available online at <http://lmmd.ecust.edu.cn:8000/>.

### 3. RESULTS AND DISCUSSION

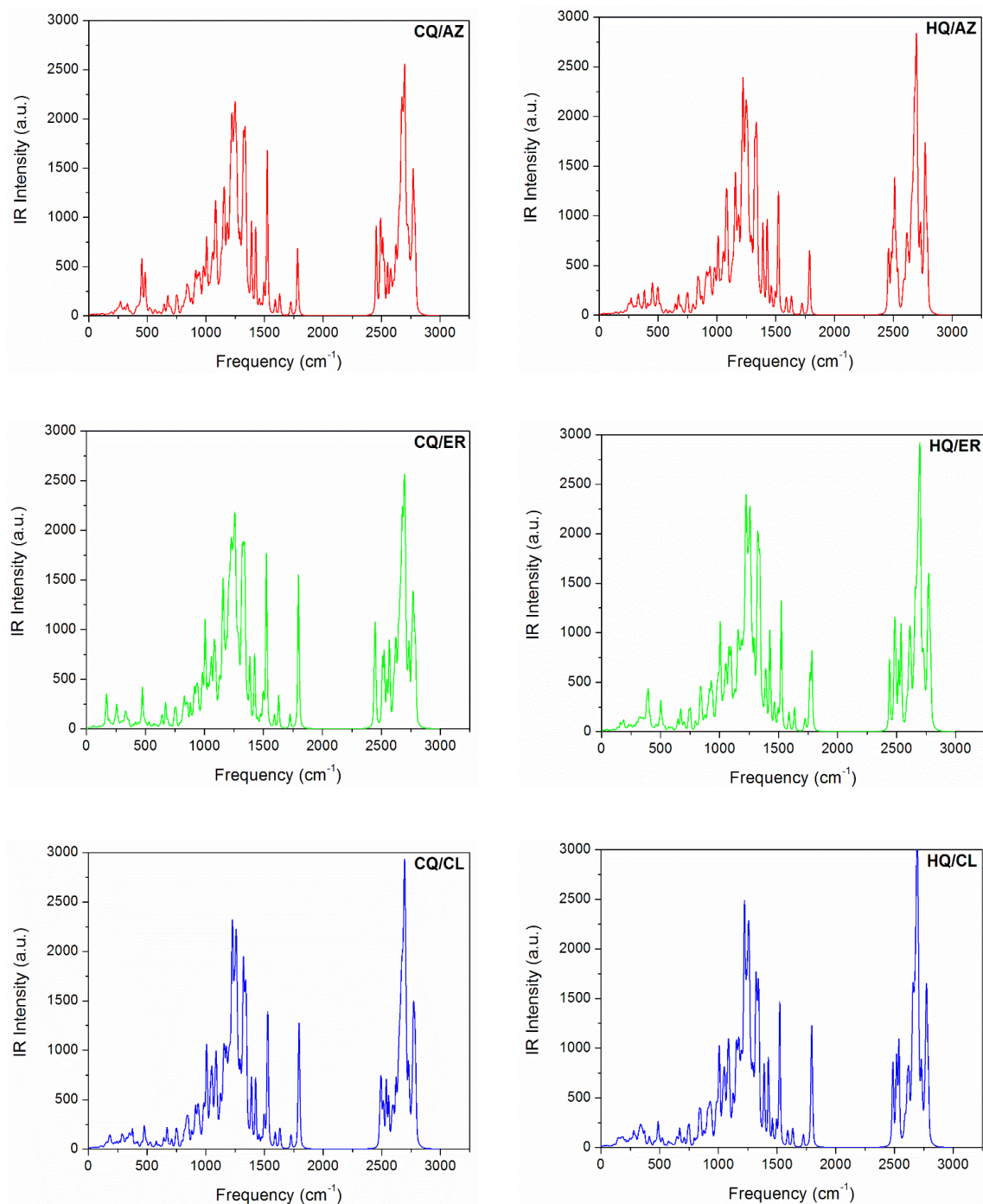
We started this study by analyzing frequency calculations for these co-crystals and the thermochemical parameters obtained (at 298.15 K and 1.00 atm) from them using the standard relations in the gas phase, and are given in Table 1. As such, the comparison of the difference

between the total electronic energy ( $\Delta E$ ), used to predict the stability of these co-crystals designed, presented in Table 1, suggests that the HQ/ER is the co-crystal more stable. In both HQ/AZ and CQ/AZ co-crystals, we can evidence that it is the least stable in their respective series. Thus, the stability order obtained for the computed co-crystals is HQ/ER > HQ/CL > CQ/ER > CQ/CL > HQ/AZ > CQ/AZ, i.e., suggesting that HQ-based co-crystals are well more stable than their CQ counterparts (see Table 1).

**Table 1.** Analysis of thermodynamic parameters computed for the co-crystals at the PM6 theoretical level.

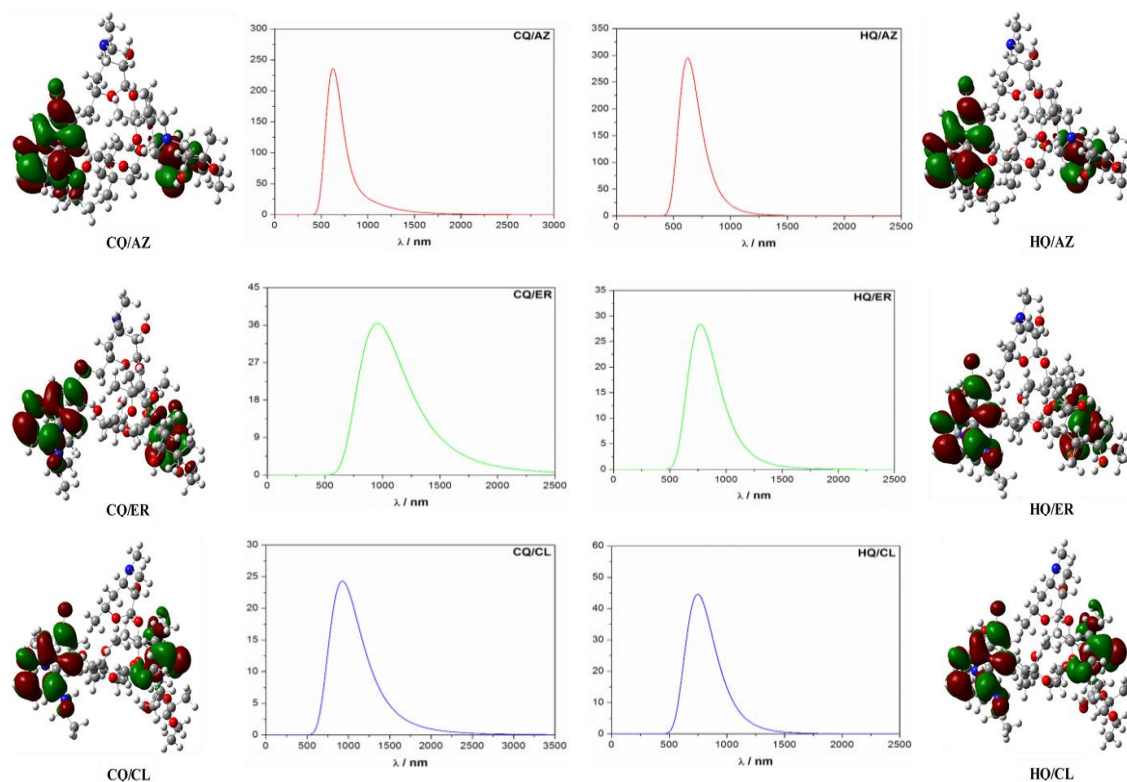
Co-crystal	$\Delta E$ (kcal.mol <sup>-1</sup> )	$H^\circ$ (kcal.mol <sup>-1</sup> )	$S^\circ$ cal (mol.K) <sup>-1</sup>	$C_v$ cal (mol.K) <sup>-1</sup>
CQ/AZ	97.2	932.4	459.3	333.9
CQ/ER	48.9	929.2	462.3	336.1
CQ/CL	52.0	946.8	476.3	342.1
HQ/AZ	52.3	935.2	469.3	337.5
HQ/ER	0.0	931.6	471.5	340.2
HQ/CL	7.6	949.5	482.5	345.6

On the whole, the typical calculated Infrared (IR) spectrum is shown in Figure 3 (a-f). According to these results, we have observed only positive modes suggesting that the structures proposed in this study are well optimized and therefore represent a minimum of energy. Also, the IR-active modes confirm of obtaining co-crystals with a monoclinic-like structure. These results are consistent with experimental observations for both (hydroxy)chloroquine and macrolide antibiotics, respectively.<sup>[1,12,32,33]</sup> As can be seen in Figure 4, the computed UV-vis absorption spectrum of these co-crystals reveals only one well-defined peak. As such, the more intense UV band located in the range of 617 nm to 771 nm for the HQ-based co-crystals (AZ to ER) is due to a predominant HOMO-to-LUMO+2 transition. In comparison, for the CQ-based co-crystals (AZ to ER) this UV band is located in the around of 624 nm to 955 nm (which is due to a predominant HOMO-to-LUMO+3 transition for CQ/AZ and both CQ/CL and CQ/ER is best assigned to HOMO-to-LUMO+2 transition), respectively.



**Figure 3.** Simulated IR spectra of the co-crystals formed between (left) Chloroquine and (right) Hydroxychloroquine with macrolide antibiotics at the PM6 theoretical level.

On the other hand, in all cases, we have observed a red-shift UV-vis absorption spectrum of HQ-based and CQ-based co-crystals in the function of increasing structural polarization (summarized by calculated dipole moment, as shown in Table 2). This was the main reason for the slight variation in the angles and bond lengths observed in the studied models (Figure 1).



**Figure 4.** Simulated UV-vis spectra and frontier molecular orbitals of the co-crystals using a contour value of 0.020. For each co-crystal, the HOMO orbitals are represented on the left and LUMO orbitals on the right in the same figure.

Additionally, the calculated value of the HOMO-LUMO energy gap ( $E_g$ ), exciton binding energy ( $E_B$ ), hardness ( $\eta$ ), softness ( $S$ ), electronegativity ( $\chi$ ), and electrophilicity ( $\omega$ ) values for the computed co-crystals at the TDDFT theoretical level are given in Table 2. According to the  $E_g$  values, we notice an increase in the order: CQ/AZ < CQ/ER < HQ/ER = HQ/AZ < HQ/CL < CQ/CL. Our results also suggest better chemical stability for the CQ/CL co-crystal. In addition, these HQ-based and CQ-based co-crystals have an  $E_B$  values range of 0.07 eV to 0.47 eV, which is typical of the organic crystals containing aromatic groups.<sup>[34]</sup>

Based on this analysis, supported by theory,<sup>[35–37]</sup> we identify that HQ and CQ moieties are donor states, and the AZ, CL, or ER moieties are acceptor states. As such, the frontier molecular orbital analysis is illustrated in Figure 4 to view the energy and charge transfer process (denoted as  $E_{CT}$ ) that occurs in these co-crystals. In general, this process has a profound impact on its functional properties of these model systems. Particularly the electronic excitation and natural bond orbital (NBO) analysis was performed using TDDFT theoretical level and hence can be used to measure  $E_{CT}$ . Thus, in this perspective, the stabilisation energy ( $E_2$ )



associated with the delocalisation of electrons between the electron donor NBO ( $i$ ) and the electron acceptor NBO ( $j$ ) is evaluated according to the following equation.<sup>[38,39]</sup>

$$E_2 = \Delta E(ij) = q_i \frac{(F(i,j))^2}{\varepsilon_j - \varepsilon_i} = q_i \frac{F_{ij}^2}{\Delta\varepsilon} \quad (4)$$

where  $q_i$  represents the orbital occupancy,  $\varepsilon_i$  and  $\varepsilon_j$  are diagonal elements (i.e., orbital energies), and  $F_{ij}$  is the off-diagonal NBO Fock matrix element. From these calculations, we have calculated the  $E_{CT}$  for these co-crystals, as shown in Table 2. As expected, the HQ-based co-crystals have higher values of  $E_{CT}$  than their CQ counterparts. Consequently, in this case, we identify that the  $E_{CT}$  process is slower and hence can more easily induce symmetric structural polarization. For the CQ-based co-crystals, this result suggesting a fast  $E_{CT}$  process that can more likely induce an asymmetric structural polarization.

**Table 2.** Comparison of dipole moment, HOMO-LUMO energy gap, exciton binding energy, hardness, softness, electronegativity and electrophilicity values for the computed co-crystals at the TDDFT theoretical level.

Co-crystal	$E_g$ (eV)	$E_B$ (eV)	$E_{CT}$	$\mu$ (D)	$\eta$ (eV)	$S$ (eV <sup>-1</sup> )	$x$ (eV)	$\omega$
CQ/AZ	1.22	0.26	0.009	-1.03	0.61	0.82	1.03	0.43
CQ/ER	1.26	0.07	0.141	-1.02	0.63	0.79	1.02	0.44
CQ/CL	1.46	0.47	0.337	-0.94	0.73	0.68	0.94	0.52
HQ/AZ	1.44	0.26	0.019	-1.10	0.72	0.69	1.10	0.46
HQ/ER	1.44	0.26	0.632	-1.13	0.72	0.70	1.14	0.45
HQ/CL	1.45	0.28	0.350	-1.12	0.73	0.69	1.12	0.46

According to the above co-crystal structure analysis, the molecular docking calculations were performed to adjust the ligands in the  $M^{pro}$  active cavity, evaluating the affinity among them. For this study, a cavity prediction algorithm based on a 3D box was employed in order to generate the binding sites. Thus, the volume of the calculated active cavity was approximately 130.56 Å<sup>3</sup>.

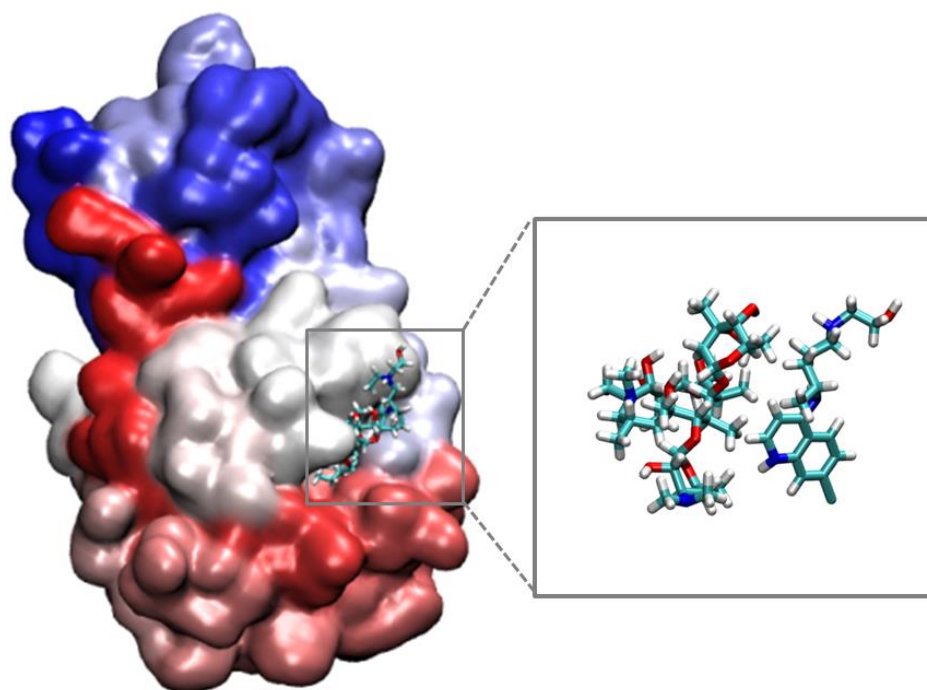
In order to understand the interaction modes of these single- and co-crystals within the SARS-CoV-2 M<sup>pro</sup> active site, in particular, some parameters that contribute to affinity were investigated. Table 3 shows the intermolecular interaction energy values and theoretical toxicity prediction for the ligands under study.

**Table 3.** Values of the parameters obtained by molecular docking calculations for the single- and co-crystals within the SARS-COV-2 M<sup>pro</sup> active site through MVD® software and toxicity prediction through ADMET.

Co-crystal	Interaction Energy (kcal mol <sup>-1</sup> )	Toxicity (LD <sub>50</sub> )
AZ	-213.2	2.54 mol kg <sup>-1</sup>
CL	-205.0	2.72 mol kg <sup>-1</sup>
CQ/AZ	-275.3	2.74 mol kg <sup>-1</sup>
CQ/CL	-240.9	2.75 mol kg <sup>-1</sup>
CQ	-141.7	2.95 mol kg <sup>-1</sup>
CQ/ER	-229.8	2.75 mol kg <sup>-1</sup>
ER	-213.1	2.23 mol kg <sup>-1</sup>
HQ/AZ	-280.7	2.74 mol kg <sup>-1</sup>
HQ/CL	-259.6	2.75 mol kg <sup>-1</sup>
HQ	-162.6	2.63 mol kg <sup>-1</sup>
HQ/ER	-275.7	2.75 mol kg <sup>-1</sup>

As shown in Table 3, all the single- and co-crystals studied interacted very well with M<sup>pro</sup> active site, with interaction energy values in the range of -141.7 to -280.7 kcal mol<sup>-1</sup>. We can also observe that the co-crystal formed by unities of HQ and AZ showed the most stabilizing interaction energy (-280.7 kcal mol<sup>-1</sup>), followed by the co-crystals HQ/ER (-275.7 kcal mol<sup>-1</sup>) and also CQ/AZ (-275.3 kcal mol<sup>-1</sup>). The conformation of HQ/AZ in the M<sup>pro</sup> active cavity is

shown in Figure 5. Note that, the single-crystals of CQ and HQ revealed interaction energies of approximately  $-141.7$  and  $-162.6$  kcal mol<sup>-1</sup>, respectively. Yet, when combined with AZ, these single-crystals gain stability and lower interaction energies. In fact, the single-crystal of AZ is much more stabilized than those of CQ and HQ when docked in the active site, and their combination with AZ leads to increased affinity toward the viral enzyme. Regarding the co-crystals formed by the combination with AZ, we have the following energy differences: HQ to HQ/AZ ( $118.1$  kcal mol<sup>-1</sup>) and CQ to CQ/AZ ( $133.6$  kcal mol<sup>-1</sup>). Based on our computations, CQ/AZ was the co-crystal that showed the more significant energy difference, followed by HQ/AZ, suggesting the suitability of combining AZ with CQ and HQ, thus boosting their therapeutic effects.

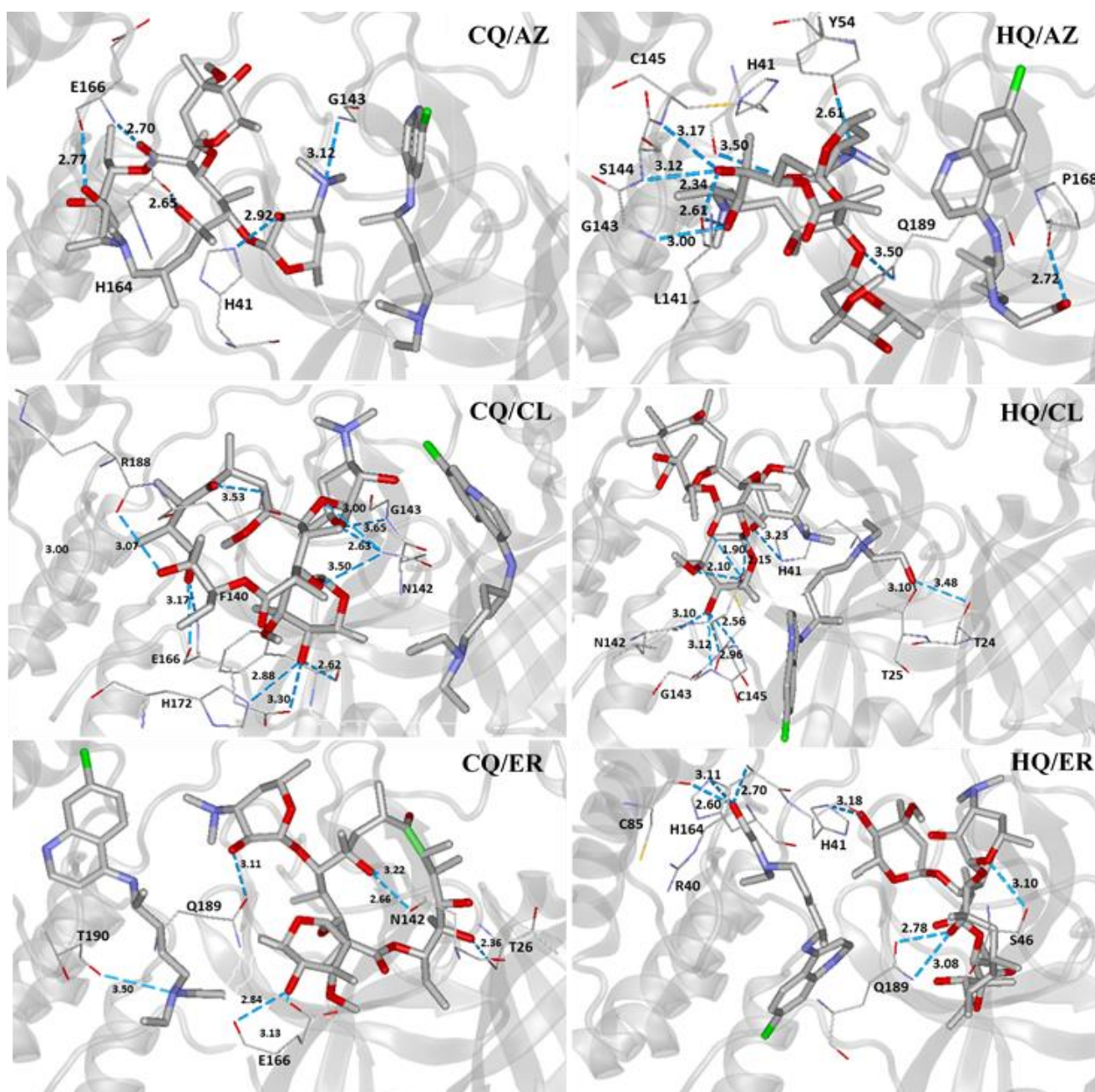


**Figure 5.** Representation of the conformation of the most stabilizing HQ/AZ in the M<sup>Pro</sup> active site.

According to Table 3, note that the combination of HQ with ER also led to quite stabilizing interaction energies, from  $-162.6$  kcal mol<sup>-1</sup> for HQ to  $-275.7$  kcal mol<sup>-1</sup> for HQ/ER. This trend is also observed for CQ, in which its interaction energy was stabilized by  $88.1$  kcal mol<sup>-1</sup> when combined with ER. Interestingly, the formation of the co-crystal HQ/ER was much more significant in energetic terms, due to the larger energy difference between single-crystal and co-crystal, of  $113.1$  kcal mol<sup>-1</sup>. In addition, with respect to the co-crystals formed by the

combination with CL, we have the following energy differences: HQ to HQ/CL ( $97.0 \text{ kcal mol}^{-1}$ ) and CQ to CQ/CL ( $99.2 \text{ kcal mol}^{-1}$ ). In general terms, all macrolide antibiotics led to the formation of low energy co-crystals and, therefore, support that such co-crystals can be easily obtained experimentally.

With respect to the interactions observed in the molecular docking, we observe that most compounds (single- and co-crystals) interacted with important residues in the site, such as the residues H41, C145, and E166. In the active site, H41 and C145 constitute the dyad catalytic of  $M^{\text{Pro}}$ , being key residues for the enzyme's inhibition process. Furthermore, E166 is also an important species for keeping the active conformation of the enzyme.<sup>[3,40,41]</sup> As a result, the interactions of all compounds investigated can be visualized in Figure S1 and Figure 6.



**Figure 6.** Intermolecular interactions of the co-crystals in the viral  $M^{\text{pro}}$  active site. E: glutamate, G: glycine, H: histidine, C: cysteine, S: serine, Y: tyrosine, L: leucine, Q: glutamine, P: proline, R: arginine, N: asparagine, F: phenylalanine, T: threonine.

Usually, the efficacy of a drug can be attributed to many factors. Along this line, the absorption-distribution-metabolism-excretion-toxicity (ADMET) evaluations involve sequential and iterative assessments of the efficacy, pharmacokinetics, pharmacodynamics, metabolic and toxicological properties in the model of therapeutic agents, and hence

contributing to design safer and more efficient drugs.<sup>[42]</sup> The ADMET analysis was carried out in order to evaluate the toxicity of our compounds, single- and co-crystals, under investigation. According to our results in Table 3, the LD<sub>50</sub> value found for ER, 2.23 mol.kg<sup>-1</sup>, indicates more toxicity in relation to other single- and co-crystal compounds. However, we can observe that its combination with CQ and HQ leads to co-crystals of lower toxicity, as well as more stabilizing interaction energies, making these efficient species candidates for the COVID-19 treatment. In addition, when using CL combined with CQ and HQ, there was a slightly decreased toxicity and significant interactions of lower energies in the M<sup>PRO</sup> active site. The most remarkable results were found for the co-crystals formed by the combination with AZ. The data reinforce our previous findings, which indicate that the co-crystals of CQ and HQ combined with AZ significantly improved the affinity and decreased toxicity, thus making them more potent therapeutic agents against SARS-CoV-2.

#### 4. CONCLUSIONS

In summary, our theoretical findings are of large importance and provided a new molecular perspective about the effectiveness and toxicity of co-crystals formed between (hydroxy)chloroquine with the macrolide antibiotics for the treatment of SARS-CoV-2 infection. Our findings also enable a new interpretation in-depth for the intramolecular energy and charge transfer process in these co-crystals, which is critical to the rationalization of their functional properties, it provides an innovative way to connects structural changes with electronic transfer kinetics. Overall, the co-crystals of CQ and HQ combined with AZ significantly improved the affinity and decreased toxicity, making them more potent therapeutic agents against SARS-CoV-2. Yet, it must be emphasized that this therapeutic option potential benefits can only be determined in the practice from rigorous clinical studies.

#### ACKNOWLEDGMENTS

The authors gratefully acknowledge the support from the Brazilian agencies CNPq, CAPES and FAPEMIG. We also especially grateful to the computational facilities at UFPA. It was supported by the Excellence project UHK.

## Compliance with ethical standards

**Reviewer disclosures:** Peer reviewers on this manuscript have no relevant financial or other relationships to disclose.

**Conflict of interest:** The authors declare that they have no conflict of interest.

## REFERENCES

- [1] L. C. Assis, A. A. de Castro, J. P. A. de Jesus, E. Nepovimova, K. Kuca, T. de C. Ramalho, F. de A. La Porta, **2020**, DOI 10.21203/rs.3.rs-32468/v1.
- [2] Y. M. Arabi, S. Murthy, S. Webb, *Intensive Care Med.* **2020**, DOI 10.1007/s00134-020-05955-1.
- [3] L. Zhang, D. Lin, X. Sun, U. Curth, C. Drosten, L. Sauerhering, S. Becker, K. Rox, R. Hilgenfeld, *Science* **2020**, *3405*, 1–9.
- [4] L. Dong, S. Hu, J. Gao, *Drug Discov. Ther.* **2020**, *14*, 58–60.
- [5] M. D. L. de Oliveira, K. M. T. de Oliveira, **2020**, DOI 10.26434/chemrxiv.12044538.v3.
- [6] A. Savarino, L. Di Trani, I. Donatelli, R. Cauda, A. Cassone, *Lancet Infect. Dis.* **2006**, *6*, 67–69.
- [7] M. Wang, R. Cao, L. Zhang, X. Yang, J. Liu, M. Xu, Z. Shi, Z. Hu, W. Zhong, G. Xiao, *Cell Res.* **2020**, *30*, 269–271.
- [8] E. S. Rosenberg, E. M. Dufort, T. Udo, L. A. Wilberschied, J. Kumar, J. Tesoriero, P. Weinberg, J. Kirkwood, A. Muse, J. DeHovitz, D. S. Blog, B. Hutton, D. R. Holtgrave, H. A. Zucker, *JAMA* **2020**, DOI 10.1001/jama.2020.8630.
- [9] N. Fintelman-Rodrigues, C. Q. Sacramento, C. R. Lima, F. S. da Silva, A. C. Ferreira, M. Mattos, C. S. de Freitas, V. C. Soares, S. da S. Gomes Dias, J. R. Temerozo, M. Miranda, A. R. Matos, F. A. Bozza, N. Carels, C. R. Alves, M. M. Siqueira, P. T. Bozza, T. M. L. Souza, *bioRxiv* **2020**, 2020.04.04.020925.
- [10] J. Geleris, Y. Sun, J. Platt, J. Zucker, M. Baldwin, G. Hripcsak, A. Labella, D. K. Manson, C. Kubin, R. G. Barr, M. E. Sobieszczyk, N. W. Schluger, *N. Engl. J. Med.* **2020**, *382*, 2411–2418.
- [11] I. F.-N. Hung, K.-C. Lung, E. Y.-K. Tso, R. Liu, T. W.-H. Chung, M.-Y. Chu, Y.-Y. Ng, J. Lo, J. Chan, A. R. Tam, H.-P. Shum, V. Chan, A. K.-L. Wu, K.-M. Sin, W.-S.

- Leung, W.-L. Law, D. C. Lung, S. Sin, P. Yeung, C. C.-Y. Yip, R. R. Zhang, A. Y.-F. Fung, E. Y.-W. Yan, K.-H. Leung, J. D. Ip, A. W.-H. Chu, W.-M. Chan, A. C.-K. Ng, R. Lee, K. Fung, A. Yeung, T.-C. Wu, J. W.-M. Chan, W.-W. Yan, W.-M. Chan, J. F.-W. Chan, A. K.-W. Lie, O. T.-Y. Tsang, V. C.-C. Cheng, T.-L. Que, C.-S. Lau, K.-H. Chan, K. K.-W. To, K.-Y. Yuen, *Lancet* **2020**, 395, 1695–1704.
- [12] V. J. Nikam, S. B. Patil, *J. Cryst. Growth* **2020**, 534, 125488.
- [13] J. W. Steed, *Trends Pharmacol. Sci.* **2013**, 34, 185–193.
- [14] M. Karimi-Jafari, L. Padrela, G. M. Walker, D. M. Croker, *Cryst. Growth Des.* **2018**, 18, 6370–6387.
- [15] C. Maheshwari, A. Jayasankar, N. A. Khan, G. E. Amidon, N. Rodríguez-Hornedo, *CrystEngComm* **2009**, 11, 493–500.
- [16] T. Leyssens, N. Tumanova, K. Robeyns, N. Candoni, S. Veessler, *CrystEngComm* **2014**, 16, 9603–9611.
- [17] J. A. Baird, B. Van Eerdenbrugh, L. S. Taylor, *J. Pharm. Sci.* **2010**, 99, 3787–3806.
- [18] N. K. Duggirala, M. L. Perry, Ö. Almarsson, M. J. Zaworotko, *Chem. Commun.* **2016**, 52, 640–655.
- [19] B. Arsic, A. Awan, R. J. Brennan, J. A. Aguilar, R. Ledder, A. J. McBain, A. C. Regan, J. Barber, *Med. Chem. Commun.* **2014**, 5, 1347–1354.
- [20] H. A. Kirst, in (Eds.: W. Schönfeld, H.A. Kirst), Birkhäuser Basel, Basel, **2002**, pp. 1–13.
- [21] J. M. McGUIRE, R. L. BUNCH, R. C. ANDERSON, H. E. BOAZ, E. H. FLYNN, H. M. POWELL, J. W. SMITH, *Antibiot. Chemother. (Northfield, Ill.)* **1952**, 2, 281–283.
- [22] R. M. Chico, R. Pittrof, B. Greenwood, D. Chandramohan, *Malar. J.* **2008**, 7, 255.
- [23] F. H. Allen, *Acta Crystallogr. Sect. B* **2002**, 58, 380–388.
- [24] M. J. Frisch, G. W. Trucks, H. B. Schlegel, G. E. Scuseria, M. Robb, J. Cheeseman, G. Scalmani, V. Barone, B. Mennucci, G. A. H. Petersson, H. Nakatsuji, M. Caricato, X. Li, H. P. Hratchian, A. F. Izmaylov, J. Bloino, G. Zheng, J. L. Sonnenberg, M. Hada, D. Fox, *Gaussian 09 (Revision A02)*, **2009**.
- [25] Z. Jin, X. Du, Y. Xu, Y. Deng, M. Liu, Y. Zhao, B. Zhang, X. Li, L. Zhang, C. Peng, Y. Duan, J. Yu, L. Wang, K. Yang, F. Liu, R. Jiang, X. Yang, T. You, X. Liu, X. Yang, F. Bai, H. Liu, X. Liu, L. W. Guddat, W. Xu, G. Xiao, C. Qin, Z. Shi, H. Jiang, Z. Rao, H. Yang, *Nature* **2020**, 582, 289–293.
- [26] R. Thomsen, M. H. Christensen, *J. Med. Chem.* **2006**, 49, 3315–3321.
- [27] T. C. Silva, M. dos S. Pires, A. A. de Castro, E. F. F. da Cunha, M. S. Caetano, T. C.



- Ramalho, *Med. Chem. Res.* **2015**, *24*, 3958–3971.
- [28] A. P. Guimaraes, A. A. Oliveira, E. F. F. da Cunha, T. C. Ramalho, T. C. C. Franco, *J. Mol. Model.* **2011**, *17*, 2939–2951.
- [29] K. S. Matos, D. T. Mancini, E. F. F. da Cunha, K. Kuca, T. C. C. Franca, T. C. Ramalho, *J. Braz. Chem. Soc.* **2011**, *22*, 1999–2004.
- [30] E. F. F. da Cunha, E. F. Barbosa, A. A. Oliveira, T. C. Ramalho, *J. Biomol. Struct. Dyn.* **2010**, *27*, 619–625.
- [31] T. C. S. Souza, D. Josa, T. C. Ramalho, M. S. Caetano, E. F. F. da Cunha, *Mol. Simul.* **2008**, *34*, 707–713.
- [32] R. F. Fernandes, P. H. F. Stroppa, G. R. Ferreira, A. D. da Silva, H. G. M. Edwards, L. F. C. de Oliveira, *Vib. Spectrosc.* **2016**, *86*, 128–133.
- [33] E. Adeli, *Brazilian J. Pharm. Sci.* **2016**, *52*, 1–13.
- [34] S. Dey, in *Emerging Res. Sci. Eng. Based Adv. Exp. Comput. Strateg. Eng. Mater.* (Eds.: F.A. LA PORTA, C.A. Taft), Springer, Cham, **2020**.
- [35] F. A. La Porta, T. C. Ramalho, R. T. Santiago, M. V. J. Rocha, E. F. F. da Cunha, *J. Phys. Chem. A* **2011**, *115*, 824–833.
- [36] R. R. da Silva, T. C. Ramalho, J. M. Santos, J. D. Figueroa-Villar, *J. Phys. Chem. A* **2006**, *110*, 1031–1040.
- [37] K. Fukui, T. Yonezawa, H. Shingu, *J. Chem. Phys.* **1952**, *20*, 722–725.
- [38] J. E. Carpenter, F. Weinhold, *J. Mol. Struct. THEOCHEM* **1988**, *169*, 41–62.
- [39] A. E. Reed, L. A. Curtiss, F. Weinhold, *Chem. Rev.* **1988**, *88*, 899–926.
- [40] S. Yang, S. J. Chen, M. F. Hsu, J. D. Wu, C. T. K. Tseng, Y. F. Liu, H. C. Chen, C. W. Kuo, C. S. Wu, L. W. Chang, W. C. Chen, S. Y. Liao, T. Y. Chang, H. H. Hung, H. L. Shr, C. Y. Liu, Y. A. Huang, L. Y. Chang, J. C. Hsu, C. J. Peters, A. H. J. Wang, M. C. Hsu, *J. Med. Chem.* **2006**, *49*, 4971–4980.
- [41] L. Zhou, Y. Liu, W. Zhang, P. Wei, C. Huang, J. Pei, Y. Yuan, L. Lai, *J. Med. Chem.* **2006**, *49*, 3440–3443.
- [42] G. Cardoso Gajo, D. Rodrigues Silva, S. J. Barigye, E. F. F. da Cunha, *Mol. Inform.* **2018**, *37*, DOI 10.1002/minf.201700080.

## **SUPPLEMENTARY MATERIAL**

*New in silico insights into the application of the (hydroxy)chloroquine with macrolide antibiotics co-crystals against the SARS-CoV-2 virus*

**Table S1.** Cartesian coordinates (in Å) for co-crystals computed at PM6.

Co-crystal CQ/AZ			
O	6.26250000	-1.23120000	-0.99040000
O	4.49360000	-2.62720000	-0.78790000
O	5.47030000	-2.61420000	2.28260000
H	4.94010000	-3.06690000	1.58250000
O	8.02220000	-2.04270000	2.11070000
H	7.49580000	-2.74000000	2.59080000
O	1.86860000	-0.71780000	-2.22610000
O	1.26480000	3.22180000	-0.77910000
O	1.56710000	0.05640000	0.94640000
H	0.85250000	-0.49360000	0.53230000
O	0.90640000	6.13430000	-2.38820000
H	0.91080000	7.07890000	-2.10510000
O	-0.55570000	3.15800000	-2.24820000
O	-0.71140000	-1.58510000	-4.42280000
O	-2.66510000	-1.88070000	-2.77860000
H	-2.47380000	-1.29880000	-3.57530000
O	0.42970000	-1.84530000	-0.80720000
N	4.09690000	0.09460000	3.02630000
N	-1.18970000	6.77760000	0.05020000
C	4.97350000	-1.60810000	-1.24120000
C	4.31740000	-0.54420000	-2.10490000
H	4.99540000	0.35330000	-2.12430000
C	2.95910000	-0.12130000	-1.47330000
H	2.89700000	-0.47540000	-0.40520000
C	2.73230000	1.40850000	-1.51840000
H	3.57250000	1.89280000	-0.95520000
C	1.41030000	1.78270000	-0.79670000
H	0.54390000	1.32510000	-1.32190000
C	1.36560000	1.46590000	0.75060000
C	2.54230000	2.12570000	1.49230000
H	2.58990000	3.19010000	1.18870000
H	3.47880000	1.65290000	1.12440000
C	2.48600000	1.98780000	3.02800000
H	1.67540000	1.25740000	3.28690000
C	3.81840000	1.44020000	3.61200000
H	4.65050000	2.12630000	3.34960000
H	3.75700000	1.42420000	4.72090000
C	5.52640000	-0.32890000	3.11840000
H	6.16300000	0.58910000	2.96200000
C	5.72070000	-1.24910000	1.87870000
H	4.97600000	-0.95200000	1.10320000
C	7.15330000	-1.27730000	1.26540000
C	7.09960000	-2.05400000	-0.09500000
H	6.61510000	-3.04610000	0.04250000
C	3.12900000	-0.93340000	3.49870000
H	3.48320000	-1.94460000	3.23880000
H	2.18140000	-0.76550000	2.94480000
H	2.92670000	-0.91010000	4.57750000
C	4.20240000	-1.09290000	-3.52540000
H	3.58440000	-0.42820000	-4.14530000
H	3.72060000	-2.07900000	-3.54470000
H	5.18610000	-1.18480000	-4.00080000
C	5.96510000	-1.00100000	4.41820000
H	5.70000000	-0.40010000	5.29220000
H	7.05050000	-1.16170000	4.42560000
H	5.49640000	-1.98860000	4.53550000
C	7.79700000	0.09270000	1.12280000
H	7.60220000	0.72650000	2.00080000
H	7.42870000	0.61520000	0.23140000
H	8.88910000	-0.00220000	1.04360000
C	8.44830000	-2.16590000	-0.79760000
H	9.23040000	-2.34590000	-0.02530000

H	8.70090000	-1.19630000	-1.27400000
C	8.46690000	-3.27940000	-1.83860000
H	9.43210000	-3.31680000	-2.35720000
H	7.69010000	-3.13080000	-2.59820000
H	8.30270000	-4.26420000	-1.38520000
C	2.76060000	1.92220000	-2.95830000
H	2.59750000	3.01110000	-3.00140000
H	1.98180000	1.44360000	-3.56440000
H	3.72520000	1.73120000	-3.43980000
C	-0.01120000	1.84530000	1.29460000
H	-0.81820000	1.25530000	0.82570000
H	-0.22800000	2.91150000	1.10330000
H	-0.07400000	1.67300000	2.37660000
C	2.16020000	3.33010000	3.69560000
H	2.03850000	3.22120000	4.77860000
H	1.22360000	3.74330000	3.30420000
H	2.94390000	4.07470000	3.52390000
C	0.58860000	3.87780000	-1.87010000
H	1.22700000	3.83910000	-2.78860000
C	0.42190000	5.30890000	-1.31030000
H	1.10360000	5.43700000	-0.43350000
C	-1.03980000	5.68820000	-0.96000000
H	-1.53480000	6.05850000	-1.90170000
C	-1.76260000	4.41790000	-0.48530000
H	-2.77360000	4.66520000	-0.09520000
H	-1.22130000	3.95060000	0.37120000
C	-1.86210000	3.43630000	-1.64890000
H	-2.42520000	3.87570000	-2.50670000
C	-2.43070000	2.08330000	-1.25780000
H	-2.43490000	1.39550000	-2.10930000
H	-3.46220000	2.18170000	-0.88720000
H	-1.84420000	1.61120000	-0.45310000
C	-0.72810000	8.08560000	-0.50220000
H	-1.42240000	8.38930000	-1.30480000
H	0.29880000	8.08480000	-0.90790000
H	-0.78850000	8.86070000	0.27870000
C	-0.52630000	6.48440000	1.35230000
H	-0.97900000	5.57830000	1.79000000
H	-0.73400000	7.30850000	2.05440000
H	0.56280000	6.33720000	1.29970000
C	1.45310000	-2.01860000	-1.78250000
H	2.25330000	-2.53510000	-1.19700000
C	1.00790000	-2.78050000	-3.03380000
H	1.23920000	-3.85500000	-2.86960000
H	1.65610000	-2.47090000	-3.88600000
C	-0.45630000	-2.64190000	-3.45950000
C	-1.41600000	-2.36970000	-2.26270000
H	-1.68190000	-3.30950000	-1.73390000
C	-0.84120000	-1.32530000	-1.28030000
H	-0.64460000	-0.35230000	-1.80200000
C	-0.92220000	-3.87030000	-4.24930000
H	-0.32010000	-3.99890000	-5.15890000
H	-1.96170000	-3.74430000	-4.58040000
H	-0.85760000	-4.79010000	-3.66170000
C	0.00080000	-0.33940000	-4.28490000
H	-0.42570000	0.26980000	-5.08870000
H	1.07600000	-0.49720000	-4.42960000
H	-0.17700000	0.11100000	-3.29530000
C	-1.67290000	-1.15050000	-0.03040000
H	-1.24710000	-0.39290000	0.65100000
H	-1.75850000	-2.07610000	0.57340000
H	-2.70290000	-0.82490000	-0.26780000
Cl	-5.18370000	3.48380000	0.85650000
N	-3.69690000	-2.69190000	3.33790000
H	-3.53790000	-2.67710000	4.35300000
N	-7.46770000	-0.91110000	2.22320000
H	-8.26060000	-0.32780000	2.52290000

N	-5.80000000	-2.83480000	-1.41910000
H	-6.62550000	-3.42300000	-1.14260000
C	-4.97070000	-0.74720000	2.54200000
C	-4.97160000	-2.05700000	3.05670000
C	-3.59050000	-4.10430000	2.83500000
H	-4.50610000	-4.70910000	3.06520000
C	-4.72350000	-3.94230000	0.56240000
H	-5.29670000	-4.88330000	0.63510000
H	-5.32700000	-3.16830000	1.11720000
C	-5.99480000	-1.45980000	-0.76060000
H	-7.05610000	-1.15100000	-0.88600000
C	-6.22490000	-2.67440000	3.38850000
H	-6.20620000	-3.61300000	3.93840000
C	-7.40580000	-2.11610000	3.03120000
H	-8.37170000	-2.53780000	3.27550000
C	-4.53290000	-3.51750000	-0.89220000
H	-3.68120000	-2.79300000	-0.98900000
H	-4.28260000	-4.38650000	-1.53480000
C	-3.80380000	0.03620000	2.35090000
H	-2.85040000	-0.39250000	2.64520000
C	-5.09900000	1.87310000	1.51530000
C	-6.24200000	-0.13070000	2.18380000
C	-3.38460000	-4.08070000	1.29660000
H	-2.85820000	-4.99250000	0.96810000
H	-2.71320000	-3.22030000	1.05560000
C	-6.30320000	1.16410000	1.69850000
H	-7.24860000	1.64140000	1.45940000
C	-5.04840000	-0.39750000	-1.26640000
H	-5.12360000	0.49440000	-0.60480000
H	-3.98460000	-0.70810000	-1.21690000
C	-3.86600000	1.33770000	1.85340000
H	-2.95910000	1.92750000	1.74710000
C	-5.75010000	-2.76960000	-2.94410000
H	-5.51230000	-3.78450000	-3.33820000
H	-4.89150000	-2.11400000	-3.24710000
C	-2.38450000	-4.77460000	3.51340000
H	-2.52300000	-4.84610000	4.59770000
H	-1.46490000	-4.19890000	3.34530000
H	-2.22050000	-5.78760000	3.13670000
C	-7.06040000	-2.26870000	-3.52220000
H	-7.01900000	-2.26780000	-4.62320000
H	-7.28650000	-1.23320000	-3.22500000
H	-7.92230000	-2.88800000	-3.24270000
H	-5.26110000	-0.05890000	-2.28360000
H	-5.96042880	-2.39417720	-1.30111629
H	-5.93451473	-1.65495708	0.29990903

---

**Co-crystal CQ/CL**


---

O	5.14400000	-2.10000000	-1.46080000
O	3.39030000	-2.98090000	-2.60270000
O	3.69710000	-3.24630000	1.29790000
H	2.86240000	-2.88790000	1.68270000
O	6.43050000	-4.07670000	1.29250000
H	5.67500000	-4.58600000	1.68310000
O	1.52160000	0.11150000	-2.74300000
O	1.69990000	3.28440000	-0.35990000
O	2.44500000	0.06780000	1.16400000
O	0.79930000	6.00540000	-2.25180000
H	0.97910000	6.96440000	-2.19000000
O	-0.50150000	3.29990000	-1.12420000
O	-1.50210000	0.94980000	-4.51140000
O	-3.29880000	0.11690000	-2.83160000
H	-3.08640000	0.99430000	-3.27160000
O	-0.06630000	-1.23480000	-1.73200000
N	0.39100000	6.99570000	0.97520000
C	4.07300000	-2.02770000	-2.30010000

C	3.89810000	-0.57220000	-2.71380000
H	4.82880000	-0.01280000	-2.42320000
C	2.70320000	0.01280000	-1.90920000
H	2.46510000	-0.65450000	-1.04270000
C	2.98520000	1.43790000	-1.38240000
H	3.94090000	1.37780000	-0.78350000
C	1.84260000	1.84470000	-0.41340000
H	0.87400000	1.39790000	-0.73720000
C	2.15330000	1.48850000	1.08580000
C	3.47910000	2.14100000	1.53240000
H	3.34280000	3.24170000	1.47650000
H	4.27600000	1.91360000	0.78460000
C	3.95640000	1.72400000	2.93130000
H	3.06600000	1.49100000	3.56690000
C	4.84960000	0.48060000	2.80080000
C	5.08310000	-2.04080000	2.94120000
H	6.18600000	-1.83140000	3.01640000
C	4.75660000	-2.27310000	1.44210000
H	4.42780000	-1.33070000	0.93940000
C	5.93770000	-2.89480000	0.63620000
C	5.44020000	-3.36980000	-0.76850000
H	4.49120000	-3.94880000	-0.67840000
C	4.49890000	-0.61770000	4.98640000
H	4.02190000	-1.43930000	5.53550000
H	4.04050000	0.31110000	5.34490000
H	5.55690000	-0.60320000	5.27750000
C	3.72960000	-0.49290000	-4.22720000
H	3.28000000	0.46690000	-4.51740000
H	3.06610000	-1.28260000	-4.60550000
H	4.69070000	-0.59240000	-4.74430000
C	4.77560000	-3.29320000	3.76420000
H	5.23300000	-3.24560000	4.75800000
H	5.17900000	-4.18920000	3.26440000
H	3.70030000	-3.45450000	3.89110000
C	7.12540000	-1.94800000	0.55230000
H	7.16530000	-1.24780000	1.40420000
H	7.08630000	-1.33470000	-0.35750000
H	8.06740000	-2.51230000	0.55060000
C	6.50600000	-4.10650000	-1.57430000
H	7.15450000	-4.67820000	-0.87240000
H	7.17110000	-3.36890000	-2.06660000
C	5.89670000	-5.04570000	-2.60860000
H	6.65960000	-5.43840000	-3.28830000
H	5.13420000	-4.53620000	-3.21580000
H	5.40300000	-5.90250000	-2.13480000
C	3.21120000	2.44200000	-2.50750000
H	3.39060000	3.44740000	-2.10290000
H	2.34370000	2.49110000	-3.17970000
H	4.08260000	2.17550000	-3.11590000
C	0.98610000	1.89620000	1.97570000
H	0.02420000	1.47570000	1.63900000
H	0.85640000	2.99580000	1.94890000
H	1.14220000	1.59610000	3.01750000
C	4.76780000	2.83330000	3.60360000
H	5.09960000	2.53980000	4.60620000
H	4.18200000	3.75280000	3.70630000
H	5.66960000	3.07340000	3.02180000
C	0.76970000	3.88470000	-1.28310000
H	1.02540000	3.63020000	-2.33740000
C	0.93600000	5.38690000	-0.95730000
H	1.97720000	5.55930000	-0.59060000
C	-0.11820000	5.96250000	0.02490000
H	-0.91890000	6.46220000	-0.59080000
C	-0.76060000	4.80800000	0.81270000
H	-1.47950000	5.20500000	1.55700000
H	0.01030000	4.25300000	1.40040000
C	-1.45340000	3.85830000	-0.16110000

H	-2.18080000	4.39850000	-0.81170000
C	-2.09540000	2.65630000	0.50470000
H	-2.60560000	2.02140000	-0.22920000
H	-2.83730000	2.95530000	1.25940000
H	-1.35030000	2.02050000	1.01180000
C	0.77660000	8.25100000	0.26500000
H	-0.07720000	8.61460000	-0.32910000
H	1.65830000	8.16900000	-0.38620000
H	0.98560000	9.02880000	1.02030000
C	1.51170000	6.51840000	1.83510000
H	1.16760000	5.65870000	2.43400000
H	1.78120000	7.31560000	2.54700000
H	2.41990000	6.21620000	1.29130000
C	0.76390000	-1.10670000	-2.87570000
H	1.41770000	-2.01060000	-2.78670000
C	0.04890000	-0.99640000	-4.22320000
H	0.07200000	-2.00060000	-4.69800000
H	0.66250000	-0.34920000	-4.89430000
C	-1.38770000	-0.46720000	-4.22380000
C	-2.12250000	-0.70840000	-2.87380000
H	-2.51230000	-1.74730000	-2.80970000
C	-1.23640000	-0.38090000	-1.65030000
H	-0.89620000	0.68740000	-1.66670000
C	-2.19630000	-1.05900000	-5.38490000
H	-1.74690000	-0.78430000	-6.34880000
H	-3.21630000	-0.65240000	-5.39080000
H	-2.25890000	-2.14910000	-5.33300000
C	-0.56640000	1.85570000	-3.89320000
H	-0.84050000	2.81860000	-4.33800000
H	0.46670000	1.58130000	-4.13790000
H	-0.70550000	1.86760000	-2.79840000
C	-1.89360000	-0.76010000	-0.34040000
H	-1.29120000	-0.46580000	0.52770000
H	-2.05310000	-1.85330000	-0.23900000
H	-2.88090000	-0.27660000	-0.22730000
Cl	-4.56990000	2.68450000	3.34270000
N	-3.58660000	-3.94570000	2.06810000
H	-3.31190000	-4.54130000	2.85870000
N	-7.19200000	-1.70080000	2.83610000
H	-7.83090000	-1.33280000	3.55370000
N	-6.34660000	-1.24510000	-1.52000000
H	-7.19840000	-1.84890000	-1.40080000
C	-4.67790000	-1.82170000	2.65390000
C	-4.78000000	-3.20510000	2.43320000
C	-3.75970000	-4.79550000	0.83890000
H	-4.71200000	-5.38660000	0.86250000
C	-5.17070000	-3.29720000	-0.66100000
H	-5.86720000	-4.09620000	-0.97180000
H	-5.55620000	-2.92250000	0.32840000
C	-6.22430000	-0.39430000	-0.24600000
H	-5.91550000	-1.09170000	0.59270000
H	-7.23590000	-0.02330000	0.03120000
C	-6.04210000	-3.85820000	2.65280000
H	-6.06910000	-4.94520000	2.62780000
C	-7.17260000	-3.15130000	2.88530000
H	-8.13880000	-3.60160000	3.07280000
C	-5.13210000	-2.16450000	-1.68480000
H	-4.20530000	-1.54380000	-1.56020000
H	-5.10510000	-2.56440000	-2.71990000
C	-3.45870000	-1.09430000	2.62750000
H	-2.54230000	-1.65120000	2.46060000
C	-4.60240000	0.95920000	3.09910000
C	-5.89100000	-1.06010000	2.92810000
C	-3.77390000	-3.88030000	-0.41400000
H	-3.42940000	-4.44150000	-1.29900000
H	-3.03220000	-3.06020000	-0.24730000
C	-5.84720000	0.30180000	3.16870000

H	-6.74150000	0.86980000	3.40630000
C	-5.23430000	0.74070000	-0.35860000
H	-5.05960000	1.16950000	0.65340000
H	-4.23740000	0.40660000	-0.71390000
C	-3.41860000	0.28040000	2.85390000
H	-2.46960000	0.80890000	2.84840000
C	-6.52620000	-0.40830000	-2.78540000
H	-6.51400000	-1.08840000	-3.66830000
H	-5.63350000	0.26180000	-2.90240000
C	-2.58090000	-5.77890000	0.75600000
H	-2.56870000	-6.46410000	1.61050000
H	-1.62040000	-5.24750000	0.75660000
H	-2.62610000	-6.38760000	-0.15100000
C	-7.81700000	0.38800000	-2.74750000
H	-7.94820000	0.95100000	-3.68560000
H	-7.83120000	1.13520000	-1.93940000
H	-8.71000000	-0.23970000	-2.63270000
H	-5.56890000	1.56180000	-0.99800000
O	5.90330000	0.51730000	2.20320000
C	4.33350000	-0.79430000	3.47490000
H	3.24420000	-0.89470000	3.23130000
C	1.33490000	-0.84950000	1.18350000
H	0.72610000	-0.75040000	0.27220000
H	1.83400000	-1.83310000	1.18980000
H	0.73590000	-0.71810000	2.08820000
H	-6.45924618	-1.05578147	-1.06675731

---

#### Co-crystal CQ/ER

---

O	5.57140000	-1.61570000	-1.20060000
O	3.93010000	-2.37420000	-2.55980000
O	4.72540000	-3.88960000	2.14640000
H	4.60130000	-4.60700000	1.48270000
O	6.80780000	-4.19570000	0.96540000
H	6.75600000	-4.35070000	1.94580000
O	1.91740000	0.53380000	-2.71850000
O	1.41000000	3.46140000	0.07930000
O	1.55220000	-0.06950000	0.82050000
O	1.14270000	6.70750000	-0.72760000
H	1.23320000	7.53040000	-0.19450000
O	-0.39330000	3.83460000	-1.35660000
O	-1.06690000	1.46470000	-4.32280000
O	-2.78610000	0.25120000	-2.89760000
H	-2.57180000	1.22800000	-3.07310000
O	0.48760000	-1.17640000	-2.07410000
N	-0.87890000	6.68630000	1.88600000
C	4.52680000	-1.44330000	-2.06600000
C	4.29390000	0.04880000	-2.25020000
H	5.08660000	0.60080000	-1.67520000
C	2.90830000	0.43620000	-1.66410000
H	2.56390000	-0.34580000	-0.93540000
C	2.91920000	1.81750000	-0.96210000
H	3.67050000	1.75670000	-0.12670000
C	1.52770000	2.08170000	-0.32820000
H	0.71620000	1.83380000	-1.06330000
C	1.30660000	1.33660000	1.04050000
C	2.36290000	1.75440000	2.07990000
H	2.26850000	2.84990000	2.24150000
H	3.37370000	1.62380000	1.63640000
C	2.24920000	0.99440000	3.41510000
H	1.40180000	0.26230000	3.35080000
C	3.55000000	0.20650000	3.63270000
C	5.03990000	-1.55820000	2.57340000
H	5.51360000	-0.64420000	2.12640000
C	5.00920000	-2.64530000	1.47400000
H	4.16970000	-2.43650000	0.76940000



C	6.33550000	-2.86870000	0.66000000
C	6.00600000	-2.98480000	-0.86100000
H	5.15650000	-3.68310000	-1.03400000
C	2.90030000	-2.17770000	3.86810000
H	3.07370000	-3.20040000	3.49220000
H	1.81820000	-2.01910000	3.91350000
H	3.29330000	-2.14680000	4.89080000
C	4.45000000	0.36880000	-3.73530000
H	4.07300000	1.37660000	-3.95790000
H	3.87430000	-0.32280000	-4.36490000
H	5.49840000	0.31890000	-4.05050000
C	5.87120000	-1.98970000	3.78100000
H	5.77890000	-1.25090000	4.59210000
H	6.93560000	-2.07240000	3.52640000
H	5.54090000	-2.96200000	4.16810000
C	7.45440000	-1.87520000	0.92870000
H	7.65070000	-1.75630000	2.00610000
H	7.22250000	-0.88850000	0.50820000
H	8.39580000	-2.21730000	0.47910000
C	7.20550000	-3.32610000	-1.74120000
H	7.86160000	-4.03510000	-1.18620000
H	7.81140000	-2.41380000	-1.91310000
C	6.78500000	-3.93980000	-3.07160000
H	7.63980000	-4.04250000	-3.74880000
H	6.02630000	-3.32910000	-3.57950000
H	6.35180000	-4.93880000	-2.93670000
C	3.34720000	2.94030000	-1.90250000
H	3.31290000	3.91360000	-1.39300000
H	2.69880000	2.98770000	-2.78650000
H	4.37600000	2.80470000	-2.25390000
C	-0.11930000	1.55170000	1.52380000
H	-0.87950000	1.34280000	0.75290000
H	-0.28050000	2.60570000	1.82050000
H	-0.36650000	0.93090000	2.39910000
C	1.99200000	1.92990000	4.59410000
H	1.83510000	1.36540000	5.52170000
H	1.10370000	2.54840000	4.42960000
H	2.84970000	2.59360000	4.77150000
C	0.77410000	4.40200000	-0.80970000
H	1.40820000	4.57910000	-1.70780000
C	0.65280000	5.64030000	0.10750000
H	1.35150000	5.51450000	0.97220000
C	-0.78780000	5.96260000	0.58320000
H	-1.25760000	6.63790000	-0.18690000
C	-1.58750000	4.65220000	0.64750000
H	-2.58850000	4.82630000	1.09260000
H	-1.09320000	3.91490000	1.32630000
C	-1.70680000	4.07840000	-0.76030000
H	-2.16400000	4.81370000	-1.46480000
C	-2.43090000	2.74420000	-0.81790000
H	-2.46080000	2.34270000	-1.84160000
H	-3.45880000	2.83870000	-0.44370000
H	-1.93910000	1.98510000	-0.18030000
C	-0.32550000	8.06820000	1.76840000
H	-0.97610000	8.65050000	1.09370000
H	0.71070000	8.12640000	1.39570000
H	-0.36390000	8.56550000	2.75150000
C	-0.25040000	5.95570000	3.02300000
H	-0.76770000	4.99070000	3.16260000
H	-0.40660000	6.53100000	3.95050000
H	0.82670000	5.75850000	2.91420000
C	1.32290000	-0.71200000	-3.12450000
H	2.08380000	-1.52920000	-3.19060000
C	0.60850000	-0.40770000	-4.44190000
H	0.68530000	-1.31210000	-5.08230000
H	1.18530000	0.37880000	-4.98290000
C	-0.85760000	0.02980000	-4.35970000

C	-1.59580000	-0.52160000	-3.10040000
H	-1.96000000	-1.55670000	-3.25960000
C	-0.72480000	-0.42250000	-1.82960000
H	-0.43390000	0.64410000	-1.62790000
C	-1.62180000	-0.35210000	-5.63240000
H	-1.17090000	0.12550000	-6.51280000
H	-2.65680000	0.01220000	-5.58080000
H	-1.64080000	-1.43180000	-5.79910000
C	-0.08630000	2.29010000	-3.66440000
H	-0.56580000	3.27770000	-3.65580000
H	0.84490000	2.29840000	-4.23690000
H	0.10460000	1.94700000	-2.62940000
C	-1.34120000	-1.10110000	-0.62290000
H	-0.71340000	-0.98120000	0.27820000
H	-1.44230000	-2.18600000	-0.76550000
H	-2.33970000	-0.68650000	-0.38440000
Cl	-3.13930000	2.17740000	2.42320000
N	-4.18480000	-4.55680000	2.28870000
H	-4.29290000	-5.14460000	3.12280000
N	-6.96710000	-1.24560000	2.33410000
H	-7.48890000	-0.62610000	2.96880000
N	-5.76630000	-1.71260000	-2.01400000
H	-6.66360000	-2.25860000	-2.05740000
C	-4.60640000	-2.14070000	2.40780000
C	-5.11630000	-3.44900000	2.36380000
C	-4.35210000	-5.39830000	1.05340000
H	-5.41170000	-5.73420000	0.91030000
C	-5.09920000	-3.77110000	-0.75130000
H	-5.82530000	-4.45890000	-1.22000000
H	-5.62790000	-3.29350000	0.11860000
C	-5.91250000	-0.70810000	-0.86030000
H	-5.93420000	-1.29610000	0.10750000
H	-6.90750000	-0.21910000	-0.94260000
C	-6.53230000	-3.65750000	2.48690000
H	-6.89620000	-4.67980000	2.56060000
C	-7.40060000	-2.61930000	2.51470000
H	-8.47160000	-2.73080000	2.62610000
C	-4.62870000	-2.70160000	-1.73690000
H	-3.75510000	-2.13880000	-1.31920000
H	-4.28660000	-3.16050000	-2.68780000
C	-3.22140000	-1.82500000	2.41350000
H	-2.51400000	-2.64980000	2.43180000
C	-3.69720000	0.52230000	2.46840000
C	-5.53620000	-1.02010000	2.45580000
C	-3.91620000	-4.56570000	-0.18230000
H	-3.48380000	-5.22170000	-0.95590000
H	-3.10700000	-3.87590000	0.14270000
C	-5.08570000	0.28780000	2.51370000
H	-5.77160000	1.12540000	2.59370000
C	-4.80300000	0.31550000	-0.81410000
H	-4.88090000	0.90830000	0.12000000
H	-3.79170000	-0.14010000	-0.77190000
C	-2.77010000	-0.50820000	2.45350000
H	-1.70230000	-0.29550000	2.48920000
C	-5.56240000	-1.04010000	-3.36970000
H	-5.33500000	-1.82300000	-4.12800000
H	-4.64600000	-0.38140000	-3.31970000
C	-3.46300000	-6.64390000	1.19570000
H	-3.77820000	-7.26730000	2.03930000
H	-2.41820000	-6.36180000	1.38150000
H	-3.49100000	-7.26590000	0.29760000
C	-6.78470000	-0.24110000	-3.78060000
H	-6.63160000	0.20480000	-4.77700000
H	-6.98860000	0.60010000	-3.10120000
H	-7.69770000	-0.84600000	-3.84690000
H	-4.81230000	1.01500000	-1.65620000
O	4.47270000	0.65600000	4.27470000

C	3.58830000	-1.16380000	2.95430000
H	2.98650000	-1.08990000	2.00200000
H	0.78430000	-0.51720000	0.38070000
H	-5.98866452	-1.46695471	-1.62498195

---

Co-crystal HQ/AZ

---

O	6.31880000	-1.29690000	-0.99920000
O	4.53930000	-2.68090000	-0.80590000
O	5.52360000	-2.63550000	2.28660000
H	4.97690000	-3.08370000	1.59650000
O	8.08470000	-2.12520000	2.09210000
H	7.54530000	-2.80770000	2.57890000
O	1.92680000	-0.69750000	-2.26740000
O	1.32080000	3.18990000	-0.84430000
O	1.64290000	0.07640000	0.98090000
H	0.91360000	-0.46610000	0.58440000
O	0.86570000	5.96610000	-2.65530000
H	0.89870000	6.92930000	-2.44800000
O	-0.59170000	3.01350000	-2.17440000
O	-0.85860000	-1.30800000	-4.30250000
O	-2.68020000	-1.77980000	-2.55230000
H	-2.55220000	-1.11840000	-3.30150000
O	0.57130000	-1.92070000	-0.84420000
N	4.21130000	0.10290000	3.01580000
N	-1.05040000	6.81550000	-0.12620000
C	5.02610000	-1.66270000	-1.25240000
C	4.38120000	-0.59060000	-2.11320000
H	5.06770000	0.30070000	-2.12790000
C	3.02410000	-0.15430000	-1.48770000
H	2.93480000	-0.53060000	-0.43050000
C	2.82950000	1.38120000	-1.51040000
H	3.67050000	1.84110000	-0.92880000
C	1.50160000	1.75590000	-0.80040000
H	0.64450000	1.25390000	-1.30330000
C	1.47150000	1.48690000	0.75460000
C	2.67180000	2.13440000	1.46850000
H	2.73690000	3.19180000	1.14610000
H	3.59360000	1.63530000	1.09720000
C	2.63250000	2.02310000	3.00710000
H	1.81310000	1.31120000	3.28820000
C	3.96260000	1.46190000	3.58380000
H	4.80280000	2.12960000	3.30080000
H	3.91430000	1.46390000	4.69340000
C	5.63450000	-0.34310000	3.09690000
H	6.28450000	0.56230000	2.92290000
C	5.80060000	-1.28050000	1.86610000
H	5.05790000	-0.97600000	1.09160000
C	7.22900000	-1.34630000	1.24560000
C	7.14860000	-2.13120000	-0.10870000
H	6.64650000	-3.11290000	0.04010000
C	3.23270000	-0.90160000	3.51550000
H	3.56550000	-1.92190000	3.26190000
H	2.28010000	-0.72420000	2.97380000
H	3.04790000	-0.86210000	4.59690000
C	4.26670000	-1.13260000	-3.53680000
H	3.59880000	-0.49740000	-4.13650000
H	3.84280000	-2.14430000	-3.55880000
H	5.24380000	-1.16440000	-4.03290000
C	6.07680000	-1.00750000	4.39950000
H	5.83360000	-0.39150000	5.26930000
H	7.15920000	-1.18810000	4.39530000
H	5.59190000	-1.98500000	4.53410000
C	7.90370000	0.00720000	1.08910000
H	7.73140000	0.65090000	1.96440000
H	7.54020000	0.53240000	0.19730000

H	8.99250000	-0.11410000	1.00150000
C	8.48850000	-2.27480000	-0.82240000
H	9.27360000	-2.46700000	-0.05620000
H	8.75680000	-1.31320000	-1.30650000
C	8.47440000	-3.39390000	-1.85740000
H	9.43360000	-3.45430000	-2.38470000
H	7.69360000	-3.23320000	-2.61050000
H	8.29360000	-4.37270000	-1.39710000
C	2.88830000	1.91420000	-2.94230000
H	2.69700000	2.99760000	-2.97720000
H	2.14380000	1.41800000	-3.57870000
H	3.87260000	1.75440000	-3.39440000
C	0.11440000	1.91680000	1.30890000
H	-0.72250000	1.40610000	0.80650000
H	-0.04020000	3.00010000	1.16080000
H	0.03570000	1.70060000	2.38120000
C	2.33850000	3.38150000	3.65630000
H	2.23310000	3.29340000	4.74280000
H	1.40200000	3.80260000	3.27310000
H	3.13060000	4.11080000	3.45900000
C	0.57480000	3.76120000	-1.93860000
H	1.14720000	3.64640000	-2.89170000
C	0.45080000	5.23350000	-1.48510000
H	1.19180000	5.42300000	-0.66920000
C	-0.98000000	5.65850000	-1.06780000
H	-1.53100000	5.97380000	-1.99850000
C	-1.68570000	4.43450000	-0.46400000
H	-2.66740000	4.72320000	-0.03110000
H	-1.09860000	4.01670000	0.38700000
C	-1.86570000	3.38030000	-1.55250000
H	-2.44750000	3.78140000	-2.41660000
C	-2.46540000	2.07970000	-1.04800000
H	-2.63140000	1.37370000	-1.86920000
H	-3.43240000	2.25900000	-0.55400000
H	-1.80870000	1.58800000	-0.30960000
C	-0.60740000	8.07500000	-0.79460000
H	-1.34820000	8.33710000	-1.56980000
H	0.39060000	8.02810000	-1.26410000
H	-0.60580000	8.90150000	-0.06590000
C	-0.30810000	6.59810000	1.14780000
H	-0.74240000	5.73030000	1.67300000
H	-0.45940000	7.47030000	1.80470000
H	0.77350000	6.42930000	1.03570000
C	1.50610000	-2.02300000	-1.90820000
H	2.33470000	-2.60580000	-1.43510000
C	0.95220000	-2.64540000	-3.19220000
H	1.18530000	-3.73100000	-3.16730000
H	1.52630000	-2.24310000	-4.05870000
C	-0.54070000	-2.45710000	-3.47460000
C	-1.39800000	-2.31020000	-2.18080000
H	-1.62710000	-3.29940000	-1.73060000
C	-0.73910000	-1.37070000	-1.14950000
H	-0.59270000	-0.34580000	-1.58160000
C	-1.08580000	-3.59520000	-4.34570000
H	-0.56870000	-3.62480000	-5.31410000
H	-2.14990000	-3.43520000	-4.56670000
H	-0.97760000	-4.57200000	-3.86690000
C	-0.16100000	-0.06690000	-4.07320000
H	-0.60210000	0.59400000	-4.82770000
H	0.91710000	-0.19210000	-4.23120000
H	-0.34620000	0.30970000	-3.05480000
C	-1.42220000	-1.33140000	0.20080000
H	-0.71580000	-1.00970000	0.98810000
H	-1.80130000	-2.31540000	0.54100000
H	-2.27760000	-0.64340000	0.22530000
Cl	-4.89540000	3.67800000	1.41250000
N	-3.56880000	-2.78290000	3.10430000

H	-3.27240000	-2.72030000	4.08760000
N	-7.30930000	-0.74550000	2.39860000
H	-8.06790000	-0.17600000	2.79700000
N	-5.87290000	-2.68040000	-1.28470000
H	-6.75270000	-3.20660000	-1.05840000
O	-5.51350000	0.40010000	-1.91660000
H	-6.02890000	1.14950000	-1.54300000
C	-4.79800000	-0.71070000	2.63890000
C	-4.83370000	-2.08220000	2.96100000
C	-3.58440000	-4.22160000	2.67540000
H	-4.53050000	-4.74700000	2.97140000
C	-4.80050000	-4.18740000	0.42990000
H	-5.28280000	-5.18080000	0.39870000
H	-5.46300000	-3.54770000	1.07110000
C	-5.84850000	-1.44690000	-0.38860000
H	-6.88310000	-1.04500000	-0.27240000
C	-6.09670000	-2.68720000	3.27330000
H	-6.09580000	-3.68780000	3.70290000
C	-7.26670000	-2.04410000	3.04480000
H	-8.23870000	-2.45610000	3.28240000
C	-4.68250000	-3.59310000	-0.97590000
H	-3.74330000	-2.98570000	-1.07690000
H	-4.62180000	-4.38860000	-1.74690000
C	-3.61030000	0.05250000	2.51770000
H	-2.66420000	-0.43070000	2.74100000
C	-4.85490000	2.01250000	1.91500000
C	-6.05580000	-0.01130000	2.39960000
C	-3.43920000	-4.28250000	1.13060000
H	-2.92030000	-5.20840000	0.83020000
H	-2.77410000	-3.43750000	0.82070000
C	-6.08090000	1.32860000	2.05760000
H	-7.01330000	1.86280000	1.90260000
C	-4.89890000	-0.35150000	-0.85920000
H	-4.63840000	0.31850000	-0.00860000
H	-3.96120000	-0.74490000	-1.31270000
C	-3.63690000	1.40510000	2.16950000
H	-2.71090000	1.97190000	2.10770000
C	-5.89810000	-2.30970000	-2.76760000
H	-4.84820000	-2.13540000	-3.12000000
H	-6.40300000	-1.31260000	-2.88490000
C	-2.40440000	-4.94850000	3.34070000
H	-2.50030000	-4.95460000	4.43230000
H	-1.45000000	-4.46010000	3.10460000
H	-2.33670000	-5.99000000	3.01420000
C	-6.59300000	-3.38080000	-3.58480000
H	-6.59110000	-3.10040000	-4.65190000
H	-7.64740000	-3.51580000	-3.30930000
H	-6.09860000	-4.35900000	-3.52560000
H	-5.75638776	-1.66901342	0.66429171
H	-5.77351762	-2.39305966	-1.69805318

---

**Co-crystal HQ/CL**


---

O	5.31360000	-2.14700000	-1.29460000
O	3.55950000	-3.24390000	-2.22920000
O	4.03410000	-2.98900000	1.65240000
H	3.18920000	-2.61190000	1.99230000
O	6.80180000	-3.69080000	1.62860000
H	6.08750000	-4.18070000	2.11010000
O	1.54470000	-0.28120000	-2.73230000
O	1.65390000	3.18380000	-0.75840000
O	2.60050000	0.21150000	1.10040000
O	0.58170000	5.63440000	-2.90130000
H	0.69640000	6.60440000	-2.94690000
O	-0.56960000	3.01460000	-1.43240000
O	-1.54530000	0.22870000	-4.46460000

O	-3.24470000	-0.42160000	-2.63410000
H	-3.06520000	0.40190000	-3.18400000
O	0.06250000	-1.57120000	-1.50950000
N	0.18520000	6.97090000	0.19420000
C	4.20690000	-2.23080000	-2.08600000
C	3.94970000	-0.85250000	-2.68000000
H	4.85850000	-0.21750000	-2.49340000
C	2.74650000	-0.21950000	-1.92500000
H	2.55670000	-0.77560000	-0.97250000
C	2.97650000	1.27390000	-1.59960000
H	3.95510000	1.33650000	-1.03970000
C	1.85200000	1.75440000	-0.64370000
H	0.89220000	1.23560000	-0.87180000
C	2.23100000	1.59900000	0.87420000
C	3.53520000	2.36410000	1.18370000
H	3.34100000	3.44120000	0.99410000
H	4.31750000	2.08060000	0.43960000
C	4.07940000	2.15280000	2.60410000
H	3.22440000	1.95760000	3.29810000
C	5.03630000	0.95080000	2.59640000
C	5.41890000	-1.51360000	3.05750000
H	6.51060000	-1.24140000	3.05380000
C	5.04760000	-1.95830000	1.61800000
H	4.65280000	-1.10710000	1.01070000
C	6.22680000	-2.62740000	0.84820000
C	5.69960000	-3.30190000	-0.46070000
H	4.78520000	-3.90640000	-0.25480000
C	4.84350000	0.14110000	4.92270000
H	4.44290000	-0.62400000	5.59960000
H	4.34580000	1.08340000	5.17880000
H	5.91060000	0.25270000	5.15390000
C	3.74270000	-0.98210000	-4.18530000
H	3.23910000	-0.09070000	-4.58500000
H	3.11040000	-1.84410000	-4.43780000
H	4.69530000	-1.10410000	-4.71300000
C	5.21320000	-2.65980000	4.04960000
H	5.69540000	-2.45380000	5.01070000
H	5.65630000	-3.58990000	3.65740000
H	4.15380000	-2.86370000	4.23490000
C	7.36230000	-1.64820000	0.59150000
H	7.39950000	-0.84170000	1.34350000
H	7.25840000	-1.16120000	-0.38720000
H	8.33030000	-2.16580000	0.62090000
C	6.76870000	-4.08830000	-1.21330000
H	7.47190000	-4.53520000	-0.47460000
H	7.37630000	-3.39150000	-1.82500000
C	6.16710000	-5.17930000	-2.09140000
H	6.92130000	-5.62150000	-2.75010000
H	5.35660000	-4.78670000	-2.72300000
H	5.73610000	-5.98920000	-1.49100000
C	3.11030000	2.12900000	-2.85510000
H	3.25040000	3.18670000	-2.59420000
H	2.21900000	2.04560000	-3.49200000
H	3.97310000	1.82550000	-3.45850000
C	1.07460000	2.05520000	1.75380000
H	0.12570000	1.54920000	1.51040000
H	0.88380000	3.13520000	1.59440000
H	1.28180000	1.90030000	2.81790000
C	4.84920000	3.37870000	3.10010000
H	5.23060000	3.23220000	4.11710000
H	4.21620000	4.27220000	3.11080000
H	5.71570000	3.58990000	2.45660000
C	0.66340000	3.63660000	-1.70380000
H	0.89670000	3.28020000	-2.73330000
C	0.76830000	5.17150000	-1.54950000
H	1.80770000	5.42780000	-1.22920000
C	-0.29140000	5.80760000	-0.61190000

H	-1.13180000	6.18990000	-1.25800000
C	-0.85340000	4.72500000	0.32510000
H	-1.57280000	5.17240000	1.04020000
H	-0.04090000	4.28070000	0.94910000
C	-1.52250000	3.63590000	-0.50910000
H	-2.29520000	4.05950000	-1.19350000
C	-2.08260000	2.48960000	0.31140000
H	-2.58360000	1.75560000	-0.33220000
H	-2.81610000	2.84060000	1.05210000
H	-1.29200000	1.95000000	0.85890000
C	0.48590000	8.15030000	-0.67020000
H	-0.40210000	8.39960000	-1.27320000
H	1.35190000	8.03390000	-1.33700000
H	0.67570000	9.02130000	-0.01870000
C	1.35030000	6.65570000	1.06970000
H	1.06580000	5.85930000	1.77730000
H	1.59600000	7.54520000	1.67260000
H	2.25890000	6.33430000	0.53780000
C	0.84480000	-1.54030000	-2.69100000
H	1.54690000	-2.39560000	-2.52460000
C	0.07550000	-1.62360000	-4.00970000
H	0.11240000	-2.67930000	-4.35360000
H	0.63920000	-1.05010000	-4.78330000
C	-1.37650000	-1.13900000	-4.01270000
C	-2.05800000	-1.23240000	-2.61580000
H	-2.43370000	-2.26040000	-2.41920000
C	-1.13860000	-0.75660000	-1.46990000
H	-0.84020000	0.31580000	-1.60820000
C	-2.20880000	-1.88880000	-5.06050000
H	-1.80450000	-1.72080000	-6.06790000
H	-3.24050000	-1.51260000	-5.07340000
H	-2.23530000	-2.96570000	-4.87540000
C	-0.62540000	1.23040000	-3.98560000
H	-0.95760000	2.12880000	-4.51750000
H	0.40780000	0.96970000	-4.24440000
H	-0.72220000	1.35540000	-2.89360000
C	-1.70810000	-1.02620000	-0.09240000
H	-0.92780000	-0.93060000	0.67890000
H	-2.11320000	-2.05150000	0.02510000
H	-2.51570000	-0.33160000	0.16910000
Cl	-4.29320000	3.16380000	3.37480000
N	-3.59880000	-3.54560000	2.42110000
H	-3.25930000	-3.94330000	3.30690000
N	-7.11650000	-1.10900000	3.01710000
H	-7.74970000	-0.68160000	3.70640000
N	-6.35090000	-1.53300000	-1.26840000
H	-7.25180000	-2.04650000	-1.10310000
O	-5.82150000	1.55200000	-0.77350000
H	-6.20200000	2.10890000	-0.05820000
C	-4.60860000	-1.35730000	2.88670000
C	-4.77680000	-2.74300000	2.70010000
C	-3.80930000	-4.65130000	1.42610000
H	-4.76720000	-5.20750000	1.60200000
C	-5.25640000	-3.64280000	-0.41850000
H	-5.82220000	-4.53460000	-0.74380000
H	-5.78170000	-3.27010000	0.49970000
C	-6.05960000	-0.72990000	-0.00520000
H	-7.01980000	-0.37760000	0.44410000
C	-6.06830000	-3.32370000	2.93510000
H	-6.14730000	-4.40910000	2.96030000
C	-7.16780000	-2.55560000	3.12210000
H	-8.15530000	-2.95230000	3.31910000
C	-5.25320000	-2.57210000	-1.51250000
H	-4.26730000	-2.03620000	-1.54700000
H	-5.39460000	-3.02290000	-2.51690000
C	-3.35620000	-0.69400000	2.86730000
H	-2.46150000	-1.29670000	2.74910000

C	-4.40530000	1.43430000	3.21590000
C	-5.78840000	-0.52710000	3.10430000
C	-3.83540000	-4.04280000	-0.00130000
H	-3.41000000	-4.75320000	-0.73030000
H	-3.15710000	-3.15210000	-0.00140000
C	-5.68340000	0.84050000	3.28200000
H	-6.55320000	1.46130000	3.47410000
C	-5.10700000	0.44310000	-0.20800000
H	-4.65060000	0.73430000	0.76560000
H	-4.30010000	0.23390000	-0.94690000
C	-3.25230000	0.68780000	3.03930000
H	-2.27640000	1.16590000	3.04210000
C	-6.52400000	-0.63520000	-2.49370000
H	-5.51380000	-0.39440000	-2.91720000
H	-6.93630000	0.35660000	-2.16250000
C	-2.64610000	-5.64870000	1.55140000
H	-2.62380000	-6.11900000	2.54060000
H	-1.67780000	-5.15140000	1.40950000
H	-2.72140000	-6.45020000	0.81110000
C	-7.42250000	-1.28880000	-3.52490000
H	-7.52730000	-0.62980000	-4.40360000
H	-8.44160000	-1.46690000	-3.15680000
H	-7.02670000	-2.24020000	-3.90310000
C	4.62290000	-0.24630000	3.45830000
H	3.53240000	-0.43490000	3.28610000
O	6.06140000	0.96040000	1.95020000
C	1.54940000	-0.73390000	1.36700000
H	0.79320000	-0.73560000	0.56510000
H	2.08590000	-1.69800000	1.37100000
H	1.09650000	-0.53790000	2.34270000
H	-5.80787841	-1.33810786	0.85102394
H	-5.95373861	-1.75140482	-1.55838099

---

**Co-crystal HQ/ER**


---

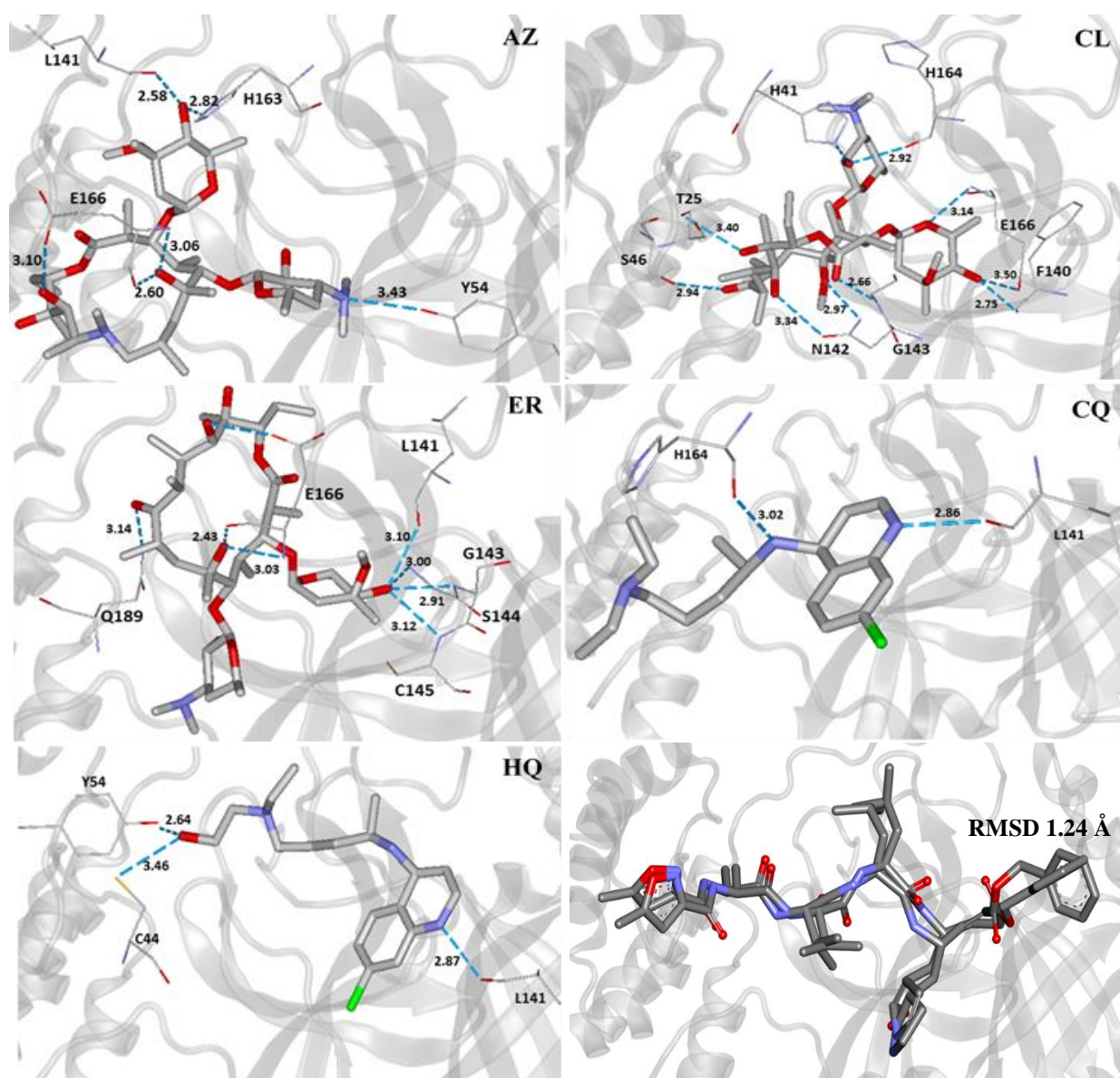
O	6.07640000	-0.96530000	-1.07530000
O	4.33100000	-2.18730000	-1.81740000
O	4.35910000	-3.03240000	1.06990000
H	4.08450000	-2.96080000	0.12110000
O	7.11160000	-2.99010000	1.77830000
H	6.43700000	-3.70230000	1.94820000
O	1.99710000	0.22970000	-2.70100000
O	1.03340000	3.46650000	-0.40980000
O	1.80310000	0.16690000	0.89680000
H	1.12090000	-0.41710000	0.46370000
O	0.06290000	6.29090000	-2.03880000
H	0.04980000	7.23980000	-1.80320000
O	-0.95330000	3.22890000	-1.60010000
O	-1.10750000	0.20920000	-4.51950000
O	-2.67300000	-0.93300000	-2.81560000
H	-2.67090000	-0.05760000	-3.31540000
O	0.76670000	-1.41060000	-1.62280000
N	-1.29750000	6.67330000	1.03530000
C	4.89880000	-1.11270000	-1.73670000
C	4.42730000	0.23310000	-2.26230000
H	5.12500000	1.02670000	-1.87910000
C	3.00530000	0.50330000	-1.69570000
H	2.81190000	-0.17080000	-0.81640000
C	2.78830000	1.97070000	-1.26100000
H	3.57410000	2.21430000	-0.49120000
C	1.40060000	2.07950000	-0.57380000
H	0.62320000	1.55410000	-1.18260000
C	1.39230000	1.55130000	0.90720000
C	2.44200000	2.27090000	1.77210000
H	2.12500000	3.32920000	1.87990000
H	3.41340000	2.32120000	1.22760000



C	2.65080000	1.62040000	3.14920000
H	1.71350000	1.08310000	3.44340000
C	3.81650000	0.62480000	3.05810000
C	4.72760000	-1.74030000	3.05100000
H	5.63000000	-1.25650000	3.51660000
C	4.96610000	-1.80540000	1.51680000
H	4.49290000	-0.94400000	0.99640000
C	6.48260000	-1.86690000	1.13750000
C	6.65780000	-2.14310000	-0.39120000
H	6.09240000	-3.05480000	-0.69040000
C	3.05420000	-0.95010000	4.82000000
H	2.69090000	-1.96140000	5.04520000
H	2.22940000	-0.26470000	5.04910000
H	3.87510000	-0.73400000	5.51390000
C	4.49320000	0.21450000	-3.78640000
H	3.97990000	1.09190000	-4.20500000
H	3.99210000	-0.66720000	-4.20670000
H	5.52880000	0.22100000	-4.14530000
C	4.58590000	-3.15240000	3.62210000
H	4.58340000	-3.15620000	4.71520000
H	5.42340000	-3.78640000	3.28910000
H	3.66600000	-3.63490000	3.26460000
C	7.24320000	-0.63230000	1.59220000
H	6.81320000	-0.19670000	2.51220000
H	7.21570000	0.16070000	0.83430000
H	8.29000000	-0.87740000	1.81030000
C	8.11230000	-2.19580000	-0.84570000
H	8.70270000	-2.72490000	-0.06290000
H	8.52410000	-1.16680000	-0.89710000
C	8.27230000	-2.89250000	-2.19200000
H	9.31980000	-2.88850000	-2.51480000
H	7.68430000	-2.39600000	-2.97300000
H	7.94810000	-3.93930000	-2.14970000
C	2.94890000	2.94360000	-2.42470000
H	2.76110000	3.97680000	-2.10230000
H	2.25930000	2.70260000	-3.24390000
H	3.96530000	2.91760000	-2.83340000
C	-0.01050000	1.65860000	1.49470000
H	-0.77570000	1.17050000	0.87000000
H	-0.31700000	2.71940000	1.57390000
H	-0.06280000	1.21220000	2.49540000
C	2.98590000	2.65790000	4.22230000
H	3.12790000	2.19110000	5.20390000
H	2.18660000	3.39990000	4.32410000
H	3.91390000	3.19500000	3.98000000
C	0.17340000	4.05170000	-1.41180000
H	0.66250000	4.03680000	-2.41160000
C	-0.01920000	5.47920000	-0.85020000
H	0.85250000	5.72270000	-0.19380000
C	-1.36630000	5.73370000	-0.12300000
H	-2.07090000	6.20110000	-0.86820000
C	-1.95900000	4.38990000	0.33050000
H	-2.89980000	4.55140000	0.89870000
H	-1.27110000	3.87000000	1.03970000
C	-2.20560000	3.51500000	-0.89430000
H	-2.81650000	4.04600000	-1.66190000
C	-2.79010000	2.15330000	-0.56940000
H	-3.06380000	1.60760000	-1.48030000
H	-3.69510000	2.24780000	0.05010000
H	-2.07650000	1.52720000	-0.00710000
C	-0.95780000	8.05970000	0.59850000
H	-1.67860000	8.39100000	-0.16620000
H	0.06300000	8.19310000	0.21310000
H	-1.08450000	8.73730000	1.46120000
C	-0.37510000	6.22500000	2.11730000
H	-0.74250000	5.26940000	2.52860000
H	-0.40430000	6.95540000	2.94220000

H	0.67290000	6.08880000	1.80960000
C	1.56310000	-1.14150000	-2.76570000
H	2.41910000	-1.84780000	-2.61530000
C	0.86920000	-1.27590000	-4.12020000
H	1.14560000	-2.26390000	-4.54530000
H	1.31420000	-0.52840000	-4.82000000
C	-0.65350000	-1.11720000	-4.14980000
C	-1.33610000	-1.45400000	-2.78950000
H	-1.46880000	-2.55010000	-2.66560000
C	-0.57420000	-0.85560000	-1.58840000
H	-0.49160000	0.26230000	-1.67330000
C	-1.27540000	-1.95450000	-5.27440000
H	-0.89460000	-1.63180000	-6.25290000
H	-2.36410000	-1.81200000	-5.30350000
H	-1.06980000	-3.02180000	-5.15910000
C	-0.43480000	1.35770000	-3.96440000
H	-0.91450000	2.18910000	-4.49360000
H	0.64190000	1.32300000	-4.16670000
H	-0.61690000	1.42940000	-2.87910000
C	-1.09790000	-1.29170000	-0.23640000
H	-0.36070000	-1.08440000	0.56040000
H	-1.29460000	-2.38030000	-0.16680000
H	-2.03680000	-0.78970000	0.03760000
Cl	-4.99530000	2.97510000	2.44850000
N	-2.79910000	-3.47040000	2.37850000
H	-2.36890000	-3.54600000	3.31050000
N	-6.79060000	-1.83810000	2.54970000
H	-7.55880000	-1.47680000	3.13020000
N	-5.53210000	-2.70330000	-1.66240000
H	-6.30090000	-3.41050000	-1.56230000
O	-5.67050000	0.45310000	-1.52550000
H	-6.25190000	1.01980000	-0.97190000
C	-4.28850000	-1.52770000	2.55160000
C	-4.13890000	-2.92790000	2.53740000
C	-2.72390000	-4.79830000	1.68220000
H	-3.58530000	-5.46850000	1.94320000
C	-4.15100000	-4.38550000	-0.39530000
H	-4.58550000	-5.37020000	-0.64250000
H	-4.78130000	-3.97010000	0.43640000
C	-5.65830000	-1.73370000	-0.49070000
H	-6.73430000	-1.53360000	-0.28080000
C	-5.28230000	-3.74860000	2.81920000
H	-5.12150000	-4.81100000	2.99690000
C	-6.53270000	-3.23020000	2.86560000
H	-7.41850000	-3.80890000	3.09300000
C	-4.19370000	-3.44560000	-1.60210000
H	-3.37350000	-2.68100000	-1.54090000
H	-4.03730000	-3.99860000	-2.55120000
C	-3.21230000	-0.60620000	2.51030000
H	-2.20040000	-0.99680000	2.51650000
C	-4.72270000	1.25850000	2.53150000
C	-5.63370000	-0.96330000	2.61330000
C	-2.72680000	-4.55720000	0.14810000
H	-2.21920000	-5.38890000	-0.36970000
H	-2.11180000	-3.64510000	-0.05200000
C	-5.84300000	0.40350000	2.61800000
H	-6.83830000	0.83130000	2.68950000
C	-4.90010000	-0.42650000	-0.69270000
H	-4.68920000	0.05360000	0.28930000
H	-3.94050000	-0.55570000	-1.24280000
C	-3.42640000	0.77450000	2.51340000
H	-2.58240000	1.45950000	2.50900000
C	-5.69630000	-1.99680000	-3.00850000
H	-4.70620000	-1.56960000	-3.32240000
H	-6.35640000	-1.09860000	-2.87100000
C	-1.42340000	-5.50640000	2.09430000
H	-1.40790000	-5.72590000	3.16780000

H	-0.5430000	-4.8870000	1.8791000
H	-1.2973000	-6.4566000	1.5672000
C	-6.2561000	-2.9413000	-4.0534000
H	-6.3542000	-2.4173000	-5.0195000
H	-7.2601000	-3.3107000	-3.8065000
H	-5.6114000	-3.8094000	-4.2418000
C	3.5020000	-0.8417000	3.3613000
H	2.6522000	-1.1485000	2.6904000
O	4.9308000	0.9973000	2.7536000
H	-5.4986640	-2.1816971	0.4789468
H	-5.0452806	-2.8371371	-1.8685270



**Figure S1.** Intermolecular interactions of single-crystals in the viral M<sup>pro</sup> active site and overlap obtained from re-docking calculations of the experimental co-crystallized active ligand N3 (PDB code: 6lu7) through MVD.

## CHAPTER 5

### *Research article*

Theoretical insights into the effect of halogenated substituent on the electronic structure and spectroscopic properties of the favipiravir tautomeric forms and its implications on the treatment of COVID-19

*Submitted to Journal of Cheminformatics*

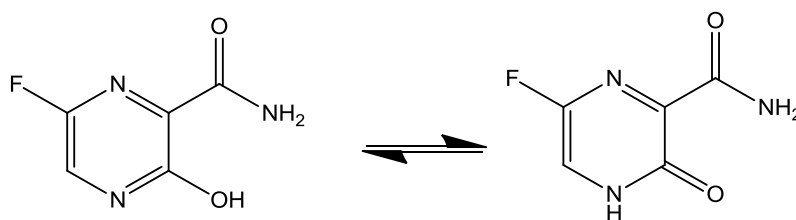
**Abstract.** In this study, we systematically investigated the electronic structure, spectroscopic (nuclear magnetic resonance, infrared, Raman, electron ionization mass spectrometry, UV-Vis, circular dichroism, and emission) properties, and tautomerism of halogenated favipiravir compounds (fluorine, chlorine, and bromine) from a computational perspective. Additionally, the effects of hydration on the proton transfer mechanism of the tautomeric forms of the halogenated favipiravir compounds are discussed. Our results suggest that spectroscopic properties allow for the elucidation of such tautomeric forms. As is well-known, the favipiravir compound has excellent antiviral properties and hence was recently tested for the treatment of new coronavirus (SARS-CoV-2). Through in silico modeling, in the current study, we evaluate the role of such tautomeric forms in order to consider the effect of drug-metabolism into the inhibition process of the main protease ( $M^{pro}$ ) and RNA-dependent RNA polymerase (RdRp) of SARS-CoV-2 virus. These findings clearly indicated that all title compounds are better as RNA-inhibiting.

**Keywords:** Favipiravir; COVID-19; In silico modeling; Tautomers; Electronic structure; Spectroscopic properties

## INTRODUCTION

Considerable efforts have been performed in a short period of time in search of therapeutic options to treatment for infection caused by a new coronavirus – SARS-CoV-2 –, which is the cause of the disease called COVID-19 [1–5]. Thus, researchers from all over the world have adopted as a strategy for treating COVID-19 infection attempt to inhibit two different types of known structural and non-structural proteins of the SARS-CoV-2 virus [6–10]. As such, the first case involves the inhibition of the main protease (abbreviated as  $M^{pro}$ ) proteins of SARS-CoV-2 [9,11–14]. Notably, this structural  $M^{pro}$  protein displays a pivotal role in the viral life-cycle due to their binding with the angiotensin-converting enzyme 2 (ACE2) receptor for the SARS-CoV-2 virus in host cells [9,11,15]. In contrast, after the SARS-CoV-2 virus enters into the host cell, it is well-known that the RNA-dependent RNA polymerase (abbreviated as RdRp), a non-structural protein, is the main enzyme for the process of SARS-CoV-2 replication [2,16–18]. Due to the eminent urgency to fight this COVID-19 outbreak, researchers around the world have widely evaluated the effectiveness of diverse approved antiviral agents for this proposed [1–3,19–21].

Among these approved drugs, in particular, favipiravir (also known as T-705) is a compound analogous to guanine, which was developed with satisfactory activity against many RNA-polymerase viruses (e.g., Ebola, chikungunya, yellow fever, influenza, norovirus and enterovirus) [22–27], showed good clinical efficacy against coronavirus [28,29]. Although the highly mobile protons in the structure of favipiravir compounds has allowed for their tautomeric forms [30,31], the interpretation of the spectroscopic properties of the tautomers has proven to be highly complex and difficult [32]. Their chemical structure and tautomeric form are shown in **Figure 1**.



**Figure 1.** Chemical structure and tautomeric form of favipiravir.

Ongoing studies have focused on the understanding of the tautomeric forms of these compounds that are critically important for elucidating the nature of their chemical molecular behaviour [30,32]. In contrast, quantum chemistry methods allow for the theoretical modelling of these spectral characteristics (i.e. to visualize this process on an atomic scale) quantitatively, which can, in principle, provide excellent opportunities for the design of new drugs [32–36].

In this study, we focused on elucidating the effect of halogen (fluorine, chlorine, and bromine) on the electronic structure, spectroscopic (nuclear magnetic resonance, infrared, Raman, electron ionization mass spectrometry, UV-Vis, circular dichroism and emission) properties, and tautomerism of the favipiravir compounds from a computational perspective. In addition, since solvation has been known to play an important role in the tautomeric equilibrium [30,32–35], the solvent effect was considered in the transition state calculations for the tautomerism of the isolated, mono-hydrate, di-hydrate and tri-hydrated forms of the different halogenated favipiravir compounds. Herein, we also used *in silico* modelling for predicting the possible effects of drug-metabolism in terms of action and toxicity for the halogenated favipiravir compounds against the SARS-CoV-2 using both  $M^{\text{pro}}$  and RdRp sites as model systems.

For the accomplishment of this work, a range of computational techniques were employed. The theoretical tools were developed, among others, for the study of complex chemical and biological systems. The emergence of quantum mechanics (QM) to study molecules at electronic level was a remarkable achievement. The growth of methods based on classical physics to study large systems at the molecular level (MM) is also of great importance in the study of large systems, such as biomacromolecules. The parallel development of molecular simulations, which connects the macroscopic and the microscopic world elucidating the dynamical properties of molecules may guide the design of active potent molecules as therapeutic agents (computer-aided molecular design). In this context, we highlight the impact of theoretical chemistry on the advancement of our comprehension of complex chemical and biological systems. Thus, the comprehension of chemical and biological systems has reached greater heights due to an excellent harmony between experiment and theory [37]. In order to illustrate the potential of theoretical and computational studies, we cite the study from Pierrefixe et al (2008), which showed how and why carbon can become truly hypervalent under certain conditions [38].

There are many positive consequences of these computational developments, particularly for treating systems in a more accurate fashion, and they can yield new insights. This study marks the first phase of a theoretical/experimental investigation of our group directed toward this goal. We hope that our results will stimulate new experimental and full-dimensional theoretical investigations that could assess the validity of this assumption.

## **METHODS: COMPUTATIONAL DETAILS**

Here, all quantum-chemical calculations were done through Gaussian 09 package [39]. Full optimization and their frequencies of halogenated favipiravir compounds (fluorine, chlorine, and bromine) were achieved with Density Functional Theory (DFT) method at the B3LYP/6-31+G(d,p) level. Then, in order to consider the effect of drug metabolism, the transition states (TS) for the tautomeric forms of title compounds were computed through DFT calculations, at the same level of theory described previously. Additionally, the solvent effect (water) was considered in the TS calculations for the tautomerism of the isolated, mono-hydrate, di-hydrate and tri-hydrated forms using the polarizable continuum model (PCM) [40,41]. In addition, NMR calculations (in the gas phase and solution) were also performed for tautomeric forms of the halogenated favipiravir compounds at the B3LYP/6-31+G(d,p) level

what do method [42–46]. Time-Dependent DFT (TD-DFT) calculations were also evaluated to obtain the UV-Vis, Electronic Circular Dichroism (ECD) and emission spectra, as well as their excitonic transitions, Molecular Orbitals (MOs) and Electrostatic Surface Potential (ESP) maps. Additionally, the Electron Ionization Mass Spectrometry (EI-MS) fragmentation spectrum for tautomeric forms and the trajectories of intermediaries were evaluated through semiempirical GFN2-xTB method as implemented in Quantum Chemistry Electron Ionization Mass Spectrometry program (QCEIMS) [47,48]. The MarvinSketch software was used to draw the 2D chemical structures (<https://chemaxon.com/products/marvin>).

The scientific impact of DFT on physics, chemistry and biology is enormous. The computational efficiency of DFT means that larger (more realistic) systems can be treated, giving electronic structure theory much more predictive power and expanding its potential for applications. This trend is further boosted by continuing improvements in computer performance. Researchers worldwide use the DFT method in an intensive way, making it the most popular QM method in present use. The accuracy of DFT has increased notably over the last few decades, being quite suitable to the study of a range of chemical systems [49].

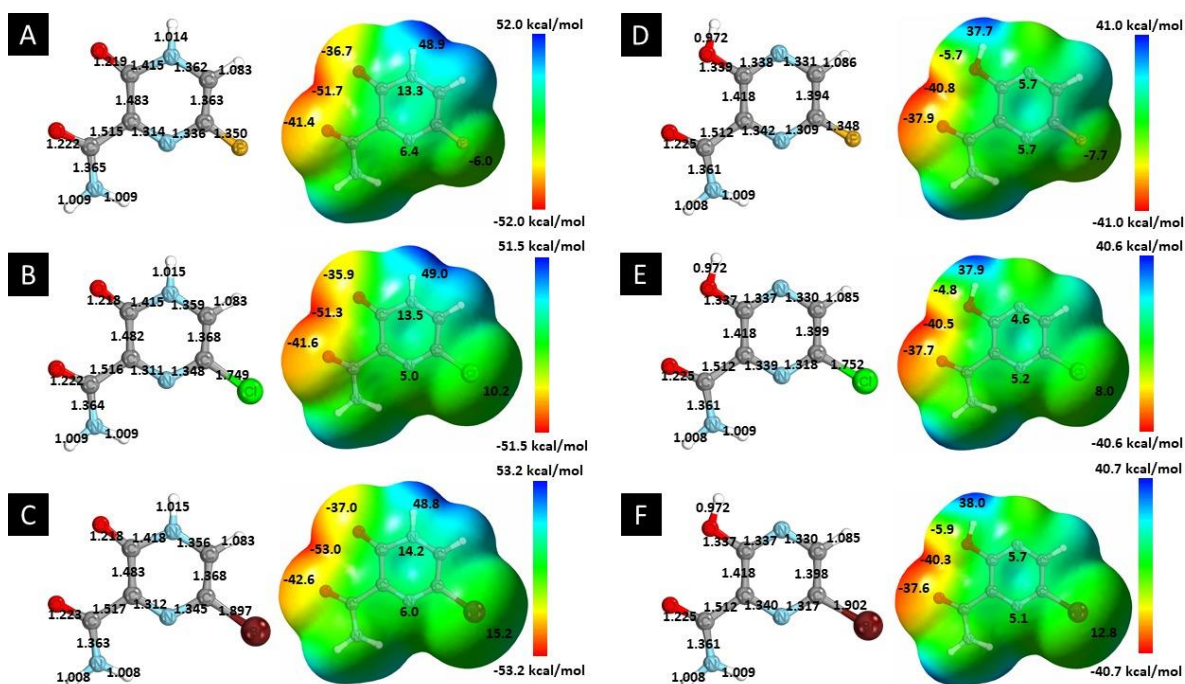
The molecular docking was conducted with the tool AutoDock Vina (version 1.1.2) [50], as implemented in the MolAr (Molecular Architecture) software [51]. For the crystallographic M<sup>PRO</sup> and RdRp polymerase structures preparation, the loop regions were rebuilt using the Modeller [52]. As such, the ions and water molecules were removed from the original PDB, with the exception of water molecules that were in the M<sup>PRO</sup> and RdRp active sites. Additionally, the polar hydrogen atoms was added in Chimera software [53] according to the protonation state of the receptor at a pH value of 7.4. For the docking protocol, both M<sup>PRO</sup> and RdRp enzymes and the structures of halogenated favipiravir tautomeric forms were used as receptor and ligands, respectively. Hence, the grid box was centered on the co-crystallized ligand (6-[ethylamino]pyridine-3-carbonitrile) of SARS-CoV-2 virus M<sup>PRO</sup> enzyme (5R82), and the coordinates were  $x = 12.053$ ,  $y = -0.871$  and  $z = 24.157$ , with 1 Å spacing. As such, the same procedure was performed for the enzyme of SARS-CoV-2 RdRp polymerase, the grid box was centered on the co-crystallized ligand cytidine-5'-triphosphate (3H5Y), and the coordinates were  $x = 30.594$ ,  $y = 0.628$  and  $z = -0.780$ , with about of 1 Å spacing. Finally, the docked poses obtained along in this procedure were then selected on the basis of scoring functions as well as protein-ligand interactions. Binding interaction figures were generated using Discovery Studio 2017 R2 [54]. We also provide a theoretical estimation for the acute



toxicity by use of LD<sub>50</sub> values obtained from a rat model-based admetSAR predictor, which is freely available online at <http://biosig.unimelb.edu.au/pkcsm/prediction>.

## RESULTS AND DISCUSSIONS

In this *in silico* study, halogenated favipiravir tautomeric forms were firstly investigated by DFT and TDDFT calculations. **Figure 2 (a-f)** shows the optimized structures, bond lengths and ESP maps for each derivative. As seen in **Figure 2**, the change from F to Cl and Br atoms do not affect significantly the molecular structure, in general, except for the C-F to C-Cl and C-Br bond lengths, which are longer than expected (due to their higher atomic radius). However, the changes in the tautomer structures are mainly seen in the OH group, which shows longer C-O and shorter O-H bonds, though some shifts in the N-C and C-C bond lengths at the main ring are seen as well. Hence, it is well-known that such structural parameters are, in principle, dependents of the nature of bonded atoms and their chemical environment. Also, we observed an increase in the dipole moment with the replacement of fluoride in the favipiravir structures. Finally, all these parameters determined for the optimized structure are consistent with the literature [55,56].

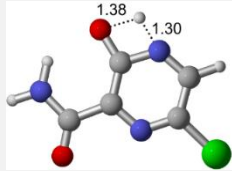
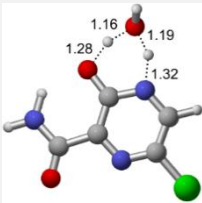
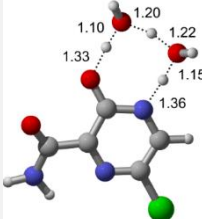


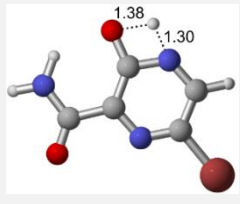
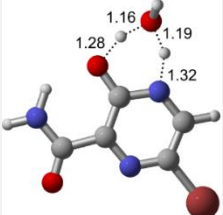
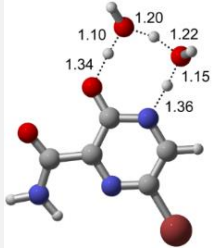
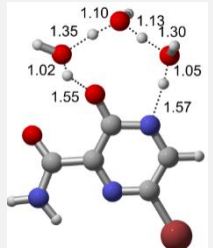
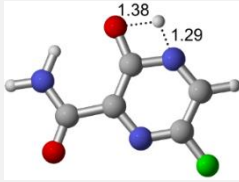
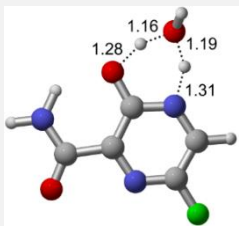
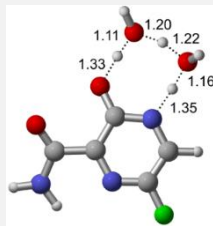
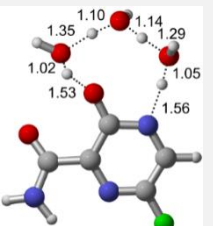
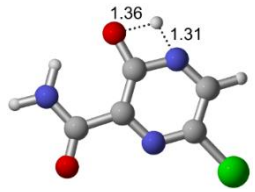
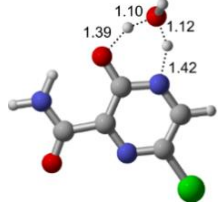
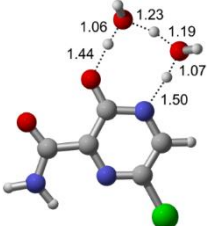
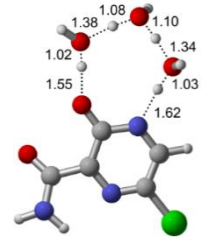
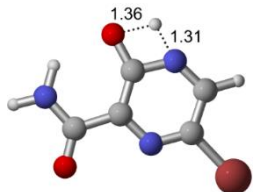
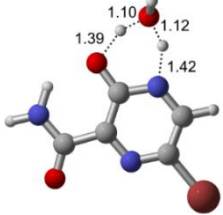
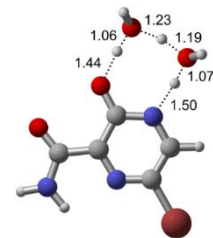
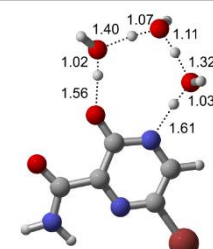
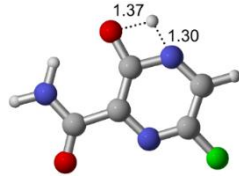
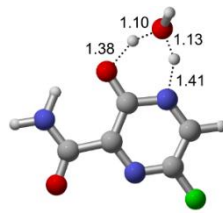
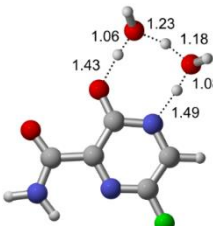
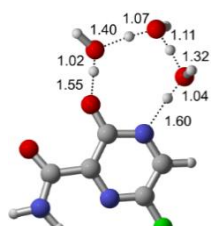
**Figure 2.** Optimized structures and ESP maps (with surface isovalue of 0.0004) for the halogenated favipiravir tautomeric forms: (a) 1-F; (b) 1-Cl; (c) 1-Br; (d) 2-F; (e) 2-Cl and (f) 2-Br. Image generated in the GaussView 6.0 <https://gaussian.com/gaussview6/>.

As for the ESP maps shown in **Figure 2 (a-f)**, the charge distribution is oriented towards the O atoms and N-H or O-H functional groups for the derivatives. These high negatively (red) and positively (blue) charged surfaces, or respectively, electrons acceptor and donor areas, show the most favorable regions for interaction between molecules, thus having a higher reactivity.<sup>1</sup> As such, the halogenic substitution does not affect the charge distribution significantly; however, the tautomer molecules are lesser polarized than the original structure due to a charge stabilization in the O-H group.

According to **Figure 1**, the agent favipiravir undergoes a tautomerism process that gives rise to its tautomeric form. Hence, from a drug-metabolism perspective, this process occurs *via* a water-based proton transfer mechanism or without water-assisted. Hence, the TS obtained through DFT calculations for both cases are shown in **Table 1**. These calculations were carried out in gas phase and water as implicit solvent (PCM). In all cases, a single imaginary frequency was obtained as shown in **Table 1**, confirming the achievement of the TS.

**Table 1.** Transition states (TS) of the tautomerism mechanism of the water-assisted process and without water, in gas phase and implicit solvent (water), respectively. Image generated in the CYLview <http://www.cylview.org/>.

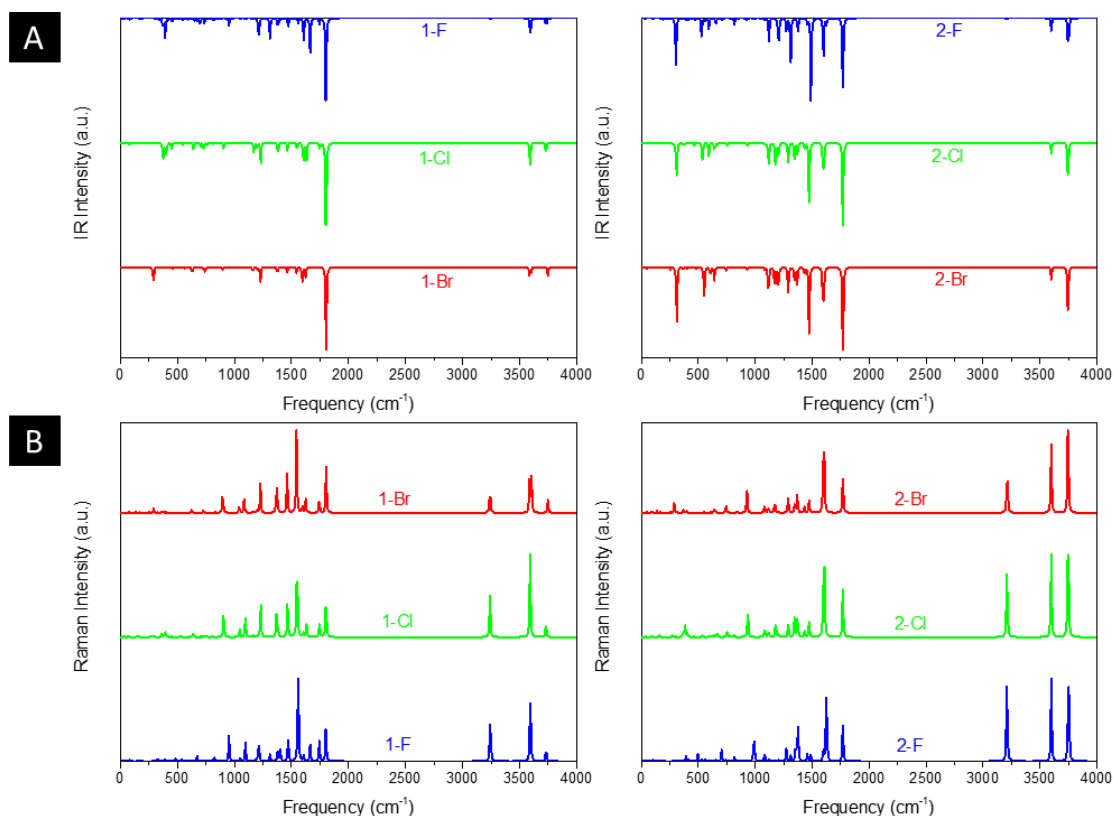
Gas phase			
Cl			
	Energy = -967.82 a.u. NIMAG = -1878.14 cm <sup>-1</sup>	Energy = -1044.31 a.u. NIMAG = -1453.72 cm <sup>-1</sup>	Energy = -1120.76 a.u. NIMAG = -1216.46 cm <sup>-1</sup>
			Energy = -1197.21 a.u. NIMAG = -357.30 cm <sup>-1</sup>

<b>Br</b>				
	Energy = -3079.35 a.u. NIMAG = -1877.99 cm <sup>-1</sup>	Energy = -3155.84 a.u. NIMAG = -1450.93 cm <sup>-1</sup>	Energy = -3232.29 a.u. NIMAG = -1214.20 cm <sup>-1</sup>	Energy = -3308.74 a.u. NIMAG = -355.42 cm <sup>-1</sup>
<b>F</b>				
	Energy = -607.47 a.u. NIMAG = -1915.94 cm <sup>-1</sup>	Energy = -683.96 a.u. NIMAG = -1003.52 cm <sup>-1</sup>	Energy = -760.41 a.u. NIMAG = -1249.76 cm <sup>-1</sup>	Energy = -836.86 a.u. NIMAG = -417.01 cm <sup>-1</sup>
<b>Implicit solvent (water)</b>				
<b>Cl</b>				
	Energy = -967.84 a.u. NIMAG = -1913.03 cm <sup>-1</sup>	Energy = -1044.33 a.u. NIMAG = -941.77 cm <sup>-1</sup>	Energy = -1120.79 a.u. NIMAG = -738.36 cm <sup>-1</sup>	Energy = -1197.24 a.u. NIMAG = -101.61 cm <sup>-1</sup>
<b>Br</b>				
	Energy = -3079.37 a.u. NIMAG = -1913.72 cm <sup>-1</sup>	Energy = -3155.86 a.u. NIMAG = -930.60 cm <sup>-1</sup>	Energy = -3232.32 a.u. NIMAG = -744.43 cm <sup>-1</sup>	Energy = -3308.77 a.u. NIMAG = -133.15 cm <sup>-1</sup>
<b>F</b>				

	Energy = -607.48 a.u. NIMAG = -1915.94 cm <sup>-1</sup>	Energy = -683.98 a.u. NIMAG = -1003.52 cm <sup>-1</sup>	Energy = -760.44 a.u. NIMAG = -753.77 cm <sup>-1</sup>	Energy = -836.89 a.u. NIMAG = -139.32 cm <sup>-1</sup>
--	--	--	---	---

According to **Table 1**, the tautomeric mechanism without water molecules showed the highest TS energy, this is, less stabilizing energies. On the other hand, the water-assisted proton transfer mechanism led to more stabilizing TS geometries and decreased energies. We also can observe that by increasing the number of water molecules in the tautomerism process, it is possible to obtain more stable geometries for the TS structure, making this process energetically more favorable. Another important trend that should be highlighted is the fact of increasing the electronegative character of the atom directly bound to the ring (Br < Cl < F). Our findings show that the replacement of the chlorine atom from favipiravir with more electronegative atoms, such as fluorine, this leads to higher TS energy values. On the other hand, in case chlorine is replaced by a less electronegative atom, such as bromine, this feature leads to decreased TS energy values. According to these results, we can observe that there were no significant differences in energy for solvent calculations. However, structural changes can be noticed by the variation of distances among atoms. From now on, the 1-F, 1-Cl and 1-Br will refer to the keto form of the derivatives. On the other hand, the 2-F, 2-Cl and 2-Br will refer to the enol form.

**Figure 3 (a)** and **(b)** shows the infrared (IR) and Raman spectrum of title compounds. As a result, the 1-F derivatives present a main intense peak at 1802 cm<sup>-1</sup> related to the stretching of C=O groups and an important signal at 1312 cm<sup>-1</sup> assigned to the stretching of C-F, being blueshifted to 1170 cm<sup>-1</sup> and 1161 cm<sup>-1</sup> for Cl and Br, respectively. The peaks localized around 3590 cm<sup>-1</sup> and 3732 cm<sup>-1</sup> are related to, respectively, the symmetrical and asymmetrical stretchings of NH<sub>2</sub> and NH groups. As for the intense Raman signal at 1557 cm<sup>-1</sup>, it is characterized by the deformation of the aromatic ring by asymmetrical stretchings of N ring atoms. All peaks discussed for these structures are both IR and Raman active-modes, showing signals located at the same IR and Raman frequencies positions. The discussed signals are shifted from the 1-F molecules, thus the C=O stretching peak is blueshifted to 1770 cm<sup>-1</sup> and the C-F stretching to 1272 cm<sup>-1</sup>, however, the Cl and Br heteroatoms are redshifted to 1179 cm<sup>-1</sup> and 1172 cm<sup>-1</sup>, respectively. For the tautomers, it is noticed the appearance of significant peaks at 1489 cm<sup>-1</sup> and 3754 cm<sup>-1</sup>, associated, respectively, to C-O and O-H stretchings of OH group. It is worth notice that 2-F molecules present an intense IR active-mode around 330 cm<sup>-1</sup>, in which is related to the bending of NH<sub>2</sub> group.



**Figure 3.** Computed (a) IR and (b) Raman spectra of the derivatives. Image generated in the Origin <https://www.originlab.com/>.

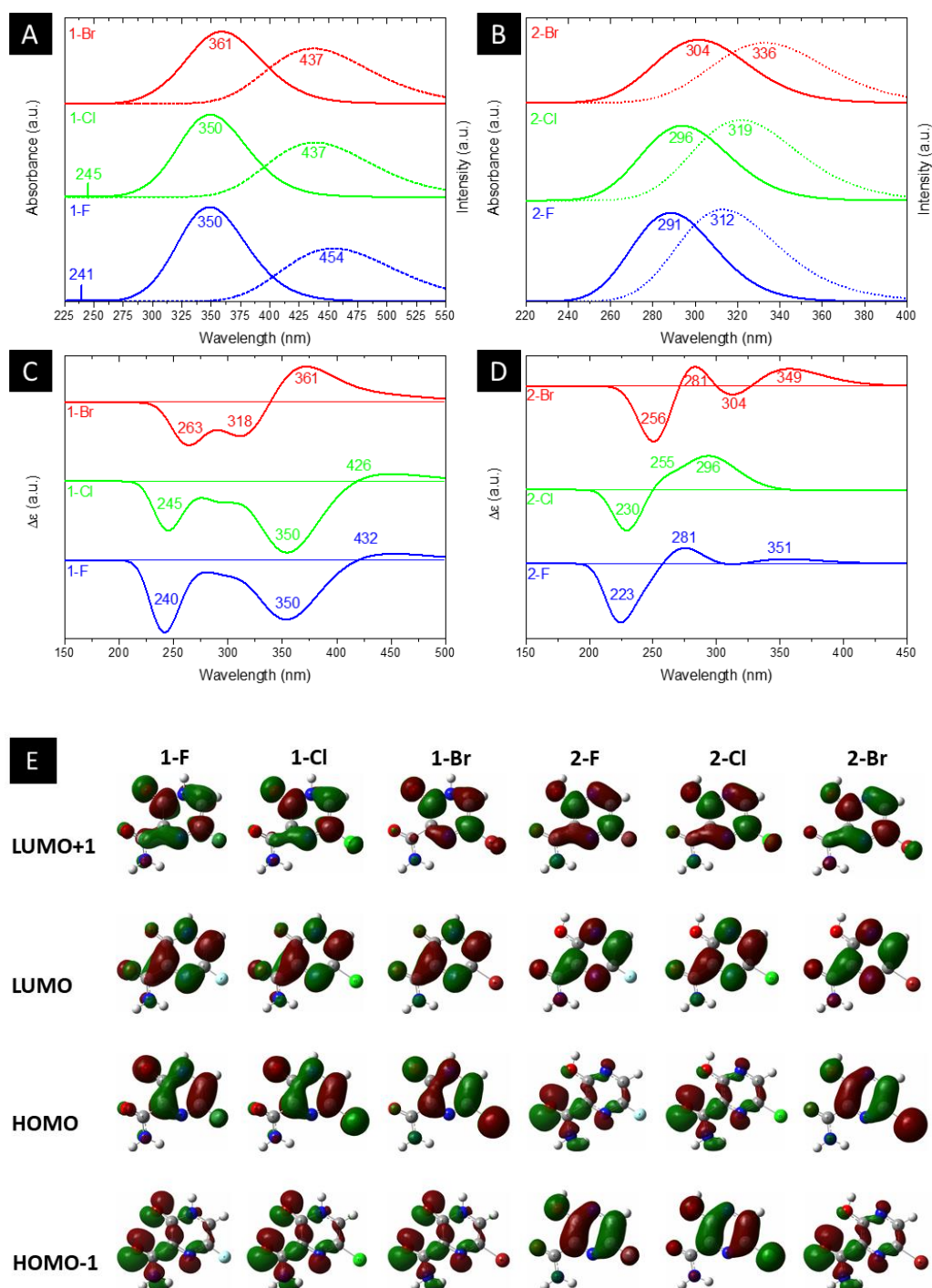
**Figure 4 (a)** and **(b)** illustrate the computed UV-Vis absorption and emission spectrum for the halogenated favipiravir compounds. For the UV-vis absorption spectrum of 1-F and 1-Cl derivatives, it is found an intense band at 350 nm and a very weak signal of high energy transition at 241 or 245 nm, respectively. In contrast, the 1-Br molecule shows only a small redshifted for the most intense band, which is located at about 361 nm (see **Figure 4 (a)**). Note that the dotted line in **Figure 4 (a)** and **(b)** corresponds to the emission spectra for such compounds. From the emission and UV-vis absorption spectra of these compounds were calculated the Stokes shifts ranging from 76 nm (1-Br) to 104 nm (1-F). As it is shown, the lower energy part of the absorbance bands is overlapped with the higher energy part of the emission bands, forming a sensitive Förster Resonance Energy Transfer (FRET) region from intramolecular mechanisms [57]. As for the emission bands, it can be noted that a large peak at about 437 nm for both 1-Cl and 1-Br compounds. In contrast, we can observe a redshift in computed emission spectra for the 1-F compound, which have emission wavelengths at 454

nm. On the other hand, as shown in **Figure 4 (b)**, the 2-F derivatives present only an intense band in the UV-vis absorption and emission spectra, with major blueshifts in the band position, ranging from 291 nm to 304 nm associated respectively to 2-F and 2-Br structures. The computed excitonic transitions, their related orbitals and the Stokes shifts for the halogenated favipiravir tautomeric forms are organized in **Table 2**.

**Table 2.** Analysis of UV-Vis and emission spectra of both 1 and 2 derivative tautomer forms.

Molecule	Excitonic transition	Absorbance wavelength	Emission	Emission wavelength	Stokes shift
<b>1-F</b>	HOMO → LUMO	350 nm	LUMO → HOMO	454 nm	104 nm
	HOMO-4 → LUMO	241 nm			
<b>1-Cl</b>	HOMO → LUMO	350 nm	LUMO → HOMO	437 nm	87 nm
	HOMO-4 → LUMO	245 nm			
<b>1-Br</b>	HOMO → LUMO	361 nm	LUMO → HOMO	437 nm	76 nm
<b>2-F</b>	HOMO-1 → LUMO	291 nm	LUMO → HOMO	312 nm	21 nm
<b>2-Cl</b>	HOMO-1 → LUMO	296 nm	LUMO → HOMO	319 nm	23 nm
<b>2-Br</b>	HOMO-2 → LUMO	304 nm	LUMO → HOMO	336 nm	32 nm

From Table 2, it is found that the excitonic transitions are mainly HOMO → LUMO for the 1-F type tautomers, while the 2-F type transitions happen from lower levels of the valence band to the LUMO orbital, as shown in **Table 2**. It is worth noticing that higher Stokes shifts of 1-F type derivatives may be a clue to a Excited States Intramolecular Proton Transfer (ESIPT) [58]. In this framework, we propose from the higher Stokes shifts that the 1-F molecule and their halogenic species are part of an ESIPT mechanism, in which the excited 1-F molecules are quickly phototautomerized into excited 2-F derivatives due to a proton transfer between the aromatic N-H and its O=C neighbor, and returning to the original structure by a reverse proton transfer after the radiative decay. However, as seen in the lower Stokes shifts, the same do not occur to the 2-F derivatives.



**Figure 4.** Computed (a and b) UV-Vis and emission, (c and d) ECD spectra and (e) MOs shapes (with a surface isovalue of 0.03) of both (a) 1 and (b) 2 derivative tautomer forms. Image generated in the Origin <https://www.originlab.com/> and GaussView 6.0 <https://gaussian.com/gaussview6/>.

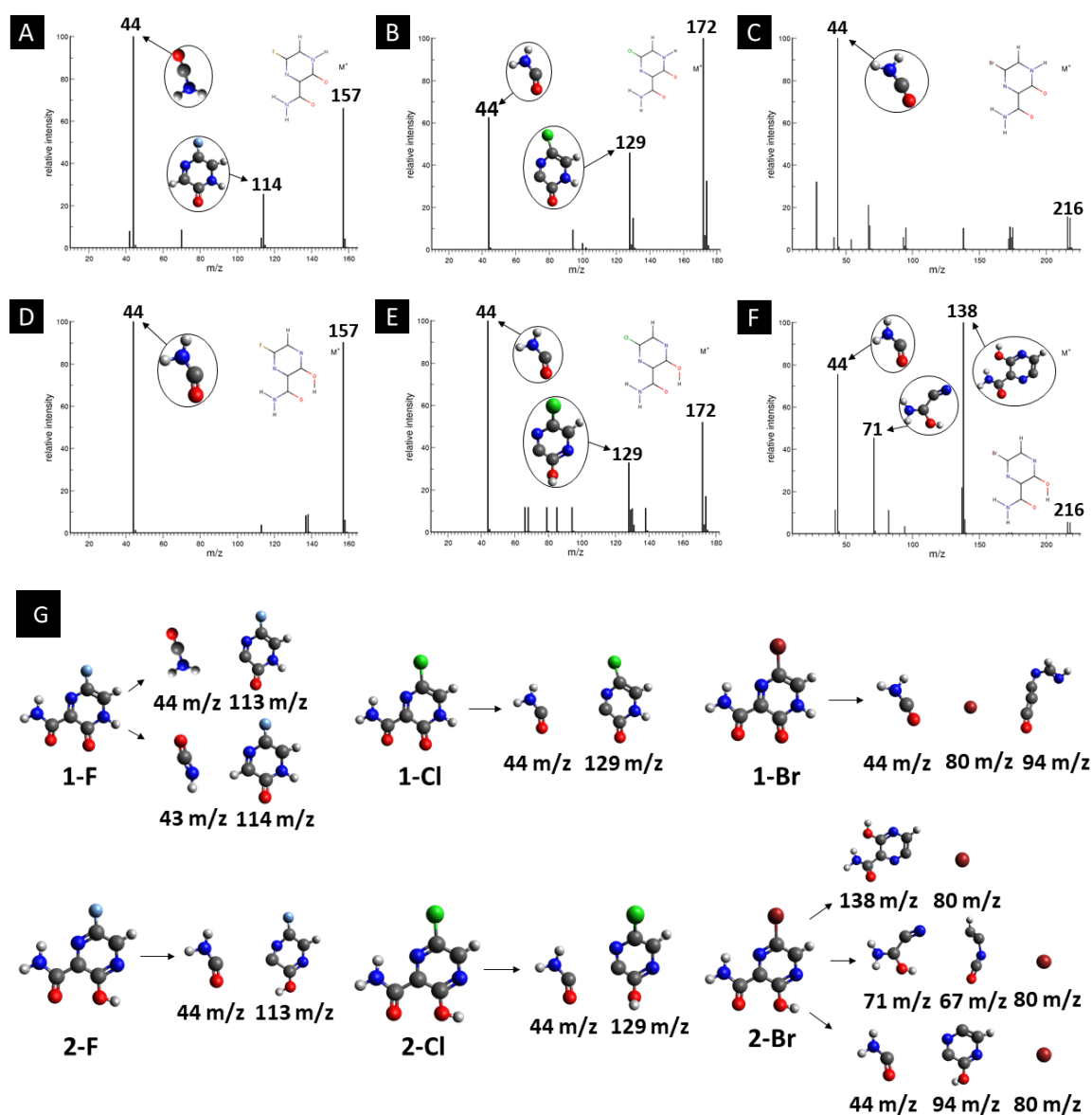
Computed ECD data are also shown in **Figure 4 (c)** and **(d)**. In the 1-F derivatives spectra, three signals are identified in the region between 220-440 nm, two being negatives (240-263 nm and 350-361 nm) and one positive (361-432 nm). As such, the 2-F and 2-Cl derivatives show three signals in the region of 200-360 nm, one negative (223-230 nm) and two positives (255-281 nm and 296-351 nm); however, there are four observed signals around 225-450 nm for the 2-Br tautomer, two being negatives (256 nm and 304 nm) and two positives (281 nm and 349 nm). Thus, it is analyzed that the change of heteroatom causes shifts in the positions and intensities of ECD signals, being the most significant modifications related to Br substitutions. **Figure 4 (e)** shows the LUMO+1, LUMO, HOMO and HOMO-1 shapes. From the HOMO and LUMO orbitals energies, the HOMO-LUMO gap and other electronic properties of the derivatives in their gas and water phase are calculated and organized in **Table 3**. Therefore, there are patterns in the HOMO-LUMO gaps, in which Cl derivatives have slightly higher energy and Br lower energy in comparison to their 1-F and 2-F tautomers. The HOMO-LUMO gaps are in accordance to the ESP maps as seen in **Figure 2**, which 1-F derivatives are more chemically reactive than 2-F due to their significantly smaller energy gaps. Along the energy gaps, other electronic properties are slightly shifted as well.

**Table 3.** Electronic properties of the derivatives in gas phase and solution.

Molecule	Gas phase				
	HOMO-LUMO	Hardness	Softness	Mulliken	Electrophilicity
	(eV)	(eV)	(eV)	Electronegativity (eV)	(eV)
1-F	3.88	1.94	0.51	-5.02	50.40
1-Cl	3.91	1.95	0.51	-4.98	49.70
1-Br	3.83	1.91	0.52	-4.98	49.70
2-F	4.62	2.31	0.43	-5.02	50.40
2-Cl	4.64	2.32	0.43	-5.00	50.00
2-Br	4.58	2.29	0.44	-4.96	49.20
Molecule	Solution				
	HOMO-LUMO	Hardness	Softness	Mulliken	Electrophilicity
	(eV)	(eV)	(eV)	Electronegativity (eV)	(eV)
1-F	3.95	1.97	0.51	-4.87	47.53
1-Cl	3.98	1.99	0.50	-4.84	46.85
1-Br	3.89	1.94	0.51	-4.83	46.75
2-F	4.70	2.35	0.42	-4.96	49.2
2-Cl	4.67	2.33	0.43	-4.91	48.31
2-Br	4.59	2.29	0.44	-4.87	47.53



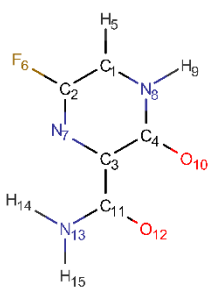
In addition, computed EI-MS spectrum were done as a mean to identify and differentiate each derivative and as well to understand their intermediary structures. **Figure 5** shows the EI-MS spectrum and their respective trajectories, as well as intermediaries for all studied compounds. In every diagram is observed a peak at 44 m/z related to the linear group fragmentation outside the main ring of their source molecules. It is observed a pattern in the fragmentation of both F and Cl derivatives, in which the main structures are divided into two fragments, giving rise to signals related to a linear part (44 m/z) and a cyclic part with the heteroatom (113-129 m/z). However, it is observed a third peak at 80 m/z associated to Br atoms in the Br derivatives, as seen in **Figure 5**.

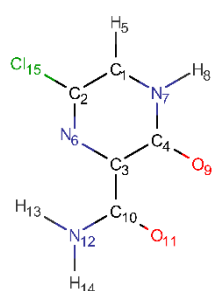


**Figure 5.** EI-MS diagrams, trajectories and intermediaries of all studied derivatives. (a) 1-F, (b) 1-Cl, (c) 1-Br, (d) 2-F, (e) 2-Cl and (f) 2-Br structures. Image generated in the Origin <https://www.originlab.com/> and GaussView 6.0 <https://gaussian.com/gaussview6/>.

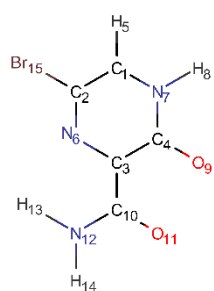
In order to best characterize the tautomers and understand their electronic structure, efforts have been made to obtain the NMR shieldings of the derivatives, as listing in **Table 4**. As such, the first is that N atoms next to the halogenic heteroatoms, and those close to OH group in the case the case of 2-F derivatives, present a relative lower shielding in comparison to other N atoms. Second, as the halogenic nuclei radius increases, the RNM shielding increases as well, ranging from 301.55 (F) to 2213.26 ppm (Br). The last conclusion to be made is that several shifts in the shieldings are observed when transitioning to solvent phase, as shown in the chemical shift  $\Delta\sigma$ , however, the chemical shift of O<sup>2-</sup> nuclei are significantly higher than other nuclei. Hence, the main reason for these higher values is due to interaction between tautomers and water molecules from the solvent, in which hydrogen bonds are formed between HO-H molecules and C=O groups of the derivatives compounds.

**Table 4.** NMR shielding on nuclei of intermediaries in gas phase and in solvent water (PCM).

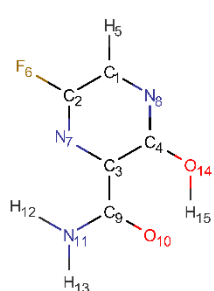
<i>Molecule</i>	<i>Nuclei</i>	<i>Shielding in gas</i> (ppm)	<i>Shielding in water</i> (ppm)	$\Delta\sigma$ (ppm)
 <p>1-F</p>	12-O	-66.26	-7.82	-58.44
	7-N	-44.26	-46.37	2.11
	10-O	-31.38	21.56	-52.94
	9-H	23.90	22.87	1.03
	5-H	24.68	24.05	0.63
	14-H	24.93	24.46	0.47
	15-H	27.08	26.61	0.47
	11-C	36.18	32.97	3.21
	4-C	48.12	44.99	3.13
	2-C	48.29	48.13	0.16
	3-C	51.00	53.71	-2.71
	1-C	79.01	73.18	5.83
	8-N	85.17	74.69	10.48
	13-N	171.85	165.03	6.82
	6-F	301.55	303.73	-2.18



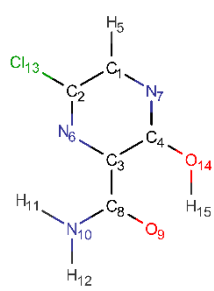
1-Cl



1-Br

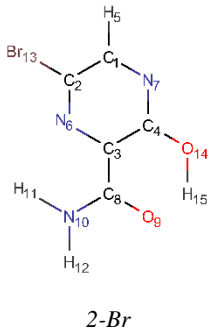


2-F



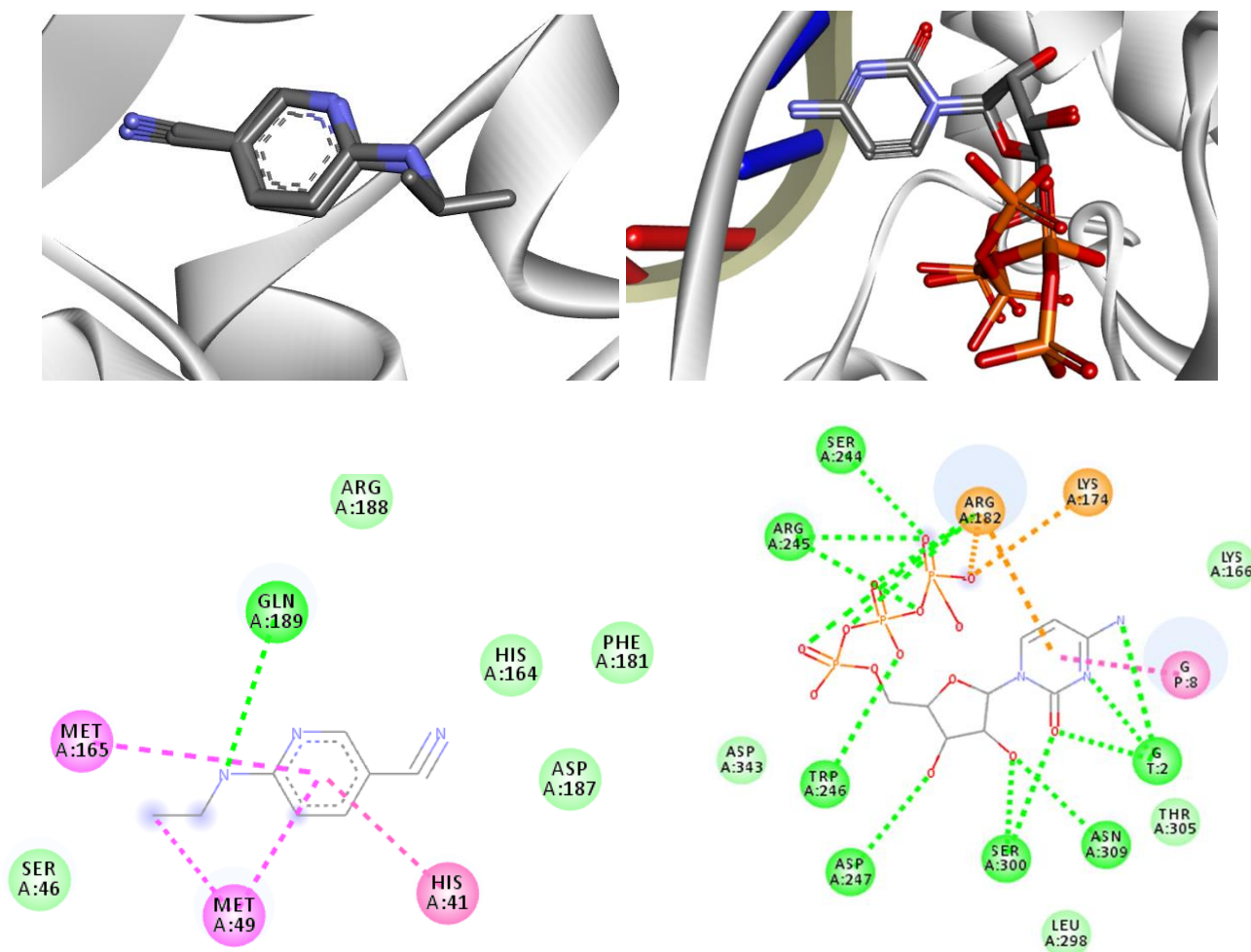
2-Cl

6-N	-67.44	-71.64	4.20
11-O	-64.36	-7.16	-57.20
9-O	-35.90	16.12	-52.02
8-H	23.71	22.74	0.97
5-H	24.62	24.04	0.58
13-H	24.93	24.46	0.47
14-H	27.10	26.64	0.46
10-C	36.37	33.16	3.21
4-C	48.75	45.66	3.09
3-C	48.76	51.05	-2.29
2-C	63.68	63.07	0.61
1-C	66.99	61.93	5.06
7-N	80.44	71.40	9.04
12-N	172.46	165.63	6.83
15-Cl	708.05	709.13	-1.08
6-N	-73.15	-78.22	5.07
11-O	-66.76	-4.09	-62.67
9-O	-37.07	15.66	-52.73
8-H	23.61	22.67	0.94
5-H	24.46	23.91	0.55
13-H	24.60	24.13	0.47
14-H	27.06	26.61	0.45
10-C	37.34	34.27	3.07
4-C	49.03	45.73	3.30
3-C	50.48	52.34	-1.86
1-C	63.45	58.69	4.76
2-C	65.41	64.33	1.08
7-N	76.38	67.91	8.47
12-N	173.11	166.53	6.58
15-Br	2213.46	2212.032	-1998.57
10-O	-54.27	-4.43	-49.84
8-N	-47.51	-46.56	-0.95
7-N	-29.68	-28.50	-1.18
5-H	23.62	23.33	0.29
12-H	24.39	23.98	0.41
15-H	25.52	25.02	0.50
13-H	26.83	26.35	0.48
9-C	36.61	33.93	2.68
4-C	39.07	38.86	0.21
2-C	40.63	40.58	0.05
1-C	62.54	59.77	2.77
3-C	67.54	68.03	-0.49
11-N	170.19	163.66	6.53
14-O	190.07	196.21	-6.14
6-F	282.12	285.63	-3.51
6-N	-61.30	-60.84	-0.46
9-O	-52.74	-3.71	-49.03
7-N	-41.79	-40.70	-1.09
5-H	23.57	23.32	0.25
11-H	24.31	23.91	0.40
15-H	25.53	25.02	0.51
12-H	26.84	26.36	0.48
8-C	36.27	33.62	2.65
4-C	38.52	38.23	0.29
2-C	49.23	49.08	0.15
1-C	51.29	49.11	2.18
3-C	65.03	65.38	-0.35
10-N	169.91	163.55	6.36
14-O	189.35	195.18	-5.83
13-Cl	686.88	689.91	-3.03



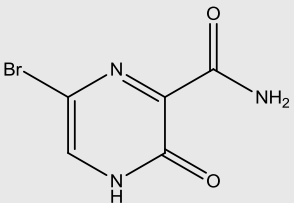
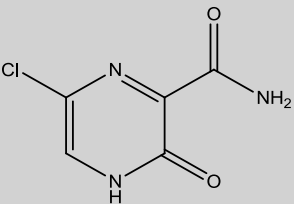
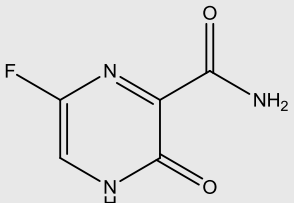
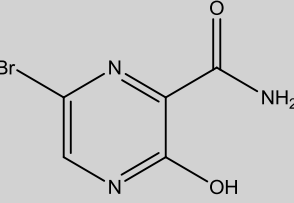
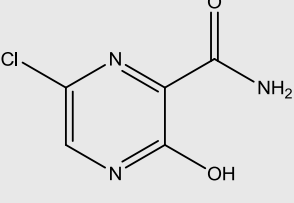
6-N	-67.78	-67.52	-0.26
9-O	-52.47	-3.52	-48.95
7-N	-41.34	-40.11	-1.23
5-H	23.43	23.20	0.23
11-H	24.30	23.89	0.41
15-H	25.56	25.04	0.52
12-H	26.83	26.36	0.47
8-C	36.39	33.75	2.64
4-C	37.97	37.70	0.27
2-C	48.40	48.12	0.28
1-C	48.60	46.62	1.98
3-C	63.70	64.03	-0.33
10-N	170.51	164.07	6.44
14-O	189.30	195.14	-5.84
13-Br	2182.22	2185.65	-3.43

In order to analyze the interaction modes that our drug candidates performed with SARS-CoV-2, the crystal structures of the viral M<sup>pro</sup> in complex with 6-(ethylamino) pyridine-3-carbonitrile and RdRp polymerase in complex with cytidine-5'-triphosphate were downloaded from Protein Data Bank (PDB), codes 5R82 and 3H5Y, respectively [59,60]. As the enzymes were prepared, the molecular docking protocol was started. Thus, to evaluate the ability of the algorithm to predict possible ligand orientations, re-docking calculations were performed using the MolAr software [51], with the implementation of the AutoDock Vina program [50]. As such, the values extracted from RMSD (5R82 = 0.94 Å / 3H5Y = 1.55 Å) indicated that Vina was able to predict the conformation that the co-crystallized ligands adopted experimentally within the SARS-CoV-2 M<sup>pro</sup> active site and SARS-CoV-2 RdRp polymerase. Thus, the re-docking overlaps are shown in **Figure 6**. All computed interaction energy results are shown in **Table 5**.



**Figure 6.** Re-docking overlaps and representation of the interactions performed by co-crystallized 6-(ethylamino)pyridine-3-carbonitrile for SARS-CoV-2 M<sup>pro</sup> and cytidine-5'-triphosphate for SARS-CoV-2 RdRp sites. Interactions: green= Hydrogen bond, pink = hydrophobic and orange= coulombians. Image generated in the Discovery Studio Software 4.5 <https://discover.3ds.com/discovery-studio-visualizer-download>.

**Table 5.** Intermolecular interaction energies obtained through Vina.

Compounds	Intermolecular interaction energy (kcal mol <sup>-1</sup> )	
	RdRp (PDB:3H5Y)	M <sup>pro</sup> (PDB:5R82)
 <b>1-Br</b>	-6.5	-4.4
 <b>1-Cl</b>	-6.5	-4.4
 <b>1-F</b>	-6.4	-4.8
 <b>2-Br</b>	-6.3	-4.6
 <b>2-Cl</b>	-6.3	-4.6

 <p style="text-align: center;"><b>2-F</b></p>	-6.3	-4.7
---	------	------

According to **Table 5**, all drug candidates studied (i.e., favipiravir and its derivatives in both tautomeric forms) interacted well with the SARS-CoV-2 RdRp site, with interaction energy values in the range of -6.3 to -6.5 kcal mol<sup>-1</sup>, respectively. These studied compounds showed lower interaction energy values than the co-crystallized ligand (-3.5 kcal mol<sup>-1</sup>) within the SARS-CoV-2 RdRp site, indicating that these compounds are very promising for the inhibition of this molecular target. Regarding the M<sup>P<sup>ro</sup></sup> enzyme, the studied compounds showed interaction energy values in a range of -4.4 to -4.8 kcal mol<sup>-1</sup>, respectively. However, these values were not lower than the co-crystallized ligand (-9.2 kcal mol<sup>-1</sup>). In general, it is noteworthy that the studied compounds had a good affinity within the active site of the molecular targets, but this class of compounds interacts better with the enzyme SARS-CoV-2 RdRp site.

Regarding interactions in the SARS-CoV-2 RdRp, the 1-Br and 1-Cl compounds showed the same interaction energy value, -6.5 kcal mol<sup>-1</sup>, being more stable than the other compounds, that is, they have settled very well in their place. Particularly, they performed hydrogen bonding interactions with Ser300, Asp247, Asp343, Trp246, Asn309, and G8, as well as Coulombian interactions with Arg182 and hydrophobic interactions with G2 and G8, respectively. It was also observed that these compounds interact with both the enzyme and RNA, remaining well accommodated in the 3H5Y site. These intermolecular interactions carried out by these compounds are important for the inhibition of this molecular target, and this can be corroborated by the interactions performed by the co-crystallized ligand at the 3H5Y site [59], as shown in **Figure 6**.

In relation to the SARS-CoV-2 RdRp site, the compounds 2-Br, 2-Cl and 2-F had the same interaction energy value (-6.3 kcal mol<sup>-1</sup>), performing interactions with Arg182, Trp246, Asn309, Asp343, G8 and G2 (**Figure 7**). In this case, the Favipiravir compound presented energy of about -6.4 kcal mol<sup>-1</sup> and made interactions with Arg182, Trp246, Asn309, Asp343 and G8. A remarkable trend can be observed from these results, all tautomers (1-F, 1-Br and 1-

Cl) showed better stability than their native forms (2-F, 2-Br and 2-Cl), that is, the tautomeric form of these compounds is very reactive at the SARS-CoV-2 RdRp site. Also, note that all of our drug candidates had key interactions for good affinity in the SARS-CoV-2 RdRp binding pocket, so we can suggest that favipiravir and its derivatives can effectively inhibit RNA polymerase, and in addition, being considered promising compounds for the treatment of COVID-19.

Regarding interactions at M<sup>pro</sup>, it was observed that the compound favipiravir was the one that best interacted with this enzyme, with an intermolecular interaction energy value of around  $-4.8 \text{ kcal mol}^{-1}$ . As such, this compound performed two hydrogen bonds with His164 and Arg188, Coulombian with Cys145 and hydrophobic interactions with Met165 and His41, as well. It is worth mentioning, according to the literature [61], that these residues are fundamental for inhibition of the viral M<sup>pro</sup> (**Figure 6 and 8**). In the case of the 1-Br compound, in particular, was the one that least interacted at the M<sup>pro</sup> active site in relation to the other compounds. According to our results, this compound performing interactions with Cys145, His41, Met49 and His154 (see **Table 5**). As shown in **Figure 8**, the other compounds also performed interactions with the aforementioned residues. It was observed that the tautomerism was not very significant for reactivity in this case. In general, our main objective was to determine whether the studied inhibitors could target the M<sup>pro</sup> enzyme. The molecular coupling posture of each drug candidate indicated that they could, in fact, fit precisely in the substrate binding pocket.

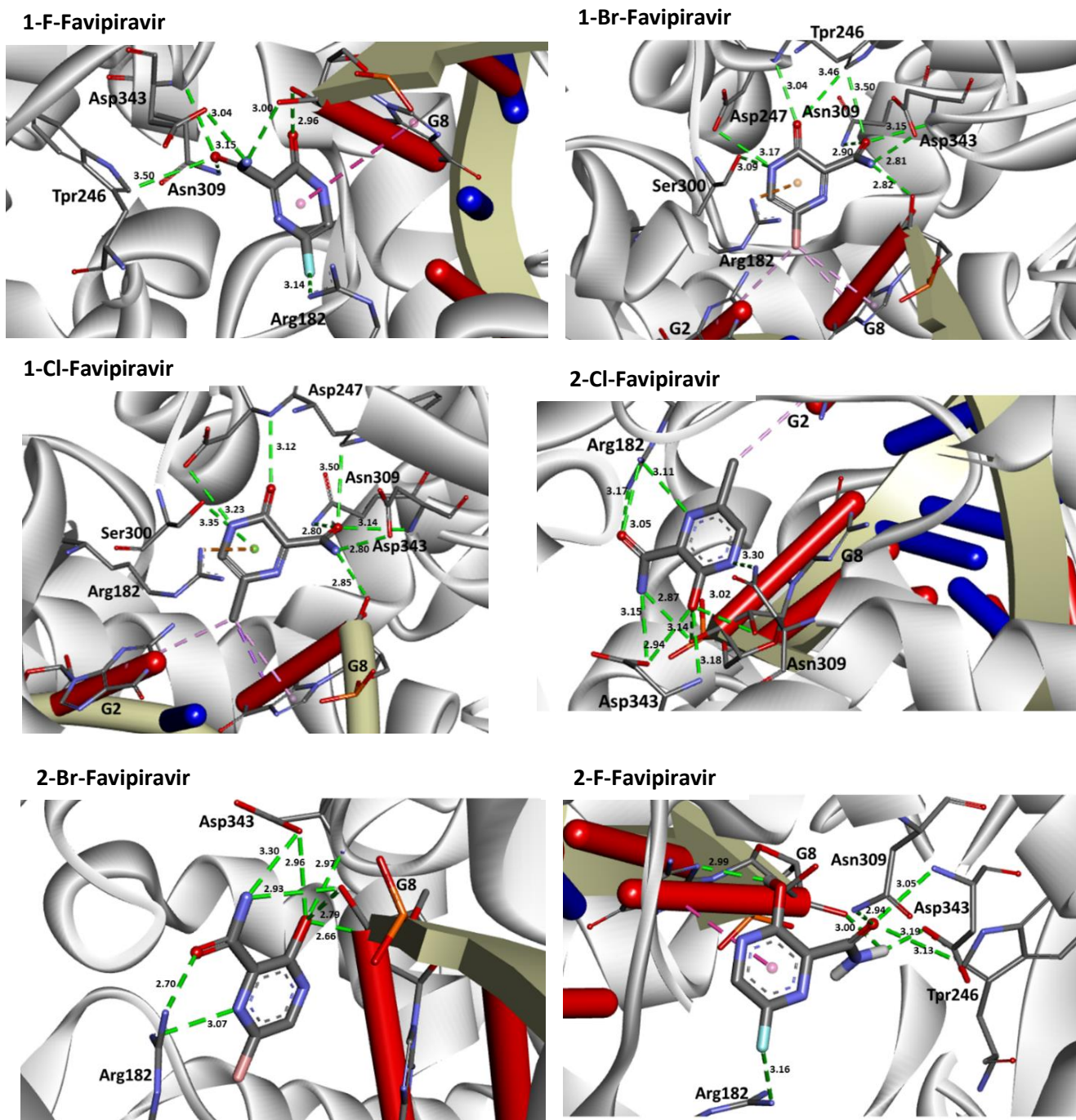
The ADMET profile (absorption, distribution, metabolism, excretion and toxicity) was obtained, and the results for each compound are shown in Table 6. Lipinski's rule of 5 (RO5) [62] was used to evaluate the potential of these favipiravir derivatives as orally active drugs in humans, where it establishes that a molecule to be a good drug must present values for 4 parameters multiple of 5: log P greater than or equal to 5, Molecular Mass less than or equal to 500, hydrogen bond acceptors less than or equal to 10 and binding donors hydrogen less than or equal to 5. We can note that the favipiravir derivatives violate the rules of maximum octanol / water partition coefficient. In addition, these compounds in their native form are more toxic than their tautomers and the halogens substitution have a significantly effect on the toxicity of these studied compounds. Therefore, these compounds have considerable drug potential.



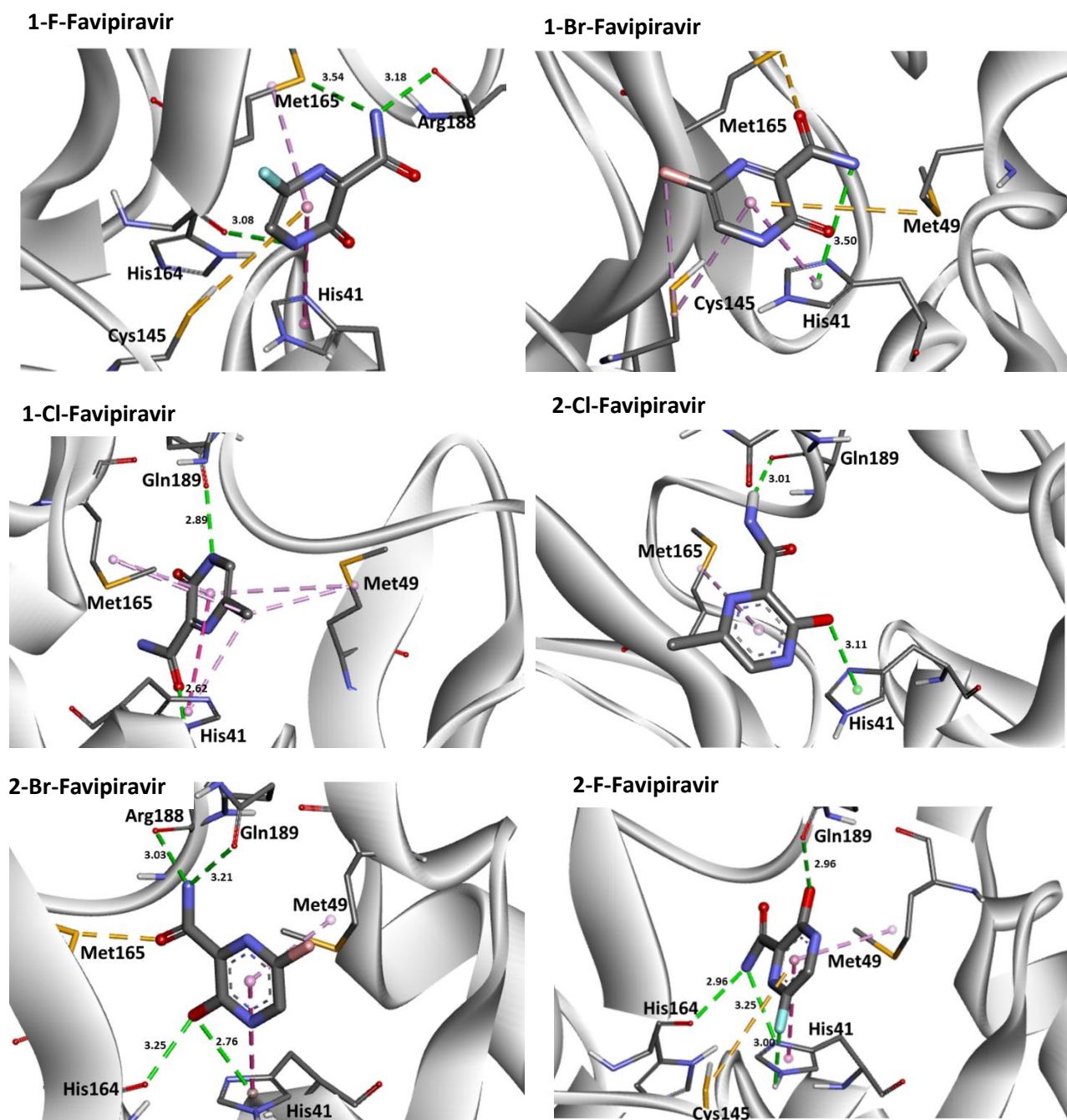
**Table 6.** ADMET profile of selected favipiravir derivatives.

Comp.	MW	logP	D.H/ A.H	logS	Intestinal Absortion (%)	CNS	Tox. (LD <sub>50</sub> )
<b>1-F</b>	157.10	-0.99	2/3	-1.45	86.80	-3.06	1.92
<b>1-Cl</b>	173.56	-0.48	2/3	-1.94	87.00	-3.07	2.12
<b>1-Br</b>	218.01	-0.37	2/3	-2.03	86.95	-3.06	2.13
<b>2-F</b>	157.10	-0.58	2/4	-1.88	86.04	-3.12	1.52
<b>2-Cl</b>	173.56	-0.06	2/4	-2.29	86.59	-3.11	1.8
<b>2-Br</b>	218.01	0.04	2/4	-2.36	86.53	-3.11	1.81

Comp = Compounds favipiravir derivatives. ADME parameters: MW = molecular weight, D.H = number of Hbonds donors, A.B. = number of Hbonds acceptors, logP = partition coefficient, logS = predicted aqueous solubility, CNS = predicted central nervous system, Tox= Oral Rat Acute Toxicity (mol Kg<sup>-1</sup>).



**Figure 7.** Representation of the interactions performed by favipiravir and its derivatives in the SARS-CoV-2 RNA polymerase site. Image generated in the Discovery Studio Software 4.5 <https://discover.3ds.com/discovery-studio-visualizer-download>.



**Figure 8.** Representation of the interactions performed by favipiravir and its derivatives in the M<sup>pro</sup> active site. Image generated in the Discovery Studio Software 4.5 <https://discover.3ds.com/discovery-studio-visualizer-download>.

## CONCLUSIONS

In conclusion, we have studied the electronic structure and spectroscopic properties of halogenated favipiravir tautomeric forms. These results are compatible with reported theoretical-experimental data (when available), allowing for a complete distinction in both tautomeric forms. Therefore, in this study, these effects were evaluated in order to consider favipiravir and its metabolic derivatives, since this compound has recently been used for the treatment of COVID-19. All halogenated favipiravir tautomeric forms were investigated against the SARS-CoV-2 using both M<sup>Pro</sup> and RdRp sites as model systems. Since all molecules have shown RNA-inhibiting properties, generating potential candidates for the COVID-19 treatment. Hence, we strongly recommend that future in silico studies address both biological targets, what could certainly contribute for the development of new therapies based on the combined use of drugs.

### Authors' Contributions

Letícia Cristina Assis, Alexandre Alves de Castro and João Paulo Almirão de Jesus performed the theoretical calculations, data analysis, elaboration of initial versions of this manuscript and figures preparation; Elaine Fontes Ferreira da Cunha, Teodorico Castro Ramalho and Felipe de Almeida La Porta contributed in the technical-scientific evaluation of the final version and adjustments of language requirements.

### Acknowledgments and Funding

The authors wish to thank the Brazilian financial agencies Conselho Nacional de Desenvolvimento Científico e Tecnológico (CNPq), Fundação de Amparo ao Ensino e Pesquisa de Minas Gerais (FAPEMIG) and Coordenação de Aperfeiçoamento de Pessoal de Nível Superior/Ministério da Defesa (CAPES/MD) for financial support, and the Federal University of Lavras (UFLA) for providing the physical infrastructure and working space. Also supported by excellence project FIM UHK.

### Competing interests

The authors declare no conflict of interest.

**REFERENCES**

1. Assis, L.C.; Castro, A.A. de; Jesus, J.P.A. de; Nepovimova, E.; Kuca, K.; Ramalho, T. de C.; Porta, F. de A. La Nitro derivatives of quinoline and quinoline N-oxide as low-cost alternative for the treatment of SARS-CoV-2 infection 2020.
2. Li, G.; De Clercq, E. Therapeutic options for the 2019 novel coronavirus (2019-nCoV). *Nat. Rev. Drug Discov.* 2020, *19*, 149–150.
3. Zhou, P.; Yang, X. Lou; Wang, X.G.; Hu, B.; Zhang, L.; Zhang, W.; Si, H.R.; Zhu, Y.; Li, B.; Huang, C.L.; et al. A pneumonia outbreak associated with a new coronavirus of probable bat origin. *Nature* 2020, *579*, 270–273.
4. Campos, E.V.R.; Pereira, A.E.S.; de Oliveira, J.L.; Carvalho, L.B.; Guilger-Casagrande, M.; de Lima, R.; Fraceto, L.F. How can nanotechnology help to combat COVID-19? Opportunities and urgent need. *J. Nanobiotechnology* 2020, *18*, 125.
5. Daré, J.K.; Silva, D.R.; Ramalho, T.C.; Freitas, M.P. Conformational fingerprints in the modelling performance of MIA-QSAR: a case for SARS-CoV protease inhibitors. *Mol. Simul.* 2020, *46*, 1055–1061.
6. Ton, A.; Gentile, F.; Hsing, M.; Ban, F.; Cherkasov, A. Rapid Identification of Potential Inhibitors of SARS-CoV-2 Main Protease by Deep Docking of 1.3 Billion Compounds. *Mol. Inform.* 2020, *39*, 2000028.
7. Elfiky, A.A. SARS-CoV-2 RNA dependent RNA polymerase (RdRp) targeting: an in silico perspective. *J. Biomol. Struct. Dyn.* 2020, 1–9.
8. Aftab, S.O.; Ghouri, M.Z.; Masood, M.U.; Haider, Z.; Khan, Z.; Ahmad, A.; Munawar, N. Analysis of SARS-CoV-2 RNA-dependent RNA polymerase as a potential therapeutic drug target using a computational approach. *J. Transl. Med.* 2020, *18*, 275.
9. Alexpandi, R.; De Mesquita, J.F.; Pandian, S.K.; Ravi, A.V. Quinolines-Based SARS-CoV-2 3CLpro and RdRp Inhibitors and Spike-RBD-ACE2 Inhibitor for Drug-Repurposing Against COVID-19: An in silico Analysis. *Front. Microbiol.* 2020, *11*.
10. Eastman, R.T.; Roth, J.S.; Brimacombe, K.R.; Simeonov, A.; Shen, M.; Patnaik, S.; Hall, M.D. Remdesivir: A Review of Its Discovery and Development Leading to Emergency Use Authorization for Treatment of COVID-19. *ACS Cent. Sci.* 2020, *6*, 672–683.

11. Jin, Z.; Du, X.; Xu, Y.; Deng, Y.; Liu, M.; Zhao, Y.; Zhang, B.; Li, X.; Zhang, L.; Peng, C.; et al. Structure of Mpro from SARS-CoV-2 and discovery of its inhibitors. *Nature* **2020**, *582*, 289–293.
12. Hoffmann, M.; Kleine-Weber, H.; Schroeder, S.; Krüger, N.; Herrler, T.; Erichsen, S.; Schiergens, T.S.; Herrler, G.; Wu, N.-H.; Nitsche, A.; et al. SARS-CoV-2 Cell Entry Depends on ACE2 and TMPRSS2 and Is Blocked by a Clinically Proven Protease Inhibitor. *Cell* **2020**, *181*, 271–280.e8.
13. Zhang, H.; Penninger, J.M.; Li, Y.; Zhong, N.; Slutsky, A.S. Angiotensin-converting enzyme 2 (ACE2) as a SARS-CoV-2 receptor: molecular mechanisms and potential therapeutic target. *Intensive Care Med.* **2020**, *46*, 586–590.
14. Letko, M.; Marzi, A.; Munster, V. Functional assessment of cell entry and receptor usage for SARS-CoV-2 and other lineage B betacoronaviruses. *Nat. Microbiol.* **2020**, *5*, 562–569.
15. Khan, R.J.; Jha, R.K.; Amera, G.M.; Jain, M.; Singh, E.; Pathak, A.; Singh, R.P.; Muthukumar, J.; Singh, A.K. Targeting SARS-CoV-2: a systematic drug repurposing approach to identify promising inhibitors against 3C-like proteinase and 2'-O-ribose methyltransferase. *J. Biomol. Struct. Dyn.* **2020**, 1–14.
16. Ruch, T.R.; Machamer, C.E. The Coronavirus E Protein: Assembly and Beyond. *Viruses* **2012**, *4*, 363–382.
17. Gao, Y.; Yan, L.; Huang, Y.; Liu, F.; Zhao, Y.; Cao, L.; Wang, T.; Sun, Q.; Ming, Z.; Zhang, L.; et al. Structure of the RNA-dependent RNA polymerase from COVID-19 virus. *Science (80- )*. **2020**, *368*, 779–782.
18. Wu, C.; Liu, Y.; Yang, Y.; Zhang, P.; Zhong, W.; Wang, Y.; Wang, Q.; Xu, Y.; Li, M.; Li, X.; et al. Analysis of therapeutic targets for SARS-CoV-2 and discovery of potential drugs by computational methods. *Acta Pharm. Sin. B* **2020**, *10*, 766–788.
19. Park, M.; Thwaites, R.S.; Openshaw, P.J.M. COVID-19: Lessons from SARS and MERS. *Eur. J. Immunol.* **2020**, *50*, 308–311.
20. Dong, L.; Hu, S.; Gao, J. Discovering drugs to treat coronavirus disease 2019 (COVID-19). *Drug Discov. Ther.* **2020**, *14*, 58–60.
21. Castro, A. de; Assis, L.; Ramalho, T.; Porta, F. La New in silico insights into the

- application of the (hydroxy)chloroquine with macrolide antibiotics co-crystals against the SARS-CoV-2 virus 2020.
22. De Clercq, E. New Nucleoside Analogues for the Treatment of Hemorrhagic Fever Virus Infections. *Chem. Asian J.* **2019**, *14*, 3962–3968.
  23. Furuta, Y.; Komeno, T.; Nakamura, T. Favipiravir (T-705), a broad spectrum inhibitor of viral RNA polymerase. *Proc. Jpn. Acad. Ser. B. Phys. Biol. Sci.* **2017**, *93*, 449–463.
  24. Mifsud, E.J.; Hayden, F.G.; Hurt, A.C. Antivirals targeting the polymerase complex of influenza viruses. *Antiviral Res.* **2019**, *169*, 104545.
  25. Jin, Z.; Smith, L.K.; Rajwanshi, V.K.; Kim, B.; Deval, J. The ambiguous base-pairing and high substrate efficiency of T-705 (Favipiravir) Ribofuranosyl 5'-triphosphate towards influenza A virus polymerase. *PLoS One* **2013**, *8*, e68347.
  26. Abuo-Rahma, G.E.-D.A.; Mohamed, M.F.A.; Ibrahim, T.S.; Shoman, M.E.; Samir, E.; Abd El-Baky, R.M. Potential repurposed SARS-CoV-2 (COVID-19) infection drugs. *RSC Adv.* **2020**, *10*, 26895–26916.
  27. Kiso, M.; Takahashi, K.; Sakai-Tagawa, Y.; Shinya, K.; Sakabe, S.; Le, Q.M.; Ozawa, M.; Furuta, Y.; Kawaoka, Y. T-705 (favipiravir) activity against lethal H5N1 influenza A viruses. *Proc. Natl. Acad. Sci.* **2010**, *107*, 882 LP – 887.
  28. Furuta, Y.; Takahashi, K.; Shiraki, K.; Sakamoto, K.; Smee, D.F.; Barnard, D.L.; Gowen, B.B.; Julander, J.G.; Morrey, J.D. T-705 (favipiravir) and related compounds: Novel broad-spectrum inhibitors of RNA viral infections. *Antiviral Res.* **2009**, *82*, 95–102.
  29. Cai, Q.; Yang, M.; Liu, D.; Chen, J.; Shu, D.; Xia, J.; Liao, X.; Gu, Y.; Cai, Q.; Yang, Y.; et al. Experimental Treatment with Favipiravir for COVID-19: An Open-Label Control Study. *Engineering* **2020**.
  30. Harismah, K.; Mirzaei, M. Favipiravir: Structural Analysis and Activity against COVID-19. *Adv. J. Chem. B* **2020**, *2*, 55–60.
  31. Antonov, L. Favipiravir tautomerism: a theoretical insight. *Theor. Chem. Acc.* **2020**, *139*, 145.
  32. Mendes, J.; de Almeida, K.J.; Neto, J.L.; Ramalho, T.C.; Duarte, H.A. Theoretical

- spectroscopic insights of tautomers and enantiomers of penicillamine. *Spectrochim. Acta Part A Mol. Biomol. Spectrosc.* **2017**, *184*, 308–317.
33. Timm, R.A.; Bonacin, J.A.; Formiga, A.L.B.; Toma, H.E. A theoretical study of the tautomerism and vibrational spectra of 4,5-diamine-2,6-dimercaptopyrimidine. *J. Braz. Chem. Soc.* **2008**, *19*, 287–292.
  34. Erdoğan, Ş.; Işın, D.Ö. Theoretical Study on the Self- and Water-Assisted Proton Transfer Reaction of Urazole. *Chem. Heterocycl. Compd.* **2014**, *50*, 986–997.
  35. Pliego, J.; Rufino, V. Mechanisms of the Formation of Imines in Aqueous Solution and the Effect of the pH: A Theoretical Analysis. *Arkivoc* **2020**, 2020.
  36. Puzzarini, C.; Barone, V. Diving for Accurate Structures in the Ocean of Molecular Systems with the Help of Spectroscopy and Quantum Chemistry. *Acc. Chem. Res.* **2018**, *51*, 548–556.
  37. Vishveshwara, S. Impact of theoretical chemistry on chemical and biological sciences. *Resonance* **2014**, *19*, 347–367.
  38. Pierrefixe, S.C.A.H.; Poater, J.; Im, C.; Bickelhaupt, F.M. Hypervalent versus nonhypervalent carbon in noble-gas complexes. *Chemistry* **2008**, *14*, 6901–6911.
  39. M. J. Frisch, G. W. Trucks, H. B. Schlegel, G. E. Scuseria, M. A. Robb, J. R. Cheeseman, G. Scalmani, V. Barone, G. A. Petersson, H. Nakatsuji, X. Li, M. Caricato, A. Marenich, J. Bloino, B. G. Janesko, R. Gomperts, B. Mennucci, H. P. Hratchian, J. V. Ort, W.C. Gaussian, Inc., Wallingford CT 2009.
  40. Miertuš, S.; Scrocco, E.; Tomasi, J. Electrostatic interaction of a solute with a continuum. A direct utilization of AB initio molecular potentials for the prevision of solvent effects. *Chem. Phys.* **1981**, *55*, 117–129.
  41. Miertuš, S.; Tomasi, J. Approximate evaluations of the electrostatic free energy and internal energy changes in solution processes. *Chem. Phys.* **1982**, *65*, 239–245.
  42. London, F. Théorie quantique des courants interatomiques dans les combinaisons aromatiques. *J. Phys. le Radium* **1937**, *8*, 397–409.
  43. McWeeny, R. Perturbation Theory for the Fock-Dirac Density Matrix. *Phys. Rev.* **1962**, *126*, 1028–1034.



44. Ditchfield, R. Self-consistent perturbation theory of diamagnetism. *Mol. Phys.* **1974**, *27*, 789–807.
45. Wolinski, K.; Hinton, J.F.; Pulay, P. Efficient implementation of the gauge-independent atomic orbital method for NMR chemical shift calculations. *J. Am. Chem. Soc.* **1990**, *112*, 8251–8260.
46. Cheeseman, J.R.; Trucks, G.W.; Keith, T.A.; Frisch, M.J. A comparison of models for calculating nuclear magnetic resonance shielding tensors. *J. Chem. Phys.* **1996**, *104*, 5497–5509.
47. Grimme, S. Towards First Principles Calculation of Electron Impact Mass Spectra of Molecules. *Angew. Chemie Int. Ed.* **2013**, *52*, 6306–6312.
48. Koopman, J.; Grimme, S. Calculation of Electron Ionization Mass Spectra with Semiempirical GFNn-xTB Methods. *ACS Omega* **2019**, *4*, 15120–15133.
49. van Mourik, T.; Bühl, M.; Gageot, M.-P. Density functional theory across chemistry, physics and biology. *Philos. Trans. A. Math. Phys. Eng. Sci.* **2014**, *372*, 20120488.
50. Trott, O.; Olson, A.J. AutoDock Vina: improving the speed and accuracy of docking with a new scoring function, efficient optimization, and multithreading. *J. Comput. Chem.* **2010**, *31*, 455–461.
51. Maia, E.H.B.; Medaglia, L.R.; da Silva, A.M.; Taranto, A.G. Molecular Architect: A User-Friendly Workflow for Virtual Screening. *ACS omega* **2020**, *5*, 6628–6640.
52. Webb, B.; Sali, A. Comparative Protein Structure Modeling Using MODELLER. *Curr. Protoc. Bioinforma.* **2016**, *54*, 5.6.1-5.6.37.
53. Novoselov, K.P.; Shirabaikin, D.B.; Umanskii, S.Y.; Vladimirov, A.S.; Minushev, A.K.; Korkin, A.A. CHIMERA: A software tool for reaction rate calculations and kinetics and thermodynamics analysis. *J. Comput. Chem.* **2002**, *23*, 1375–1389.
54. Accelrys Software Discovery Studio Modeling Environment 2012.
55. Shi, F.; Li, Z.; Kong, L.; Xie, Y.; Zhang, T.; Xu, W. Synthesis and crystal structure of 6-fluoro-3-hydroxypyrazine-2-carboxamide. *Drug Discov. Ther.* **2014**, *8*, 117–120.
56. Rhyman, L.; Tursun, M.; Abdallah, H.H.; Choong, Y.S.; Parlak, C.; Kharkar, P.; Ramasami, P. Theoretical investigation of the derivatives of favipiravir (T-705) as

- potential drugs for Ebola virus. *Phys. Sci. Rev.* **3**, 20170198.
57. Sahoo, H. Förster resonance energy transfer – A spectroscopic nanoruler: Principle and applications. *J. Photochem. Photobiol. C Photochem. Rev.* **2011**, *12*, 20–30.
58. Sedgwick, A.C.; Wu, L.; Han, H.-H.; Bull, S.D.; He, X.-P.; James, T.D.; Sessler, J.L.; Tang, B.Z.; Tian, H.; Yoon, J. Excited-state intramolecular proton-transfer (ESIPT) based fluorescence sensors and imaging agents. *Chem. Soc. Rev.* **2018**, *47*, 8842–8880.
59. Zamyatkin, D.F.; Parra, F.; Machín, A.; Grochulski, P.; Ng, K.K.-S. Binding of 2'-amino-2'-deoxycytidine-5'-triphosphate to norovirus polymerase induces rearrangement of the active site. *J. Mol. Biol.* **2009**, *390*, 10–16.
60. Berman, H.M.; Westbrook, J.; Feng, Z.; Gilliland, G.; Bhat, T.N.; Weissig, H.; Shindyalov, I.N.; Bourne, P.E. The Protein Data Bank. *Nucleic Acids Res.* **2000**, *28*, 235–242.
61. Yang, H.; Yang, M.; Ding, Y.; Liu, Y.; Lou, Z.; Zhou, Z.; Sun, L.; Mo, L.; Ye, S.; Pang, H.; et al. The crystal structures of severe acute respiratory syndrome virus main protease and its complex with an inhibitor. *Proc. Natl. Acad. Sci. U. S. A.* **2003**, *100*, 13190–13195.
62. Lipinski, C.A.; Lombardo, F.; Dominy, B.W.; Feeney, P.J. Experimental and computational approaches to estimate solubility and permeability in drug discovery and development settings. *Adv. Drug Deliv. Rev.* **1997**, *23*, 3–25.

## CHAPTER 6

### *Research article*

Effect of drug metabolism in the treatment of SARS-CoV-2 from an entirely  
computational perspective

*Submitted to Nature Scientific Reports*

## ABSTRACT

Understanding the effects of metabolism on the rational design of novel and more effective drugs is still a considerable challenge. To the best of our knowledge, there are no entirely computational strategies that make it possible to predict these effects. From this perspective, the development of such methodologies could contribute to significantly reduce the side effects of medicines, leading to the emergence of more effective and safer drugs. Thereby, in this study, our strategy is based on simulating the electron ionization mass spectrometry (EI-MS) fragmentation of the drug molecules and combined with molecular docking and ADMET models in two different situations. In the first model, the drug is docked without considering the possible metabolic effects. In the second model, each of the intermediates from the EI-MS results is docked, and metabolism occurs before the drug accesses the biological target. As a proof of concept, in this work, we investigate the main antiviral drugs used in clinical research to treat COVID-19. As a result, our strategy made it possible to assess the biological activity and toxicity of all potential by-products. We believed that our findings provide new chemical insights that can benefit the rational development of novel drugs in the future.

## Introduction

Since the start of the last year, the novel coronavirus SARS-CoV-2, which is responsible for the disease designated like Coronavirus Disease 2019 (abbreviated as, COVID-19), has led to the death of over 2.7 million peoples.<sup>1-10</sup> Moreover, the pandemic significantly impacted regular operations and economies of several countries, ultimately affecting millions of people both directly and indirectly. To combat the disease, the scientific community is developing vaccines and medicines; however, to date, there is no proven effective treatment for COVID-19.<sup>1-9</sup> Considering the increasing global caseload, there is substantial pressure to discover and develop new antiviral drugs and vaccines to treat COVID-19.

Recent studies suggest that the structure of the SARS-CoV-2 virus is suitable for hosting interactions between its active sites and other molecules. The current focus of new drug treatments is to target the essential areas of the virus, including the Spike (S) protein, 3C-like protease (3CLpro), papain-like protease (PLpro), RNA-dependent RNA polymerase (RdRp), and also serine protease TMPRSS2.<sup>1,3-7</sup> Molecules that show favourable interactions with the active sites of these proteins may inhibit their enzymatic activities and hinder the essential mechanism of viral pathogenicity. Possible candidates for the treatment of COVID-19 include

the antiviral drugs Favipiravir, Galidesivir, Nitazoxanide, Remdesivir, Ribavirin, Chloroquine, and Hydroxychloroquine due to their ability for the enzymatic inhibition of SARS-CoV-2.<sup>7-13</sup>

In addition to the effectiveness of a particular drug in the treatment of a disease, drug design must also consider xenobiotics, or the mechanism via which the by-products of a medicine interact with and exit the human body.<sup>14-17</sup> As is well known, the general mechanism of xenobiotics involves three main phases: Phase I, drug activation through oxidation, reduction, and hydrolysis; Phase II, drug inactivation by means of conjugation with proteins to yield water-soluble metabolites that can be eliminated from the body; and Phase III, biotransformation by enzymes before the waste leaves the body.<sup>14-17</sup> However, predicting the details of this effect remains a challenge.

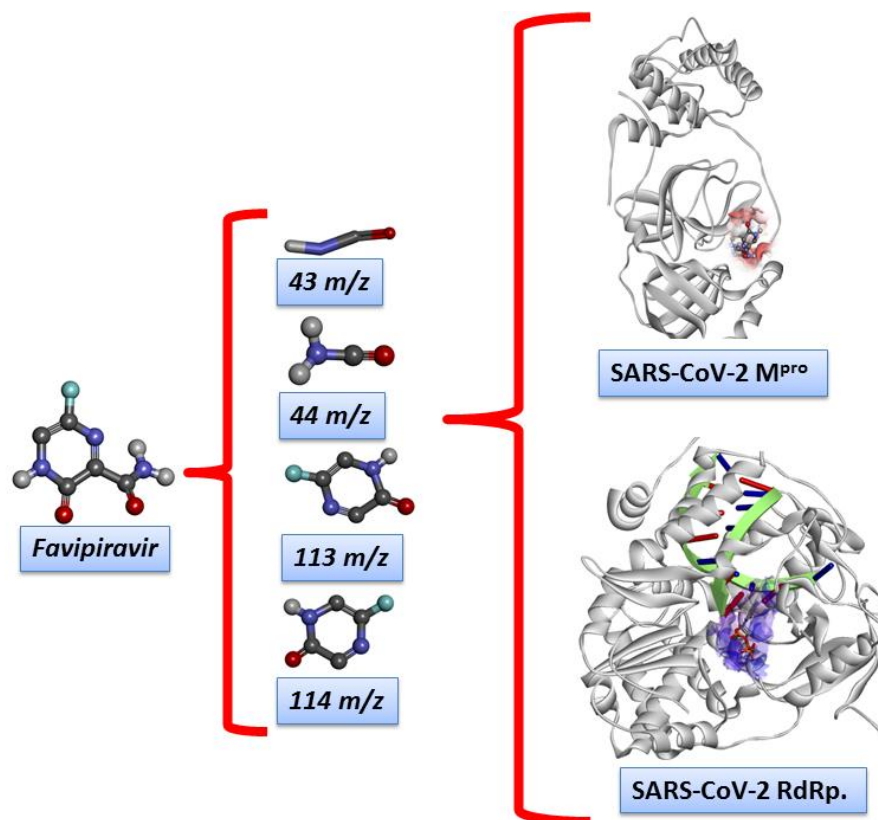
The present work proposes a theoretical methodology to predict the potential by-products of the abovementioned drugs used to treat COVID-19. This novel method simulates the electron ionization mass spectrometry (EI-MS) fragmentation of the drug molecules used to treat COVID-19 and evaluates the structures of the intermediates to explain the possible xenobiotic metabolism for each species. These results revealed two different molecular docking models to inhibit the main protease ( $M^{pro}$ ) and RdRp of the SARS-CoV-2 virus. In the first model, the drug is docked without considering the possible metabolic effects. In the second model, each of the intermediates from the EI-MS results is docked, and metabolism occurs before the drug accesses the biological target. To the best of our knowledge, this is the first study to present an entirely theoretical approach for modelling drug metabolism in the treatment of COVID-19. Therefore, we present a novel methodology that may contribute to the design of new drugs.

### **Computational models and methods**

All structures were fully optimized and confirmed as a minimum of potential energy by means of the Density Functional Theory (DFT) method at the B3LYP level with the 6-31+G(d,p) basis set. These optimized structures were then used in all subsequent calculations, including energy calculations were carried out through Time-Dependent DFT (TD-DFT). All of DFT and TDDFT calculations were performed on Gaussian 09 package.<sup>18</sup> Then, the trajectories of fragmentation and computed EI-MS spectrum for the main antiviral drugs used in COVID-19 treatment were predicted by the QCEIMS program,<sup>19,20</sup> and these results were visualized in Grace software (<https://plasma-gate.weizmann.ac.il/Grace/>). For these

simulations, two semiempirical methods (GFN1-xTB and GFN2-xTB) were initially considered for the Chloroquine and Hydroxychloroquine drugs and compared with experimental data.<sup>20</sup> In both cases, the GFN2-xTB method better reproduces experimental data, as shown in **Figure S1** of supplementary material, being therefore chosen for the calculations of all compounds investigated in this study. In all cases, the total simulation time was 5 ps, initial temperature of the vaporized substrate of 500 K, and impact excess energy of 0.6 eV atom<sup>-1</sup>.<sup>19,20</sup> From the computed EI-MS spectrum were identified the intermediaries' structures and plotted in the Avogadro code.<sup>21</sup> All 2D structures were drawn in the MarvinSketch 20.10 software (<https://chemaxon.com/products/marvin>).

Three different molecular docking models were prepared in this study as strategy to investigate the possible metabolic effects, as shown in **Figure 1**, and all these calculations were performed with the tool AutoDock Vina (version 1.1.2),<sup>22</sup> as implemented in the MolAr (Molecular Architecture) software.<sup>23</sup> The crystallographic M<sup>pro</sup> and RdRp structures used in this simulation were prepared according to our previous studies.<sup>12,13,24</sup> Based on this strategy, we also investigate the absorption, distribution, mechanism, excretion, and toxicity (ADMET) properties for antiviral target drugs and their by-products metabolic. Thereby, the acute toxicity and other relevant pharmacokinetics parameters can easily be obtained from a rat model-based admetSAR predictor (<http://biosig.unimelb.edu.au/pkcsmprediction>). This ADMET procedure has been used previously in similar systems with large success.<sup>12,13,25</sup>



**Figure 1.** Schematic representation of computational strategy proposed in this study to the investigation of the metabolism effect in drug design. The strategy used to build these models have based on three different situations: (a) no previous metabolism and (b) prior effect of metabolism to the inhibitory process.

## Results and discussions

In this work, we proposed a novel strategy to predict the metabolism of the possible by-products of the drugs cited in the introduction session.

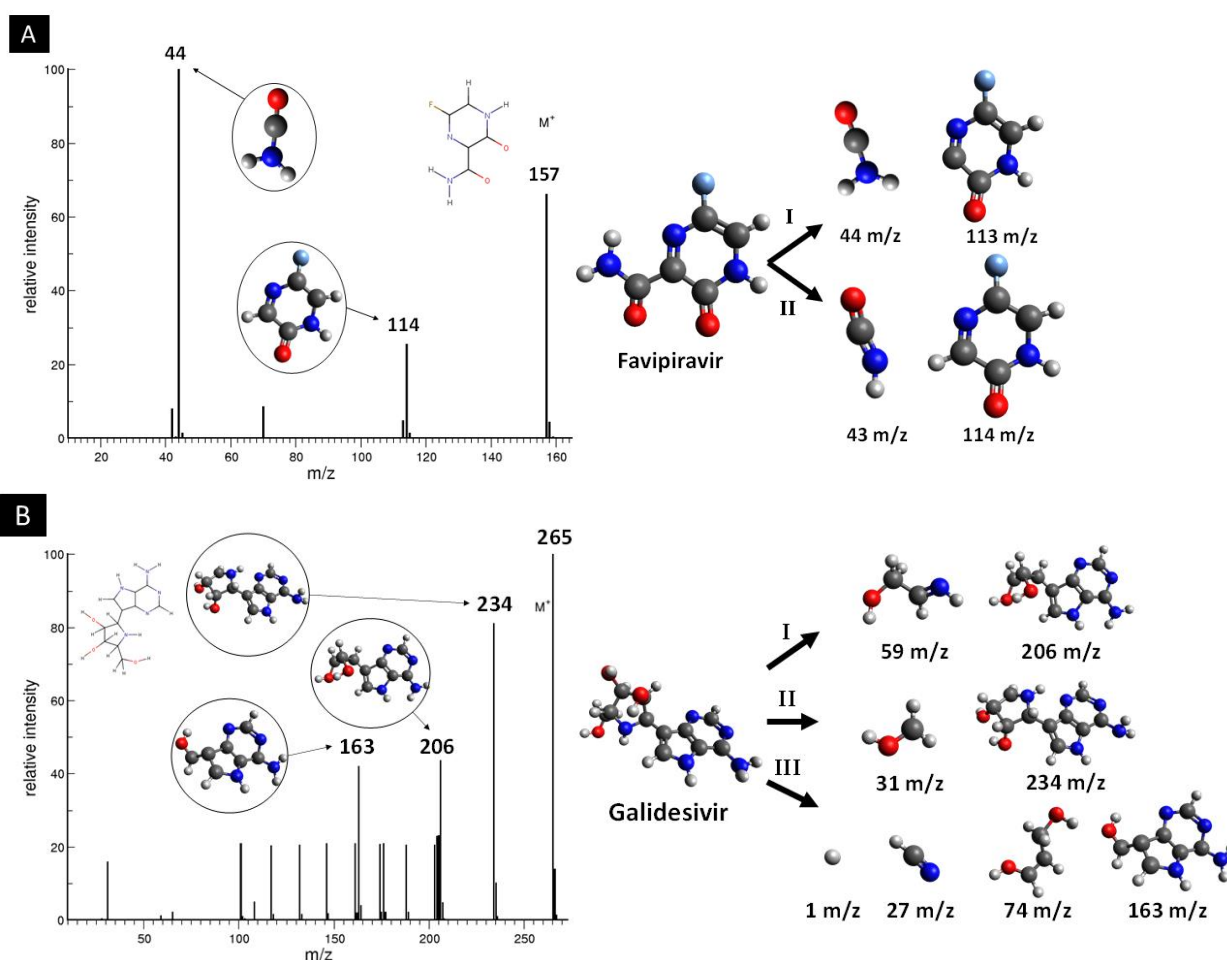
As seen in the **Figure S5 (a)**, the EI-MS diagram from the GFN2-xTB method, in principle, presented most of the intermediaries of the Chloroquine molecule, in agreement with the experimental data profile (NIST MS 42361), with slight deviation of intensity. The most intense signal 86 m/z and its respective intermediary are also identified in the theoretical plot and the resultant trajectory described. As for the Hydroxychloroquine spectra in **Figure S5 (b)**, the most intense peaks from the experimental data (NIST MS 246973) are not identified in the theoretical data, still, some of the signals are found with distinct intensity from the experimental spectra. In order to evaluate the results between the theoretical methods, **Figure S5 (c)** shows

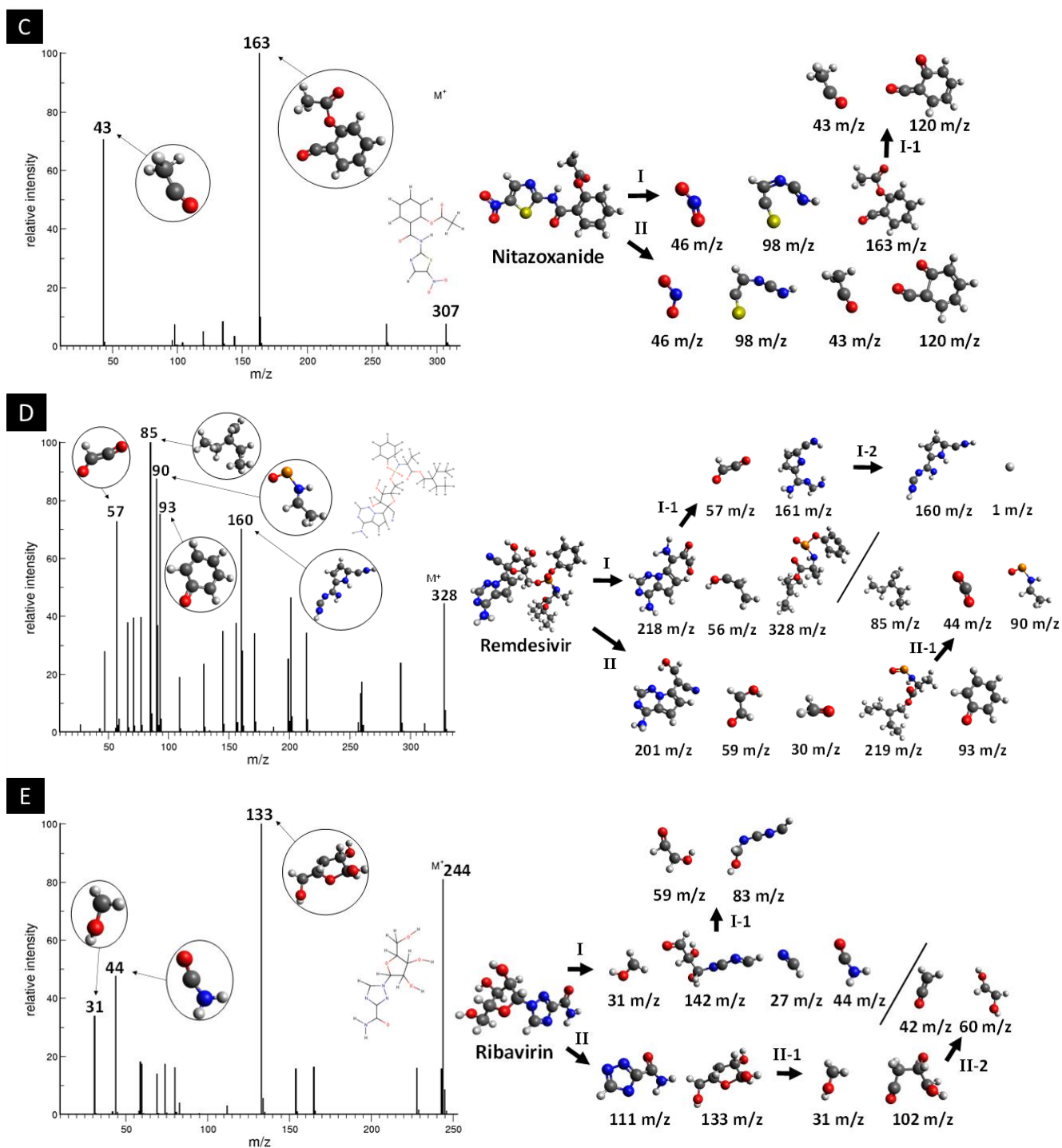
the EI-MS spectra of the Chloroquine obtained using the GFN1-xTB method in comparison with the same experimental profile. In this manner, the spectra from the GFN1-xTB did not match the intermediaries mass/charge rate and intensity as well as its analog method, revealing that the GFN2-xTB is the best option for this calculation. Transitioning to the Hydroxychloroquine in **Figure S5 (d)**, the spectra acquired from the GFN1-xTB approach did not show significant improvements over the GFN2-xTB, and the most intense signals of the NIST profile are not identified as well. In general, an increasing on the molecular dynamics parameters could lead to a better prediction of the EI-MS spectra and its intermediaries in exchange of meaningful computational cost, however, as the current methodology with GFN2-xTB provided satisfactory results for the Chloroquine drug, it has been chosen as the default semiempirical method to the study of the other drugs.

Henceforth, the discussion of the EI-MS spectra and trajectories will be done in the context of xenobiotics metabolism, evaluating the obtained intermediaries as drug by-products, their metabolism and toxicity when possible. Thus, returning to the Chloroquine drug, the spectra and trajectories are shown in **Figure S5 (a)**. The Chloroquine molecule contains polar amine and chloride groups in its structure, showing an aromatic region with more polar character than the other extremity. The first trajectory showed the fragmentation of Chloroquine around the amine that bond the aromatic and the alkane regions, leading to the following intermediaries: the I-177 m/z 7-chloro-4-aminoquinoline, containing the aromatic region, deprotonated amine and chloride polar groups, is a toxic and major metabolite from the oxidation of Chloroquine by the cytochrome P-450 enzyme;<sup>26,27</sup> the deprotonated I-57 m/z butane and I-29 m/z ethane, both nonpolar hydrocarbons which can be oxidized into polar species in Phase I of metabolism; and the I-56 m/z deprotonated amine, a polar and likely water-soluble molecule that may metabolize directly in Phase II. The trajectory II leads to the high molecular mass fragment II-233 m/z similar to the I-177 m/z, with an alkane extremity that may be target of oxidation in Phase I; and the II-86 m/z, the specie also identified in the experimental spectra, show very low polar character and may be almost insoluble in water, possible target of oxidative reactions in Phase I metabolism before conjugation in Phase II. The last trajectory for Chloroquine gives the following intermediaries: the III-205 m/z, a specie like the I-177 m/z and II-233 m/z, with a shorter alkane segment which may be oxidized in Phase I, and share the behavior of its analog molecules; the deprotonated organic molecules III-29 m/z ethane and III-28 m/z ethene, both nonpolar and likely targets to oxidizing reactions in Phase I, leading to polar conjugates to metabolize in Phase II; and the protonated form of I-56 m/z.



The **Figure S5 (b)** shows the EI-MS spectra and unique trajectory of the Hydroxychloroquine drug. The molecular structure of this drug is a more polar analog of the Chloroquine due to the addition of a hydroxide group. The calculations for the Hydroxychloroquine resulted in a single trajectory: the I-142 m/z, a deprotonated aminoquinoline similar to the 7-chloro-4-aminoquinoline from the metabolization of Quinoline, which is a metabolite from the Hydroxychloroquine;<sup>28</sup> the I-35 m/z chloride ion; and the I-144 m/z, with polar amine and alcohol groups, and the nonpolar extremities likely submitted to oxidative reactions in Phase I that may lead to smaller and polar fragments. This last fragment is further cleaved into two more species: the I-1-31 m/z molecule, which is deprotonated into a highly water-soluble and toxic formaldehyde form, being rapidly metabolized into formate by the alcohol dehydrogenase enzyme;<sup>29,30</sup> and the I-1-113 m/z, an amine with pentane and ethane extremities, and a possible target for Phase I oxidative reactions that have as products smaller and polar molecules, further being transformed into metabolites in Phase II.





**Figure 2.** EI-MS fragmentation spectra and trajectories of a) Favipiravir, b) Galidesivir, c) Nitazoxanide, d) Remdesivir and e) Ribavirin.

As shown for the Chloroquine and Hydroxychloroquine, the theoretical EI-MS calculations done with our methodology were able to predict the main metabolites of these drugs, the 7-chloro-4-aminoquinoline and aminoquinoline, respectively. In this framework, we

suggest a possible metabolism pathway for the Favipiravir, Galidesivir, Nitazoxanide, Remdesivir, and Ribavirin drugs, as they are receiving substantial attention due to the SARS-CoV-2 outbreak. In our previous work, we estimated the EI-MS spectra and identified the possible trajectories for the Favipiravir molecule and its tautomers.<sup>12</sup> In the current work, we expanded our analysis to evaluate each intermediary species' biochemical activity. The computed EI-MS spectrum of Favipiravir has two main trajectories that yield similar species (**Figure 2 (a)**). The fragments shown in Trajectory I are the unstable analogues of Trajectory II; thus, the existence of the II-43 m/z and II-114 m/z species is the most probable mechanism. The fragments in Trajectory I are easily transformed into Trajectory II via the exchange of protons between the molecules due to the difference in charge. Both fragments obtained in Trajectory II are polar and water-soluble due to hydrogen bonds in the C=O, N-H, and C=N groups, respectively.<sup>31,32</sup> Therefore, the Favipiravir waste molecules can be directly transformed into metabolites through conjugation with proteins in Phase II of the metabolism.

**Figure 2 (b)** shows three trajectories for Galidesivir. The structure of Galidesivir includes several polar groups showing two extremities with alcohol and amine groups. Consequently, the molecular structure is fragmented around the alcohol extremity, resulting in a main cyclic molecule, including the amine extremity and other smaller linear by-products with hydroxide groups. The heavier fragments I-206 m/z, II-234 m/z, and III-163 m/z consist of several polar groups, including O-H, N-H, N-H<sub>2</sub>, and C=N. These are soluble in water due to hydrogen bonds and are efficiently metabolized in Phase II. It is possible that Phase I hydrolysis can also occur in the O-H and N-H groups, leading to smaller polar fragments. Regarding the smaller by-products of Galidesivir, the I-59 m/z fragment is easily transformed into a metabolite due to its polar O-H and N-H groups. The II-31 m/z fragment is unstable in its present form, and it transfers a proton to its main molecule to adopt a formaldehyde form. The III-74 m/z fragment is stable and water-soluble due to the diol group in its extremity. However, the III-27 m/z fragment is hydrogen cyanide, a water-soluble and extremely poisonous molecule. It is well known for its inhibition of oxidative phosphorylation through binding with the cytochrome enzyme, halting the aerobic metabolism.<sup>33</sup> The III-1 m/z fragment is a proton, which is unlikely to exist in this form and may bond to its respective III-163 m/z molecule. The results show that all the waste molecules from the alcohol extremity of Galidesivir are directly metabolised in Phase II, without the need for Phase I transformations. However, due to the possible toxic by-products, we encourage further studies of this molecule from an experimental perspective.

The computed EI-MS spectra and trajectories for Nitazoxanide are shown in **Figure 2 (c)**. The molecular structure of this drug includes multiple polar functional groups, such as nitro, sulphide, amine, amide, and ester. Nitazoxanide fragmentation predominantly occurs at the amide carbonyl, pentacyclic carbon, and nitro groups, resulting in three main species. The I-163 m/z fragment is polar (due to the ester and carbonyl groups) and highly nucleophilic due to the carbonyl group, and it most probably exists in a protonated form, and hence expected to be oxidized in Phase I of metabolism. The I-98 m/z fragment is nucleophilic (due to two amines and one sulphide groups) and probably exists in an isomer form due to proton transfer among the N-H and the C-S extremity, both with significant polarity. The I-46 m/z fragment is a polar and highly reactive nitro radical that quickly transforms into other species. The I-163 m/z fragment may separate into two nucleophilic by-products, the I-1-120 m/z and I-1-43 m/z fragments, both of which are polar and easily protonated. In particular, the I-1-120 m/z fragment stabilization through proton acceptance, likely to be moderately water-soluble due to its polar carbonyl and ketone groups, and may suffer oxidative reactions in Phase I metabolism before its synthesis step. This results in alcohol in the case of the I-1-120 m/z fragment. While the I-1-43 m/z fragment, is protonated into the water-soluble and toxic acetaldehyde in an acid environment, further metabolized into acetic acid by the aldehyde dehydrogenases enzyme.<sup>34</sup> The by-products are the same for Trajectory II. All the waste products attributed to nitazoxanide have significant polarity. Therefore, they can easily transform into metabolites during the xenobiotic metabolism processes.

The computed EI-MS spectrum and trajectories for Remdesivir are illustrated in **Figure 2 (d)**. The molecular structure of this drug is large and contains amine, alcohol, ether, ester, and diazo groups. Hence, Remdesivir is cleaved around the sulfur centre, leading to two major molecules, the I-218 m/z fragment (similar to the II-201 m/z fragment), I-328 m/z fragment (related to the II-219 m/z fragment), and other smaller fragments. Trajectory I resulted in three molecules: an I-218 m/z fragment with most of the amine, carbonyl, aldehyde (previously alcohol), and diazo polar groups; an I-328 m/z fragment with a polar PNO<sub>2</sub><sup>-</sup> centre, and ester groups and nonpolar extremities; and an I-56 m/z alcohol fragment, being directly metabolized in Phase II by synthesis with glutathione enzyme.<sup>35</sup> All these species are deprotonated during fragmentation and may be re-protonated in an acidic environment. In Trajectory I, the I-218 m/z can be further separated into two other polar molecules: the I-1-57 m/z fragment, which can be stabilized into an ethylene dione by means of deprotonation; however, experimental and theoretical studies suggest that this molecule is extremely short-lived and quickly dissociated

into two CO molecules,<sup>36</sup> and the I-1-161 m/z fragment, which contains only amine groups due to the cleavage of the diazo group. As such, the I-2-160 m/z fragment is unlikely to exist. Instead, the I-1-161 m/z can be stabilized through intramolecular proton transfer, showing the possibility of hydrolyzation through these sites or direct metabolization in Phase II. The intermediates in Trajectory II are structurally similar to those of Trajectory I, resulting in the following deprotonated fragments: the II-201 m/z fragment, an analogue to the I-218 m/z fragment with polar amine, diazo, and alcohol groups; II-59 m/z fragment, a polar deprotonated diol; the II-30 m/z fragment, a polar and toxic formaldehyde; the II-219 m/z fragment, an unstable molecule similar to the I-328 m/z fragment without the phenolate ring and containing  $\text{PON}^{2-}$  and ester groups at its polar extremities; and the II-93 m/z fragment, a phenolate that may exist in a barely water-soluble and toxic phenol form.<sup>37</sup> Then, the II-219 m/z intermediary is posteriorly cleaved into three other by-products: the nonpolar II-1-85 m/z alkene, the nonpolar II-1-44 m/z carbon dioxide, and the polar and unstable II-1-90 m/z fragment with the  $\text{PON}^{2-}$  group. From these results, we can infer that most of the waste by-products of Remdesivir are polar species and can be transformed into metabolites via conjugation with the metabolism proteins. The II-93 m/z and II-1-85 m/z fragments, which are nonpolar or barely polar, are targets of oxidative reactions in Phase I, leading to water-soluble polar products that can be further transformed into metabolites in Phase II.

The data obtained in the EI-MS calculations of Ribavirin are shown by the **Figure 2 (e)**. The molecular structure of this drug contains alcohol, ether, diazo, amine, and amide groups along the molecule. Trajectory I shows a more fragmented path resulted from the electron ionization process than II: a I-31 m/z specie, that similar to the case of Galidesivir, can be further deprotonated into polar and toxic formaldehyde; the I-142 m/z with polar aldehyde, alcohol, and amine groups, which is unstable and may accept two protons, a likely water-soluble specie that may directly synthesize metabolites in Phase II metabolism; the I-27 m/z extremely poison and polar hydrogen cyanide, as also shown for Galidesivir; and the I-44 m/z, which can be further protonated into water-soluble formamide, a very important specie with role in the synthesis of nucleic bases, phosphorylation of nucleosides and other essential biological mechanism.<sup>38-40</sup> The I-142 m/z can be further dissociated into two more fragments: the I-1-59 m/z, accepting a proton and transforming into the same diol as shown for Remdesivir II-59 m/z; and the I-1-83 m/z, a deprotonated form with amine and alcohol groups and thus possibly water-soluble, likely metabolized in Phase II. Trajectory II leads to the II-111 m/z, a molecule with a polar nitrogenous ring and amide extremity, and the II-133 m/z, a polar oxygenated fragment

with alcohol and ether groups, expecting appreciable water solubility and conjugation with proteins in Phase II of metabolism for both species. As such, the II-133 m/z fragment can be further cleaved, resulting in the II-1-31 m/z, lately being deprotonated into formaldehyde, and the II-1-102 m/z, a deprotonated polar molecule and possibly water-soluble due to its alcohol groups, also participating in Phase II. Additionally, the II-1-102 m/z fragment is after dissociated into II-2-42 m/z water-soluble and toxic ethenone,<sup>41</sup> and the II-2-60 m/z molecule, the same diol formed from Remdesivir II-59 m/z.

As such, the metabolism process for some relatively large molecules, yet unexplored by the literature, was predicted in this study and likely might be obtained by oxidation or hydrolysis reactions in Phase I or directly in Phase II. These results, however, showed various intermediary molecules with different toxicity levels. Hence, the metabolism study may give insight into the drug's possible counter-effects due to the metabolites' respective known reactions in the human organism.

### Docking results and ADMET

To investigate the interaction modes that our drug candidates performed with viral M<sup>pro</sup> and RdRp of SARS-CoV-2 (PDB codes 5R82 and 3H5Y), respectively.<sup>42,43</sup> In order to assess the ability of the algorithm to predict likely ligand orientations, in particular, re-docking calculations were then performed in this study using the MolAr software,<sup>23</sup> with the implementation of the AutoDock Vina program.<sup>22</sup> As a result, it is important to note that the values extracted from RMSD (5R82 = 0.94 Å / 3H5Y = 1.55 Å) showed that the program used in this study is adequate for predicting the conformation that the co-crystallized ligands adopted experimentally within the viral M<sup>pro</sup> and RdRp of SARS-CoV-2.<sup>12,13,25</sup> The re-docking configurations were maintained to perform the docking calculations of the drugs investigated as well as their metabolism fragments. All computed interaction energy results are exhibited in **Table 1**.

**Table 1.** Interaction energy (in kcal mol<sup>-1</sup>) of drugs and their metabolism fragments computed through AutoDock Vina program.

<b>Drugs</b>	<b>Metabolism fragments</b>	<b>Interaction Energy (M<sup>pro</sup> / kcal mol<sup>-1</sup>)</b>	<b>Interaction Energy (RdRp / kcal mol<sup>-1</sup>)</b>
<b>Favipiravir</b>		-4.8	-6.5
	44 m/z	-1.9	-2.7
	113 m/z	-3.7	-4.8
	43 m/z	-2.0	-2.8
<b>Galidesivir</b>	114 m/z	-3.7	-4.9
		-3.9	-8.1
	59 m/z	-2.4	-3.2
	206 m/z	-4.7	-7.1
	31 m/z	-1.5	-2.1
	234 m/z	-4.3	-7.7
	27 m/z	-1.1	-1.3
	74 m/z	-2.6	-3.5
	163 m/z	-4.6	-6.0
		-5.6	-7.9
	<b>Nitazoxanide</b>	43 m/z	-1.8
120 m/z		-4.0	-5.0
46 m/z		-2.0	-3.1
98 m/z		-2.8	-3.5
163 m/z		-4.3	-5.9
		-4.9	-9.9
<b>Remdesivir</b>	57 m/z	-2.1	-2.9
	161 m/z	-4.4	-6.2
	160 m/z	-4.6	-6.7
	218 m/z	-4.1	-7.4
	56 m/z	-2.3	-3.2
	328 m/z	-3.4	-7.6
	85 m/z	-2.8	-3.3
	44 m/z	-1.7	-2.6
	90 m/z	-2.5	-3.4
	201 m/z	-5.0	-6.8
	59 m/z	-2.3	-3.0
	30 m/z	-1.3	-1.8
	219 m/z	-4.1	-5.7
	93 m/z	-3.5	-4.5
<b>Ribavirin</b>		-4.6	-7.7
	59 m/z	-2.3	-3.0
	83 m/z	-2.8	-3.9
	31 m/z	-1.5	-2.1

	142 m/z	-4.0	-5.3
	27 m/z	-1.1	-1.3
	44 m/z	-2.0	-2.7
	60 m/z	-2.4	-3.1
	111 m/z	-4.0	-5.2
	133 m/z	-3.7	-5.1
	102 m/z	-3.2	-4.3
<b>Chloroquine</b>		-2.9	-6.9
	29 m/z	-1.3	-1.6
	56 m/z	-2.0	-2.5
	57 m/z	-2.1	-2.8
	177 m/z	-4.5	-6.3
	86 m/z	-2.6	-3.1
	233 m/z	-3.2	-6.3
	28 m/z	-1.3	-1.6
	205 m/z	-4.2	-6.5
<b>Hydroxychloroquine</b>		-3.2	-7.3
	142 m/z	-4.6	-6.2
	144 m/z	-	-
	113 m/z	-3.1	-3.9
	31 m/z	-1.5	-2.1

As shown in **Table 1**, all drugs investigated and their fragments stably interacted within the viral M<sup>Pro</sup> (with interaction energy values in the range of 0 to -5.6 kcal mol<sup>-1</sup>) and RdRp sites (with interaction energy values in the range of 0 to -9.9 kcal mol<sup>-1</sup>). In addition, the ADMET results are shown in **Table 2**.

**Table 2.** ADMET profile of diverse anti-viral drugs and their metabolism fragments.

Compounds	MS Fragments	Molecular Weight	logP	D.H/ A.H	logS (mol L <sup>-1</sup> )	Intestinal Absorption (%)	CNS	LD <sub>50</sub> (mol Kg <sup>-1</sup> )
<b>Favipiravir</b>		157.104	-0.992	2/3	-2.103	81.635	-3.111	1.929
	44 m/z	47.057	-1.105	2/2	1.465	84.154	-2.696	1.878
	113 m/z	114.079	-0.091	1/2	-0.781	94.787	-2.932	2.131
	43 m/z	43.025	-0.099	2/1	0.747	94.232	-2.638	2.200
	114 m/z	116.095	-0.517	1/2	-0.001	100	-2.996	2.208
<b>Galidesivir</b>		267.289	-1.847	7/7	-2.467	45.167	-4.859	2.548



	59 m/z	59.068	-0.372	2/2	0.967	85.397	-2.910	1.996
	206 m/z	208.221	-0.755	5/5	-2.394	65.857	-3.948	2.338
	31 m/z	32.042	-0.392	1/1	1.075	98.165	-2.566	2.029
	234 m/z	237.263	-1.208	6/6	-2.626	58.026	-4.036	2.509
	27 m/z	27.026	0.140	1/0	0.162	100	-2.375	2.351
	74 m/z	76.095	-0.639	2/2	0.973	84.782	-2.841	1.522
	163 m/z	170.216	-2.148	4/5	-1.142	65.04	-3.959	2.081
<b>Nitazoxanide</b>		307.287	2.229	1/7	-3.826	79.029	-2.979	2.472
	43 m/z I	46.069	-0.001	1/1	0.782	98.262	-2.611	2.028
	120 m/z	122.123	0.663	0/2	-0.501	100	-2.681	1.862
	46 m/z	49.029	-0.646	3/3	1.299	77.865	-3.499	2.359
	98 m/z	106.194	-0.578	3/3	0.821	81.893	-2.996	2.244
	163 m/z	168.192	1.250	0/3	-0.868	100	-2.887	1.891
	43 m/z II	46.069	-0.001	1/1	0.782	98.262	-2.611	2.028
<b>Remdesivir</b>		602.585	2.312	13/13	-3.56	43.813	-5.006	2.213
	57 m/z	58.036	-0.110	2/1	1.199	95.919	-2.705	2.030
	161 m/z	166.208	-2.321	8/4	-1.112	56.409	-3.974	1.992
	160 m/z	169.232	-1.675	4/5	-1.091	54.990	-4.000	2.029
	218 m/z	223.236	-2.129	3/7	-1.957	63.682	-3.675	2.226
	56 m/z	60.096	0.389	1/1	0.360	96.667	-2.537	1.984
	328 m/z	329.333	3.123	2/4	-3.279	89.124	-2.817	2.511
	85 m/z	86.178	2.442	0/0	-2.547	95.502	-2.113	1.944
	44 m/z	47.057	-1.105	2/2	1.465	84.154	-2.696	1.878
	90 m/z	93.066	0.097	2/2	0.311	93.366	-2.994	2.169
	201 m/z	203.205	-0.089	2/6	-2.983	76.079	-3.111	2.222
	59 m/z	62.068	-1.029	2/2	1.664	86.716	-2.932	1.857
	30 m/z	30.026	-0.185	1/0	0.722	100	-2.393	2.040
	219 m/z	219.221	2.151	1/3	-1.619	92.118	-2.947	3.026
	93 m/z	98.145	1.520	1/0	-0.963	97.244	-2.739	2.040
<b>Ribavirin</b>		166.208	-2.321	4/3	-1.112	56.409	-3.974	1.996
	59 m/z	60.052	-0.882	2/1	1.156	95.474	-2.743	1.846
	83 m/z	90.126	-1.297	3/3	0.140	80.546	-2.923	1.765
	31 m/z I	32.042	-0.392	1/1	1.075	98.165	-2.566	2.029

	142 m/z	144.130	-1.406	2/4	0.04	77.520	-3.167	1.914
	27 m/z	27.026	0.140	1/0	0.162	100	-2.375	2.351
	44 m/z	47.057	-1.105	2/2	1.465	84.154	-2.696	1.878
	60 m/z	62.068	-1.029	2/2	1.310	86.376	-2.916	1.570
	111 m/z	112.092	-1.096	2/3	-1.065	73.849	-3.903	1.900
	133 m/z	134.131	-1.553	3/4	-0.108	73.940	-3.855	1.215
	31 m/z II	32.042	-0.392	1/1	1.075	98.165	-2.566	2.029
	102 m/z	104.105	-1.071	2/3	1.030	81.777	-3.420	1.378
<b>Chloroquine</b>		319.880	4.811	3/1	-4.014	89.244	-2.963	2.982
	29 m/z	30.070	1.026	0/0	-0.623	100	-2.344	2.182
	56 m/z	59.112	0.226	1/1	0.452	100	-2.673	2.198
	57 m/z	57.096	0.707	1/0	-0.156	100	-2.505	2.277
	177 m/z	182.654	2.155	2/2	-1.710	88.700	-2.218	3.261
	86 m/z	87.166	0.958	1/0	-0.303	100	-2.807	2.173
	233 m/z	236.746	3.875	2/1	-2.174	88.330	-2.294	3.332
	28 m/z	30.070	1.026	0/0	-0.623	100	-2.344	2.182
	205 m/z	206.676	3.320	2/1	-3.236	91.953	-2.331	2.516
<b>Hydroxychloroquine</b>		321.852	3.740	4/2	-3.347	89.139	-2.194	2.770
	142 m/z	148.209	1.502	2/2	-1.437	90.287	-2.172	3.233
	144 m/z	145.246	1.488	2/1	-0.765	92.423	-2.900	2.123
	113 m/z	115.220	1.786	1/1	-1.367	93.158	-2.545	2.334
	31 m/z	32.042	-0.391	1/1	1.075	98.165	-2.566	2.029

\*ADMET parameters: log P = partition coefficient, D.H/A.H. = number of hydrogen bonds donors/acceptors, logS = predicted aqueous solubility, CNS = predicted central nervous system.

Our ADMET analysis (**Table 2**) shows that the drugs Favipiravir and Chloroquine are more toxic than their main fragments. Remdesivir has a toxicity similar to its main fragments. While the Hydroxychloroquine, Galidesivir, Nitazoxanide and Ribavirin are less toxic than their fragments. Further, comparing the median lethal dose (LD<sub>50</sub>) for all antiviral drugs studied, which showed the following order for the acute toxicity data Favipiravir > Ribavirin > Remdesivir > Nitazoxanide > Galidesivir > Hydroxychloroquine > Chloroquine. Thus, this study points out the importance of verifying the effects of these pharmacophoric groups

(fragments) for the contribution of developing new less toxic and more efficient drugs for the COVID-19 treatment.

### Favipiravir

According to our results, Favipiravir showed a more stabilizing interaction energy ( $-4.8 \text{ kcal mol}^{-1}$ ) in both SARS-CoV-2  $M^{\text{pro}}$  and RdRp binding sites, in comparison with its fragments. From our results, we can also notice that Favipiravir and its fragments had more stabilizing energies when docked in the RdRp binding site, in relation to our values found for the  $M^{\text{pro}}$  enzyme. This same trend can be observed for the other drugs investigated. Regarding the intermolecular interactions in the RdRp binding site, Favipiravir performed hydrogen bonds with the residues Asn309, Ser306, Asp343 and Arg182, and hydrophobic interaction with RNA (**Figure 3**). In addition, in the  $M^{\text{pro}}$  binding site, there were interactions with the residues Met165, His164, Cys145, His41 and Arg188 (**Figure 4**). In the RdRp binding site, as well as in the  $M^{\text{pro}}$  site, the fragments 113 m/z ( $M^{\text{pro}}$ :  $-3.7 \text{ kcal mol}^{-1}$ , RdRp:  $-4.8 \text{ kcal mol}^{-1}$ ) and 114 m/z ( $M^{\text{pro}}$ :  $-3.7 \text{ kcal mol}^{-1}$ , RdRp:  $-4.9 \text{ kcal mol}^{-1}$ ) showed the most stabilizing interaction energies in these target sites. These species also carried out the largest number of intermolecular interactions, like hydrophobic interactions and hydrogen/halogen bonds, as can be observed in **Figures S.6.1 and S.6.2** of supplementary material. According to the pharmacophoric graphs, the largest fragments of Favipiravir exhibited better interaction energies and a range of intermolecular interactions, probably due to the presence of more pharmacophoric groups in comparison with smaller fragments. In the RdRp site, it was observed different kinds of interaction with RNA from the fragments, such as hydrophobic interactions (fragments 43 m/z and 44 m/z), halogen bond (fragment 113 m/z) and hydrogen bond (fragment 114 m/z). From these results, we can observe that the bulkier fragments of Favipiravir more strongly interacted in the RdRp binding site. On the other hand, in the  $M^{\text{pro}}$  site, only the fragment 44 m/z interacted with both residues of the catalytic dyad (Cys145 and His41).

### Galidesivir

Regarding Galidesivir ( $M^{\text{pro}}$ :  $-3.9 \text{ kcal mol}^{-1}$ ), the docking of its fragments exhibited three species with more stabilizing interaction energies in the  $M^{\text{pro}}$  binding site, in comparison with the non-metabolized drug. These species were the fragments 206 m/z ( $M^{\text{pro}}$ :  $-4.7 \text{ kcal mol}^{-1}$ )

<sup>1</sup>, RdRp: -7.1 kcal mol<sup>-1</sup>), 234 m/z (M<sup>pro</sup>: -4.3 kcal mol<sup>-1</sup>, RdRp: -7.7 kcal mol<sup>-1</sup>) and 163 m/z (M<sup>pro</sup>: -4.6 kcal mol<sup>-1</sup>, RdRp: -6.0 kcal mol<sup>-1</sup>) (**Table 1**). Our findings, however, indicate that these fragments have a better affinity in the binding site of M<sup>pro</sup> than Galidesivir. On the other hand, in the RdRp, the non-metabolized drug showed a more stabilizing interaction energy than its fragments. In general, Galidesivir and its fragments showed a more stabilizing interaction in the RdRp binding site. By analysing the intermolecular interactions of Galidesivir in the RdRp site, this drug performed hydrogen bonds with Glu168 and RNA, and hydrophobic interactions with Arg182 and RNA (**Figure 3**). In the M<sup>pro</sup>, Galidesivir carried out a hydrogen bond with His164, in addition to hydrophobic interactions with Met49, Met165, His41 as well as His164 (**Figure 4**). The intermolecular interactions of its fragments can be observed in **Figures S.6.3 and S.6.4**. In the RdRp binding site, it is interesting to notice that most fragments presented hydrophobic interactions with RNA. In addition, several fragments showed hydrophobic interactions with the catalytic dyad in the M<sup>pro</sup> enzyme. These interactions are important for therapeutic activity.<sup>24</sup>

### Nitazoxanide

In this work, the interaction modes of a range of fragments of several drugs were analyzed toward the viral M<sup>pro</sup> enzyme and RdRp, and in the case of Nitazoxanide, differently from Galidesivir, the non-metabolized drug showed more stabilizing interactions than all fragments obtained through QCEIMS, being these values -5.6 kcal mol<sup>-1</sup> for M<sup>pro</sup> and -7.9 kcal mol<sup>-1</sup> for RdRp. The species with lower energies, that is, with more stabilizing energies, are the fragments 120 m/z (M<sup>pro</sup>: -4.0 kcal mol<sup>-1</sup>, RdRp: -5.0 kcal mol<sup>-1</sup>) and 163 m/z (M<sup>pro</sup>: -4.3 kcal mol<sup>-1</sup>, RdRp: -5.9 kcal mol<sup>-1</sup>). In general, when the non-metabolized drug is fragmented into larger fragments, these bulkier fragments often interact better in the binding site. Probably, this trend comes from the fact of these fragments present more pharmacophoric groups capable of performing intermolecular interactions in the target site. Note that this trend does not apply to all situations. For instance, another interesting fact is the possibility of some smaller fragments interact in a more stabilizing form due to the formation of charged atoms, favoring a specific kind of intermolecular interaction, that is, the well-known electrostatic interactions. This kind of interaction contributes to the total interaction energy of the ligand, in addition to the formation of stabilizing hydrogen bonds. Nitazoxanide performed hydrogen bonds with Arg182, Trp246, Asp343, Asp242 and Arg392 in the RdRp site, with no interactions with RNA (**Figure 3**). In the M<sup>pro</sup> active site, it was observed hydrogen bond interactions with Gln189 and

His164, and hydrophobic interactions with Cys145, Met49 and Met165 (**Figure 4**). According to the pharmacophoric graphs, the fragments carried out diverse intermolecular interactions. The fragments 43 m/z and 120 m/z interacted with RNA through hydrogen bonds, while the fragments 98 m/z and 163 m/z interacted through hydrophobic interactions (**Figures S.6.5**). In the viral M<sup>pro</sup> site, e.g. only the fragment 163 m/z interacted with both residues of the catalytic dyad (**Figures S.6.6**).

### Remdesivir

For Remdesivir (M<sup>pro</sup>: -4.9 kcal mol<sup>-1</sup>, RdRp: -9.9 kcal mol<sup>-1</sup>), this antiviral resulted in a big amount of fragments from the study of metabolism. Note that some of its fragments showed interaction energies very close to that of the non-metabolized drug. These species were the fragments 161 m/z (M<sup>pro</sup>: -4.4 kcal mol<sup>-1</sup>), 160 m/z (M<sup>pro</sup>: -4.6 kcal mol<sup>-1</sup>) and 201 m/z (M<sup>pro</sup>: -5.0 kcal mol<sup>-1</sup>), whose values highlighted here refer to the docking within the M<sup>pro</sup> enzyme. In turn, Remdesivir was significantly more stabilized in the binding site of RdRp than its fragments. Remdesivir and its fragments showed more stabilizing interaction energies in the RdRp binding site, as can be observed in **Table 1**. Regarding the intermolecular interactions, Remdesivir performed hydrogen bond interactions with the residues Asp343 and RNA, and hydrophobic interactions with Lys174, Lys180, Phe70, Arg182 and RNA in the RdRp site (**Figure 3**). As well, this drug interacted with Cys145, Met49 and Glu166 through hydrogen bonds in the M<sup>pro</sup> site, along with Coulombian interactions with Cys145 and Glu166, and hydrophobic interaction with His41 (**Figure 4**). Most fragments of Remdesivir interacted with RNA through hydrogen bonds and with some amino acid residues through hydrophobic interactions (**Figures S.6.7-a and S.6.7-b**). These fragments also showed a range of intermolecular interactions with diverse amino acid residues in the binding site. In the M<sup>pro</sup> site, a lot of fragments interacted with the catalytic dyad through hydrophobic interactions and hydrogen bonds, they are the fragments 161 m/z, 160 m/z, 218 m/z, 56 m/z, 328 m/z, 201 m/z and 219 m/z (**Figures S.6.8-a and S.6.8-b**).

### Ribavirin

Another important antiviral investigated was Ribavirin. For this compound, the non-metabolized drug presented a more stabilizing interaction energy (M<sup>pro</sup>: -4.6 kcal mol<sup>-1</sup>, RdRp:

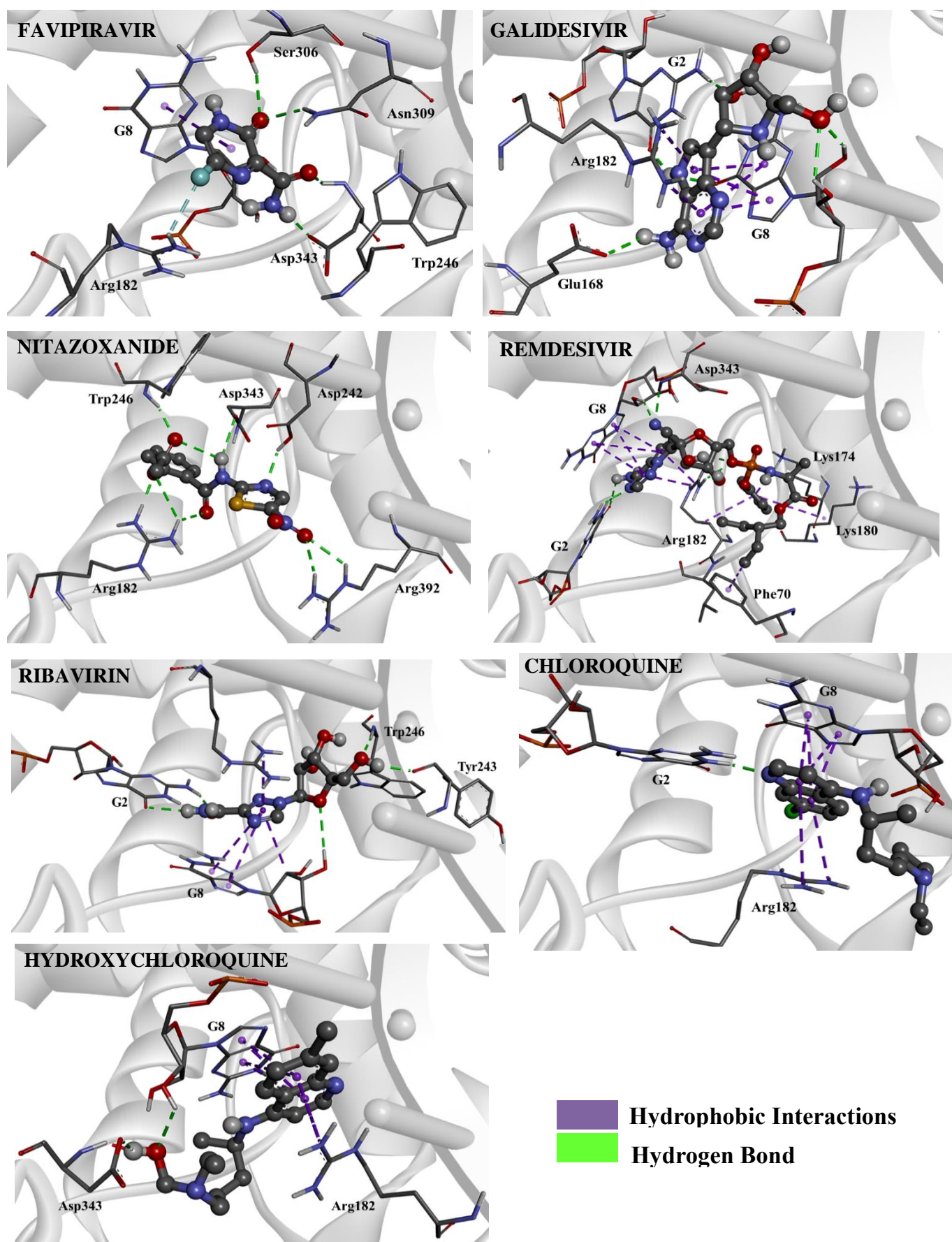
-7.7 kcal mol<sup>-1</sup>) than its fragments. The species that best interacted with the biomacromolecules were the fragments 142 m/z (M<sup>pro</sup>: -4.0 kcal mol<sup>-1</sup>, RdRp: -5.3 kcal mol<sup>-1</sup>), 111 m/z (M<sup>pro</sup>: -4.0 kcal mol<sup>-1</sup>, RdRp: -5.2 kcal mol<sup>-1</sup>) and 133 m/z (M<sup>pro</sup>: -3.7 kcal mol<sup>-1</sup>, RdRp: -5.1 kcal mol<sup>-1</sup>). In the RdRp site, Ribavirin carried out hydrogen bonds with RNA and the residues Trp246 and Tyr243, in addition to hydrophobic interactions with RNA (**Figure 3**). On the other hand, this drug interacted with only two residues in the M<sup>pro</sup> binding site, being hydrogen bonds with Glu166, and one residue of the catalytic dyad, the residue His41 (**Figure 4**). By analysing the pharmacophoric maps of the fragments (**Figure S.6.9 and Figure S.6.10**), most fragments stably interacted with RNA through hydrogen bonds. Furthermore, most fragments interacted with the residues of the catalytic dyad. This is an important finding, keeping in mind that the non-metabolized drug did not show interactions with the catalytic residue Cys145.

## Chloroquine

Going deeper into this investigation, and based on the results computed for Chloroquine with the viral M<sup>pro</sup> enzyme, the fragments 177 m/z (M<sup>pro</sup>: -4.5 kcal mol<sup>-1</sup>), 233 m/z (M<sup>pro</sup>: -3.2 kcal mol<sup>-1</sup>) and 205 m/z (M<sup>pro</sup>: -4.2 kcal mol<sup>-1</sup>) showed interaction energies more stable than that of the non-metabolized drug (M<sup>pro</sup>: -2.9 kcal mol<sup>-1</sup>). Now taking into account the interaction modes obtained for the docking in the RdRp binding site, Chloroquine (RdRp: -6.9 kcal mol<sup>-1</sup>) showed more stabilizing interaction energy than its fragments. The fragments 177 m/z, 233 m/z and 205 m/z exhibited interaction energy values close to that obtained for the non-metabolized drug. In the RdRp binding site, Chloroquine carried out hydrogen bond only with RNA, as well as hydrophobic interactions with RNA and the residue Arg182 (**Figure 3**). In turn, in the M<sup>pro</sup> binding site, Chloroquine interacted of different ways, such as through halogen bond with Met165, hydrogen bond with His41 and hydrophobic interactions with Cys145, Met165, Met49 and Gln189 (**Figure 4**). Almost all fragments in the RdRp binding site interacted with RNA, except the fragments 28 m/z and 29 m/z (**Figure S.6.11**). From these results, we can observe that the small fragments without hydrogen bond donor interacted less with DNA. In the M<sup>pro</sup> binding site, most residues interacted with the residues of the catalytic dyad (**Figure S.6.12**).

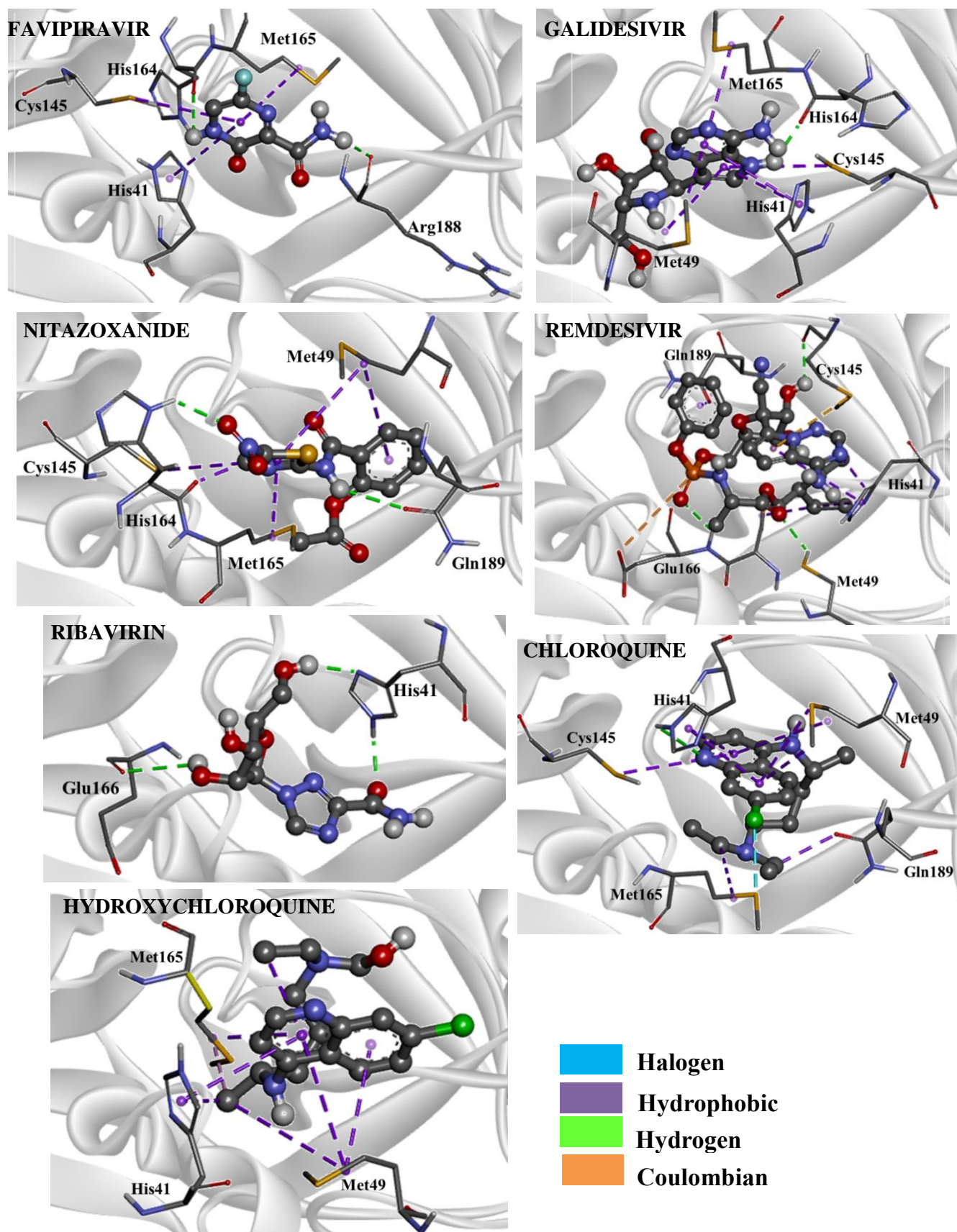
## Hydroxychloroquine

For Hydroxychloroquine, the fragment 142 m/z ( $M^{\text{pro}}$ :  $-4.6 \text{ kcal mol}^{-1}$ ) was significantly more stable than the non-metabolized drug ( $M^{\text{pro}}$ :  $-3.2 \text{ kcal mol}^{-1}$ ), based on the results acquired from the docking with the viral  $M^{\text{pro}}$ . On the other hand, like Chloroquine, Hydroxychloroquine showed an interaction energy more stable in the RdRp binding site than those of its fragments. The fragment 144 m/z did not present any results. In the target site of RdRp, the fragments interacted with RNA through hydrophobic interactions, and only the fragment 142 m/z performed hydrogen bond with RNA (**Figure S.6.13**). In the  $M^{\text{pro}}$  binding site, only the fragment 142 m/z interacted with both residues of the catalytic dyad, through hydrophobic interactions (**Figure S.6.14**). Our results show the potential of this fragment from Hydroxychloroquine in the COVID-19 treatment. The non-metabolized Hydroxychloroquine interacted with Arg182 and RNA through hydrophobic interactions and with the residue Asp343 through hydrogen bond, in the RdRp binding site (**Figure 3**). In the  $M^{\text{pro}}$  site, it was observed, from docking calculations, that only one type of intermolecular interaction occurred, the hydrophobic one, with the catalytic residue His41, as well as with the residues Met165 and Met49 (**Figure 4**).



**Figure 3.** Intermolecular interactions of the drugs investigated in the RdRp binding site.





**Figure 4.** Intermolecular interactions of the drugs investigated in the  $M^{\text{pro}}$  binding site.

## Finals remarks

Herein, our main goal was to investigate the interaction modes of diverse drugs for the COVID-19 treatment, as well as the interaction modes of their fragments formed in the study of metabolism by using the tool QCEIMS. Our outcomes indicate that the fragments of these drugs can also target the viral M<sup>pro</sup> enzyme and RdRp polymerase. It is noteworthy that each species' molecular docking pose showed that they could fit accurately within the substrate-binding pocket. Thus, the analysis of the fragments generated from each drug is a crucial step to better comprehend the action modes of these drugs toward two different important molecular targets for COVID-19 treatment, that is, M<sup>pro</sup> and RdRp. In this work, we noticed that the fragments interacted with RNA of different ways, indeed the larger fragments as well as the fragments with hydrogen bond donors contribute to more stabilized interactions with RNA. This same trend can be observed for the interaction of these fragments in the M<sup>pro</sup> binding site, this is because larger fragments more often interact with both residues of the catalytic dyad, Cys145 and His41. Among the compounds analyzed, Nitazoxanide was the one that provided a more stable receptor-ligand complex ( $-5.6 \text{ kcal mol}^{-1}$ ) within M<sup>pro</sup> binding site. The amount of energy required for a molecule to bind to a specific molecular target interferes with its biological activity, because the more stable the complex formed, the less energy is required for this interaction to occur. Therefore, when comparing the results obtained for all analyzed ligands, it is clear that the ligands that presented binding energies lower than that of the natural product, that is, those that presented lower energy values, in theory, are more active, as it will bind more easily to the molecular target. Thus, it is expected that Nitazoxanide presents good results of biological activity when performed experimental studies. In the RdRp binding site, Remdesivir presented the lowest interaction energy ( $-9.9 \text{ kcal mol}^{-1}$ ), that is, this drug is more stabilized in the target site than the other drugs investigated.

According to the metabolism study of the drugs approached in this work, these drugs can generate more stabilizing or less stabilizing fragments, even with fragments interacting better in the target site than the non-metabolized drug. These trends can vary according to the drug investigated, as shown along of this theoretical study. Equally important is the formation of more toxic or less toxic fragments. Some drugs, for example, revealed fragments less toxic than the drugs themselves. The set of the analyses developed in this study can bring about great contributions for the development of drugs for COVID-19 treatment, as well as for the development of drugs for the treatment of other diseases.

## Acknowledgements

The authors gratefully acknowledge the support from the Brazilian agencies CNPq, CAPES and FAPEMIG.

## References

1. Báez-Santos, Y. M., St. John, S. E. & Mesecar, A. D. The SARS-coronavirus papain-like protease: Structure, function and inhibition by designed antiviral compounds. *Antiviral Res.* **115**, 21–38 (2015).
2. WHO Coronavirus Disease (COVID-19) Dashboard. *World Health Organization*.
3. Hoffmann, M. *et al.* SARS-CoV-2 Cell Entry Depends on ACE2 and TMPRSS2 and Is Blocked by a Clinically Proven Protease Inhibitor. *Cell* **181**, 271-280.e8 (2020).
4. Morse, J. S., Lalonde, T., Xu, S. & Liu, W. R. Learning from the Past: Possible Urgent Prevention and Treatment Options for Severe Acute Respiratory Infections Caused by 2019-nCoV. *ChemBioChem* **21**, 730–738 (2020).
5. Shang, J. *et al.* Structural basis of receptor recognition by SARS-CoV-2. *Nature* **581**, 221–224 (2020).
6. Lan, J. *et al.* Structure of the SARS-CoV-2 spike receptor-binding domain bound to the ACE2 receptor. *Nature* **581**, 215–220 (2020).
7. Li, H. *et al.* Overview of therapeutic drug research for COVID-19 in China. *Acta Pharmacol. Sin.* **41**, 1133–1140 (2020).
8. Bobrowski, T. *et al.* Discovery of Synergistic and Antagonistic Drug Combinations Against SARS-CoV-2 In Vitro. *SSRN Electron. J.* (2020) doi:10.2139/ssrn.3666250.
9. Elfiky, A. A. Ribavirin, Remdesivir, Sofosbuvir, Galidesivir, and Tenofovir against SARS-CoV-2 RNA dependent RNA polymerase (RdRp): A molecular docking study. *Life Sci.* **253**, 117592 (2020).
10. Wang, Y., Li, W., Jiang, Z., Xi, X. & Zhu, Y. Assessment of the efficacy and safety of Ribavirin in treatment of coronavirus-related pneumonia (SARS, MERS and COVID-19). *Medicine (Baltimore)*. **99**, e22379 (2020).
11. Wang, M. *et al.* Remdesivir and chloroquine effectively inhibit the recently emerged novel coronavirus (2019-nCoV) in vitro. *Cell Res.* **30**, 269–271 (2020).
12. Assis, L. C., Castro, A. A. de, Jesus, J. P. A. de, Ramalho, T. de C. & Porta, F. de A. La. Theoretical Insights into the Effect of Halogenated Substituent on the Electronic Structure and Spectroscopic Properties of the Favipiravir Tautomeric Forms and Its Implications on the Treatment of COVID-19. *ChemRxiv* (2020).
13. Castro, A. de, Assis, L., Ramalho, T. & Porta, F. La. New in silico insights into the application of the (hydroxy)chloroquine with macrolide antibiotics co-crystals against the SARS-CoV-2 virus. (2020) doi:10.21203/rs.3.rs-66640/v1.
14. Döring, B. & Petzinger, E. Phase 0 and phase III transport in various organs:

- Combined concept of phases in xenobiotic transport and metabolism. *Drug Metab. Rev.* **46**, 261–282 (2014).
15. Williams, R. T. *Detoxification mechanisms : the metabolism and detoxification of drugs, toxic substances and other organic compounds*. (Chapman and Hall, 1959). doi:Detoxification mechanisms : the metabolism and detoxification of drugs, toxic substances and other organic compounds.
  16. Gillette, J. R. Metabolism of Drugs and Other Foreign Compounds by Enzymatic Mechanisms. in *Progress in Drug Research / Fortschritte der Arzneimittelforschung / Progrès des recherches pharmaceutiques* 11–73 (Birkhäuser Basel, 1963). doi:10.1007/978-3-0348-7050-4\_1.
  17. Ishikawa, T. The ATP-dependent glutathione S-conjugate export pump. *Trends Biochem. Sci.* **17**, 463–468 (1992).
  18. M. J. Frisch, G. W. Trucks, H. B. Schlegel, G. E. Scuseria, M. A. Robb, J. R. Cheeseman, G. Scalmani, V. Barone, G. A. Petersson, H. Nakatsuji, X. Li, M. Caricato, A. Marenich, J. Bloino, B. G. Janesko, R. Gomperts, B. Mennucci, H. P. Hratchian, J. V. Ort, W. C. Gaussian, Inc., Wallingford CT. (2009).
  19. Grimme, S. Towards First Principles Calculation of Electron Impact Mass Spectra of Molecules. *Angew. Chemie Int. Ed.* **52**, 6306–6312 (2013).
  20. Koopman, J. & Grimme, S. Calculation of Electron Ionization Mass Spectra with Semiempirical GFNn-xTB Methods. *ACS Omega* **4**, 15120–15133 (2019).
  21. Hanwell, M. D. *et al.* Avogadro: an advanced semantic chemical editor, visualization, and analysis platform. *J. Cheminform.* **4**, 17 (2012).
  22. Trott, O. & Olson, A. J. AutoDock Vina: improving the speed and accuracy of docking with a new scoring function, efficient optimization, and multithreading. *J. Comput. Chem.* **31**, 455–461 (2010).
  23. Maia, E. H. B., Medaglia, L. R., da Silva, A. M. & Taranto, A. G. Molecular Architect: A User-Friendly Workflow for Virtual Screening. *ACS omega* **5**, 6628–6640 (2020).
  24. Assis, L. C. *et al.* Nitro derivatives of quinoline and quinoline N-oxide as low-cost alternative for the treatment of SARS-CoV-2 infection. (2020) doi:10.21203/rs.3.rs-32468/v1.
  25. Assis, L. C. *et al.* Computational evidence for nitro derivatives of quinoline and quinoline N-oxide as low-cost alternative for the treatment of SARS-CoV-2 infection. *Sci. Rep.* **11**, 6397 (2021).
  26. Ducharme, J. & Farinotti, R. Clinical Pharmacokinetics and Metabolism of Chloroquine. *Clin. Pharmacokinet.* **31**, 257–274 (1996).
  27. Ette, E. I., Essien, E. E., Thomas, W. O. A. & Brown-Awala, E. A. Pharmacokinetics of Chloroquine and Some of Its Metabolites in Healthy Volunteers: A Single Dose Study. *J. Clin. Pharmacol.* **29**, 457–462 (1989).
  28. McChesney, E. W., Banks, W. F. & Sullivan, D. J. Metabolism of chloroquine and hydroxychloroquine in albino and pigmented rats. *Toxicol. Appl. Pharmacol.* **7**, 627–636 (1965).

29. Reingruber, H. & Pontel, L. B. Formaldehyde metabolism and its impact on human health. *Curr. Opin. Toxicol.* **9**, 28–34 (2018).
30. Eells, J. T. Formaldehyde Poisoning. *JAMA* **246**, 1237 (1981).
31. Roberts, J. M. *et al.* Isocyanic acid in the atmosphere and its possible link to smoke-related health effects. *Proc. Natl. Acad. Sci.* **108**, 8966–8971 (2011).
32. Wang, Z. *et al.* Protein carbamylation links inflammation, smoking, uremia and atherogenesis. *Nat. Med.* **13**, 1176–1184 (2007).
33. Vogel, S. N., Sultan, T. R. & Ten Eyck, R. P. Cyanide Poisoning. *Clin. Toxicol.* **18**, 367–383 (1981).
34. Jenkins, W. J. & Peters, T. J. SELECTIVELY REDUCED HEPATIC ACETALDEHYDE DEHYDROGENASE IN ALCOHOLICS. *Lancet* **315**, 628–629 (1980).
35. Stevens, J. F. & Maier, C. S. Acrolein: Sources, metabolism, and biomolecular interactions relevant to human health and disease. *Mol. Nutr. Food Res.* **52**, 7–25 (2008).
36. Schröder, D. *et al.* Ethylenedione: An Intrinsically Short-Lived Molecule. *Chem. - A Eur. J.* **4**, 2550–2557 (1998).
37. Baker, E. L. *et al.* Phenol Poisoning Due to Contaminated Drinking Water. *Arch. Environ. Heal. An Int. J.* **33**, 89–94 (1978).
38. Saladino, R., Crestini, C., Ciciriello, F., Costanzo, G. & Di Mauro, E. Formamide Chemistry and the Origin of Informational Polymers. *Chem. Biodivers.* **4**, 694–720 (2007).
39. Costanzo, G., Saladino, R., Crestini, C., Ciciriello, F. & Di Mauro, E. Nucleoside Phosphorylation by Phosphate Minerals. *J. Biol. Chem.* **282**, 16729–16735 (2007).
40. Saladino, R., Crestini, C., Pino, S., Costanzo, G. & Di Mauro, E. Formamide and the origin of life. *Phys. Life Rev.* **9**, 84–104 (2012).
41. Huang, J.-F., Zhu, D.-M., Ma, J.-F. & Zhong, M. Acute respiratory distress syndrome due to exposure to high-concentration mixture of ethenone and crotonaldehyde. *Toxicol. Ind. Health* **31**, 585–587 (2015).
42. Zamyatkin, D. F., Parra, F., Machín, A., Grochulski, P. & Ng, K. K.-S. Binding of 2'-amino-2'-deoxycytidine-5'-triphosphate to norovirus polymerase induces rearrangement of the active site. *J. Mol. Biol.* **390**, 10–16 (2009).
43. Berman, H. M. *et al.* The Protein Data Bank. *Nucleic Acids Res.* **28**, 235–242 (2000).

**SUPPLEMENTARY MATERIAL**

*Effect of drug metabolism in the treatment of sars-cov-2 from an entirely  
computational perspective*

**S.1 – CARTESIAN COORDINATES OF THE OPTIMIZED STRUCTURES****FAVIPIRAVIR**

0 1

C	2.18836100	0.64798800	0.04520100
C	1.75736500	-0.64557300	0.03915200
C	-0.47168600	-0.06847900	-0.00944400
C	-0.16571900	1.38067200	-0.08102400
H	3.22924300	0.94356700	0.08491800
F	2.65106500	-1.65708700	0.06968800
N	0.46588900	-0.98812200	0.01742300
N	1.22782000	1.61227600	-0.00278400
H	1.48788200	2.59244500	-0.02767800
O	-0.93389800	2.31765400	-0.21524400
C	-1.90803200	-0.54426200	0.05786800
O	-2.81863700	0.18619200	0.42024500
N	-2.07818700	-1.84818500	-0.30794200
H	-1.27791300	-2.45166800	-0.42699400
H	-2.98890700	-2.25517700	-0.15485400

**GALIDESIVIR**

0 1

C	2.77059800	0.52044300	-0.28610200
C	1.69928000	-0.11565800	0.37586900
C	3.16146700	-1.30239800	1.60272600
C	4.08024200	0.14410400	0.05498500
C	0.85416700	1.36213900	-1.09324400
C	0.47933500	0.42573600	-0.15619600
H	3.36463100	-2.03576900	2.37904400
H	2.73809400	2.12777700	-1.69522000

H	0.23295400	2.00616700	-1.69820100
N	5.20536800	0.70855000	-0.51499200
H	6.06219000	0.22547300	-0.27442400
H	5.14863200	0.98452800	-1.48558500
N	4.25409900	-0.76785700	1.01620100
N	1.88509800	-1.05001400	1.33821900
N	2.23358300	1.41339200	-1.19494300
C	-0.90411800	0.02489600	0.24848500
C	-1.43130600	-1.29696200	-0.34581400
H	-0.91169600	-0.09945000	1.34541600
C	-3.25299000	0.30899400	-0.05223500
C	-2.93650800	-1.21873500	0.00516900
H	-0.93749600	-2.17977000	0.06319100
H	-3.88728100	0.50508100	-0.92783600
H	-3.09280800	-1.59205700	1.02484500
N	-1.93702800	0.96008200	-0.23739200
H	-1.90273300	1.86818400	0.22002700
C	-3.98967900	0.79293900	1.19928500
H	-4.94565600	0.25905900	1.29886900
H	-3.39349600	0.58636300	2.09496800
O	-4.18723300	2.21007100	1.20027400
H	-4.84949900	2.43462700	0.53302700
O	-3.74305100	-2.01203200	-0.84196900
H	-3.26805800	-2.06964000	-1.68862100
O	-1.28112400	-1.35961200	-1.76533500
H	-1.33728600	-0.45005200	-2.10047900

NITAZOXANIDE

0 1



C	4.94095400	-1.43761600	0.26540500
C	4.12481100	-2.55520600	0.06720800
C	2.74670000	-2.39477700	-0.02006400
C	2.14839300	-1.12581800	0.08509300
C	2.99426700	-0.01599700	0.27478700
C	4.37582200	-0.16788400	0.37066500
H	6.01826800	-1.54995300	0.33812100
H	4.56095000	-3.54535600	-0.01550200
H	2.09196300	-3.24564100	-0.17135900
H	4.99904300	0.70617200	0.51557500
O	2.43007000	1.25665700	0.43548800
C	2.80946300	2.30299400	-0.40541700
C	2.08057800	3.55921800	-0.01626700
H	2.40117400	4.37312700	-0.66551900
H	0.99875000	3.41711800	-0.10910800
H	2.29009100	3.80680000	1.02876200
O	3.60362500	2.17060200	-1.29784300
C	0.65371400	-1.10703100	-0.01741000
O	0.00924400	-2.09445900	-0.36144000
N	-0.00151900	0.06406000	0.31379700
C	-1.36281600	0.24553100	0.26555900
C	-3.23126100	1.38910700	0.46496800
C	-3.74677500	0.17994100	0.07329700
H	-3.82286300	2.26954600	0.67929900
S	-2.49013900	-1.01301400	-0.18631700
N	-1.87519800	1.42395300	0.57305800
N	-5.12376300	-0.13567200	-0.12273000
O	-5.95440200	0.75749200	0.07846600
O	-5.39330100	-1.28940700	-0.48258100
H	0.54323500	0.86817000	0.60825800

## REMDESIVIR

0 1

P	-1.28189400	1.67359000	-0.61719300
O	-0.11630400	2.23915900	-1.34205700
O	1.17063900	2.86871300	1.83719900
H	1.38645300	2.87255500	2.78296500
O	2.38137200	-0.52716500	1.58182500
O	3.24784300	1.89344400	3.15177300
H	4.09604900	1.69329300	3.57383500
N	4.55130200	-1.21636800	-0.47081800
N	-2.38671900	0.98027300	-1.66885200
H	-1.93206800	0.61947000	-2.50301100
O	-0.94010900	0.60559800	0.55179100
O	-3.89799900	-1.93036500	-0.13005000
N	5.37363000	-0.61341100	3.23290400
O	-2.08143100	-1.81587600	-1.47589000
N	5.80040700	-2.32061600	-3.70819100
H	5.97624000	-3.22024100	-4.13107900
H	5.64416600	-1.52934700	-4.31102700
N	4.54887600	-2.37858700	0.23966800
C	-3.49587200	0.15007400	-1.20802800
H	-3.86155000	0.55709200	-0.26110700
O	-2.19304100	2.65244000	0.29698700
N	5.37733900	-3.45640700	-1.74674800
C	4.59602800	-0.35384600	2.41008600
C	3.63203700	0.16709900	1.41418800
C	1.86405600	1.79289700	1.24542900
H	1.84942500	1.97929800	0.16925200
C	3.31262300	1.65729700	1.75556100
H	4.01488600	2.34609800	1.27651900

C	-3.05117300	-1.29754200	-0.95816400
C	4.33362300	0.92558300	-1.03087000
H	4.11284800	1.98190700	-0.98325600
C	5.37275400	-2.31334800	-2.41961000
C	4.17031400	0.00732900	0.01191500
C	4.95397100	-1.09612800	-1.80077500
C	0.28979300	-0.15060900	0.51470100
H	0.73941000	-0.12209400	-0.48168200
H	0.03230500	-1.18414100	0.75440200
C	4.96896000	-3.41003300	-0.45170000
H	4.98195800	-4.34833500	0.09343600
C	-3.81070700	5.80984400	-0.66754700
H	-4.77492200	6.15603900	-1.02823200
C	1.27064600	0.39516600	1.55254400
H	0.79611400	0.40806300	2.54151800
C	-2.78321600	6.72381000	-0.41882900
H	-2.94568900	7.78435700	-0.58621200
C	-4.64187400	0.17041700	-2.23500300
H	-4.97610400	1.19957100	-2.38788800
H	-5.48567400	-0.43209100	-1.88805900
H	-4.30338000	-0.22732200	-3.19800000
C	-3.61542700	-3.32856000	0.15731200
H	-2.61402300	-3.38571900	0.59017900
H	-3.60304800	-3.88069700	-0.78755000
C	4.82127000	0.24552100	-2.16074200
H	5.05002500	0.68379600	-3.12165600
C	-4.68300400	-3.84777100	1.11874400
H	-4.66287200	-3.19089300	2.00064000
C	-2.36436700	4.01202500	0.01170900
C	-3.60458700	4.44409400	-0.45385500

H	-4.39059900	3.71941300	-0.63762900
C	-1.54701400	6.26866900	0.05076400
H	-0.74679700	6.97564700	0.24951300
C	-1.32771700	4.90730800	0.27430700
H	-0.38072300	4.53383300	0.64912300
C	-6.11094200	-3.75940300	0.53060100
H	-6.81532500	-4.03198400	1.32732900
H	-6.32101100	-2.71230200	0.28407200
C	-4.32823100	-5.27495700	1.59538900
H	-4.14345500	-5.92321200	0.72848400
H	-5.21154700	-5.68976000	2.09789700
C	-6.38985300	-4.63372100	-0.70065700
H	-7.42454300	-4.50056500	-1.03398800
H	-6.25006900	-5.69892600	-0.48855100
H	-5.74293700	-4.37497100	-1.54631600
C	-3.13357200	-5.35574500	2.55654900
H	-2.19695900	-5.03709800	2.08730100
H	-2.98617100	-6.38337300	2.90506400
H	-3.29470600	-4.72579800	3.43912100

## RIBAVIRIN

0 1

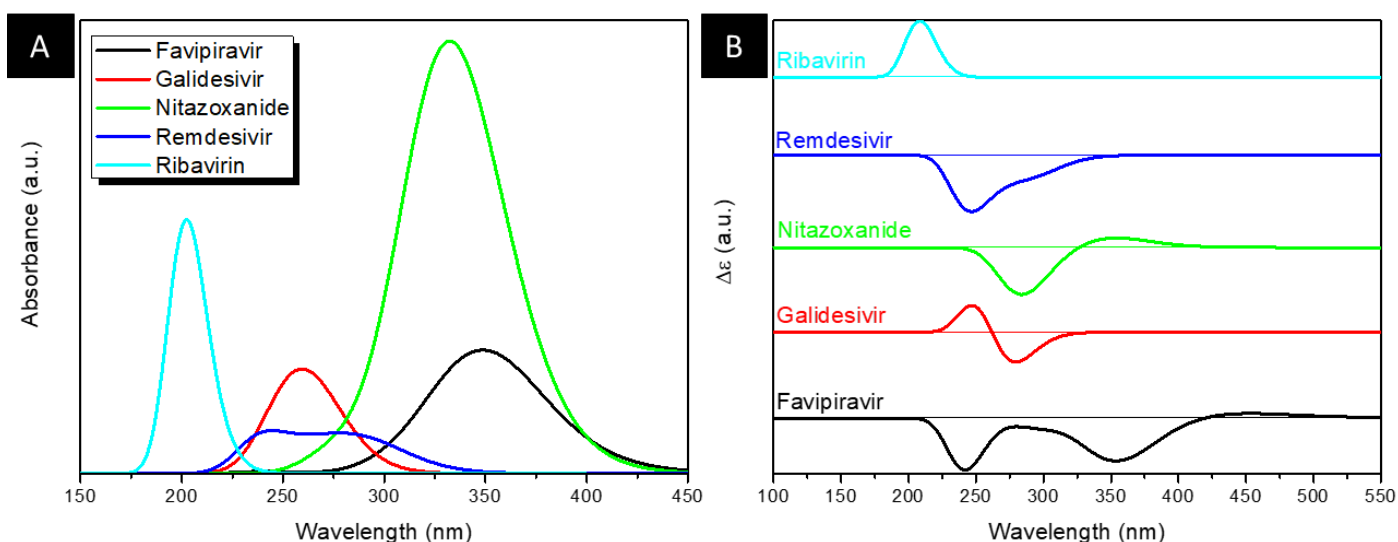
C	2.58967500	0.40027500	0.40092300
O	1.45090600	0.60481800	1.25984100
C	0.52229000	-0.45689700	1.09699500
C	1.11314400	-1.44320600	0.07592500
C	2.07881000	-0.53730800	-0.70359200
H	3.38166800	-0.11097100	0.96544400
H	0.34267100	-0.95167900	2.05555800

H	0.33423200	-1.89159100	-0.54852200
H	1.51630200	0.03942900	-1.45282600
O	1.82185500	-2.42734600	0.81027700
H	2.50523200	-2.78789300	0.22407900
O	3.08406200	-1.31736400	-1.32130800
H	3.74987600	-0.70671000	-1.67338200
C	3.10173700	1.73880800	-0.11677900
H	2.31265500	2.25524700	-0.67285600
H	3.42231200	2.38754100	0.70588800
O	4.17270800	1.49264200	-1.04235000
H	5.01968100	1.56047600	-0.58456400
N	-0.74598100	0.13217400	0.63245400
C	-1.12974800	1.43301500	0.60256500
H	-0.47573600	2.24740100	0.87124100
C	-2.74268100	0.20951100	0.01634000
N	-1.77501200	-0.66448600	0.27029500
N	-2.38900300	1.51703600	0.20761700
C	-4.10725200	-0.20554600	-0.44581200
O	-4.41766300	-1.37393200	-0.63708800
N	-4.95092700	0.84916400	-0.62677700
H	-5.89307700	0.66498100	-0.93531600
H	-4.64014500	1.79408400	-0.45423600



mostly homogeneously around the structure body and shows two poles with high negative and positive potentials, due to a hydroxide and amine groups, respectively.

### S.3 – ESTIMATED a) UV-VIS AND b) ECD SPECTRA OF THE DRUGS



In the Figure S.3.A are shown the UV-Vis spectra of the drugs. The Nitazoxanide molecule shows the most intense absorbance at 333 nm (HOMO  $\rightarrow$  LUMO), followed by the slightly minor absorbance of Ribavirin at 202 nm (HOMO-2  $\rightarrow$  LUMO), then moderate intensities for Favipiravir and Galidesivir, respectively at 350 nm (HOMO  $\rightarrow$  LUMO) and 257 nm (HOMO-3  $\rightarrow$  LUMO), and lastly the low intensity peaks of Remdesivir at 241 nm (HOMO  $\rightarrow$  LUMO+2) and 269 nm (HOMO  $\rightarrow$  LUMO+1). From the ECD spectra shown in S.3.B, it is observed that Favipiravir drug shows two negative signals at 241 nm and 350 nm, one positive signal at 247 nm and one negative at 269 nm for the Galidesivir, the inverse for Nitazoxanide with one negative at 287 nm and positive around 340 nm, a broad positive signal in the range of 215-350 nm for Remdesivir and a single positive peak at 209 nm for Ribavirin. Information regarding the electronic properties of the studied molecules are found in S.4.

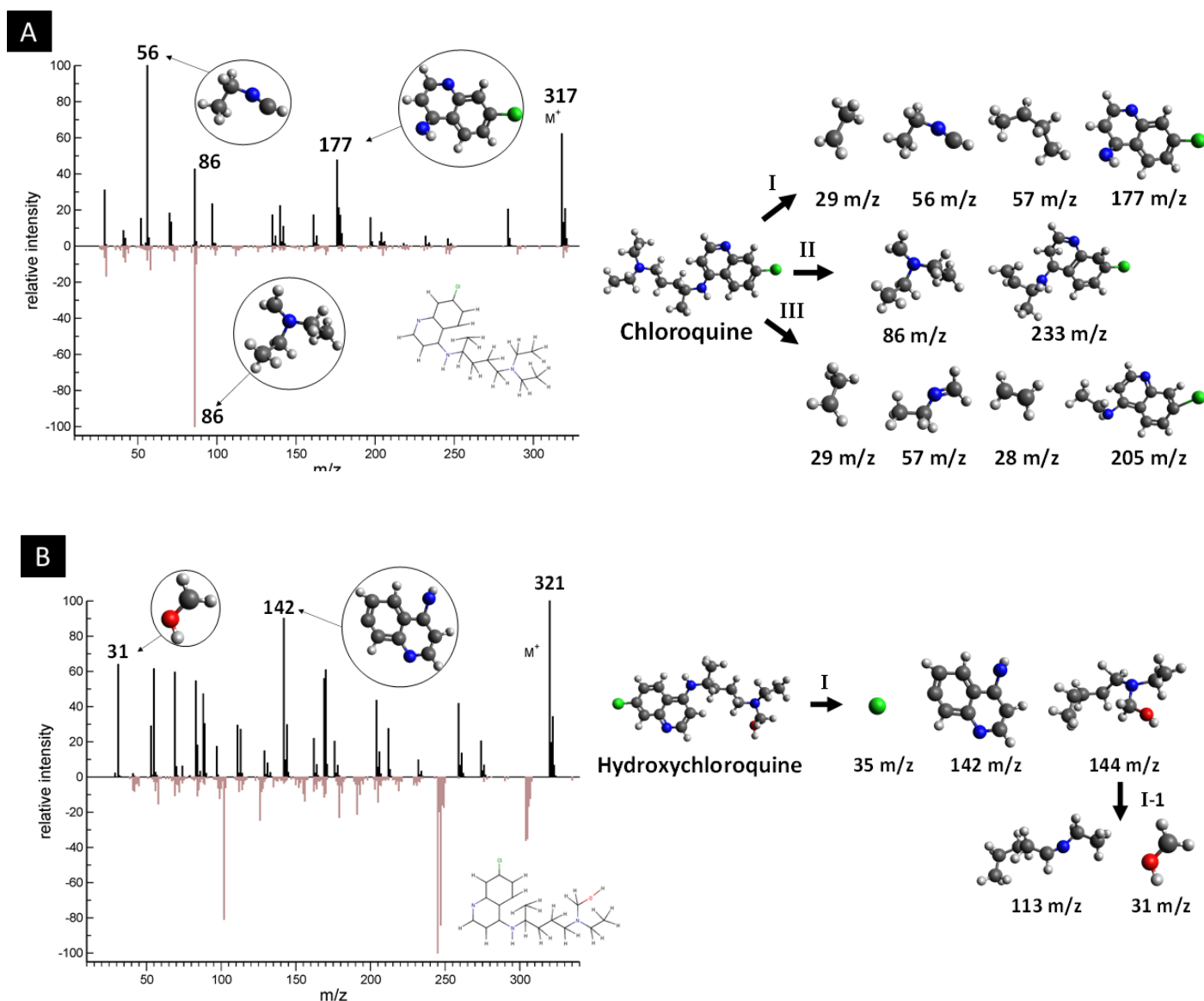
#### S.4 - ELECTRONIC PROPERTIES OF THE DRUGS.

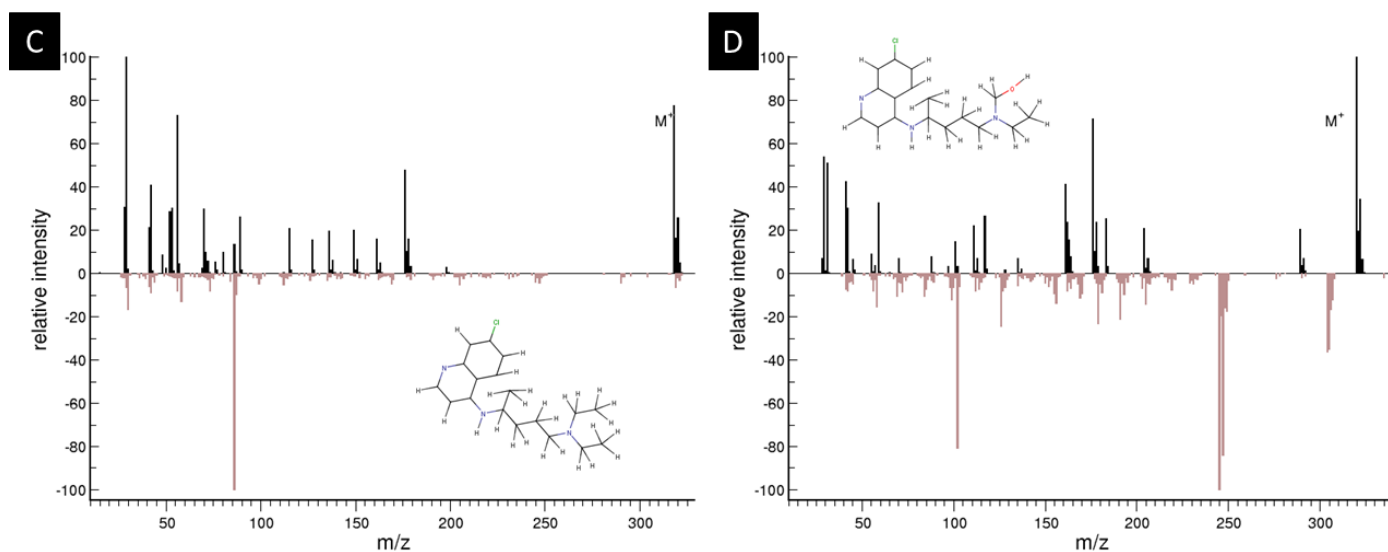
Molecule	LUMO - HOMO (eV)	Hardness (eV)	Softness (eV)	Mulliken Electronegativity (eV)	Electrophilicity (eV)
Favipiravir	3.87	1.94	0.52	-5.02	50.40
Galidesivir	5.21	2.60	0.38	-3.69	27.24
Nitazoxanide	4.09	2.05	0.49	-5.12	52.54
Remdesivir	4.82	2.41	0.41	-3.92	30.74
Ribavirin	6.02	3.01	0.33	-4.14	34.21

The Table above organizes the electronic properties of the drugs, in which are in agreement with the expected values for molecules. It is observed that the Favipiravir shows the smallest LUMO-HOMO energy, followed by Nitazoxanide, Remdesivir, Galidesivir and then Ribavirin, which these energies may in principle indicate the order of reactivity of these molecules, being Favipiravir the most reactive and Ribavirin the lowest. As expected, the hardness follows the same tendency and is inverse to the softness, indicating that the calculations are in order. As for the electronegativity, it increases from Galidesivir to Remdesivir, Ribavirin, Favipiravir and Nitazoxanide, which is the same tendency as the electrophilicity.



**S.5 - THEORETICAL (BLACK) AND EXPERIMENTAL (PINK) EI-MS SPECTRA OF a) CHLOROQUINE AND b) HYDROXYCHLOROQUINE, AND THEIR RESPECTIVE TRAJECTORIES, BY MEANS OF GFN2-XTB. THEORETICAL (BLACK) AND EXPERIMENTAL (PINK) EI-MS SPECTRA OF c) CHLOROQUINE AND d) HYDROXYCHLOROQUINE RESULTED FROM THE GFN1-XTB METHOD. STRUCTURES. PLOTS GENERATED IN THE GRACE SOFTWARE [HTTPS://PLASMA-GATE.WEIZMANN.AC.IL/GRACE/](https://plasma-gate.weizmann.ac.il/grace/)**





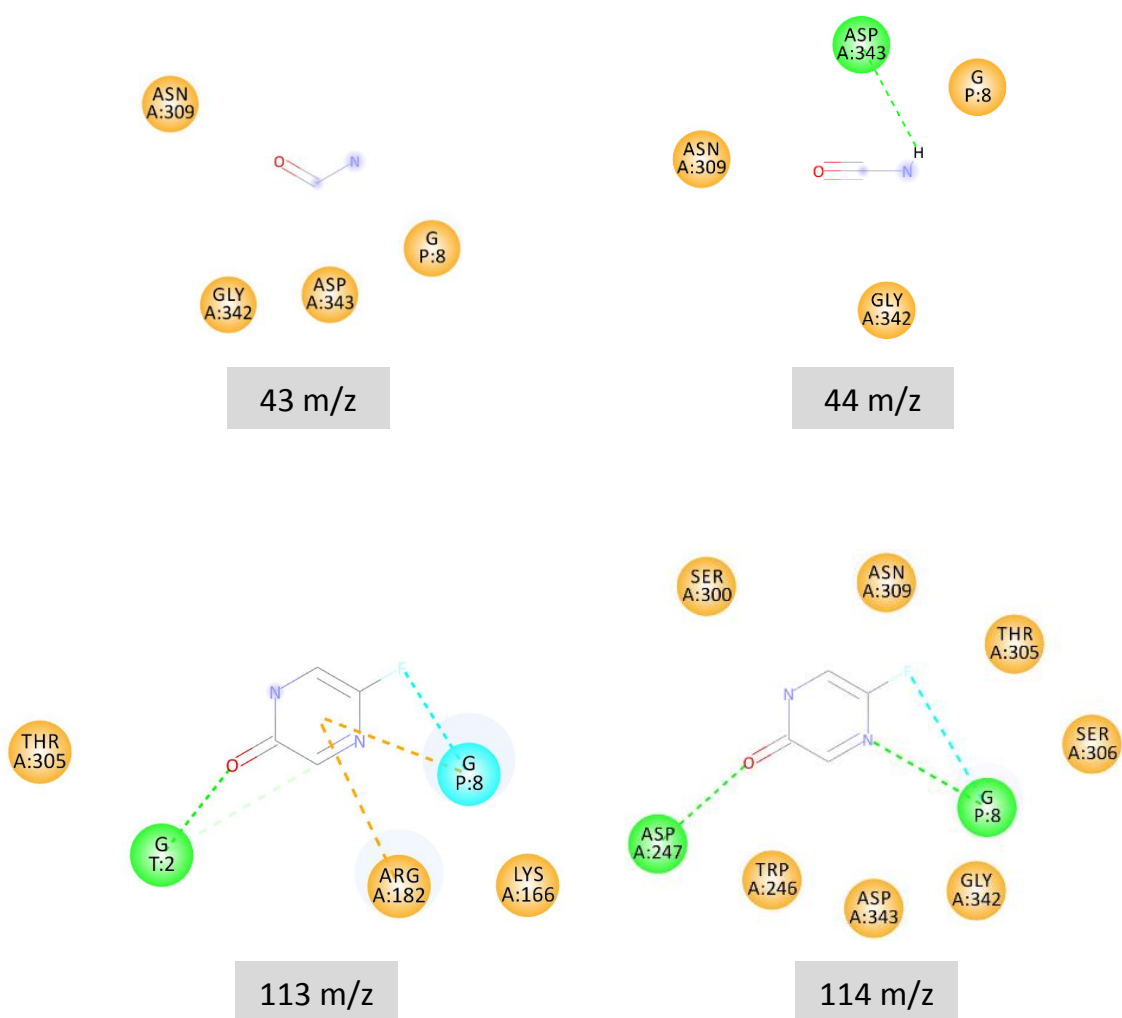
As seen in the S.5.A above, the EI-MS diagram from the GFN2-xTB method, in principle, presented most of the intermediaries of the Chloroquine molecule, in agreement with the experimental data profile (NIST MS 42361), with slight deviation of intensity. The most intense signal 86 m/z and its respective intermediary are also identified in the theoretical plot and the resultant trajectory described. As for the Hydroxychloroquine spectra in S.5.B, the most intense peaks from the experimental data (NIST MS 246973) are not identified in the theoretical data, still, some of the signals are found with distinct intensity from the experimental spectra. In order to evaluate the results between the theoretical methods, S.5.C shows the EI-MS spectra of the Chloroquine obtained using the GFN1-xTB method in comparison with the same experimental profile. In this manner, the spectra from the GFN1-xTB did not match the intermediaries mass/charge rate and intensity as well as its analog method, revealing that the GFN2-xTB is the best option for this calculation. Transitioning to the Hydroxychloroquine in S.5.D, the spectra acquired from the GFN1-xTB approach did not show significant improvements over the GFN2-xTB, and the most intense signals of the NIST profile are not identified as well. In general, an increasing on the molecular dynamics parameters could lead to a better prediction of the EI-MS spectra and its intermediaries in exchange of meaningful computational cost, however, as the current methodology with GFN2-xTB provided satisfactory results for the Chloroquine drug, it has been chosen as the default semiempirical method to the study of the other drugs. For more information regarding the characterization and details of Chloroquine and Hydroxychloroquine, please check our other works with these drugs.<sup>1,2</sup>

Henceforth, the discussion of the EI-MS spectra and trajectories will be done in the context of xenobiotics metabolism, evaluating the obtained intermediaries as drug by-products, their metabolism and toxicity when possible. Thus, returning to the Chloroquine drug, the spectra and trajectories are shown in S.5.A. The Chloroquine molecule contains polar amine and chloride groups in its structure, showing an aromatic region with more polar character than the other extremity. The first trajectory showed the fragmentation of Chloroquine around the amine that bond the aromatic and the alkane regions, leading to the following intermediaries: the I-177 m/z 7-chloro-4-aminoquinoline, containing the aromatic region, deprotonated amine and chloride polar groups, is a toxic and major metabolite from the oxidation of Chloroquine by the cytochrome P-450 enzyme;<sup>3,4</sup> the deprotonated I-57 m/z butane and I-29 m/z ethane, both nonpolar hydrocarbons which can be oxidized into polar species in Phase I of metabolism; and the I-56 m/z deprotonated amine, a polar and likely water-soluble molecule that may metabolize directly in Phase II. The trajectory II leads to the high molecular mass fragment II-233 m/z similar to the I-177 m/z, with an alkane extremity that may be target of oxidation in Phase I; and the II-86 m/z, the specie also identified in the experimental spectra, show very low polar character and may be almost insoluble in water, possible target of oxidative reactions in Phase I metabolism before conjugation in Phase II. The last trajectory for Chloroquine gives the following intermediaries: the III-205 m/z, a specie like the I-177 m/z and II-233 m/z, with a shorter alkane segment which may be oxidized in Phase I, and share the behavior of its analog molecules; the deprotonated organic molecules III-29 m/z ethane and III-28 m/z ethene, both nonpolar and likely targets to oxidizing reactions in Phase I, leading to polar conjugates to metabolize in Phase II; and the protonated form of I-56 m/z.

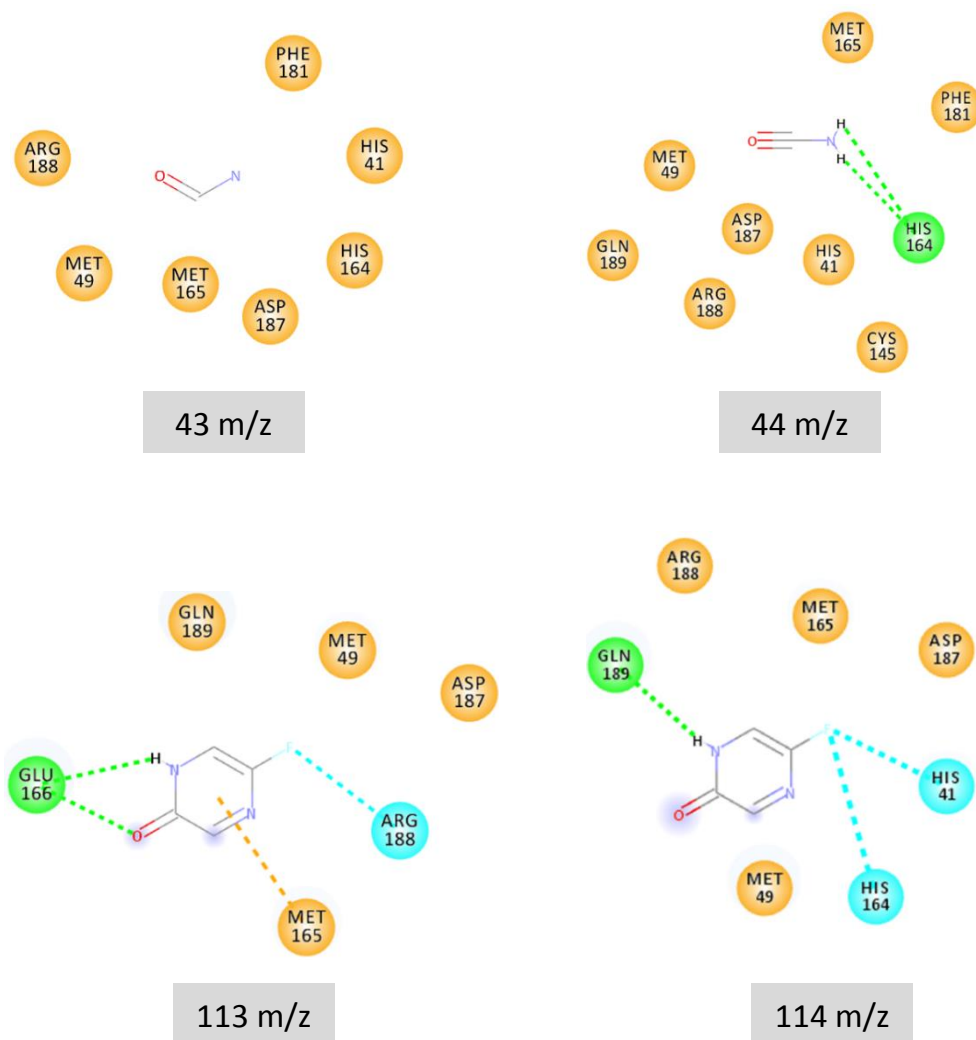
The S.5.B shows the EI-MS spectra and unique trajectory of the Hydroxychloroquine drug. The molecular structure of this drug is a more polar analog of the Chloroquine due to the addition of a hydroxide group. The calculations for the Hydroxychloroquine resulted in a single trajectory: the I-142 m/z, a deprotonated aminoquinoline similar to the 7-chloro-4-aminoquinoline from the metabolization of Quinoline, which is a metabolite from the Hydroxychloroquine;<sup>5</sup> the I-35 m/z chloride ion; and the I-144 m/z, with polar amine and alcohol groups, and the nonpolar extremities likely submitted to oxidative reactions in Phase I that may lead to smaller and polar fragments. This last fragment is further cleaved into two more species: the I-1-31 m/z molecule, which is deprotonated into a highly water-soluble and toxic formaldehyde form, being rapidly metabolized into formate by the alcohol dehydrogenase enzyme;<sup>6,7</sup> and the I-1-113 m/z, an amine with pentane and ethane extremities, and a possible

target for Phase I oxidative reactions that have as products smaller and polar molecules, further being transformed into metabolites in Phase II.

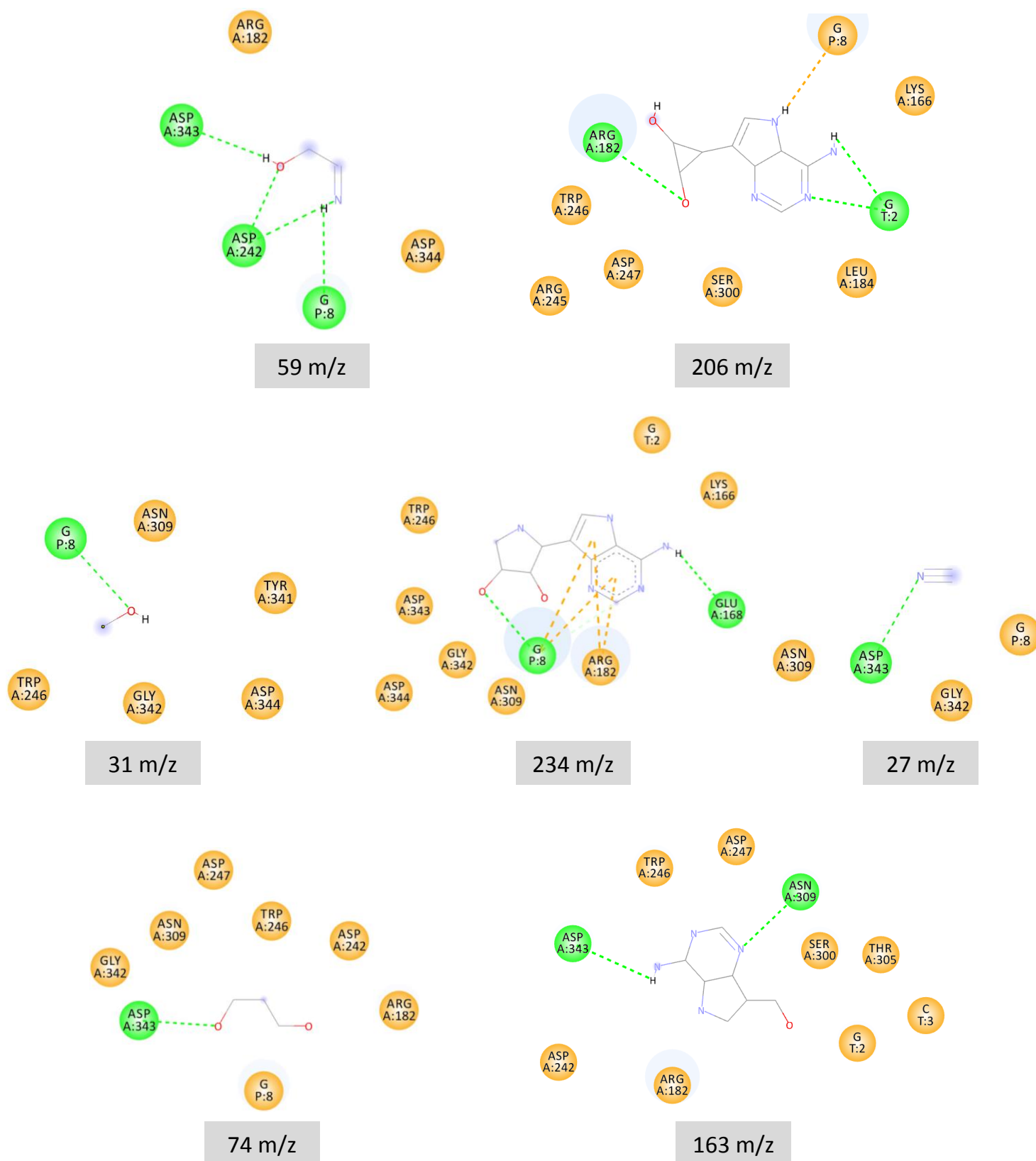
### S.6 – Pharmacophoric maps showing the intermolecular interactions of the fragments of diverse drugs in the RdRp and M<sup>pro</sup> active site



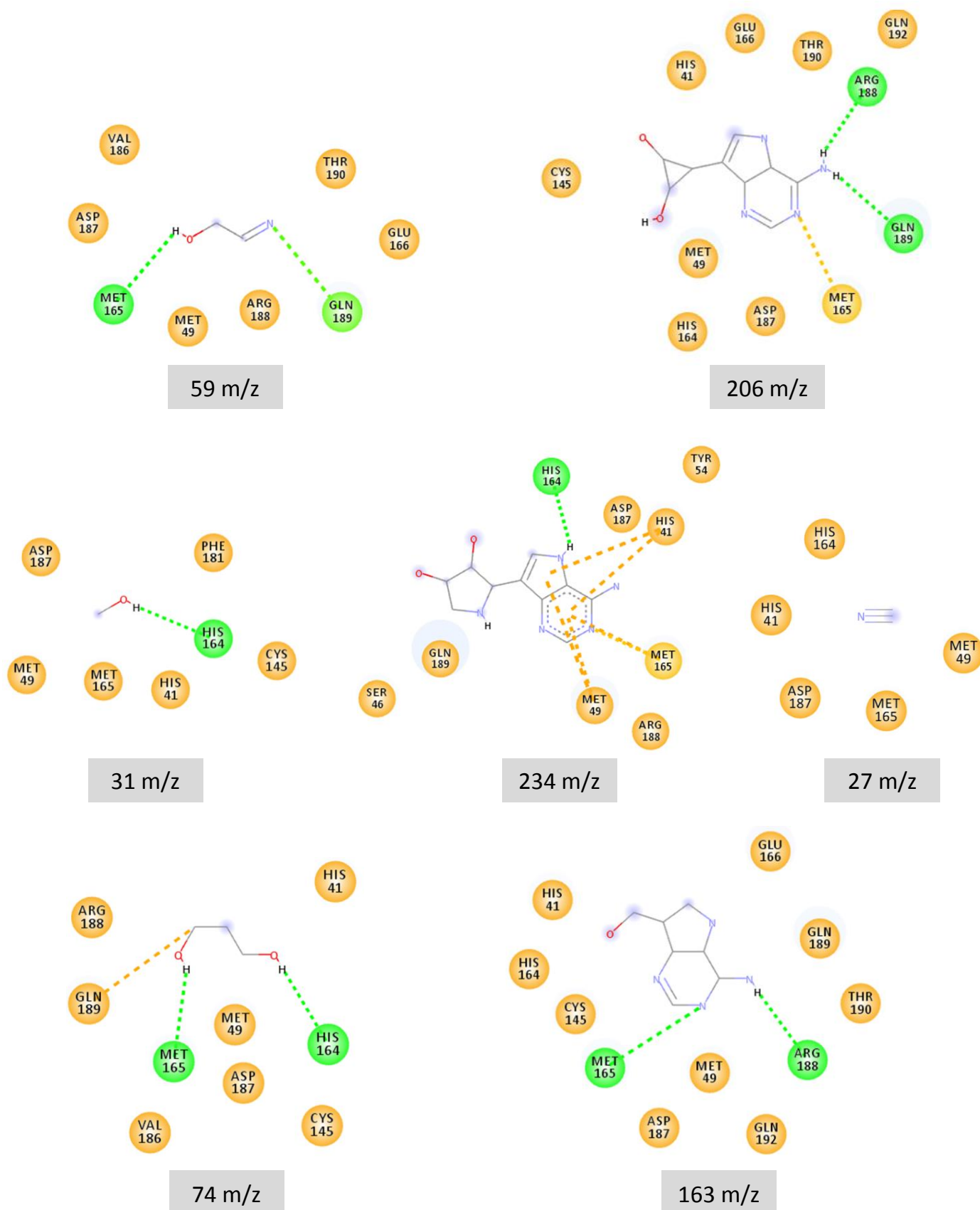
**Figure S.6.1.** Intermolecular interactions of the fragments of Favipiravir in the RdRp binding site. Green = hydrogen bond, Orange = hydrophobic interaction, Blue = halogen bond.



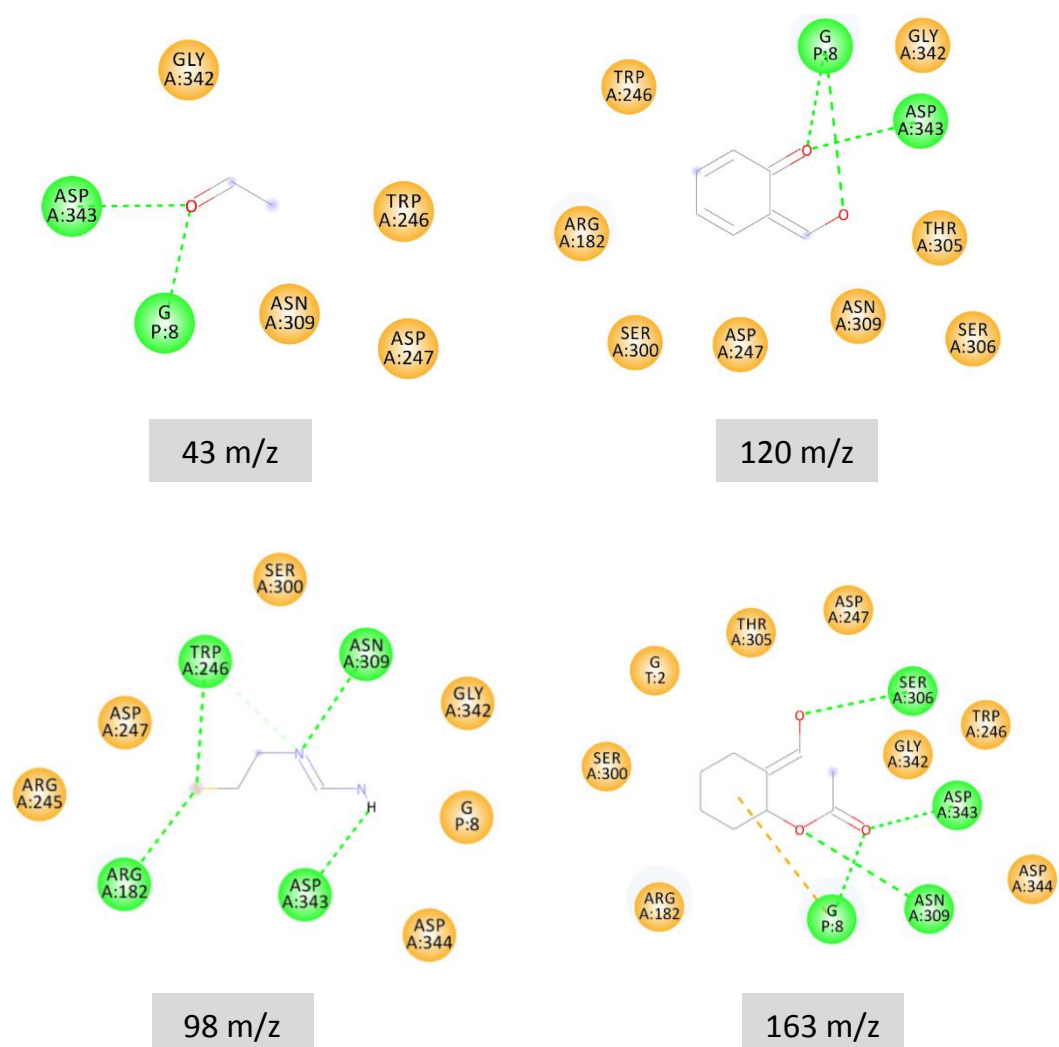
**Figure S.6.2.** Intermolecular interactions of the fragments of Favipiravir in the  $M^{Pro}$  binding site. Green = hydrogen bond, Orange = hydrophobic interaction, Blue = halogen bond.



**Figure S.6.3.** Intermolecular interactions of the fragments of Galidesivir in the RdRp binding site. Green = hydrogen bond, Orange = hydrophobic interaction.

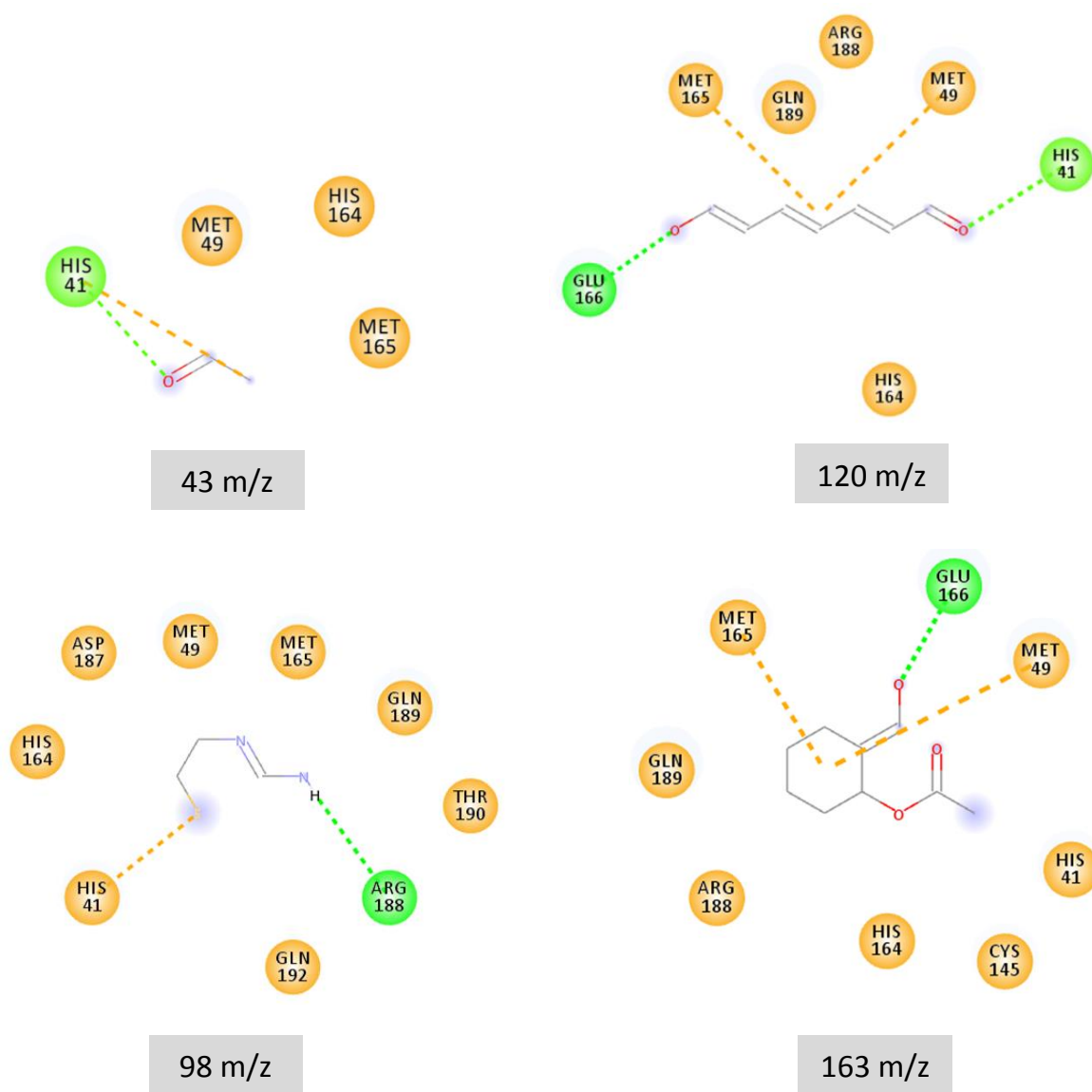


**Figure S.6.4.** Intermolecular interactions of the fragments of Galidesivir in the  $M^{\text{pro}}$  binding site. Green = hydrogen bond, Orange = hydrophobic interaction.

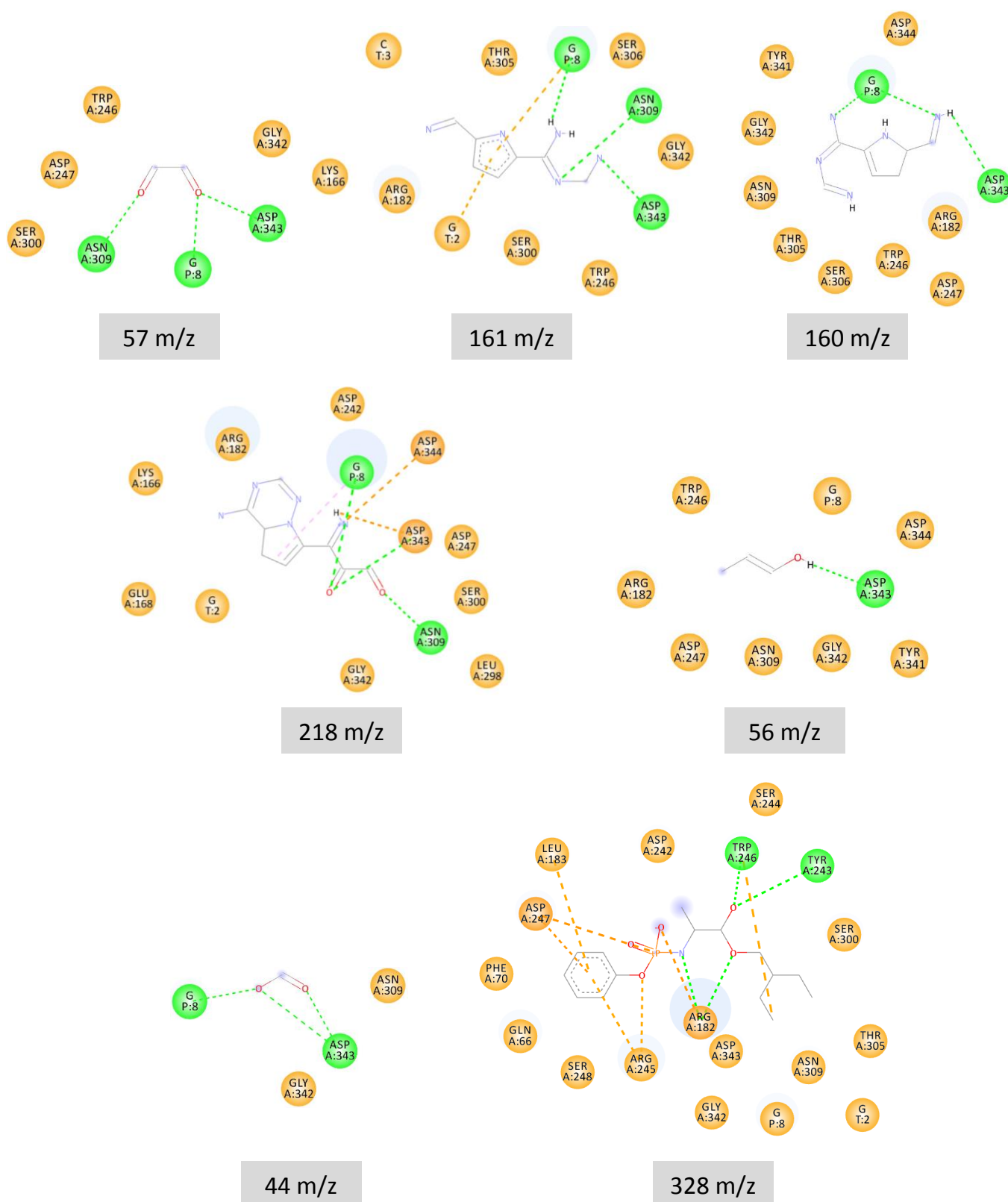


**Figure S.6.5.** Intermolecular interactions of the fragments of Nitazoxanide in the RdRp binding site. Green = hydrogen bond, Orange = hydrophobic interaction. No interaction found for fragment 46 m/z.

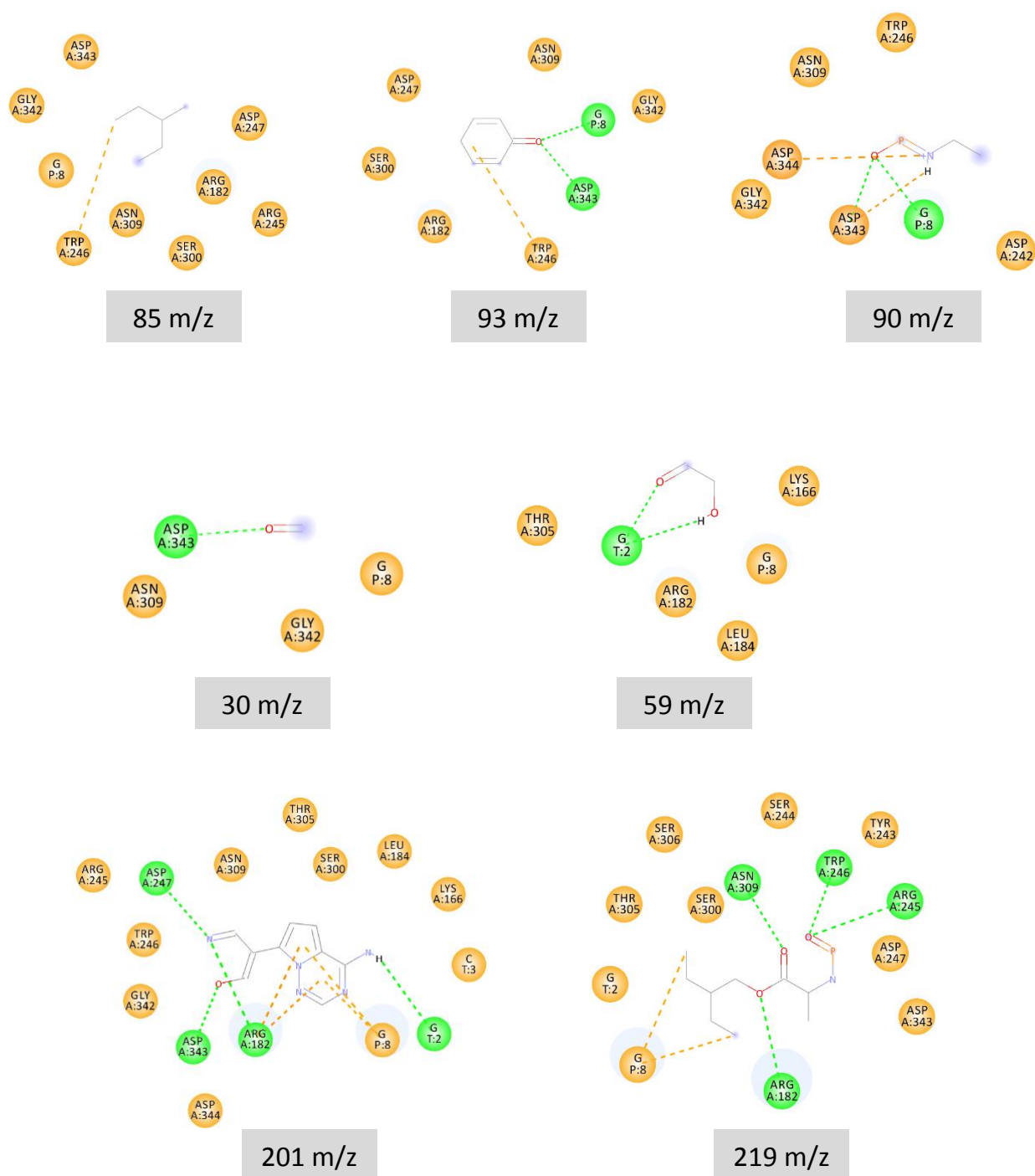




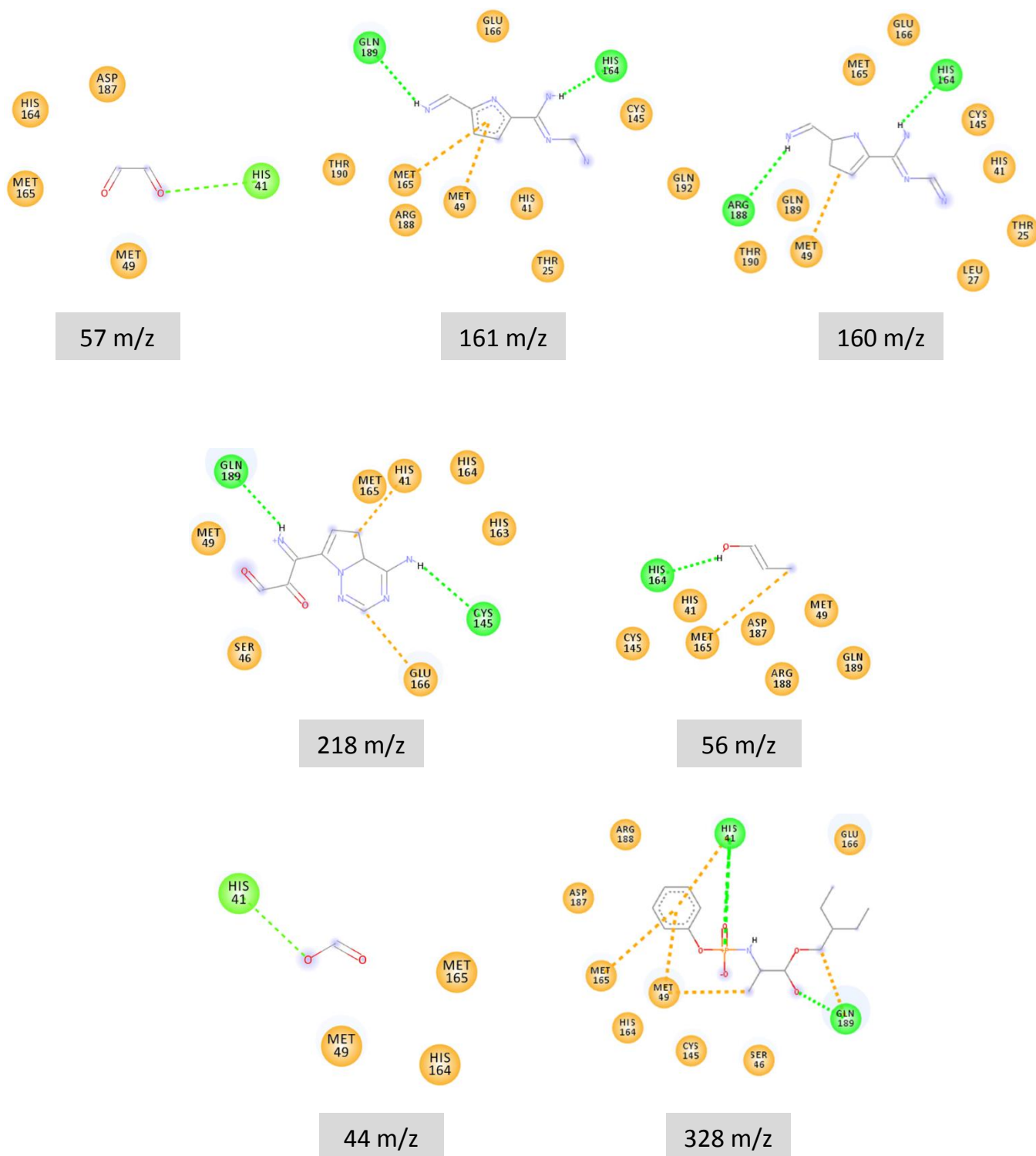
**Figure S.6.6.** Intermolecular interactions of the fragments of Nitazoxanide in the  $M^{\text{pro}}$  binding site. Green = hydrogen bond, Orange = hydrophobic interaction. No interaction found for fragment 46 m/z.



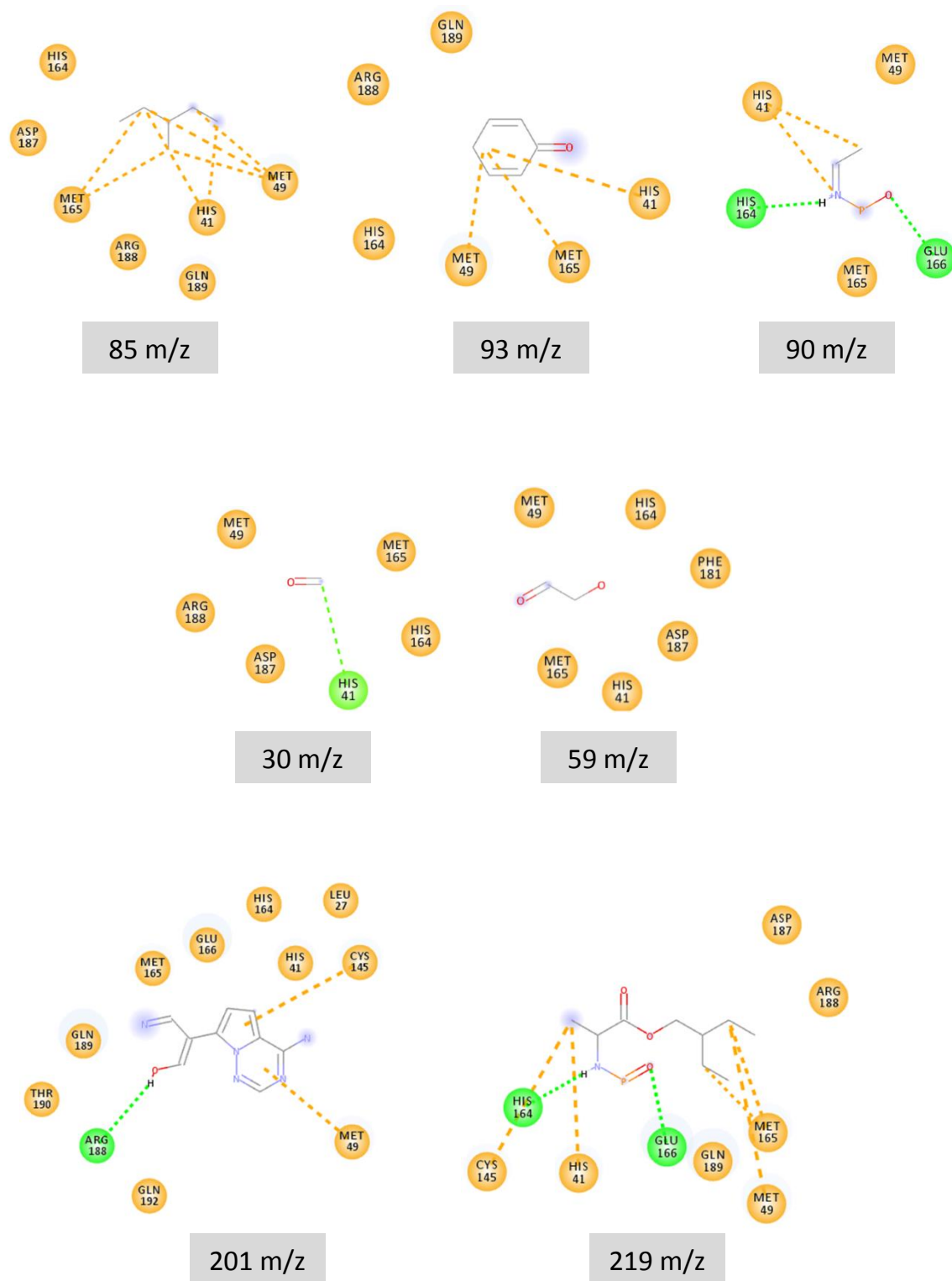
**Figure S.6.7-a.** Intermolecular interactions of the fragments of Remdesivir in the RdRp binding site. Green = hydrogen bond, Orange = hydrophobic interaction.



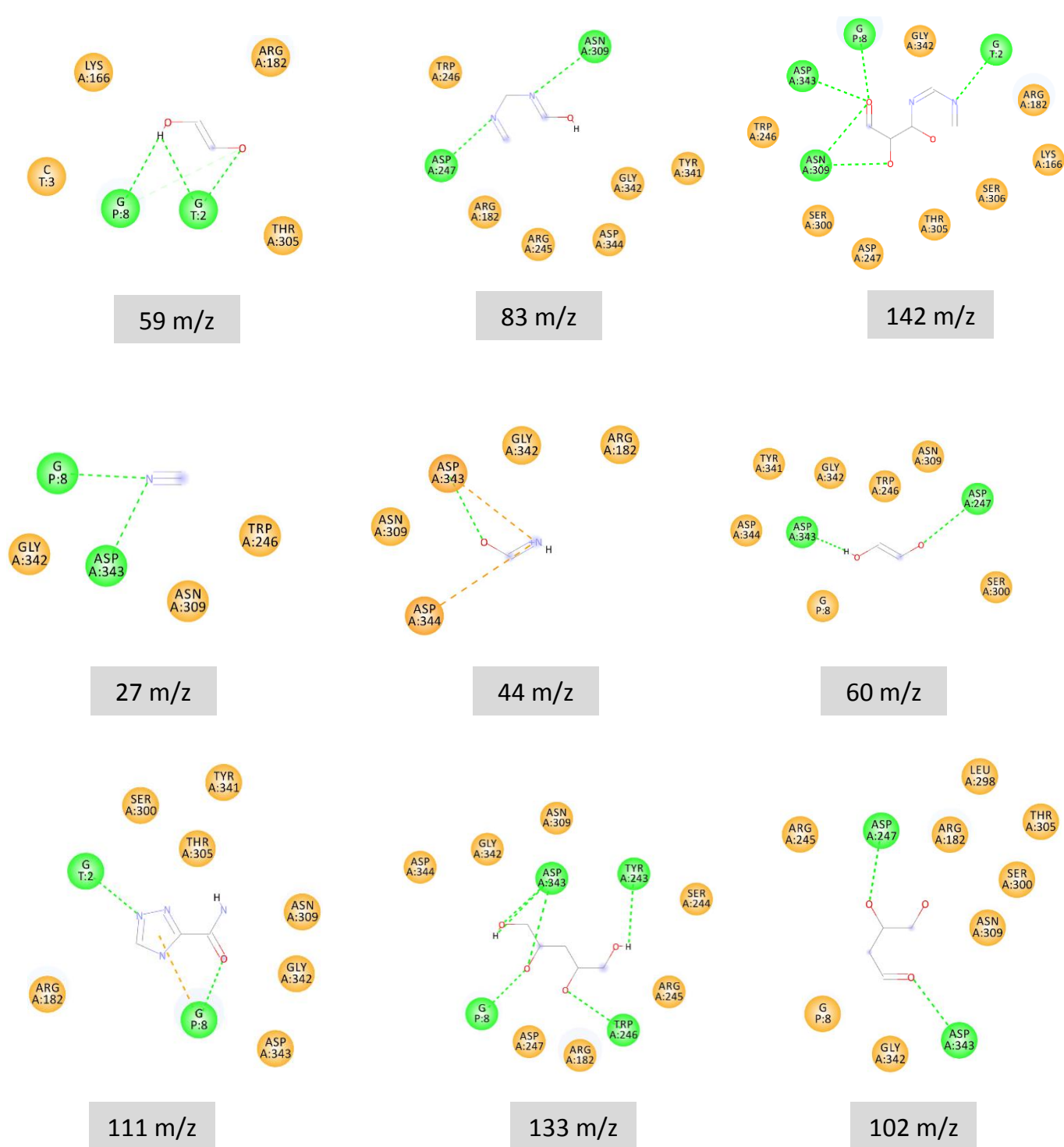
**Figure S.6.7-b.** Intermolecular interactions of the fragments of Remdesivir in the RdRp binding site. Green = hydrogen bond, Orange = hydrophobic interaction.



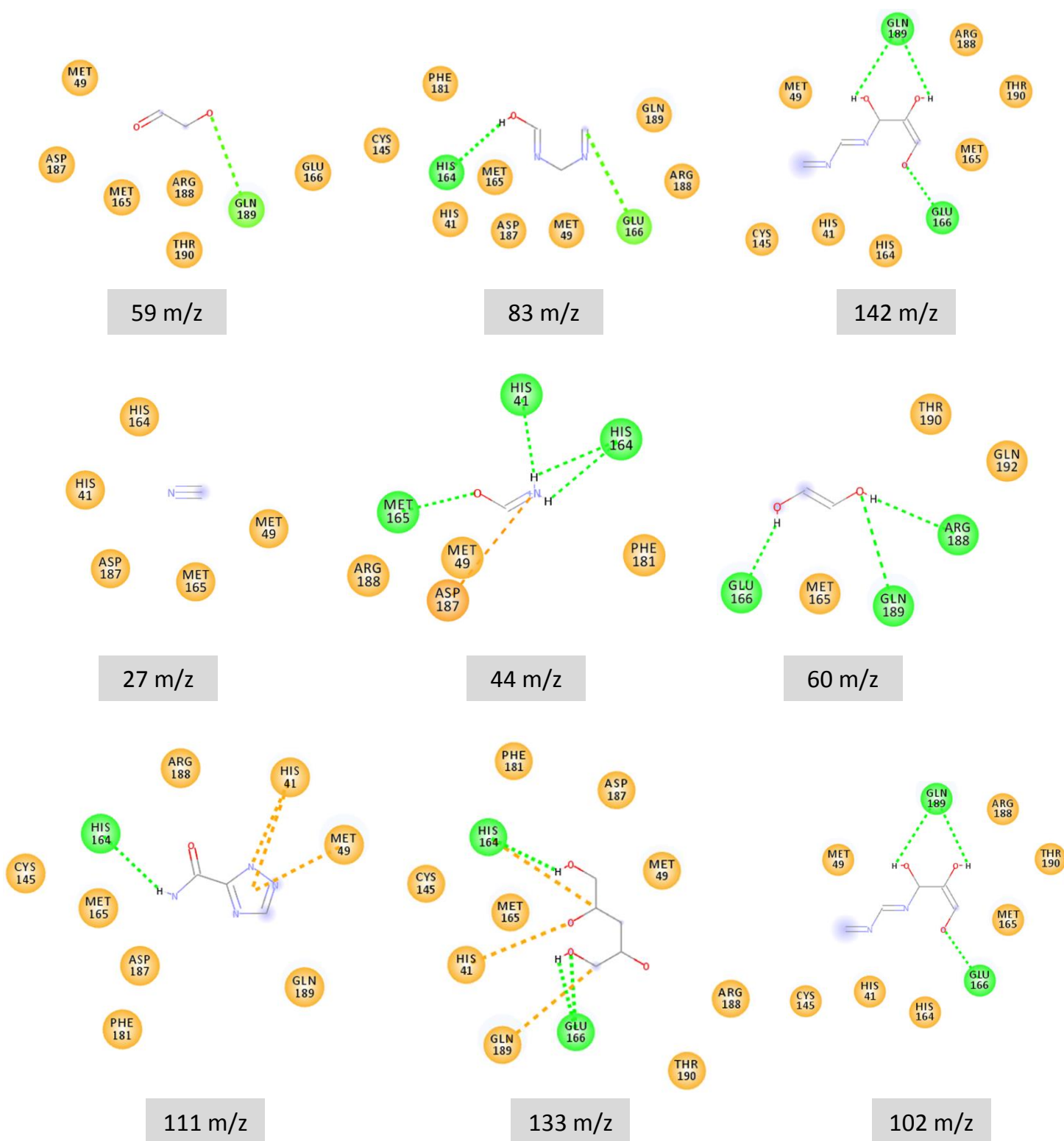
**Figure S.6.8-a.** Intermolecular interactions of the fragments of Remdesivir in the  $M^{\text{pro}}$  binding site. Green = hydrogen bond, Orange = hydrophobic interaction.



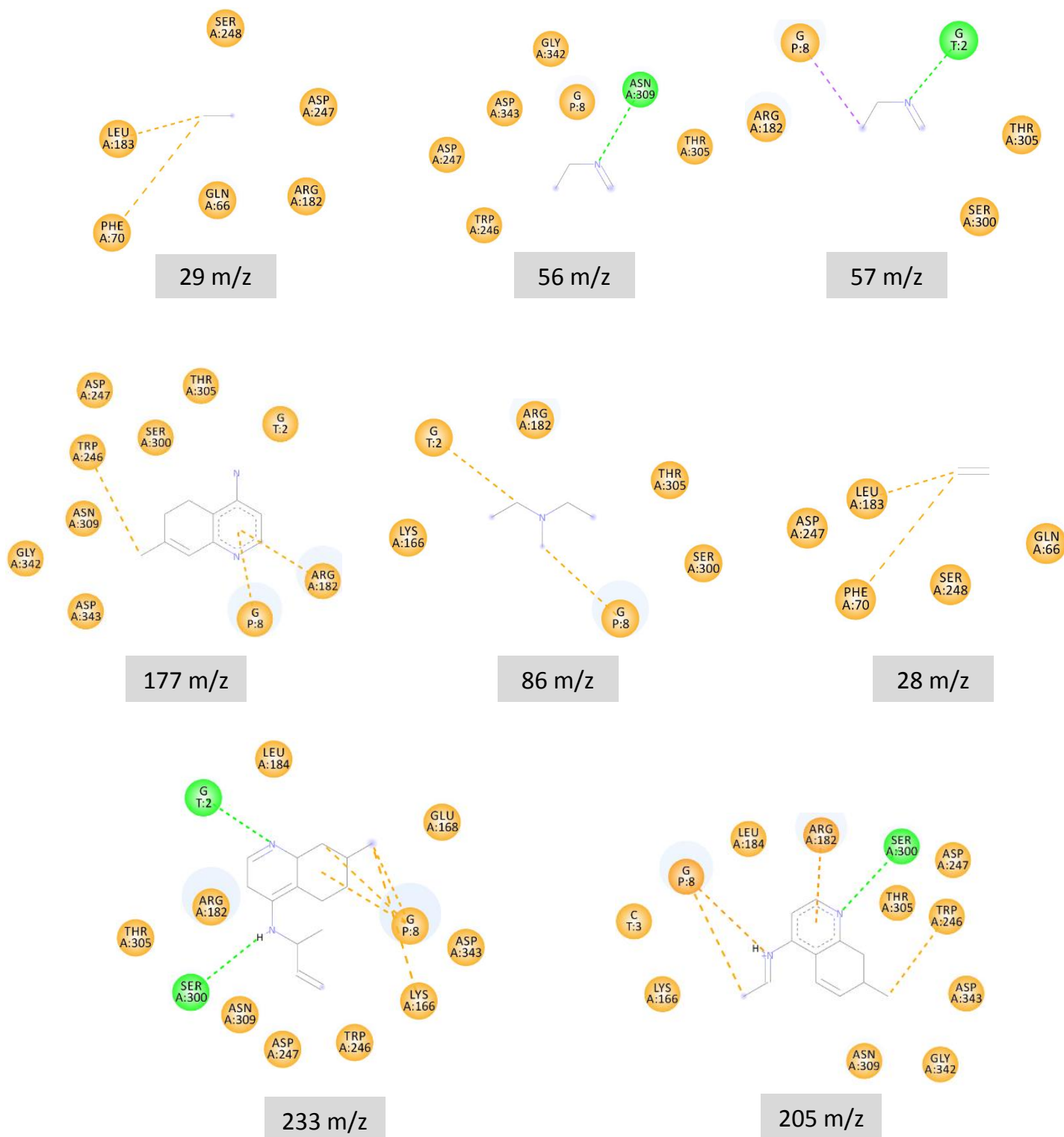
**Figure S.6.8-b.** Intermolecular interactions of the fragments of Remdesivir in the  $M^{Pro}$  binding site. Green = hydrogen bond, Orange = hydrophobic interaction.



**Figure S.6.9.** Intermolecular interactions of the fragments of Ribavirin in the RdRp binding site. Green = hydrogen bond.

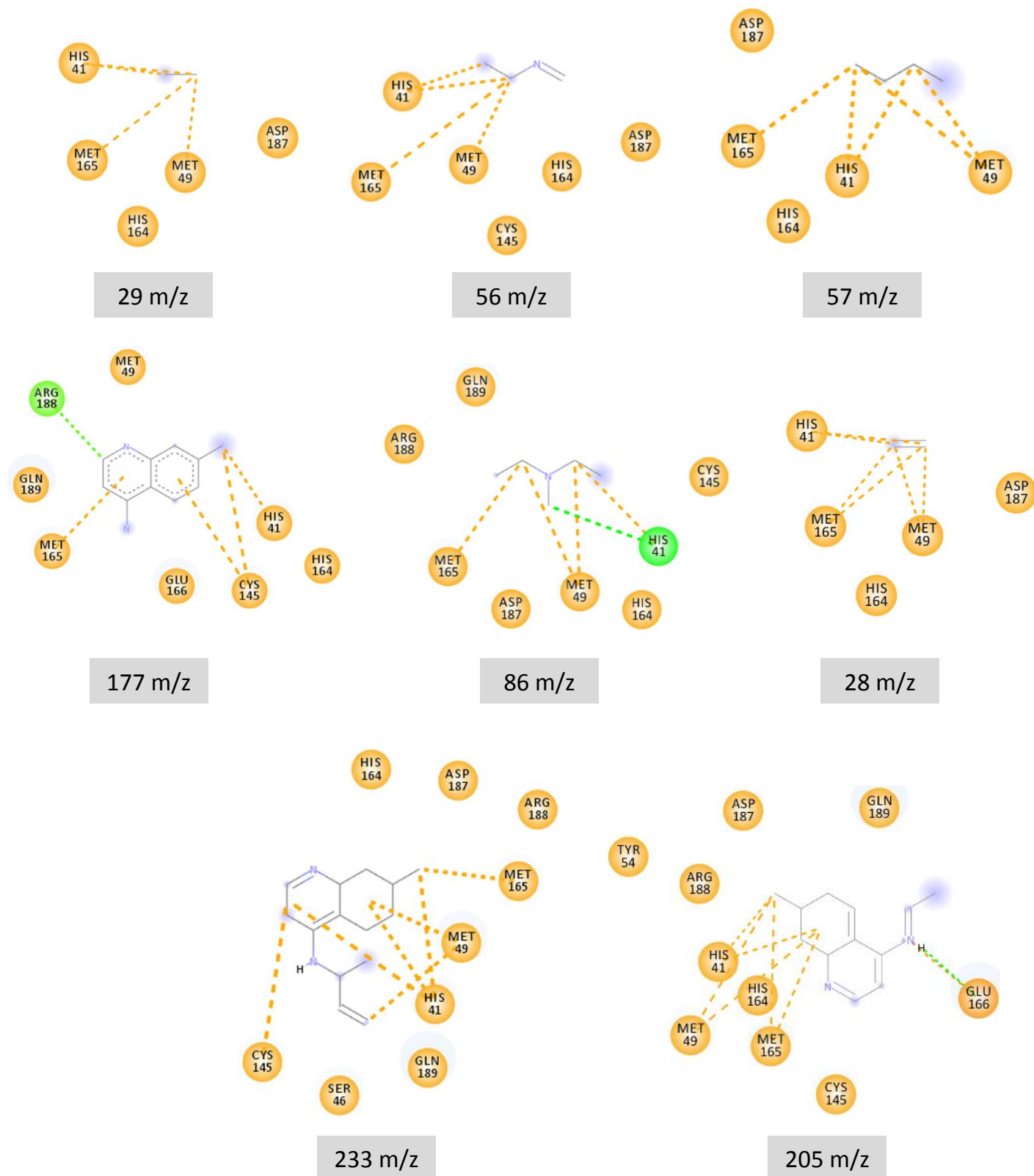


**Figure S.6.10.** Intermolecular interactions of the fragments of Ribavirin in the  $M^{\text{pro}}$  binding site. Green = hydrogen bond, Orange = hydrophobic interaction.

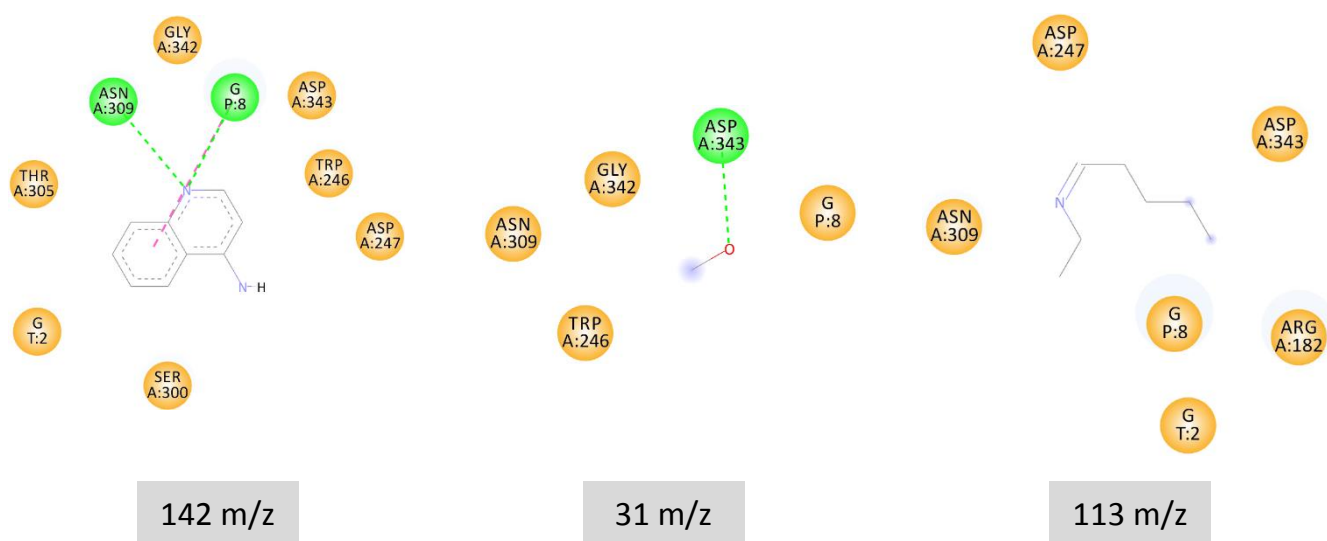


**Figure S.6.11.** Intermolecular interactions of the fragments of Chloroquine in the RdRp binding site. Green = hydrogen bond, Orange = hydrophobic interaction.

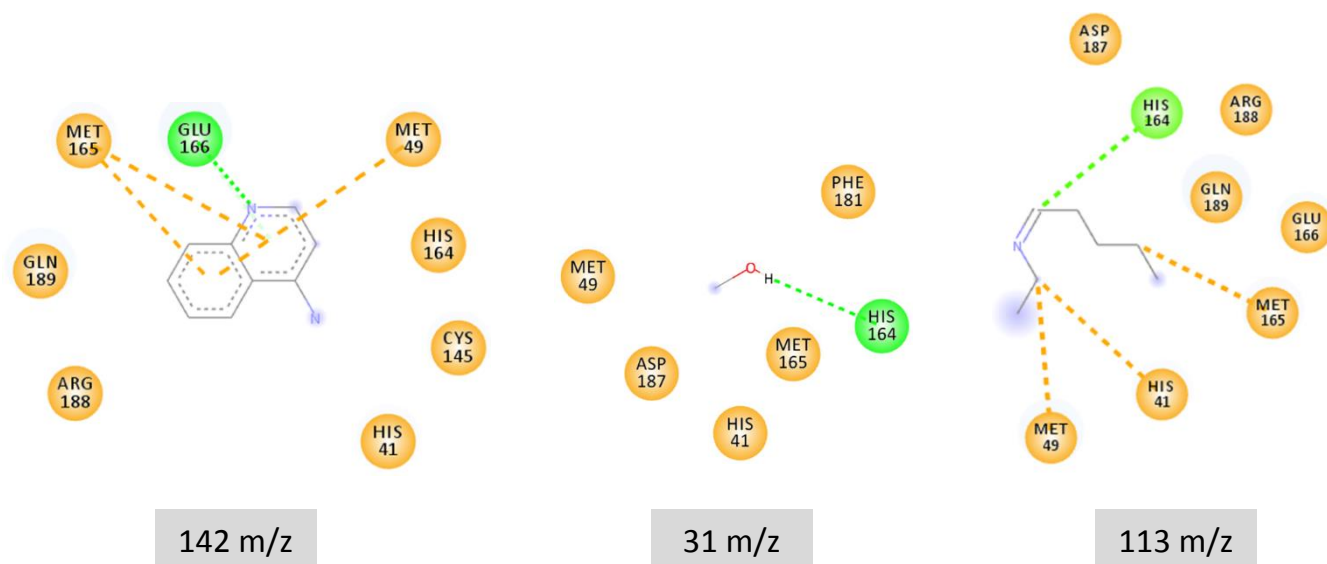




**Figure S.6.12.** Intermolecular interactions of the fragments of Chloroquine in the  $M^{pro}$  binding site. Green = hydrogen bond, Orange = hydrophobic interaction.



**Figure S.6.13.** Intermolecular interactions of the fragments of Hydroxychloroquine in the RdRp binding site. Green = hydrogen bond.



**Figure S.6.14.** Intermolecular interactions of the fragments of Hydroxychloroquine in the M<sup>pro</sup> binding site. Green = hydrogen bond, Orange = hydrophobic interaction.

**REFERENCES**

1. Assis, L. C. *et al.* Nitro Derivatives of Quinoline and Quinoline N-Oxide as Low-Cost Alternative for the Treatment of SARS-CoV-2 Infection. *ResearchSquare* (2020) doi:<https://doi.org/10.21203/rs.3.rs-32468/v1>.
2. Castro, A. A. de, Assis, L. C., Ramalho, T. de C. & Porta, F. de A. La. New in silico insights into the application of the (hydroxy)chloroquine with macrolide antibiotics co-crystals against the SARS-CoV-2 virus. *ResearchSquare* (2020) doi:<https://doi.org/10.21203/rs.3.rs-66640/v1>.
3. Ducharme, J. & Farinotti, R. Clinical Pharmacokinetics and Metabolism of Chloroquine. *Clin. Pharmacokinet.* **31**, 257–274 (1996).
4. Ette, E. I., Essien, E. E., Thomas, W. O. A. & Brown-Awala, E. A. Pharmacokinetics of Chloroquine and Some of Its Metabolites in Healthy Volunteers: A Single Dose Study. *J. Clin. Pharmacol.* **29**, 457–462 (1989).
5. McChesney, E. W., Banks, W. F. & Sullivan, D. J. Metabolism of chloroquine and hydroxychloroquine in albino and pigmented rats. *Toxicol. Appl. Pharmacol.* **7**, 627–636 (1965).
6. Reingruber, H. & Pontel, L. B. Formaldehyde metabolism and its impact on human health. *Curr. Opin. Toxicol.* **9**, 28–34 (2018).
7. Eells, J. T. Formaldehyde Poisoning. *JAMA* **246**, 1237 (1981).

## GENERAL CONCLUSIONS

A more aggressive strain of coronavirus, the so-called SARS-CoV-2, has spread across the planet. Due to its high transmission rate and the significant time-space between infection and manifestation of symptoms, the WHO recently declared this a pandemic. Because of the exponentially growing number of new cases of both infections and deaths, the development of new therapeutic options to help fight this pandemic is urgently needed. In this line, the computational chemistry plays a crucial role in the processes of discovery and development of new drugs for the COVID-19 treatment. From this thesis, we conclude that *in silico* studies can bring about a great contribution toward the rational design of more efficient drugs. Through the computational tools, we were able to investigate, at the atomic and molecular level, the biochemical properties involving a range of drug candidates. In this case, the computational drug repositioning showed itself as the fastest strategy to help in choosing the best candidates for use in clinical trials, contributing to the emergence of new therapeutic options. It is essential the development of ways to accelerate the development of novel therapies against SARS-CoV-2. In this context, computational drug repositioning has intensively been explored as a solid strategy in the search for an effective treatment protocol against SARS-CoV-2 infection, capable of boosting and optimizing novel drug development and discovery. In this line, the computational chemistry provides a range of methods capable of resulting in reduction of time and research costs for researches. In this thesis, our findings are regarded as a promising approach to help combat COVID-19, providing some therapeutic alternatives and computational tools in computer-aided drug design.

**ATTACHMENT**

**Works Developed**

[Ciência e Agrotecnologia](#)

versão impressa ISSN 1413-7054 versão On-line ISSN 1981-1829

Ciênc. agrotec. vol.41 no.5 Lavras set./out. 2017

<https://doi.org/10.1590/1413-70542017415000417>

REVIEW

## Enzimas degradantes de organofosforados: Base molecular e perspectivas para biorremediação enzimática de agroquímicos

### Organophosphorus degrading enzymes: Molecular basis and perspectives for enzymatic bioremediation of agrochemicals

Alexandre Alves de Castro<sup>1</sup>

Ingrid Guarnetti Prandi<sup>2</sup>

Kamil Kuca<sup>3</sup>

Teodorico Castro Ramalho<sup>1</sup> \*

AIMS Microbiology



2017, Volume 3, Issue 1: 108-135. doi: [10.3934/microbiol.2017.1.108](https://doi.org/10.3934/microbiol.2017.1.108)

Research article

[Previous Article](#)

[Next Article](#)

## Computational enzymology for degradation of chemical warfare agents: promising technologies for remediation processes

Alexandre A. de Castro<sup>1</sup>, Letícia C. Assis<sup>1</sup>, Daniela R. Silva<sup>1</sup>, Silviana Corrêa<sup>1</sup>, Tamiris M. Assis<sup>1</sup>, Giovanna C. Gajo<sup>1</sup>, Flávia V. Soares<sup>1</sup>, Teodorico C. Ramalho<sup>1,2</sup>,  














1. Department of Chemistry, Federal University of Lavras, 37200-000, Lavras, Brazil

2. Center for Basic and Applied Research, Faculty of Informatics and Management, University of Hradec Kralove, Rokitanskeho 62, 50003, Czech Republic

Received: 15 December 2016 | Accepted: 14 February 2017 | Published: 14 March 2017

Open Access Article

## Theoretical Studies Applied to the Evaluation of the DFPase Bioremediation Potential against Chemical Warfare Agents Intoxication

by  Flávia V. Soares<sup>1</sup>,  Alexandre A. De Castro<sup>1</sup>,  Ander F. Pereira<sup>1</sup>,  Daniel H. S. Leal<sup>1,2</sup>,  
 Daiana T. Mancini<sup>1</sup>,  Ondrej Krejcar<sup>3</sup> ,  Teodorico C. Ramalho<sup>1,3</sup> ,  Elaine F. F. Da Cunha<sup>1</sup> and  
 Kamil Kuca<sup>3,\*</sup>  

<sup>1</sup> Laboratory of Molecular Modeling, Chemistry Department, Federal University of Lavras, 37200-000 Lavras, MG, Brazil

<sup>2</sup> Department of Health Sciences, Federal University of Espírito Santo, 29932-540 São Mateus, ES, Brazil


<sup>3</sup> Center for Basic and Applied Research, Faculty of Informatics and Management, University Hradec Kralove, 50003 Hradec Kralove, Czech Republic

\* Author to whom correspondence should be addressed.

*Int. J. Mol. Sci.* **2018**, *19*(4), 1257; <https://doi.org/10.3390/ijms19041257>

Research article | [Open Access](#) | Published: 21 February 2018

## A newly developed oxime K203 is the most effective reactivator of tabun-inhibited acetylcholinesterase

[Kamil Kuca](#) , [Kamil Musilek](#), [Daniel Jun](#), [Jana Zdarova-Karasova](#), [Eugenie Nepovimova](#), [Ondrej Soukup](#), [Martina Hrabnova](#), [John Mikler](#), [Tanos C. C. Franca](#), [Elaine F. F. Da Cunha](#), [Alexandre A. De Castro](#), [Martin Valis](#) & [Teodorico C. Ramalho](#)

*BMC Pharmacology and Toxicology* **19**, Article number: 8 (2018) | [Cite this article](#)

2212 Accesses | 23 Citations | 0 Altmetric | [Metrics](#)



Purchase PDF

Review Article

## Insights into the Drug Repositioning Applied to the Alzheimer's Disease Treatment and Future Perspectives

Author(s): Alexandre A. de Castro, Elaine F.F. da Cunha, Ander F. Pereira, Flavia V. Soares, Daniel H.S. Leal, Kamil Kuca, Teodorico C. Ramalho\*

Journal Name: Current Alzheimer Research

Volume 15 , Issue 12 , 2018

DOI : 10.2174/1567205015666180813150703

[Journal Home](#)

[Translate in Chinese](#)



ELSEVIER





Progress in Neurobiology

Volume 169, October 2018, Pages 135-157



Review article

## Insights into the pharmaceuticals and mechanisms of neurological orphan diseases: Current Status and future expectations

Teodorico C. Ramalho <sup>a, b</sup>  , Alexandre A. de Castro <sup>a</sup>, Tássia S. Tavares <sup>a</sup>, Maria C. Silva <sup>a</sup>, Daniela R. Silva <sup>a</sup>, Pedro H. Cesar <sup>a</sup>, Lucas A. Santos <sup>a</sup>, Elaine F.F. da Cunha <sup>a</sup>, Eugenie Nepovimova <sup>c</sup>, Kamil Kuca <sup>c</sup>  





Environmental Pollution  
Volume 242, Part A, November 2018, Pages 863-871



Biotransformation of disperse dyes using nitroreductase immobilized on magnetic particles modified with tosyl group: Identification of products by LC-MS-MS and theoretical studies conducted with DNA ☆

Jefferson Honorio Franco <sup>a</sup> ✉, Bianca F. da Silva <sup>a</sup>, Alexandre A. de Castro <sup>b</sup>, Teodorico C. Ramalho <sup>b</sup>, Maria Isabel Pividori <sup>c</sup>, Maria Valnice Boldrin Zanoni <sup>a</sup>

☆



Ecotoxicology and Environmental Safety  
Volume 160, 30 September 2018, Pages 114-126



Influence of auxochrome group in disperse dyes bearing azo groups as chromophore center in the biotransformation and molecular docking prediction by reductase enzyme: Implications and assessment for environmental toxicity of xenobiotics

Jefferson Honorio Franco <sup>a</sup>, Bianca F. da Silva <sup>a</sup>, Elisangela Franciscan G. Dias <sup>b</sup>, Alexandre A. de Castro <sup>c</sup>, Teodorico C. Ramalho <sup>c</sup>, Maria Valnice Boldrin Zanoni <sup>a</sup> ✉

Issue 19, 2018

[Previous Article](#)[Next Article](#)

From the journal:  
**RSC Advances**

## Peroxonibium inhibits leukemia cell growth†



[Elene C. Pereira-Maia](#),<sup>\*a</sup> [Ivina P. Souza](#),<sup>†a</sup> [Kelen J. R. C. Nunes](#),<sup>†a</sup> [Alexandre A. Castro](#),<sup>†b</sup> [Teodorico C. Ramalho](#),<sup>id †b</sup> [Fernando Steffler](#),<sup>a</sup> [Helio A. Duarte](#),<sup>id a</sup> [Ana Pacheli](#),<sup>id †a</sup> [Poliana Chagas](#)<sup>†a</sup> and [Luiz C. A. Oliveira](#)<sup>\*a</sup>



Science of The Total Environment

Volumes 613–614, 1 February 2018, Pages 1093–1103



### Identification of biotransformation products of disperse dyes with rat liver microsomes by LC-MS/MS and theoretical studies with DNA: Structure-mutagenicity relationship using *Salmonella*/microsome assay

Jefferson Honorio Franco<sup>a</sup>, Bianca F. da Silva<sup>a</sup>, Regina V. Oliveira<sup>b</sup>, Gabriela Meireles<sup>c</sup>, Danielle Palma de Oliveira<sup>c</sup>, Alexandre A. de Castro<sup>d</sup>, Teodorico C. Ramalho<sup>d</sup>, Maria V.B. Zanoni<sup>a</sup>

## Review Article

## Anti-Virulence Strategy against the Multidrug-Resistant Bacterial Pathogen *Pseudomonas aeruginosa*: Pseudolysin (Elastase B) as a Potential Druggable Target

**Author(s):** Anna Clara M. Galdino, Matheus P. de Oliveira, Teodorico C. Ramalho, Alexandre A. de Castro, Marta H. Branquinha\*, André L.S. Santos\*

**Journal Name:** Current Protein & Peptide Science

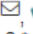





**Volume 20 , Issue 5 , 2019**

**DOI :** 10.2174/1389203720666190207100415

## Open Access

## Review

## Future Therapeutic Perspectives into the Alzheimer's Disease Targeting the Oxidative Stress Hypothesis

by  Jéssika P. Teixeira<sup>1</sup> ,  Alexandre A. de Castro<sup>1</sup> ,  Flávia V. Soares<sup>1</sup> ,  Elaine F. F. da Cunha<sup>1</sup>  and  Teodorico C. Ramalho<sup>1,2,\*</sup> 

<sup>1</sup> Department of Chemistry, Federal University of Lavras, 37200-000 Lavras, Minas Gerais, Brazil

<sup>2</sup> Center for Basic and Applied Research, Faculty of Informatics and Management, University of Hradec Kralove, 500 03 Hradec Kralove, Czech Republic

\* Author to whom correspondence should be addressed.

# Disarming *Pseudomonas aeruginosa* Virulence by the Inhibitory Action of 1,10-Phenanthroline-5,6-Dione-Based Compounds: Elastase B (LasB) as a Chemotherapeutic Target

Anna Clara M. Galdino<sup>1,2</sup>, Lívia Viganor<sup>1,3</sup>, Alexandre A. de Castro<sup>4</sup>, Elaine F. F. da Cunha<sup>4</sup>, Thaís P. Mello<sup>1</sup>, Larissa M. Mattos<sup>2</sup>, Marcos D. Pereira<sup>2</sup>, Mary C. Hunt<sup>3</sup>, Megan O'Shaughnessy<sup>3</sup>, Orla Howe<sup>3</sup>, Michael Devereux<sup>3</sup>, Malachy McCann<sup>5</sup>, Teodorico C. Ramalho<sup>4</sup>, Marta H. Branquinha<sup>1</sup> and André L. S. Santos<sup>1,2\*</sup>

<sup>1</sup>Department of General Microbiology, Institute of Microbiology Paulo de Góes, Federal University of Rio de Janeiro, Rio de Janeiro, Brazil

<sup>2</sup>Postgraduate Program in Biochemistry, Institute of Chemistry, Federal University of Rio de Janeiro, Rio de Janeiro, Brazil

<sup>3</sup>The Centre for Biomimetic and Therapeutic Research, Focas Research Institute, Technological University Dublin, Dublin, Ireland

<sup>4</sup>Department of Chemistry, Federal University of Lavras, Lavras, Brazil

<sup>5</sup>Department of Chemistry, Maynooth University, Maynooth, Ireland



Chemico-Biological Interactions

Volume 309, 25 August 2019, 108671



Slight difference in the isomeric oximes K206 and K203 makes huge difference for the reactivation of organophosphorus-inhibited AChE: Theoretical and experimental aspects

Daniel A. Polisel<sup>a</sup>, Alexandre A. de Castro<sup>a</sup>, Daiana T. Mancini<sup>a</sup>, Elaine F.F. da Cunha<sup>a, b, 1</sup>, Tanos C.C. França<sup>b, c</sup>, Teodorico C. Ramalho<sup>a, e, 1</sup> ✉, Kamil Kuca<sup>d, e, 1</sup> ✉

[Submit an article](#)[Journal homepage](#)

Review

# Non-conventional compounds with potential therapeutic effects against Alzheimer's disease

Alexandre A. de Castro, Flávia V. Soares, Ander F. Pereira, Daniel A. Polisel, Melissa S. Caetano, Daniel H. S. Leal, ...show all

Pages 375-395 | Received 20 Oct 2018, Accepted 15 Apr 2019, Accepted author version posted online: 19 Apr 2019, Published online: 29 Apr 2019





Chemico-Biological Interactions

Volume 308, 1 August 2019, Pages 323-331



## Development of technologies applied to the biodegradation of warfare nerve agents: Theoretical evidence for asymmetric homogeneous catalysis

Ander Francisco Pereira <sup>a</sup>, Alexandre A. de Castro <sup>a</sup>, Flavia Villela Soares <sup>a</sup>, Daniel Henriques Soares Leal <sup>a, c</sup>, Elaine F.F. da Cunha <sup>a</sup>, Daiana Teixeira Mancini <sup>a</sup>, Teodorico C. Ramalho <sup>a, b</sup>  

Submit an article

Journal homepage

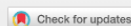
Research Article

# Asymmetric biodegradation of the nerve agents Sarin and VX by human dUTPase: chemometrics, molecular docking and hybrid QM/MM calculations

Alexandre A. de Castro, Flávia Villela Soares, Ander Francisco Pereira, Telles Cardoso Silva, Daniela Rodrigues Silva, Daiana Teixeira Mancini, ... show all

Pages 2154-2164 | Received 16 Jan 2018, Accepted 20 Mar 2018, Accepted author version posted online: 25 Jul 2018, Published online: 09 Jan 2019

Download citation <https://doi.org/10.1080/07391102.2018.1478751>



International Journal of  
*Molecular Sciences*

Submit to this Journal

Review for this Journal

Edit a Special Issue

## Article Menu

### Article Overview

- Abstract
- Open Access and Permissions
- Share and Cite
- Article Metrics
- Related Articles

Open Access Review

## Recent Developments in Metal-Based Drugs and Chelating Agents for Neurodegenerative Diseases Treatments

by Thais A. Sales<sup>1</sup>, Ingrid G. Prandi<sup>1</sup>, Alexandre A. de Castro<sup>1</sup>, Daniel H. S. Leal<sup>2</sup>, Elaine F. F. da Cunha<sup>1</sup>, Kamil Kuca<sup>3,4,\*†</sup> and Teodorico C. Ramalho<sup>1,3,\*†</sup>

<sup>1</sup> Laboratory of Molecular Modeling, Department of Chemistry, Federal University of Lavras, 37200-000 Lavras, MG, Brazil

<sup>2</sup> Department of Health Sciences, Federal University of Espírito Santo, 29932-540 São Mateus, ES, Brazil

<sup>3</sup> Department of Chemistry, Faculty of Science, University of Hradec Kralove, 500 03 Hradec Kralove, Czech Republic

<sup>4</sup> Biomedical Research Center, University Hospital Hradec Kralove, 500 03 Hradec Kralove, Czech Republic

\* Authors to whom correspondence should be addressed.

† These authors contributed equally to this work.

*Int. J. Mol. Sci.* **2019**, *20*(8), 1829; <https://doi.org/10.3390/ijms20081829>



International Journal of  
*Molecular Sciences*

Submit to this Journal

Review for this Journal

Edit a Special Issue

## Article Menu

### Article Overview ^

- Abstract
- Open Access and Permissions
- Share and Cite
- Article Metrics
- Related Articles
- Order Article Reprints

Article Versions ^

Open Access Article

## Understanding the Interaction Modes and Reactivity of Trimedoxime toward *Mm*AChE Inhibited by Nerve Agents: Theoretical and Experimental Aspects

by Alexandre A. de Castro <sup>1</sup> , Daniel A. Polisel <sup>1</sup> , Bruna T. L. Pereira <sup>1</sup> , Elaine F. F. da Cunha <sup>1,\*</sup> , Kamil Kuca <sup>2,3,\*</sup> , Eugenie Nepovimova <sup>3</sup> and Teodorico C. Ramalho <sup>1,3,\*</sup>

<sup>1</sup> Department of Chemistry, Federal University of Lavras, 37200-000 Lavras, Brazil

<sup>2</sup> Biomedical Research Center, University Hospital Hradec Kralove, 500 05 Hradec Kralove, Czech Republic

<sup>3</sup> Department of Chemistry, Faculty of Science, University of Hradec Kralove, 500 03 Hradec Kralove, Czech Republic

\* Authors to whom correspondence should be addressed.

*Int. J. Mol. Sci.* **2020**, *21*(18), 6510; <https://doi.org/10.3390/ijms21186510>

Received: 15 August 2020 / Revised: 31 August 2020 / Accepted: 2 September 2020 / Published: 5 September 2020

(This article belongs to the Special Issue Computational Studies of Biomolecules)

View Full-Text

Download PDF

Browse Figures

Citation Export



Ecotoxicology and Environmental Safety

Volume 202, 1 October 2020, 110895



## Experimental and theoretical affinity and catalysis studies between halogenated phenols and peroxidases: Understanding the bioremediation potential

Raphael Resende Bretz <sup>a</sup>, Alexandre A. de Castro <sup>b</sup>, Igor F. Lara Ferreira <sup>a</sup>, Teodorico C. Ramalho <sup>b, c</sup>,  
Maria Cristina Silva <sup>a</sup>

Research Articles

# Oxime K074 – *in vitro* and *in silico* reactivation of acetylcholinesterase inhibited by nerve agents and pesticides

Kamil Kuca , Kamil Musilek , Daniel Jun , Eugenie Nepovimova , Ondrej Soukup , Jan Korabecny , ...show all

Pages 157-166 | Received 01 Apr 2018, Accepted 03 Jun 2018, Published online: 31 Jul 2018

 Download citation  <https://doi.org/10.1080/15569543.2018.1485702> Check for updates Full Article Figures & data References Citations Metrics Reprints & Permissions

Get access



Submit to this Journal

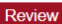
Review for this Journal

Edit a Special Issue






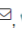









## Article Menu

### Article Overview

- Abstract
- Open Access and Permissions

Open Access 

## Trends in the Recent Patent Literature on Cholinesterase Reactivators (2016–2019)

by  Alexandre A. de Castro <sup>1</sup> ,  Leticia C. Assis <sup>1</sup> ,  Flávia V. Soares <sup>1</sup> ,  Kamil Kuca <sup>2,\*</sup>  ,  Daniel A. Polisel <sup>1</sup> ,  Elaine F. F. da Cunha <sup>1</sup>  and  Teodorico C. Ramalho <sup>1,2,\*</sup> <sup>1</sup> Department of Chemistry, Federal University of Lavras, Lavras 37200-000, Brazil<sup>2</sup> Department of Chemistry, Faculty of Science, University of Hradec Kralove, 500 03 Hradec Kralove, Czech Republic

\* Authors to whom correspondence should be addressed.

† These authors contributed equally to this work.

*Biomolecules* 2020, 10(3), 436; <https://doi.org/10.3390/biom10030436>





Bioorganic Chemistry

Volume 109, April 2021, 104662



## Cathepsin K inhibitors based on 2-amino-1,3,4-oxadiazole derivatives

Talita B. Gontijo <sup>a</sup>, Patrícia S. Lima <sup>b</sup>, Marcelo Y. Icimoto <sup>b</sup>, Raquel Leão Neves <sup>b</sup>, Érika C. de Alvarenga <sup>c</sup>, Adriana K. Carmona <sup>b</sup>, Alexandre A. de Castro <sup>d</sup>, Teodorico C. Ramalho <sup>d</sup>, Eufrânio N. da Silva Júnior <sup>a</sup>, Rossimiriam P. de Freitas <sup>a</sup> 